

UC Irvine

UC Irvine Previously Published Works

Title

Vibrational Spectroscopic Map, Vibrational Spectroscopy, and Intermolecular Interaction.

Permalink

<https://escholarship.org/uc/item/6zz3q8x3>

Journal

Chemical reviews, 120(15)

ISSN

0009-2665

Authors

Baiz, Carlos R
Błasiak, Bartosz
Bredenbeck, Jens
[et al.](#)

Publication Date

2020-08-01

DOI

10.1021/acs.chemrev.9b00813

Supplemental Material

<https://escholarship.org/uc/item/6zz3q8x3#supplemental>

Peer reviewed

Vibrational Spectroscopic Map, Vibrational Spectroscopy, and Intermolecular Interaction

Carlos R. Baiz¹, Bartosz Błasiak², Jens Bredenbeck³, Minhaeng Cho^{*,4,5}, Jun-Ho Choi⁶, Steven A. Corcelli⁷, Arend G. Dijkstra⁸, Chi-Jui Feng⁹, Sean Garrett-Roe¹⁰, Nien-Hui Ge¹¹, Magnus W. D. Hanson-Heine¹², Jonathan D. Hirst¹², Thomas L. C. Jansen¹³, Kijeong Kwac⁴, Kevin J. Kubarych¹⁴, Casey H. Londergan¹⁵, Hiroaki Maekawa¹¹, Mike Reppert¹⁶, Shinji Saito¹⁷, Santanu Roy¹⁸, James L. Skinner¹⁹, Gerhard Stock²⁰, John E. Straub²¹, Megan C. Thielges²², Keisuke Tominaga²³, Andrei Tokmakoff⁹, Hajime Torii²⁴, Lu Wang²⁵, Lauren J. Webb²⁶, and Martin T. Zanni²⁷

¹Department of Chemistry, University of Texas at Austin, Austin, TX 78712, U.S.A.

²Department of Physical and Quantum Chemistry, Wrocław University of Science and Technology, Wybrzeże Wyspiańskiego 27, 50-370 Wrocław, Poland. ³Johann Wolfgang Goethe-University, Institute of Biophysics, Max-von-Laue-Str. 1, 60438, Frankfurt am Main, Germany. ⁴Center for Molecular Spectroscopy and Dynamics, Seoul 02841, Republic of Korea.

⁵Department of Chemistry, Korea University, Seoul 02841, Republic of Korea. ⁶Department of Chemistry, Gwangju Institute of Science and Technology, Gwangju 61005, Republic of Korea.

⁷Department of Chemistry and Biochemistry, University of Notre Dame, Notre Dame, IN 46556, U.S.A. ⁸School of Chemistry and School of Physics and Astronomy, University of Leeds, Leeds LS2 9JT, U.K. ⁹Department of Chemistry, James Franck Institute and Institute for Biophysical

Dynamics, University of Chicago, Chicago, IL 60637, U.S.A. ¹⁰Department of Chemistry, University of Pittsburgh, Pittsburgh, PA 15260, U.S.A. ¹¹Department of Chemistry, University

of California at Irvine, Irvine, CA 92697-2025, U.S.A. ¹²School of Chemistry, University of Nottingham, Nottingham, University Park, Nottingham, NG7 2RD, U.K. ¹³University of

Groningen, Zernike Institute for Advanced Materials, Nijenborgh 4, 9747 AG Groningen, The Netherlands. ¹⁴Department of Chemistry, University of Michigan, 930 N. University Ave., Ann

Arbor, MI 48109, U.S.A. ¹⁵Department of Chemistry, Haverford College, Haverford, Pennsylvania 19041, U.S.A. ¹⁶Chemical Physics Theory Group, Department of Chemistry,

University of Toronto, Toronto, Ontario M5S 3H6, Canada. ¹⁷Department of Theoretical and Computational Molecular Science, Institute for Molecular Science, Myodaiji, Okazaki, 444-

8585, Japan. ¹⁸Chemical Sciences Division, Oak Ridge National Laboratory, Oak Ridge, Tennessee 37831-6110, U.S.A. ¹⁹Institute for Molecular Engineering, University of Chicago,

Chicago, IL 60637, U.S.A. ²⁰Biomolecular Dynamics, Institute of Physics, Albert Ludwigs University, 79104 Freiburg, Germany. ²¹Department of Chemistry, Boston University, Boston,

MA 02215, U.S.A. ²²Department of Chemistry, Indiana University, 800 East Kirkwood, Bloomington, Indiana 47405, U.S.A. ²³Molecular Photoscience Research Center, Kobe

University, Nada, Kobe 657-0013, Japan ²⁴Department of Applied Chemistry and Biochemical Engineering, Faculty of Engineering, and Department of Optoelectronics and Nanostructure

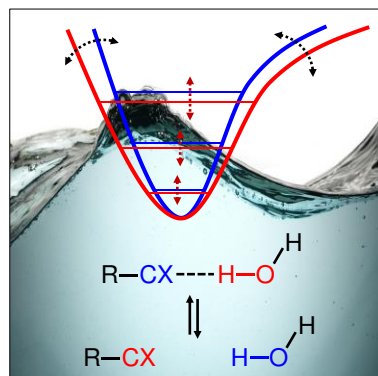
Science, Graduate School of Science and Technology, Shizuoka University, 3-5-1 Johoku, Naka-Ku, Hamamatsu 432-8561, Japan. ²⁵Department of Chemistry and Chemical Biology,

Institute for Quantitative Biomedicine, Rutgers University, 174 Frelinghuysen Road, Piscataway, NJ 08854, U.S.A. ²⁶Department of Chemistry, The University of Texas at Austin,

1 105 E. 24th Street, STOP A5300, Austin, Texas 78712, U.S.A. ²⁷Department of Chemistry,
2 University of Wisconsin-Madison, Madison, Wisconsin 53706-1396, U.S.A.

3
4 *Email: mcho@korea.ac.kr (MC)

5
6 **Abstract.** Vibrational spectroscopy is an essential tool in
7 chemical analyses, biological assays, and studies of functional
8 materials. Over the past decade, various coherent nonlinear
9 vibrational spectroscopic techniques have been developed and
10 enabled researchers to study time-correlations of the fluctuating
11 frequencies that are directly related to solute-solvent dynamics,
12 dynamical changes in molecular conformations and local
13 electrostatic environments, chemical and biochemical
14 reactions, protein structural dynamics and functions,
15 characteristic processes of functional materials, and so on. In
16 order to gain incisive and quantitative information on the local electrostatic environment,
17 molecular conformation, protein structure and inter-protein contacts, ligand binding kinetics,
18 and electric and optical properties of functional materials, a variety of vibrational probes have
19 been developed and site-specifically incorporated into molecular, biological, and material
20 systems for time-resolved vibrational spectroscopic investigation. However, still, an all-
21 encompassing theory that describes the vibrational solvatochromism, electrochromism, and
22 dynamic fluctuation of vibrational frequencies has not been completely established mainly due
23 to the intrinsic complexity of intermolecular interactions in condensed phases. In particular,
24 the amount of data obtained from the linear and nonlinear vibrational spectroscopic
25 experiments has been rapidly increasing, but the lack of a quantitative method to interpret these
26 measurements has been one major obstacle in broadening the applications of these methods.
27 Among various theoretical models, one of the most successful approaches is a semi-empirical
28 model generally referred to as the vibrational spectroscopic map that is based on a rigorous
29 theory of intermolecular interactions. Recently, genetic algorithm, neural network, and
30 machine learning approaches have been applied to the development of vibrational
31 solvatochromism theory. In this review, we provide comprehensive descriptions of the
32 theoretical foundation and various examples showing its extraordinary successes in the
33 interpretations of experimental observations. In addition, a brief introduction to a newly created
34 repository website (<http://frequencymap.org>) for vibrational spectroscopic maps is presented.
35 We anticipate that a combination of the vibrational frequency map approach and state-of-the-
36 art multidimensional vibrational spectroscopy will be one of the most fruitful ways to study the
37 structure and dynamics of chemical, biological, and functional molecular systems in the future.



38

39

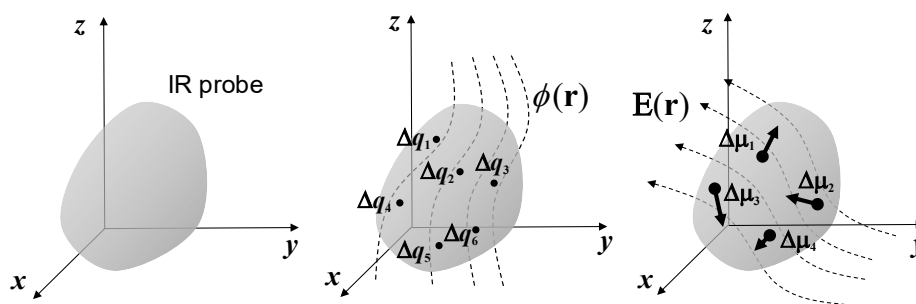
1	Contents
2	
3	1. Introduction
4	2. A Brief Theoretical Account of Vibrational Spectroscopy
5	2.1. Radiation-matter interaction and time-dependent perturbation theory
6	2.2. Linear response vibrational spectroscopy
7	2.3. Time-resolved vibrational spectroscopy
8	2.4. Two-dimensional lineshape analysis and spectral diffusion
9	2.5. Numerical integration of the vibrational Schrödinger equation
10	3. Vibrational Solvatochromism
11	3.1. Intermolecular interaction potential and its solute-solvent separability
12	3.2. Theoretical foundations of vibrational spectroscopic mapping
13	3.3. Vibrational solvatochromism: Bulk phenomenological descriptions
14	3.4. Onsager reaction field theory: Dipolar solute and <i>continuum</i> solvent model
15	3.5. Electrostatic effect: Distributed multipole analysis
16	3.6. Electrostatic and non-electrostatic interactions: Effective fragment potential
17	approach
18	4. Semiempirical Approaches: Vibrational Spectroscopic Maps
19	4.1. General consideration and motivation: Linear combination of basis functions
20	based on physical approximations
21	4.2. General parameterization method
22	4.3. Amide I vibration: Frequency and coupling maps
23	4.4. Amide I vibration: Isotope-labeled proteins
24	4.5. Amide II and III vibrations
25	4.6. Nitrile stretch
26	4.7. Thiocyanato stretch
27	4.8. Selenothiocyano stretch
28	4.9. Azido stretch
29	4.10. Carbonmonoxy stretch
30	4.11. Ester carbonyl stretch
31	4.12. Carbonate carbonyl stretch
32	4.13. Water OH and OD stretch modes: Frequency map, non-Condon effect, and
33	anharmonicity
34	4.14. Strongly correlated OH stretch modes: Local mode or collective mode
35	4.15. C-D stretch: Non-perturbative IR probe
36	4.16. S=O stretch
37	4.17. Phosphate modes
38	4.18. Nucleic acid base modes
39	4.19. Other vibrational frequency maps
40	4.19.1. Alcohols
41	4.19.2. Water bending mode
42	4.19.3. Mapping of strongly coupled vibrations
43	5. Repository, Perspective, and a few Concluding Remarks
44	5.1. Vibrational frequency map repository
45	5.2. Format of the deposited map file

1	5.3. New approaches based on genetic algorithm, neural network, and machine
2	learning
3	5.4. Perspective
4	5.5. Summary and a few concluding remarks
5	6. Glossary of Acronyms
6	Author Information
7	Acknowledgments
8	References
9	

1. Introduction

The vibrational spectra of a polyatomic molecule, which depend strongly on its chemical structure and interactions with the surrounding environment and dynamical transformations between multiple conformations, can be accurately measured with linear absorption and inelastic light scattering spectroscopy in both the gas and condensed phases.^{1,2} As such, Fourier-transform IR absorption and Raman scattering spectroscopy have become essential tools in chemical analyses, biological assays, and studies of functional materials. Over the past decade, we have witnessed revolutionary developments in coherent nonlinear vibrational spectroscopy such as multidimensional electronic, IR, THz, IR-Raman, IR-vis, vis-IR, and THz-Raman techniques.³⁻³⁷ From the coherent multidimensional spectroscopy measurements, researchers have extracted the solvation-induced frequency shifts and the time-correlations of the fluctuating frequencies and provided crucial insights into the spontaneously fluctuating motions of solvent molecules, dynamical changes in molecular conformations and local electrostatic environments, chemical and biochemical reactions, protein structural dynamics and functions, characteristic processes of functional materials, and so on.

To quantitatively analyze and interpret the spectroscopic observations, researchers have site-specifically introduced vibrational probes into molecular, biological, and material systems using a variety of organic and biochemical techniques.³⁸⁻⁵¹ Such vibrational probes could be invasive when they are added to a solvated molecular system via their hydrogen-bonding interactions with surrounding solvent molecules or biomolecular residues. However, they are still significantly smaller than fluorophores, which makes them attractive probes for studying local environments. These IR-probe-labeled molecules, proteins, nucleic acids, functional materials, and chemically reactive systems have been subject to linear and nonlinear vibrational spectroscopic investigations to gain incisive and quantitative information on the local electric field, molecular conformation, protein contacts, energy transfer, ligand binding kinetics, and function-defining features of materials. This rapidly expanding library of experimental results has been reviewed recently by a few groups of researchers.³⁸⁻⁴² However, the data generated through these experiments have inevitably required an interpretive method with atom-level chemical accuracy. Despite prolonged efforts in this area, an all-encompassing theory that describes the vibrational solvatochromism, electrochromism, and dynamic fluctuation of vibrational frequencies and how they reflect the chemistry and biology of the molecules has not been established. This is not only because the intermolecular interactions in the condensed phases are intrinsically complex,⁵²⁻⁶⁵ but also because the vibrational frequency shifts induced by the varying intermolecular interactions are very small quantities, e.g., fractions of thermal energy, and are difficult to model even with high-level quantum chemistry calculation methods.



$$\omega = \omega_0 + \sum_x \Delta q_x \phi(\mathbf{r}_x) - \sum_j \Delta \mu_j \cdot \mathbf{E}(\mathbf{r}_j)$$

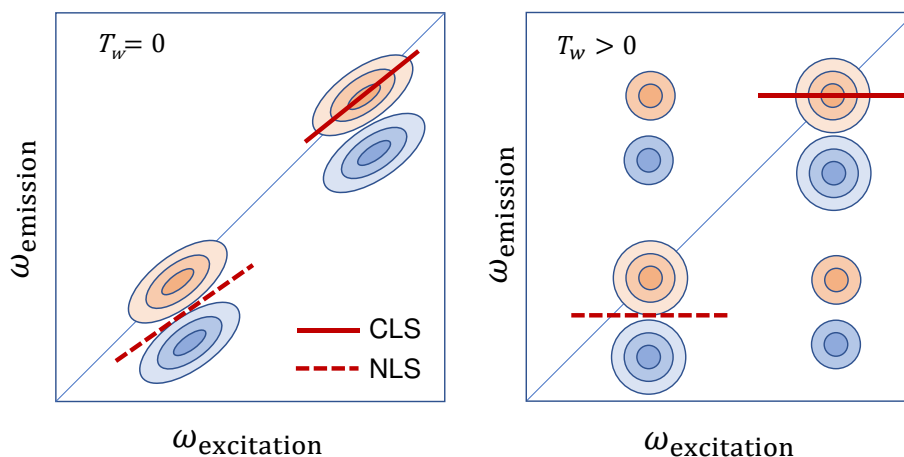
Figure 1. Vibrational frequency mapping with solvent electric potential and field. The vibrational frequency ω of a normal mode of an IR probe is mapped onto a set of points, called distributed sites, that interact with the electrostatic potential ϕ and electric field \mathbf{E} exerted by the molecular environment. Note that the map parameters Δq_x , which are vibrational solvatochromic charges, are scalar quantities whereas $\Delta \mu_x$, which are vibrational solvatochromic dipoles, are Cartesian vectors. The vibrational reference frequency, ω_0 , which could also be a part of the map, corresponds to that of the IR probe in the absence of solvent electrostatic potential and electric field.

To describe vibrational solvatochromic effects on molecular spectra quantitatively, a community of researchers have worked assiduously to find systematic and theoretically sound approaches by considering electric potential and field expansion of intermolecular interaction, distributed multipole analysis, effective fragment potential, and/or hybrid quantum chemistry-molecular mechanics simulation methods. They have designed a series of *ab initio*, semiempirical, or empirical models for specific IR probes of interest and referred to them as *vibrational spectroscopic maps*, which we will abbreviate jointly as the VSMs in this review. Using a rigorous theory of intermolecular interactions, extensive *ab initio* calculation results, and sometimes experimentally measured spectroscopic data, a variety of VSMs have been developed and successfully used to interpret the linear and nonlinear vibrational spectroscopic signals of complex systems at the molecular level.^{38,40,66-69} An example of such a vibrational frequency map is schematically depicted in Figure 1. The vibrational frequency of a localized vibrational mode is mapped onto a set of points, called the distributed sites, which are located within the IR chromophore and sense the spatial distribution of local electrostatic potential and electric field around it much like an antenna. Therefore, the VSMs correctly capture the sensitivity of the IR chromophores to their electrostatic environment and can be readily applied to study spontaneous fluctuation-induced chemical and physical processes in the condensed phases with unprecedented time and spatial resolution, in conjunction with the coherent nonlinear vibrational spectroscopy experiments.

To demonstrate the working principles of linear and nonlinear vibrational spectroscopy techniques, we first note that molecular spectroscopy involves an interaction of the oscillating charged particles in a molecule with an external electromagnetic field whose frequency is close to one of the vibrational or electronic oscillations. Upon resonance between the molecular vibrations and the electromagnetic waves, the quantum transition amplitude becomes very large, which results in a high transition probability between two vibrational eigenstates of the

1 molecule. IR absorption spectroscopy measures the distribution of these transition probabilities
 2 by detecting the attenuation of the incident IR beam, and Raman spectroscopy probes the
 3 inelastic light scattering cross-section of the molecule of interest.

4 As one of the recent additions to the inventory of molecular spectroscopic techniques,
 5 coherent multidimensional vibrational spectroscopy^{4,5,70} can be considered as a vibrational
 6 analog of multidimensional NMR spectroscopy.^{71,72} In general, such an experiment involves
 7 multiple ultrashort pulses with controlled delay times. More specifically, a series of coherent
 8 laser pulses with specific relative phases are used to interrogate the molecular system and to
 9 probe the correlation between distinctive vibrational transitions at different times. These pulses
 10 induce multiple transitions in the molecule, create nonlinear polarization in the system, and
 11 generate the electric field that carries the quantitative information about the multi-point time
 12 correlations of these vibrational transitions. Thus, the detected signal is intrinsically
 13 multidimensional in the time domain, and its Fourier transforms with respect to the judiciously
 14 chosen delay times give the time-resolved multidimensional spectra. For example, coherent
 15 two-dimensional (2D) vibrational spectroscopy employs three femtosecond laser pulses in the
 16 IR frequency range to induce the third-order polarization in molecular systems, which produces
 17 the third-order electric field oscillating with a frequency determined by the molecular
 18



19 **Figure 2.** Schematic diagram of the 2D IR spectra of two oscillators. The x and y axes represent the
 20 excitation (pump) and emission (probe) frequencies, respectively. Here, it should be mentioned that
 21 sometimes 2D spectra are plotted with the two axes swapped. Two diagonal peaks with positive (red)
 22 amplitudes originate from the ground-state bleach and stimulated emission, whereas those with
 23 negative (blue) amplitudes are from the excited-state absorption. The center line slope (CLS) and nodal
 24 line slope (NLS) are related to the frequency-frequency correlation function and the inhomogeneity of
 25 the transition frequencies.⁷³ If the two oscillators are coupled with each other via wave function overlap,
 26 one can find cross-peaks at zero waiting time. If the two oscillators exchange energy or undergo
 27 chemical exchange, the cross-peaks in the off-diagonal region of the 2D IR spectrum appear as the
 28 waiting time, T_w , increases.
 29

30
 31 vibrational frequency. As demonstrated in Figure 2, the generated signal electric field can be
 32 measured and presented in two frequency dimensions that are conjugate to the time intervals
 33 between the first and second pulses, τ , and between the third pulse and the detection, t . One
 34 can then plot a series of 2D IR spectra with respect to the waiting time, T_w , which is defined as

1 the time interval between the second and the third pulses, to track the time evolution of the
2 vibrational excitations.

3 Clearly, 2D vibrational spectroscopy is an ultrafast measurement technique. In a 2D
4 spectrum, the changes of the diagonal and off-diagonal peaks provide unique information on
5 the molecular vibrations, which cannot be extracted from the conventional one-dimensional
6 vibrational spectroscopy. To name a few, these include the homogeneous and inhomogeneous
7 line-broadenings, the anharmonic frequency shift of a given normal mode, the solute-solvent
8 interaction induced spectral diffusion, and mode-mode vibrational coupling constants. As a
9 result, 2D IR and other multidimensional spectroscopy techniques have been used as powerful
10 tools for studying (i) the structure and dynamics of peptides,⁷⁴⁻⁸² proteins,^{25,44,83-92} protein-
11 ligand complexes,⁹³ DNA,⁹⁴⁻⁹⁷ RNA,⁹⁸ and lipid bilayers,^{99,100} (ii) the energy transfer dynamics
12 between coupled oscillators in condensed phases,^{23,101-103} (iii) the hydrogen-bonding (H-
13 bonding) structure and dynamics of liquid water and its isotopologues,^{104,105} (iv) the
14 configurational and H-bonding dynamics of biomolecules,^{106,107} (v) the molecular exciton
15 dynamics in photovoltaic materials,¹⁰⁸ etc.

16 The amount of data obtained from the linear and nonlinear vibrational spectroscopic
17 experiments has been rapidly increased, but the lack of a quantitative method to interpret
18 various vibrational spectroscopic observations has often been one major obstacle in broadening
19 the applications of these methods. Motivated by experimental needs, there has been rapid
20 development of vibrational frequency maps of localized modes of molecules in the condensed
21 phases, vibrational coupling maps for interacting vibrational modes, and vibrational transition
22 dipole/polarizability maps for determining the corresponding IR/Raman transition amplitudes
23 over the past decades. To collect all those vibrational spectroscopy maps reported and to make
24 them available to everyone who is interested in utilizing such maps or developing a new map
25 for different vibrational probes, a repository internet site (<http://frequencymap.org/>) has been
26 created. We thus anticipate that the marriage of vibrational frequency map approach with state-
27 of-the-art multidimensional vibrational spectroscopy will be one of the most fruitful ways to
28 study the structure and dynamics of chemical, biological, and functional molecular systems in
29 the future.

30
31

2. A Brief Theoretical Account of Vibrational Spectroscopy

2.1. Radiation-matter interaction and time-dependent perturbation theory

In molecular spectroscopy,³ the system of interest interacts with the incident electric field. In the electric dipole approximation, the interaction Hamiltonian can be written as

$$H_{\text{int}}(t) = -\hat{\boldsymbol{\mu}} \cdot \mathbf{E}(\mathbf{r}, t), \quad (1)$$

where $\hat{\boldsymbol{\mu}}$ is the electric dipole operator and $\mathbf{E}(\mathbf{r}, t)$ is the electric field. In the case of inelastic scattering spectroscopy utilizing spontaneous Raman, stimulated Raman, or coherent anti-Stokes Raman scattering processes of polyatomic molecules induced by electronically non-resonant electric fields, the effective field-matter interaction Hamiltonian is approximately given by $-\hat{\boldsymbol{\alpha}} : \mathbf{E}(\mathbf{r}, t) \mathbf{E}(\mathbf{r}, t)$, where $\hat{\boldsymbol{\alpha}}$ is the electric polarizability operator.⁴ In the semiclassical approximation where the external electromagnetic field is treated classical mechanically, whereas the molecular system is quantum mechanically, the total Hamiltonian of the composite system is assumed to be the sum of the material Hamiltonian in the absence of radiation and the interaction Hamiltonian, $H_{\text{int}}(t)$. More specifically, the total Hamiltonian is given by

$$H(t) = H_S + H_{\text{Bath}} + H_{\text{Rad}} + H_{S-B} + H_{\text{int}}(t), \quad (2)$$

where H_S is the molecular Hamiltonian of the system, H_{Bath} the bath Hamiltonian, H_{Rad} that of the radiation, and H_{S-B} represents the solute-bath interaction energy. Hereafter, the radiation Hamiltonian is ignored, and the zeroth-order Hamiltonian H_0 is assumed to be the sum of the solute, bath, and solute-bath interaction energies.

The system evolves in time according to the quantum Liouville equation for the density operator $\rho(t)$ of the system as follows

$$\frac{\partial \rho(\mathbf{r}, t)}{\partial t} = -\frac{i}{\hbar} [H_0 + H_{\text{int}}(\mathbf{r}, t), \rho(\mathbf{r}, t)]. \quad (3)$$

Quantitative information about physical observables of the system, denoted as $A(t)$, can be obtained through the expectation value $\text{Tr}[\hat{A}\rho(t)]$ where Tr denotes the trace of a matrix and \hat{A} is the corresponding quantum operator associated with observable A . A diagonal element ρ_{aa} of the density matrix in a basis set $\{|a\rangle\}$ represents the probability that the system is in state a , or the *population* of the system in state a . The off-diagonal element ρ_{ab} of the density matrix, which is related to *coherence* or super-position state evolution of two states a and b , gives rise to the temporal oscillation of the aforementioned probability with a frequency $\omega \approx \omega_{ab} \equiv (E_a - E_b)/\hbar$ determined by the energy difference of the two states.

Treating $H_{\text{int}}(t)$ as the perturbation to the reference molecular Hamiltonian H_0 , Eq. (3) can be formally solved by applying the time-dependent perturbation theory. The solution is, in general, expressed as a power series expansion of $\rho(t)$ in interaction Hamiltonian,^{3,4} i.e., $\rho(\mathbf{r}, t) = \rho^{(0)}(\mathbf{r}, t) + \rho^{(1)}(\mathbf{r}, t) + \dots$, where the zeroth-order term is just the equilibrium density operator for the unperturbed system $\rho^{(0)}(t) = \rho_{\text{eq}}$ in the absence of external radiation. The

1 n th-order correction term denoted as $\rho^{(n)}(t)$ contains $H_{\text{int}}(t)$ in the n th power in a time-
 2 ordered Dyson integral accounting for all possible field-matter interactions.

3 From the perturbation expansion form of the system density operator $\rho(t)$, one can
 4 calculate the material polarization induced by field-matter interactions and the n th-order
 5 polarization $\mathbf{P}^{(n)}(\mathbf{r}, t)$, which is given by $\mathbf{P}^{(n)}(\mathbf{r}, t) = \text{Tr}[\hat{\boldsymbol{\mu}}\rho^{(n)}(\mathbf{r}, t)]$, is

$$6 \quad \mathbf{P}^{(n)}(\mathbf{r}, t) = \int_0^\infty dt_n \cdots \int_0^\infty dt_1 \mathbf{R}^{(n)}(t_n, \dots, t_1) : \mathbf{E}(\mathbf{r}, t - t_n) \cdots \mathbf{E}(\mathbf{r}, t - t_n \cdots - t_1), \quad (4)$$

7 where the n th-order molecular response function is defined as

$$8 \quad \mathbf{R}^{(n)}(t_n, \dots, t_1) = \left(\frac{i}{\hbar} \right)^n \theta(t_n) \cdots \theta(t_1) \left\langle \boldsymbol{\mu}(t_n + \cdots + t_1) [\boldsymbol{\mu}(t_{n-1} + \cdots + t_1), [\cdots [\boldsymbol{\mu}(t_1), [\boldsymbol{\mu}(0), \rho_{\text{eq}}]] \cdots]] \right\rangle. \quad (5)$$

9 with the Heaviside step functions $\theta(t)$ due to the causality principle. Here,
 10 $\boldsymbol{\mu}(t) = \exp(iH_0 t/\hbar) \hat{\boldsymbol{\mu}} \exp(-iH_0 t/\hbar)$ is the dipole operator in the interaction picture, and the
 11 angular bracket denotes the trace of a matrix. The linear response corresponds to the case of
 12 $n=1$ in Eqs. (6) and (7). The second- and third-order polarizations that are related to the surface
 13 vibrational spectroscopy and four-wave-mixing-type time-resolved vibrational spectroscopy,
 14 respectively, are determined by the corresponding the second- and third-order response
 15 functions. Note that $\mathbf{R}^{(n)}$ is a real function because $\mathbf{P}^{(n)}(\mathbf{r}, t)$ and $\mathbf{E}(\mathbf{r}, t)$ in Eq. (4) are
 16 both real quantities, even though individual terms comprising $\mathbf{R}^{(n)}$ are complex in general
 17 and represent different quantum transition pathways.

20 **2.2. Linear response vibrational spectroscopy**

21 The IR absorption (Raman scattering) spectroscopy can be fully described by considering the
 22 expectation value of the time-evolved electric dipole (polarizability) operator.^{3,4} Using the
 23 cumulant expansion technique,³ one can obtain an approximate expression for the linear
 24 response function, which is given by

$$25 \quad \mathbf{R}^{(1)}(t) = \frac{i}{\hbar} \theta(t) \{ \boldsymbol{\mu}_{ge} \boldsymbol{\mu}_{eg} e^{-i\bar{\omega}t - g(t) - \gamma t} - c.c. \} = -\frac{2}{\hbar} \theta(t) \text{Im}[\boldsymbol{\mu}_{ge} \boldsymbol{\mu}_{eg} e^{-i\bar{\omega}t - g(t) - \gamma t}], \quad (6)$$

26 where $\boldsymbol{\mu}_{eg} = \langle e | \hat{\boldsymbol{\mu}} | g \rangle$ and $\bar{\omega}$ represents the average transition frequency determined by
 27 the energy difference between the ground ($|g\rangle$) and excited ($|e\rangle$) states. Here, γ is the relaxation
 28 constant introduced in an *ad hoc* manner to take into account both the finite lifetime of the
 29 excited state and the rotational relaxation time of chromophores in solutions. In Eq. (6), the
 30 line-broadening function that mainly determines the frequency-dependent lineshape of the
 31 absorption spectrum is

$$32 \quad g(t) = \int_0^t d\tau_2 \int_0^{\tau_2} d\tau_1 C(t), \quad (7)$$

33 where the autocorrelation function of fluctuating chromophore-solvent interaction energy can
 34 be related to the fluctuating vibrational frequency-frequency correlation function (FFCF) as

$$35 \quad C(t) = \langle \delta\omega(t) \delta\omega(0) \rangle, \quad (8)$$

1 In the above equation, the angle bracket on the right-hand side of Eq. (8) represents the classical
 2 mechanical average over the phase space spanned by the bath degrees of freedom. From Eqs.
 3 (7), we now have the line-broadening function $g(t)$ related to the FFCF as

$$4 \quad g(t) = \int_0^t d\tau_2 \int_0^{\tau_2} d\tau_1 \langle \delta\omega(t) \delta\omega(0) \rangle, \quad (9)$$

5 Note that the instantaneous vibrational frequency of a given mode of the j th solute molecule at
 6 time t can be decomposed into three terms as

$$7 \quad \omega_j(t) = \omega_0 + \Delta\omega + \delta\omega_j(t), \quad (10)$$

8 where ω_0 is the vibrational frequency of the IR probe mode when the solute molecule is in
 9 the gas phase, $\Delta\omega$ is the average frequency shift due to the vibrational solvatochromism, and
 10 $\delta\omega_j(t)$ is the fluctuating part of the vibrational frequency of the j th molecule. The average
 11 vibrational frequency is given by the sum of ω_0 and $\Delta\omega$, i.e., $\bar{\omega} = \omega_0 + \Delta\omega$. From the
 12 decomposed expression (Eq. (10)) for the instantaneous vibrational frequency of the j th
 13 molecule, it becomes clear that the theoretical description of the solvation-induced vibrational
 14 frequency shift, $\Delta\omega$, in terms of chromophore-solvent interactions is immensely important to
 15 understand the changes in the peak position of the IR absorption spectrum due to varying
 16 solvent properties such as polarity, hydrophobicity, proticity, and so on. From the peak
 17 frequency $\bar{\omega}$ of the IR absorption spectrum, one can accurately measure the solvatochromic
 18 vibrational frequency shift $\Delta\omega$ within the Condon approximation.

19 In addition, the width of each IR spectrum is related to the standard deviation of
 20 $\delta\omega_j(t)$, i.e., $\langle \delta\omega^2 \rangle^{1/2}$, when the line-broadening is dictated by pure dephasing process.
 21 However, in general, the width of the IR absorption spectrum is determined not just by
 22 $\langle \delta\omega^2 \rangle^{1/2}$ but also by the width of the inhomogeneous distribution of transition frequency and
 23 the rates of vibrational energy and rotational relaxation processes. If there is no static
 24 inhomogeneity in vibrational frequencies and if the vibrational lifetime-broadening and
 25 rotational relaxation-induced dephasing are negligibly small, the whole line broadening is
 26 determined by the pure dephasing, which makes the linear response function decay as described
 27 by $\exp(-g(t))$ in Eq. (6). Kubo's exponential model for $C(t)$ has long been used to describe the
 28 lineshape of the linear vibrational spectrum.^{3,4} Let us assume that the FFCF is an exponentially
 29 decaying function as

$$30 \quad C(t) = \langle \delta\omega^2 \rangle \exp(-\Gamma t), \quad (11)$$

31 where the decay constant Γ corresponds to the loss rate of correlation between vibrational
 32 frequencies at two different times. With this exponential FFCF, the correlation time is given
 33 by

$$34 \quad t_c = \int_0^\infty dt C(t) / C(0) = 1/\Gamma. \quad (12)$$

35 Inserting Eq. (11) into (9), one can find

$$36 \quad g(t) = \langle \delta\omega^2 \rangle t_c^2 \{ \exp(-t/t_c) + t/t_c - 1 \}. \quad (13)$$

1 If the correlation time t_c is much shorter than the inverse of $\langle \delta\omega^2 \rangle^{1/2}$, that is the case
2 when the vibrational frequency loses its memory almost instantaneously. This is the Markovian
3 limit and the line-broadening function $g(t)$ becomes a linear function of time as

$$4 \quad g(t) = \langle \delta\omega^2 \rangle t_c t, \quad (14)$$

5 and the linear response function decays exponentially with respect to t . Within this Markovian
6 approximation to the FFCF, the absorption spectrum in the frequency domain becomes a
7 Lorentzian function.

8 If the correlation time t_c is much longer than the inverse of $\langle \delta\omega^2 \rangle^{1/2}$, the line-
9 broadening function in Eq. (13) can be approximated as a quadratic function of time, i.e.,

$$10 \quad g(t) = (1/2) \langle \delta\omega^2 \rangle t^2. \quad (15)$$

11 Then, the lineshape of the absorption spectrum becomes a Gaussian function with a width
12 determined by $\langle \delta\omega^2 \rangle^{1/2}$. If the line-broadening function $g(t)$ is assumed to be a sum of
13 exponential and Gaussian functions in the time domain, the corresponding absorption lineshape
14 in the frequency domain becomes the well-known Voigt profile.

15 The linear response function that determines the lineshape of the absorption and
16 emission spectra of optical and vibrational chromophores can be approximately described in
17 terms of the instantaneous fluctuations of the vibrational transition frequencies and dipole
18 moments. Therefore, if an accurate VSM is available for a given set of vibrational modes of
19 molecules in condensed phases, the center frequencies of the absorption and emission spectra
20 and their linewidths can be reproduced and even predicted by using MD simulations combined
21 with the VSM theory. Nevertheless, it should be emphasized that even though the lineshape
22 analysis of linear spectra provides invaluable information about chromophore-solvent
23 interaction strength, it is impossible to extract direct information about the time correlation
24 function of the chromophore-solvent dynamics from the corresponding 1D spectrum.
25 Furthermore, if inhomogeneous-broadening effects are not negligible, one cannot extract
26 quantitative information about $\langle \delta\omega^2 \rangle^{1/2}$ from the 1D spectrum because the full-width-at-
27 half-maximum of the spectrum is determined by both the standard deviation of fluctuating
28 frequency and the width of the inhomogeneous frequency distribution. In this respect, time-
29 resolved vibrational spectroscopy has found its use for studying such locally heterogeneous
30 environments around IR probes and for measuring time scales of vibrational energy relaxation,
31 rotational dynamics, transitions from one conformer to another, chemical exchange dynamics
32 among non-covalently bonded chemical species, energy or particle transfer processes from one
33 state to another, and transient dynamics between different solvation configurations. All these
34 transient processes involve changes in vibrational frequencies of solute molecules because any
35 molecular structural changes affect the multidimensional potential energy surface of the
36 molecule, which then induce changes in vibrational frequencies.

37 38 **2.3. Time-resolved vibrational spectroscopy**

39 In general, most nonlinear vibrational spectroscopic measurements are conducted in two steps.
40 The first is the preparation step, where molecular systems under investigation are excited by
41 incident radiations. The second is the detection step, where the signal generated through

1 nonlinear field-matter interactions is measured and presented. In time-resolved IR pump-probe
 2 (PP), the first two electric field-matter interactions occur with the pump pulse. The time-
 3 delayed probe pulse interacts with the molecules in the sample, which generates the third-order
 4 macroscopic polarization in the sample. The macroscopic material polarization is usually a
 5 linear sum of all the third-order dipole moments of chromophores dissolved in solutions when
 6 their couplings are weak. The generated IR PP signal field interferes with the same incident
 7 probe field, and the interference term is selectively measured.

8 For 2D IR spectroscopy, the system is usually irradiated with three coherent laser
 9 pulses. The generated 2D IR signal field is heterodyne-detected, and the 2D IR spectrum is
 10 presented in two frequency dimensions representing two distinct vibrational coherence
 11 oscillations separated by a waiting (population) time T_w .^{4,5,70} The 2D IR is four-wave-mixing
 12 spectroscopy because the signal field arises from three preceding field-matter interactions that
 13 are each linear in the applied electromagnetic field. In each of the four field-matter interaction
 14 events, a quantum transition takes place between vibrational states of the system. Depending
 15 on the configuration of the optical laser pulses such as the frequency, direction of propagation
 16 (wavevector), and polarization, as well as on the detection methods, different quantum
 17 transition pathways can be differently generated and selectively measured.⁴

18 Time-resolved IR spectroscopy, e.g., IR pump-probe and 2D IR, involves quantum
 19 transitions up to the second vibrational excited state denoted as $|f\rangle$. Therefore, a three-level
 20 system with eigenstates $|g\rangle$, $|e\rangle$, and $|f\rangle$ is a useful model for developing a theory of
 21 nonlinear response function that is directly relevant to time-resolved four-wave-mixing
 22 spectroscopy in general. As well-known, the third-order vibrational response function vanishes
 23 for a perfect bosonic oscillator; the model system should represent an anharmonic oscillator
 24 where the fundamental transition frequency ω_{eg} differs from ω_{fe} .

25 The evaluation of a realistic response function critically depends on the accurate
 26 description of the system-bath interactions or generally intermolecular interactions that are
 27 responsible for chemical dynamics and spectroscopic phenomena such as dephasing, relaxation,
 28 reorientation, spectral diffusion, and population and coherence transfers. Methods to
 29 incorporate the effect of the environment as well as the multimode vibrational coupling have
 30 been discussed in various review articles and books.^{3-5,7,70} Here, we briefly outline the theory
 31 of nonlinear vibrational response function and its interplay with vibrational solvatochromism
 32 and vibrational frequency-frequency correlation function. We focus on a simple three-level
 33 chromophore interacting with the environment, where the corresponding Hamiltonian is given
 34 by

$$35 \quad H_0 = \sum_{m=g,e,f} [\hbar\omega_m + V_m(\mathbf{q}) + H_B(\mathbf{q})] |m\rangle\langle m|, \quad (16)$$

36 where $\hbar\omega_m$ is the energy of state m ($m = g, e, f$) in the absence of bath, $V_m(\mathbf{q})$ is the
 37 chromophore-bath interaction energy of the state m that depends on the bath degrees of freedom
 38 \mathbf{q} , $H_B(\mathbf{q})$ is the energy of the bath, and the basis states $|m\rangle$ are chosen as eigenstates of an
 39 isolated chromophore. Note that the off-diagonal elements of the chromophore-bath interaction
 40 such as $J_{mn}|m\rangle\langle n|$ that approximately describe state-to-state vibrational energy transfer

1 processes are assumed negligible for the sake of simplicity. Thus, the chromophore-bath
 2 interaction described by Eq. (16) modulates the energy gap between two different eigenstates
 3 of the target oscillator.

4 The third-order signal electric field $\mathbf{E}_s^{(3)}(\mathbf{r}, t)$ that is under detection in nonlinear
 5 spectroscopy is obtained by solving Maxwell's equation taking the nonlinear polarization
 6 $\mathbf{P}^{(3)}(\mathbf{r}, t)$ as the radiation source. Often, the following assumptions are made: (i) the signal
 7 field is only weakly absorbed by the medium, (ii) the envelopes of polarization and signal fields
 8 vary slowly in time compared to the optical period, (iii) the signal field envelope spatially
 9 varies slowly compared to its wavelength, (iv) the frequency dispersion of the medium
 10 refractive index is weak. The approximate solution for the signal electric field envelope is given
 11 by

$$12 \quad \mathbf{E}_s^{(3)}(t) \propto \frac{i\omega_s}{n(\omega_s)} \mathbf{P}_s^{(3)}(t). \quad (17)$$

13 Here $n(\omega)$ is the refractive index of the medium and $\mathbf{P}_s^{(3)}(t)$ is the polarization component
 14 propagating with wave vector \mathbf{k}_s and frequency ω_s that are one of the combinations
 15 $\pm\mathbf{k}_1 \pm \mathbf{k}_2 \pm \mathbf{k}_3$ and $\pm\omega_1 \pm \omega_2 \pm \omega_3$, respectively. Note that Eq. (17) gives the approximate signal
 16 field arising from a single Fourier component of the third-order polarization expanded as^{3,4}

$$17 \quad \mathbf{P}^{(3)}(\mathbf{r}, t) = \sum_l \mathbf{P}_l^{(3)}(t) \exp(i\mathbf{k}_l \cdot \mathbf{r} - i\omega_l t). \quad (18)$$

18 By changing the location of the detector appropriately, individual components of the
 19 polarization with different \mathbf{k}_s can be selectively measured. Note that the assumption (ii) known
 20 as slowly-varying-envelope approximation becomes invalid for far-IR and THz spectroscopy
 21 because typical pulse duration time is quantitatively similar to the period of such low-frequency
 22 far-IR and THz radiation. In that case, one should solve the corresponding Maxwell's wave
 23 equation rather numerically, which is not of major difficulty. In the present work, we shall
 24 focus on IR probes whose oscillation frequencies are in mid-IR and near-IR domains (>1000
 25 cm^{-1}), so the slowly-varying-envelope approximation is still valid.

26 The general third-order response function in Eq. (5) has three nested commutators, so
 27 it can be expanded and rewritten as the sum of eight terms^{3,109}

$$28 \quad \mathbf{R}^{(3)}(t_3, t_2, t_1) = \left(\frac{i}{\hbar}\right)^3 \theta(t_3)\theta(t_2)\theta(t_1) \sum_{i=1}^4 [\mathbf{R}_i(t_3, t_2, t_1) - \mathbf{R}_i^*(t_3, t_2, t_1)] \quad (19)$$

29 where the components $\mathbf{R}_i(t_3, t_2, t_1)$ are given by

$$30 \quad \mathbf{R}_1(t_3, t_2, t_1) = \boldsymbol{\mu}_{ge} \boldsymbol{\mu}_{eg} \boldsymbol{\mu}_{ge} \boldsymbol{\mu}_{eg} \exp[i(-\bar{\omega}_{eg} t_3 - \bar{\omega}_{eg} t_1)] F_1^{gege}(t_3, t_2, t_1) \\ + \boldsymbol{\mu}_{ge} \boldsymbol{\mu}_{ef} \boldsymbol{\mu}_{fe} \boldsymbol{\mu}_{eg} \exp[i(\bar{\omega}_{fe} t_3 - \bar{\omega}_{eg} t_1)] F_1^{gefe}(t_3, t_2, t_1)$$

$$31 \quad \mathbf{R}_2(t_3, t_2, t_1) = \boldsymbol{\mu}_{ge} \boldsymbol{\mu}_{eg} \boldsymbol{\mu}_{ge} \boldsymbol{\mu}_{eg} \exp[i(-\bar{\omega}_{eg} t_3 + \bar{\omega}_{eg} t_1)] F_2^{gege}(t_3, t_2, t_1) \\ + \boldsymbol{\mu}_{ge} \boldsymbol{\mu}_{ef} \boldsymbol{\mu}_{fe} \boldsymbol{\mu}_{eg} \exp[i(\bar{\omega}_{fe} t_3 + \bar{\omega}_{eg} t_1)] F_2^{gefe}(t_3, t_2, t_1)$$

$$32 \quad \mathbf{R}_3(t_3, t_2, t_1) = \boldsymbol{\mu}_{ge} \boldsymbol{\mu}_{eg} \boldsymbol{\mu}_{ge} \boldsymbol{\mu}_{eg} \exp[i(-\bar{\omega}_{eg} t_3 + \bar{\omega}_{eg} t_1)] F_3^{gege}(t_3, t_2, t_1) \\ + \boldsymbol{\mu}_{ge} \boldsymbol{\mu}_{ef} \boldsymbol{\mu}_{fe} \boldsymbol{\mu}_{eg} \exp[i(\bar{\omega}_{fe} t_3 + \bar{\omega}_{fg} t_2 + \bar{\omega}_{eg} t_1)] F_3^{gefe}(t_3, t_2, t_1)$$

$$\begin{aligned} \mathbf{R}_4(t_3, t_2, t_1) = & \boldsymbol{\mu}_{ge} \boldsymbol{\mu}_{eg} \boldsymbol{\mu}_{ge} \boldsymbol{\mu}_{eg} \exp\left[i(-\bar{\omega}_{eg} t_3 - \bar{\omega}_{eg} t_1)\right] F_4^{gege}(t_3, t_2, t_1) \\ & + \boldsymbol{\mu}_{ge} \boldsymbol{\mu}_{ef} \boldsymbol{\mu}_{fe} \boldsymbol{\mu}_{eg} \exp\left[i(-\bar{\omega}_{eg} t_3 - \bar{\omega}_{fg} t_2 - \bar{\omega}_{eg} t_1)\right] F_4^{gefe}(t_3, t_2, t_1). \end{aligned} \quad (20)$$

Here, $\boldsymbol{\mu}_{ab}$ is the transition dipole between states a and b , $\hbar\bar{\omega}_{ab} = \hbar(\omega_a - \omega_b) + \langle V_a(\mathbf{q}) - V_b(\mathbf{q}) \rangle_B$ is the energy gap averaged over bath degrees of freedom, and $F_n^{gabc}(t_3, t_2, t_1)$ is the line shape function which can be approximated by exponential functions containing difference potential energies $U_{ab}(\mathbf{q}) = U_a(\mathbf{q}) - U_b(\mathbf{q})$.⁴ Alternatively, one can invoke the second-order cumulant expansion approximation, which becomes exact when the fluctuation of the energy gap obeys the Gaussian statistics, to obtain

$$\begin{aligned} \mathbf{R}_{1A}(t_3, t_2, t_1) &= \boldsymbol{\mu}_{ge} \boldsymbol{\mu}_{eg} \boldsymbol{\mu}_{ge} \boldsymbol{\mu}_{eg} \exp(-i\bar{\omega}_{eg} t_3 - i\bar{\omega}_{eg} t_1) \exp\left[-g^*(t_3) - g(t_1) - f_+(t_3, t_2, t_1)\right] \\ \mathbf{R}_{1B}(t_3, t_2, t_1) &= \boldsymbol{\mu}_{ge} \boldsymbol{\mu}_{ef} \boldsymbol{\mu}_{fe} \boldsymbol{\mu}_{eg} \exp(i\bar{\omega}_{fe} t_3 - i\bar{\omega}_{eg} t_1) \\ &\quad \times \exp\left[-g^*(t_3) - g(t_1) + g^*(t_2) - g(t_1 + t_2) - g^*(t_2 + t_3) + g(t_1 + t_2 + t_3)\right] \\ \mathbf{R}_{2A}(t_3, t_2, t_1) &= \boldsymbol{\mu}_{ge} \boldsymbol{\mu}_{eg} \boldsymbol{\mu}_{ge} \boldsymbol{\mu}_{eg} \exp(-i\bar{\omega}_{eg} t_3 + i\bar{\omega}_{eg} t_1) \exp\left[-g^*(t_3) - g^*(t_1) + f_+(t_3, t_2, t_1)\right] \\ \mathbf{R}_{2B}(t_3, t_2, t_1) &= \boldsymbol{\mu}_{ge} \boldsymbol{\mu}_{ef} \boldsymbol{\mu}_{fe} \boldsymbol{\mu}_{eg} \exp(i\bar{\omega}_{fe} t_3 + i\bar{\omega}_{eg} t_1) \\ &\quad \times \exp\left[-g^*(t_3) - g^*(t_1) - g(t_2) + g^*(t_1 + t_2) + g(t_2 + t_3) - g^*(t_1 + t_2 + t_3)\right] \\ \mathbf{R}_3(t_3, t_2, t_1) &= \boldsymbol{\mu}_{ge} \boldsymbol{\mu}_{eg} \boldsymbol{\mu}_{ge} \boldsymbol{\mu}_{eg} \exp(-i\bar{\omega}_{eg} t_3 + i\bar{\omega}_{eg} t_1) \exp\left[-g(t_3) - g^*(t_1) + f_-(t_3, t_2, t_1)\right] \\ \mathbf{R}_4(t_3, t_2, t_1) &= \boldsymbol{\mu}_{ge} \boldsymbol{\mu}_{eg} \boldsymbol{\mu}_{ge} \boldsymbol{\mu}_{eg} \exp(-i\bar{\omega}_{eg} t_3 - i\bar{\omega}_{eg} t_1) \exp\left[-g^*(t_3) - g(t_1) - f_-(t_3, t_2, t_1)\right]. \end{aligned} \quad (21)$$

where the auxiliary functions are given by

$$\begin{aligned} f_+(t_3, t_2, t_1) &= g^*(t_2) - g^*(t_2 + t_3) - g(t_1 + t_2) + g(t_1 + t_2 + t_3) \\ f_-(t_3, t_2, t_1) &= g(t_2) - g(t_2 + t_3) - g(t_1 + t_2) + g(t_1 + t_2 + t_3). \end{aligned} \quad (22)$$

and $g(t)$ defined by Eq.(9). The other contributions to \mathbf{R}_3 and \mathbf{R}_4 , which involve coherence evolution of $|f\rangle\langle g|$ during t_2 , are not included in Eq. (21) and the energy fluctuation between states g and f is usually assumed to be twice that between g and e , i.e., $\delta\omega_{fg}(t) \cong 2\delta\omega_{eg}(t)$.⁴

The six response functions in Eq. (21) can be classified, based on their physical interpretation, as ground state bleach (GB) and stimulated emission (SE) that involve transitions between g and e , and excited-state absorption involving transitions between e and f . They can also be classified into rephasing and non-rephasing terms, depending on whether the optical coherence during the times t_1 and t_3 evolves in the same or opposite direction. If chromophores have a broad distribution of heterogeneous environments, which makes the vibrational transition frequency broadly distributed, the molecular nonlinear response function should be calculated by averaging over the inhomogeneous distribution $f(\varpi)$ of vibrational frequencies, i.e.,

$$\bar{\mathbf{R}}_j(t_3, t_2, t_1) = \int d\varpi \mathbf{R}_j(t_3, t_2, t_1; \varpi) f(\varpi), \quad (23)$$

where ϖ is the variable representing the frequency shift due to heterogeneously distributed local solute-solvent interaction environments, solute conformations, phases, or microscopic states. For instance, the first nonlinear response function after average over the normalized distribution $f(\varpi)$ is given by

$$\bar{\mathbf{R}}_{1A}(t_3, t_2, t_1) = \int d\varpi \mathbf{R}_{1A}(t_3, t_2, t_1; \varpi) f(\varpi) = \mathbf{R}_{1A}(t_3, t_2, t_1) \tilde{f}(t_3 + t_1), \quad (24)$$

where $\tilde{f}(t)$ is the inverse Fourier transformation of $f(\varpi)$. As t_1 and t_3 increase, due to the inhomogeneous distribution of vibrational frequencies, the response function additionally decays and it does not produce any echo signal. In contrast with $\bar{\mathbf{R}}_{1A}(t_3, t_2, t_1)$, the averaged nonlinear response function of $\mathbf{R}_{2A}(t_3, t_2, t_1; \varpi)$ over ϖ becomes

$$\bar{\mathbf{R}}_{2A}(t_3, t_2, t_1) = \int d\varpi \mathbf{R}_{2A}(t_3, t_2, t_1; \varpi) f(\varpi) = \mathbf{R}_{2A}(t_3, t_2, t_1) \tilde{f}(t_3 - t_1). \quad (25)$$

Since $\tilde{f}(t)$ peaks at $t = 0$, $\tilde{f}(t_3 - t_1)$ with respect to t_3 reaches its maximum at $t_3 = t_1$, which is the signature of echo generation due to inhomogeneity-induced rephasing process. Therefore, \mathbf{R}_2 and \mathbf{R}_3 are rephasing terms that are responsible for the generation of the photon echo (PE) signal from chromophores having a broad inhomogeneous frequency distribution, and \mathbf{R}_1 and \mathbf{R}_4 are referred to as non-rephasing terms.

When the vibrational modes are spectators in chemical reactions the Gaussian approximation^{109,110} making the foundation of the line-broadening function breaks down. The response function formulation presented above is still valid, but they need to be evaluated explicitly including the resulting non-Gaussian fluctuations.¹¹¹⁻¹²⁰ In these cases, the numerical integration of the Schrödinger equation (NISE)¹²¹ and the non-linear exciton propagation (NEP) algorithms¹²² should be of use.¹¹⁰

2.4. Two-dimensional lineshape analysis and spectral diffusion

The average vibrational frequency shift of IR-active modes, which is induced by solute-solvent interactions, can be accurately measured by analyzing the FTIR spectra of IR probes. However, to obtain information on the time scale of vibrational frequency fluctuation, it is necessary to use nonlinear vibrational spectroscopic techniques as they are capable of measuring the frequency-frequency correlation function. Photon echo spectroscopy has been used as one of the most popular techniques for studying ultrafast solvent dynamics, through measuring photon echo peak shift (PEPS) in the time domain.^{4,123} More recently, 2D vibrational, electronic, and electronic-vibrational spectroscopy experiments have been extensively performed to extract solvent dynamics and frequency-frequency correlation function from the analyses of nodal line slope, center line slope, and ellipticity of two-dimensional peaks on the diagonal and off-diagonal regions of the 2D spectra (Figure 2).^{4,5,7,70,73}

Using the FFCF formulation to describe the solute-solvent interaction-induced fluctuation of vibrational frequency, one can, in principle, calculate the nonlinear response functions in Eq. (21). However, the more useful information can be extracted by analyzing the 2D lineshape changes in time. To establish the relationship between the analytical expressions for the nonlinear response functions and the waiting time-dependent 2D lineshape, one can use a short-time approximation to the line-broadening function.^{4,5,7,73} Assuming that the pulse envelope function can be approximated as a Dirac delta function and carrying out the two-dimensional Fourier transformations of the PE signal field, it was shown that the complex 2D photon echo spectrum of an anharmonic oscillator system, which can be approximated as a three-level system, is given by

$$\tilde{\mathbf{E}}_{PE}(\omega_t, T, \omega_\tau) = \tilde{\mathbf{E}}_{PE}^{SE}(\omega_t, T, \omega_\tau) + \tilde{\mathbf{E}}_{PE}^{GB}(\omega_t, T, \omega_\tau) + \tilde{\mathbf{E}}_{PE}^{EA}(\omega_t, T, \omega_\tau), \quad (26)$$

where SE, GB, and EA represent the stimulated emission, ground-state bleaching, and excited-state absorption (EA) terms, respectively, and they are

$$\begin{aligned} \tilde{\mathbf{E}}_{PE}^{SE}(\omega_t, T, \omega_\tau) &= \frac{\pi[\boldsymbol{\mu}_{ge}\boldsymbol{\mu}_{eg}\boldsymbol{\mu}_{ge}\boldsymbol{\mu}_{eg}]:\mathbf{e}_3\mathbf{e}_2\mathbf{e}_1}{C(0)\sqrt{(1-\bar{C}^2(T))}} \exp(-x^2) \left\{ \exp(-y^2(T)) + \frac{2i}{\sqrt{\pi}} F(y(T)) \right\} \\ \tilde{\mathbf{E}}_{PE}^{GB}(\omega_t, T, \omega_\tau) &= \frac{\pi[\boldsymbol{\mu}_{ge}\boldsymbol{\mu}_{eg}\boldsymbol{\mu}_{ge}\boldsymbol{\mu}_{eg}]:\mathbf{e}_3\mathbf{e}_2\mathbf{e}_1}{C(0)\sqrt{(1-\bar{C}^2(T))}} \exp(-x^2) \left\{ \exp(-z^2(T)) + \frac{2i}{\sqrt{\pi}} F(z(T)) \right\} \\ \tilde{\mathbf{E}}_{PE}^{EA}(\omega_t, T, \omega_\tau) &= -\frac{\pi[\boldsymbol{\mu}_{ef}\boldsymbol{\mu}_{fe}\boldsymbol{\mu}_{eg}\boldsymbol{\mu}_{ge}]:\mathbf{e}_3\mathbf{e}_2\mathbf{e}_1^*}{C(0)\sqrt{(1-\bar{C}^2(T))}} \exp(-x^2) \left\{ \exp(-w^2(T)) + \frac{2i}{\sqrt{\pi}} F(w(T)) \right\}. \end{aligned} \quad (27)$$

Here, the vectorial dipole moment associated with the transition from the ground state g to the first excited state e is denoted as $\boldsymbol{\mu}_{eg}$ and the unit vector of the polarization of the j th pulsed electric field is as \mathbf{e}_j . In Eq. (27), $\bar{C}(t)$ is the normalized FFCF defined as

$$\bar{C}(t) = C(t) / C(0). \quad (28)$$

The auxiliary functions in Eq. (27) are defined as, with $\beta = 1/k_B T$,

$$\begin{aligned} x &\equiv \frac{\omega_\tau - \bar{\omega}_{eg}}{\sqrt{2C(0)}} \\ y(T) &\equiv \frac{\omega_t - \bar{\omega}_{eg} + 2\{\lambda / \hbar\}(1 - \bar{C}(T)) - (\omega_\tau - \bar{\omega}_{eg})\bar{C}(T)}{\sqrt{2C(0)(1 - \bar{C}^2(T))}} \\ z(T) &\equiv \frac{\omega_t - \bar{\omega}_{eg} - (\omega_\tau - \bar{\omega}_{eg})\bar{C}(T)}{\sqrt{2C(0)(1 - \bar{C}^2(T))}} \\ w(T) &\equiv \frac{\omega_t - \bar{\omega}_{fe} + 2\{\lambda / \hbar\}(1 - \bar{C}(T)) - (\omega_\tau - \bar{\omega}_{eg})\bar{C}(T)}{\sqrt{2C(0)(1 - \bar{C}^2(T))}}. \end{aligned} \quad (29)$$

In Eq. (27), $F(x)$ is the Dawson integral defined as $F(x) = e^{-x^2} \int_0^x du e^{u^2}$. In Eq. (29), λ is the solvent reorganization energy, and it is related to the variance of fluctuating vibrational frequency as $C(0) = \langle \delta\omega^2 \rangle \cong 2\lambda k_B T / \hbar^2$. Typical vibrational lifetime and rotational relaxation time of small molecules are on the order of a few picoseconds, and the vibrational absorption linewidth is mainly determined by the standard deviation of fluctuating vibrational frequency, which is $\langle \delta\omega^2 \rangle^{1/2} \cong (2\lambda k_B T)^{1/2} / \hbar$. If the linewidth is 30 cm^{-1} , the solvent reorganization energy λ is about 2 cm^{-1} at room temperature. Therefore, unlike UV-vis spectroscopy involving electronic transitions of optical chromophores in condensed phases, the Stokes shift or the vibrational excitation-induced solvent reorganization energy is negligibly small compared to the absorption linewidth and anharmonic frequency shift $\bar{\omega}_{eg} - \bar{\omega}_{fe}$.

1 Therefore, in the interpretation of 2D IR spectral evolution, the Stokes shift or solvation
 2 dynamics of the vibrationally excited state is not taken into consideration.

3 To obtain the above approximately 2D Gaussian line-shape function expression for the
 4 real part of the 2D photon echo spectrum, we assumed that the coupled bath mode frequencies
 5 are smaller than $k_B T$ at room temperature. These approximate descriptions are not valid at low
 6 temperatures. From Eqs. (26)-(29), one can predict the time-dependent changes in center and
 7 nodal line slopes of 2D peak, the frequency difference between SE+GB peak and EA peak
 8 along the ω_t axis, ellipticity of each diagonal peak, and both the diagonal and antidiagonal
 9 linewidths of diagonal peak in terms of the waiting time-dependent FFCF, $C(T)$ (see Figure 2).
 10 More specifically, the nodal and center line slopes, NLS and CLS , with respect to waiting time
 11 T are approximately given by⁷³

$$12 \quad NLS(T) = CLS(T) = \bar{C}(T). \quad (30)$$

13 The full-width-at-half-maximum (FWHM) of the diagonal peak along the diagonal line, which
 14 is denoted as $\Delta\omega_{diag}(T)$, and that along the anti-diagonal line, denoted as $\Delta\omega_{anti-diag}(T)$, are
 15 also determined by the FFCF as

$$16 \quad \Delta\omega_{diag}(T) = 2\sqrt{C(0)\ln 2}\sqrt{1+\bar{C}(T)}$$

$$17 \quad \Delta\omega_{anti-diag}(T) = 2\sqrt{C(0)\ln 2}\sqrt{1-\bar{C}(T)}. \quad (31)$$

18 From Eq. (31), the ratio of diagonal width to anti-diagonal width becomes a function of waiting
 19 time as, at $T > 0$,^{4,73}

$$20 \quad \frac{\Delta\omega_{diag}(T)}{\Delta\omega_{anti-diag}(T)} \cong 1 + \bar{C}(T). \quad (32)$$

21 Equation (32) clearly shows that the 2D peak-shape at a short waiting time is diagonally
 22 elongated, but the degree of such diagonal elongation decreases in waiting time and approaches
 23 zero. Therefore, after a long waiting time $T \gg t_c$, the 2D peak-shape becomes round with the
 24 same diagonal and anti-diagonal widths. Again, from the waiting time-dependence of diagonal
 25 elongation, it is possible to extract direct information on the normalized FFCF.

26 In this section, we specifically discussed how 2D vibrational spectroscopy can be used
 27 to study ultrafast solute-solvent interaction dynamics through analyzing 2D peak-shape
 28 evolution in waiting time. For certain vibrational modes, e.g., OH and OD stretch modes of
 29 HDO in water or heavy water, the FFCF extracted from the 2D IR data was directly compared
 30 with that predicted using vibrational solvatochromism theory and molecular dynamics
 31 simulation methods. However, still, such quantitative comparisons between theory and
 32 experiment for many IR probes incorporated into complicated biological molecules or
 33 functional materials are very challenging and have rarely been reported. Only when the
 34 numerically calculated FFCF and average solvatochromic frequency shift of a given IR
 35 oscillator with quantum chemistry calculation, MD simulation, or any combination of
 36 electronic structure calculation and molecular simulation are in quantitative agreement with
 37 experimental results, one can conclude that the computational methods used are quantitatively
 38 reliable and spectroscopically valid.

2.5. Numerical integration of the vibrational Schrödinger equation

A variety of applications of ab initio MD simulation methods to the studies of chemical and biological reactions and processes have been reported. However, still, it is prohibitively expensive to use such methods to accurately calculate the fluctuating vibrational frequencies and transition dipole moments of molecules in condensed phases. In contrast, the combination of VSMs, i.e., vibrational frequency, transition dipole, vibrational coupling constant, and anharmonicity maps, and classical MD simulations provides an efficient means to calculate various linear and nonlinear IR spectra when using Eqs. (6), (20) and (21). In a more general case, when multiple vibrational modes are non-negligibly coupled and non-adiabatic effects on the vibrational eigenstates need to be considered, the required computational step is to develop a method to numerically solve the corresponding time-dependent vibrational Schrödinger equations. This approach, widely referred to as Numerical Integration of the Schrödinger Equation (NISE) theory,¹²⁴ assumes that a given vibrational mode can be approximated as a weakly anharmonic oscillator so that only the lowest three vibrational levels are enough for modeling 2D vibrational spectroscopy. When the oscillators are close to one another through space or chemical bonds, their vibrations are correlated. Such vibrational coupling effects can also be quantitatively described by using various VSMs. Here, the vibrational frequencies, transition dipole moments, and even anharmonic frequency shifts fluctuate in time due to the solute-solvent interactions. These intermolecular interaction-induced fluctuations are all taken into account by considering their time-dependent modulation of the parameters of the quantum oscillator.

In general, for coupled multi-oscillator systems interacting with external electric fields, the corresponding time-dependent Hamiltonian can be written as

$$\begin{aligned}
 H(t) = & \sum_n^N \hbar \omega_n(t) a_n^\dagger a_n + \sum_{n,m}^N J_{nm}(t) a_n^\dagger a_m - \frac{1}{2} \sum_n^N \Delta_n(t) a_n^\dagger a_n^\dagger a_n a_n \\
 & + \sum_n^N \mathbf{E}(t) \cdot \boldsymbol{\mu}_n(t) (a_n^\dagger + a_n) + \sum_n^N \mathbf{E}(t) \cdot \boldsymbol{\alpha}_n(t) \cdot \mathbf{E}(t) (a_n^\dagger + a_n).
 \end{aligned}
 \tag{33}$$

Here, a_n^\dagger and a_n are the creation and annihilation operators of the n th harmonic oscillator considered quantum mechanically. The individual local vibrations are characterized by their frequency $\omega_n(t)$, transition dipole $\boldsymbol{\mu}_n(t)$, transition polarizability $\boldsymbol{\alpha}_n(t)$, and anharmonicity $\Delta_n(t)$. Any pair of local vibrations are mixed by their mutual couplings $J_{nm}(t)$. In this approach, the time dependence of these parameters strictly arises from the coupling of each individual oscillator with bath degrees of freedom. The last two terms in Eq. (33) account for the interaction of the oscillating dipoles and molecular polarizabilities with the applied electric field(s) $\mathbf{E}(t)$, respectively, depending on the specific experimental configuration.

Determining the fluctuating frequencies, transition moments, and coupling constants in the above time-dependent Hamiltonian depends on the system under consideration.¹¹⁰ Once there exist quantitatively reliable models for these parameters, time-evolution operator approaches can be used to calculate the response functions. The critical step is to divide the propagation time into sufficiently short time intervals so that the Hamiltonian during these

1 intervals is approximately independent of time. The solution for the time-dependent
2 Schrödinger equation for each short time interval can then be easily obtained. Successive
3 applications of the finite-difference time-evolution operators for neighboring time-intervals
4 enable the time-dependent vibrational wavefunction of the coupled multi-oscillator systems to
5 be calculated. Open source implementations of NISE and closely related variations¹²² are
6 available.^{125,126}

7 The success of this NISE approach^{120,127-130} relies on the accuracy of the computed
8 parameters needed to construct the time-dependent Schrödinger equation. The vibrational
9 frequency and transition dipole moment of a given oscillator depend on the local environment
10 and are determined by the intermolecular interaction potential and the anharmonicity of the
11 multidimensional intramolecular vibrational potential. For instance, an early attempt to
12 calculate the solute-solvent interaction-induced shift of vibrational frequency assumes that the
13 solute-solvent interaction is dictated by electrostatic interactions. The vibrational frequency
14 shift of an oscillator was considered to be dependent on the solvent electric potential, electric
15 field, or sometimes the electric field gradient on specific sites of the solute molecule. These
16 vibrational frequency mappings have allowed the frequency trajectories of the coupled
17 oscillators to be obtained from equilibrium MD trajectories. However, recently, it has been
18 shown that the vibrational solvatochromic frequency shift is determined by not just electrostatic
19 interactions but also dispersive interaction, short-range Pauli repulsion, polarization, and even
20 multipole-multipole interactions.⁴⁰

21 The anharmonicity of a given molecular vibration also depends on its interaction with
22 the solvent molecules. For multi-oscillator systems, the vibrational coupling constant between
23 any pair of local modes should be accurately calculated to describe the delocalized nature of
24 the vibrational modes. One of the most popular models is the transition-dipole coupling model,
25 which assumes that the two oscillators interact with each other through electric dipole-dipole
26 interactions. So far, this form of semiempirical mapping has been found to be exceptionally
27 useful, achieving a spectroscopic accuracy within a few wavenumbers, something which
28 cannot be easily achieved using current classical or even *ab initio* MD simulation methods.

29 The quantum-classical methods discussed here have a number of crucial advantages.¹¹⁰
30 One of the commonly used methods, which incorporates second-order cumulant approximation
31 or other methods that require an assumption that the coupled bath degrees of freedom are
32 harmonic oscillators obeying Gaussian statistics, cannot account for intermolecular interaction-
33 induced effects properly. On the other hand, quantum-classical methods take them correctly.
34 Nevertheless, hybrid quantum-classical methods still have definite limitations. The time-
35 dependent Hamiltonian for NISE does not allow for the relaxations between the different
36 excitation manifolds.¹¹⁰ Furthermore, while these quantum-classical methods are able to
37 account for the effect that the bath exerts on the system, the feedback of the system to the bath
38 when in an excited state is unable to be considered. Consequently, the method cannot reproduce
39 the correct thermalization in quantum systems, which results in artifacts at low temperatures.
40 Another inherent difficulty of NISE is that quantum mechanical oscillators need to be well
41 defined and localized. If the nature of an oscillator changes over time (e.g., H-bond vibrations
42 and delocalized intermolecular modes), it is not possible to treat them quantum mechanically.

1 As mentioned in this section, despite the prolonged efforts to develop approximate
2 theory and computational methods, clear limitations in the accurate calculation of the coherent
3 multidimensional spectra of molecules in condensed phases still exist. Although a simple
4 approach for modeling absorption lineshape such as Kubo model has been widely used in many
5 cases, it is also true that more advanced methods for accurately computing both linear and
6 nonlinear vibrational spectra are available. However, it must be emphasized that they all require
7 an accurate mapping of the vibrational frequency to local environments around the mode of
8 interest, which is the reason why the development of vibrational maps has been one of the most
9 important research subjects in the field.

10
11
12

3. Vibrational Solvatochromism

3.1. Intermolecular interaction potential and its solute-solvent separability

The frequencies associated with transitions between vibrational quantum states of polyatomic molecules under IR absorption or Raman scattering processes depend on their structure, i.e., atomic configuration. In solutions, the surrounding microscopic environment inevitably exerts external forces on the normal modes, which affect their force constants, vibrational transition dipole moment and polarizability, and the couplings between modes leading to vibrational energy relaxations. Consequently, the vibrational frequencies of molecules in solutions differ from those in the gas phase, which has been referred to as vibrational solvatochromism. Here, the intermolecular interaction potential⁵² essentially determines a variety of the vibrational solvatochromism phenomena such as vibrational frequency shifts and transition moment changes.³⁸⁻⁴⁰ Since the development of VSMs requires separability in terms of the well-defined independent constituents, the intermolecular interaction potential needs to be described in terms of solute (IR probe) and solvent (environment) parts of the whole system separately.

One of the most frequently used approaches to describe the intermolecular interaction potential approximately is to treat the solute's molecular surroundings by continuum solvent models.¹³¹ In the simplest and oldest variant of this approach,¹³²⁻¹³⁵ the solute molecule is represented by its total charge, dipole moment, and higher multipole moments (quadrupole, octupole and so on), and placed at the center of a dielectric cavity that is surrounded by a dielectric continuum that is entirely characterized by dielectric constant, ϵ . The solute's multipole moments approximately reflect its charge distribution $\rho(\mathbf{r})$, whereas the cavity approximately represents the shape and dimension of the solute molecule as well as defines the boundary between solute and its environment. In the special case that the cavity can be modeled as a sphere of a vacuum of radius a_0 and the solute molecule is neutral in charge, the leading contribution to the interaction potential is given by the dipole-dipole term, i.e.,

$$U^{\text{Ons}} = -\frac{1}{2} \boldsymbol{\mu}_0 \cdot \mathbf{E}^{\text{Ons}}, \quad (34)$$

where $\boldsymbol{\mu}_0$ is the solute's permanent dipole moment and the so-called Onsager reaction field is

$$\mathbf{E}^{\text{Ons}} = \frac{2g}{a_0^3} \boldsymbol{\mu}(\epsilon, a_0) \quad (35)$$

with $\boldsymbol{\mu}(\epsilon, a_0)$ being the total solute's (permanent and induced) dipole moment and $g \equiv \frac{\epsilon-1}{2\epsilon+1}$, the so-called Onsager factor. Eq. (34) together with Eq. (35) describes the Onsager dipole model of solvation. Although the essential element of the solvent effect on the solvation energy is qualitatively captured by this model for moderately polar solute molecules dissolved in aprotic polar solvents, it cannot encompass a variety of specific effects originating from detailed structures and charge distributions of complicated solute molecules in condensed phases. For instance, the model is inaccurate not only when the dominant interaction is from H-bonds but also when the solute molecule has a solvent-accessible surface that is notably different from a sphere. In modern versions of continuum models of solvation, such as the polarizable continuum model^{136,137} (PCM) or the conductor-like screening model¹³⁸ (COSMO) for example, electrostatic and non-electrostatic effects have been taken into account significantly in details, which allow improved and quantitative modeling of static solvation

1 effects in isotropic solutions. However, it is not straightforward to separate the solute and
2 solvent contributions to the PCM or COSMO interaction potentials, making it challenging to
3 be used for developing VSMs.

4 However, to describe far more complicated heterogeneous environments around solute
5 molecules and to study real-time molecular dynamics, it is necessary to simulate solute-solvent
6 interactions at the atomistic level by considering all the molecular surroundings explicitly. To
7 achieve this, one should parameterize the total energy of the system with an efficient and
8 sufficiently accurate functional form that involves atomic and possibly also non-atomic sites
9 of solute and surrounding solvent molecules. According to the molecular mechanics (MM)
10 approximation (known as force field approximation), the total potential energy function is
11 decomposed into a ‘bonded’ part associated with the changes in the bond lengths, bond angles,
12 and dihedral angles, and the ‘non-bonded’ part that involves through-space interactions such
13 as long-range electrostatic and short-range van der Waals interactions. In this way, the solute-
14 solvent interaction potential can be partitioned into parameters associated with particular
15 fragments, or residues, fitting into a requirement to build a VSM.

16 Unfortunately, even though these MM approaches were found to be usually quite
17 sufficient for the description of the intermolecular forces and molecular dynamics of complex
18 molecular systems in their electronic ground states, commonly used force field parameters are
19 not accurate enough to reproduce the vibrational properties such as vibrational frequencies and
20 transition moments.¹³⁹ Therefore, they cannot be used to simulate vibrational spectra of the IR
21 probes that are either useful normal modes or small chemical groups site-specifically
22 incorporated into biomolecules or functional materials in condensed phases. This lack of
23 spectroscopic accuracy of force fields for spectroscopic applications stimulated extensive
24 research to develop significantly sophisticated and accurate models that connect solute-solvent
25 interaction potentials to vibrational spectroscopic properties.

26 Contrary to most of the semiempirical force field methods, quantum chemistry
27 calculation approach provides a quantitative description of the intermolecular potential in terms
28 of the physically sound and intuitive solute-solvent contributions such as electrostatics,
29 dispersive, and repulsive interactions.^{52,64,65,131,140-142} One of the most rigorous, accurate, and
30 sophisticated approach is the symmetry adapted perturbation theory (SAPT), which partitions
31 the intermolecular interaction operator into electron correlation perturbation and
32 intermolecular interaction energy perturbation by using the double exchange-perturbation
33 theory.¹⁴¹ Among many contributions to the SAPT interaction energy, the most important
34 components is the pseudo-classical Coulombic interaction energy between the unperturbed
35 solute and solvent charge densities, the associated exchange-repulsion energy, the induction
36 and exchange-induction interaction energies, and the intermolecular dispersion energy. As the
37 order of electron correlation increases, more contributions to the interaction potential are to be
38 included, but their physical meanings become less intuitive, and they just reflect the
39 technicality of the wavefunction model based on the series expansion of Slater determinants.
40 For the sake of practical applications in condensed phase systems, one might require a
41 computationally more efficient model of the intermolecular interaction potential which can be
42 made entirely separable between solute and solvent. Here, we consider an approximation to

1 SAPT in which the intramolecular electron correlation corrections are ignored, and the electron
 2 exchange effects are included only in the first order with respect to the interaction Hamiltonian.
 3 The Coulombic interaction energy is given by

$$4 \quad E_{\text{Coul}} = \langle 0_A \otimes 0_B | \mathcal{V}^{AB} | 0_A \otimes 0_B \rangle, \quad (36)$$

5 where $|0_A \otimes 0_B\rangle$ is the Hartree product of the unperturbed solute and solvent wavefunctions.
 6 The exchange-repulsion interaction energy can be obtained from

$$7 \quad E_{\text{Ex-Rep}} = \frac{\langle \mathcal{A}0_A 0_B | \mathcal{V}^{AB} | \mathcal{A}0_A 0_B \rangle}{\langle \mathcal{A}0_A 0_B | \mathcal{A}0_A 0_B \rangle} - E_{\text{Coul}}, \quad (37)$$

8 where $|0_A 0_B\rangle$ is the wavefunction of the solute-solvent complex and \mathcal{A} is the
 9 standard antisymmetrization operator that exchanges the labels of electron pairs in between
 10 $|0_A\rangle$ and $|0_B\rangle$. For a typical molecular complex in the equilibrium geometry, $E_{\text{Ex-Rep}}$ is
 11 substantial and cannot be neglected. Induction and dispersion interaction energies are, up to the
 12 second-order in the intermolecular interaction, given as

$$13 \quad E_{\text{Ind}} = - \sum_{m \neq 0} \frac{\langle 0_A 0_B | \mathcal{V}^{AB} | m 0_B \rangle \langle m 0_B | \mathcal{V}^{AB} | 0_A 0_B \rangle}{\hbar \omega_{m 0_A}} - \sum_{n \neq 0} \frac{\langle 0_A 0_B | \mathcal{V}^{AB} | 0_A n \rangle \langle 0_A n | \mathcal{V}^{AB} | 0_A 0_B \rangle}{\hbar \omega_{n 0_B}}$$

14 (38)

$$15 \quad E_{\text{Disp}} = - \sum_{m \neq 0} \sum_{n \neq 0} \frac{\langle 0_A 0_B | \mathcal{V}^{AB} | mn \rangle \langle mn | \mathcal{V}^{AB} | 0_A 0_B \rangle}{\hbar (\omega_{m 0_A} + \omega_{n 0_B})},$$

16 (39)

17 where $\omega_{m 0_A} = \omega_m - \omega_{0_A}$ and the summations count all the electronically excited states.

18 To evaluate expressions in Eqs. (36)-(39) and to achieve solute-solvent separability,
 19 \mathcal{V}^{AB} can be approximated by the multipole expansion of the electrostatic potential operator
 20 and its spatial derivatives⁵²

$$21 \quad \underbrace{\nabla_{\mathbf{a}} \otimes \cdots \otimes \nabla_{\mathbf{a}}}_{\mathbf{r}} \hat{\phi} \approx \sum_{b \in B} \left\{ \hat{q}_a T^{(ab;r)} - \hat{\boldsymbol{\mu}}_a \cdot \mathbf{T}^{(ab;r+1)} + \frac{1}{3} \hat{\boldsymbol{\Theta}}_a \cdot \mathbf{T}^{(ab;r+2)} - \dots \right\}, \quad (40)$$

22 where A and B are interacting molecules, \hat{q}_a , $\hat{\boldsymbol{\mu}}_a$ and $\hat{\boldsymbol{\Theta}}_a$ are the distributed charge, dipole,
 23 and quadrupole operators associated with the a th site on A , $\nabla_{\mathbf{a}} \equiv \sum_{\zeta}^{x,y,z} \hat{\mathbf{i}}_{\zeta} \frac{\partial}{\partial \zeta_a}$ and $\mathbf{T}^{(ab;n)}$ are
 24 the n th-rank interaction tensors. The first few interaction tensors in Eq. (60) are given by¹⁴³

$$25 \quad T^{(ab;0)} = \frac{1}{|\mathbf{r}_{ab}|} \quad (41)$$

$$26 \quad T_{\alpha}^{(ab;1)} = - \frac{\mathbf{r}_{ab;\alpha}}{|\mathbf{r}_{ab}|^3} \quad (42)$$

$$27 \quad T_{\alpha\beta}^{(ab;2)} = 3 \frac{\mathbf{r}_{ab;\alpha} \mathbf{r}_{ab;\beta}}{|\mathbf{r}_{ab}|^5} - \frac{\delta_{\alpha\beta}}{|\mathbf{r}_{ab}|^3} \quad (43)$$

$$28 \quad T_{\alpha\beta\gamma}^{(ab;3)} = -15 \frac{\mathbf{r}_{ab;\alpha} \mathbf{r}_{ab;\beta} \mathbf{r}_{ab;\gamma}}{|\mathbf{r}_{ab}|^7} + 3 \frac{\mathbf{r}_{ab;\alpha} \delta_{\beta\gamma} + \mathbf{r}_{ab;\beta} \delta_{\alpha\gamma} + \mathbf{r}_{ab;\gamma} \delta_{\alpha\beta}}{|\mathbf{r}_{ab}|^5} \quad (44)$$

1 with $\mathbf{r}_{ab} = \mathbf{r}_a - \mathbf{r}_b$. Under this approximation, the interaction potential operator adopts the
 2 following familiar form

$$\begin{aligned}
 3 \quad \mathcal{V}^{AB} &\approx \sum_a \left\{ \hat{q}_a \phi_a + \hat{\boldsymbol{\mu}}_a \cdot \nabla \hat{\phi}_a + \frac{1}{3} \hat{\boldsymbol{\Theta}}_a : \nabla \otimes \nabla \hat{\phi}_a + \frac{1}{15} \hat{\boldsymbol{\Omega}}_a : \nabla \otimes \nabla \otimes \nabla \hat{\phi}_a + \dots \right\} \\
 4 \quad &= \sum_{a \in A} \sum_{b \in B} \left\{ \hat{q}_a \hat{q}_b T^{(ab;0)} + (\hat{\boldsymbol{\mu}}_a \hat{q}_b - \hat{\boldsymbol{\mu}}_b \hat{q}_a) \cdot \mathbf{T}^{(ab;1)} + \hat{\boldsymbol{\mu}}_a \otimes \hat{\boldsymbol{\mu}}_b : \mathbf{T}^{(ab;2)} + \frac{1}{3} (\hat{\boldsymbol{\Theta}}_a \hat{q}_b - \right. \\
 5 \quad &\left. \hat{\boldsymbol{\Theta}}_b \hat{q}_a) \cdot \mathbf{T}^{(ab;3)} + \dots \right\}. \tag{45}
 \end{aligned}$$

6 Replacing the operators in Eq. (45) with the corresponding expectation values leads to the
 7 approximate expression for the electrostatic interaction energy. Eq. (45) can also be used to
 8 approximate the induction and dispersion interaction energies. For instance, for a single closed-
 9 shell molecule in a uniform external electric field, Eq. (38) can be written as

$$E_{\text{Ind}} = -\frac{1}{2} \boldsymbol{\alpha}_A : \mathbf{E} \otimes \mathbf{E}, \tag{46}$$

10 where the ground-state polarizability tensor is defined as

$$\boldsymbol{\alpha}_A = 2 \sum_{m \neq 0} \frac{\langle 0_A | \hat{\boldsymbol{\mu}} | m \rangle \otimes \langle m | \hat{\boldsymbol{\mu}} | 0_A \rangle}{\hbar \omega_{m0_A}}. \tag{47}$$

11 Equations (36)-(39) serve as the theoretical basis for the effective fragment potential (EFP2)
 12 method⁶⁴ that is one of the most efficient non-empirical methods used in a variety of molecular
 13 dynamics simulations. The EFP2 potential, which is an *ab initio* force field with parameters
 14 derived from first-principles rather than fitting to some benchmark data, can be written as

$$U^{\text{EFP2}} = U^{\text{Coul}} + U^{\text{Ex-Rep}} + U^{\text{Ind}} + U^{\text{Disp}} + U^{\text{CT}}. \tag{48}$$

15 In the above equation, the Coulomb, exchange-repulsion, induction, dispersion, and charge-
 16 transfer contributions are functions of the effective fragment parameters that consist of the
 17 atomic numbers and coordinates, distributed multipole moments up to octupoles, distributed
 18 dipole-dipole static and frequency-dependent polarizabilities, Gaussian basis set used to
 19 expand the wavefunction along with the associated atomic orbital-molecular orbital (AO-MO)
 20 coefficients, and the Fock matrix in AO basis. EFP2 interaction potential is quite similar to the
 21 SAPT interaction potential but is formulated within the Hartree-Fock (HF) or the density
 22 functional theory (DFT) methods only, in which the many-electron wavefunction can be
 23 approximated by a single Slater determinant. Moreover, EFP2 model is an effective one-
 24 electron potential, hence only the evaluation of computationally inexpensive one-electron
 25 integrals is necessary to calculate the entire interaction potential, unlike SAPT and full quantum
 26 mechanical methods that require calculations of electron repulsion integrals as well. The
 27 charge-transfer contribution, U^{CT} , which is a part of induction energy in the SAPT model, is
 28 separately calculated in the EFP2 model,¹⁴⁴ though it is rarely evaluated due to its relatively
 29 high computational cost.

30 In summary, the intermolecular interaction potential is a very complicated function of
 31 the atomic coordinates and, in general, quantum mechanical description of the solute-solvent
 32 complex is necessary to accurately describe molecular vibrations induced by detailed structural

1 distortions due to the solute-solvent interactions. Using the multipole expansion of the
 2 intermolecular interaction potential operator \mathcal{V}^{AB} , one can describe the intermolecular
 3 interaction in terms of the solute- and solvent dependent parts separately, which in turn enabled
 4 us to develop various *ab initio* and semiempirical VSMs. We next discuss the fundamentals of
 5 VSMs that are based on quantitative relationships between vibrational observables and
 6 intermolecular interaction potentials.

8 **3.2. Theoretical foundations of vibrational spectroscopic mapping**

9
 10 The vibrational frequency shift of the j th normal mode can be defined as a difference between
 11 the actual vibrational frequency of the mode in solution and that in a reference state, typically
 12 in the gas phase, i.e.,

$$\Delta\omega_j \equiv \omega_j - \omega_{j,0} . \quad (49)$$

13 The frequency ω_j depends on the electronic structure of the IR probe and its molecular
 14 surroundings. The general theory describing the vibrational solvatochromism of a spatially
 15 localized normal mode based on the intermolecular interaction potential was developed by
 16 Buckingham^{62,145,146}, and later generalized to any arbitrary normal mode by Cho.^{147,148} The
 17 vibrational frequency spectrum of the solute in the presence of molecular environment is
 18 determined by the effective Hamiltonian,

$$H = \sum_i \frac{P_i^2}{2M_i} + V(\mathbf{Q}) . \quad (50)$$

19 where P_i are the vibrational momentum operators and the vibrational potential energy function
 20 is defined up to a constant offset by

$$V(\mathbf{Q}) = \frac{1}{2}M_i\omega_i^2 Q_i^2 + \frac{1}{6} \sum_{ijk} g_{ijk} Q_i Q_j Q_k + \dots + U(\mathbf{Q}) . \quad (51)$$

21 Here, M_i and ω_i are the gas-phase reduced mass and the vibrational frequency of the i th
 22 normal mode Q_i , respectively. g_{ijk} is the cubic anharmonic constant, whereas U denotes the
 23 solute-solvent interaction potential, a function of solute's molecular structure \mathbf{Q} . U can be
 24 expanded in a Taylor series around the equilibrium geometry of solute in the gas phase,

$$U(\mathbf{Q}) = U_0 + \sum_i \left. \frac{\partial U(\mathbf{Q})}{\partial Q_i} \right|_{\mathbf{Q}_0} Q_i + \frac{1}{2} \sum_{ij} \left. \frac{\partial^2 U(\mathbf{Q})}{\partial Q_j \partial Q_k} \right|_{\mathbf{Q}_0} Q_i Q_j + \dots \quad (52)$$

25 The resulting vibrational potential energy function in Eq. (52) with $U(\mathbf{Q})$ in Eq. (52) can be
 26 directly compared with the potential energy re-expressed in the normal coordinates in the
 27 solute-solvent cluster $\bar{\mathbf{Q}}$,

$$V(\bar{\mathbf{Q}}) = V_0 + \frac{1}{2} \bar{M}_i \bar{\omega}_i \bar{Q}_i^2 + \frac{1}{6} \sum_{ijk} \bar{g}_{ijk} \bar{Q}_i \bar{Q}_j \bar{Q}_k + \dots \quad (53)$$

1 for which it must hold that

$$\sum_i \left. \frac{\partial V(\bar{\mathbf{Q}})}{\partial \bar{Q}_i} \right|_{\bar{\mathbf{Q}}_0} = 0 \quad \text{for all } i, \quad (54)$$

2 because the system is at the lowest energy. From the above condition, it follows that the new
3 normal coordinates are approximately given by

$$\bar{Q}_j \approx Q_j - \left. \frac{1}{M_j \omega_j^2} \frac{\partial U(\mathbf{Q})}{\partial Q_j} \right|_{\mathbf{Q}_0}. \quad (55)$$

4 Applying this linear transformation to Eq. (53), one can immediately identify the effective
5 vibrational force constant (or Hessian) matrix¹⁴⁸ as

$$k_{jk} \approx M_j \omega_j^2 \delta_{jk} + \left. \frac{\partial^2 U(\mathbf{Q})}{\partial Q_j \partial Q_k} \right|_{\mathbf{Q}_0} - \sum_i \left. \frac{g_{ijk}}{M_i \omega_i^2} \frac{\partial U(\mathbf{Q})}{\partial Q_i} \right|_{\mathbf{Q}_0}. \quad (56)$$

6 Note that the effective force constants in the Hessian matrix explicitly depend on not U but its
7 first and second derivatives evaluated for the gas-phase geometry, \mathbf{Q}_0 . Solvation-induced
8 vibrational frequencies and the resulting new set of normal modes of the solute molecule in
9 solutions can be directly obtained by diagonalizing the Hessian matrix with elements k_{jk} .

10 In the limiting case that the vibrational couplings of the normal mode of interest with
11 other vibrational degrees of freedom are relatively weak, it is possible to approximately express
12 the vibrational frequency shift and the change of the vibrational transition dipole as functions
13 of the derivatives of the intermolecular interaction potential. Under such a weak-coupling
14 approximation (WCA) that has been found to be valid for spatially localized vibrational modes,
15 the vibrational solvatochromic frequency shift from the gas-phase frequency is given by,^{62,148}

$$\Delta\omega_j^{\text{WCA}} = [\hat{F}_j^{\text{EA}} + \hat{F}_j^{\text{MA}}]U(\mathbf{Q}). \quad (57)$$

16 where the electric anharmonicity (EA) and mechanical anharmonicity (MA) operators, \hat{F}_j^{EA}
17 and \hat{F}_j^{MA} , respectively, defined as¹⁴⁸

$$\hat{F}_j^{\text{EA}} = \left. \frac{1}{2M_j \omega_j} \frac{\partial^2}{\partial Q_j^2} \right|_{\mathbf{Q}_0} \quad (58)$$

$$\hat{F}_j^{\text{MA}} = - \left. \frac{1}{2M_j \omega_j} \sum_i \frac{g_{ijj}}{M_i \omega_i^2} \frac{\partial}{\partial Q_i} \right|_{\mathbf{Q}_0}. \quad (59)$$

18 A few quantum chemistry calculation studies were performed to test the validity of the
19 theoretical expressions given in Eq. (57) for modes that are highly localized on two atoms in

1 small molecules¹⁴⁹⁻¹⁵³ as well as for multiple normal modes in polyatomic molecules.^{143,154-156}
 2 It was found that the WCA and the resulting theory for vibrational solvatochromism are
 3 quantitatively reliable for a variety of localized modes such as C-H stretch,¹⁵³ amide I
 4 mode,^{143,154} and -C≡N¹⁵⁵ and -N≡C¹⁵⁶ stretches. In fact, these small IR-active vibrations have
 5 served as important IR probes and widely used to study the structure and dynamics of
 6 biomolecules and materials in combination with the linear and non-linear vibrational
 7 spectroscopic methods. Despite the success of the WCA-based vibrational solvatochromism
 8 theories, there exist cases that one might need to go beyond the WCA limit. For example, when
 9 normal modes become coupled and delocalized, and when the solute-solvent interactions
 10 induce mode mixings, the WCA cannot be acceptable. In the simplest case, i.e., where normal
 11 modes are coupled in a pairwise manner, the vibrational frequency shift becomes

$$\Delta\omega_j \cong \Delta\omega_j^{\text{WCA}} + \Gamma_{jk}, \quad (60)$$

12 where the mode coupling contribution to the frequency shift is

$$\Gamma_{jk} = \frac{2}{M_j M_k \omega_j (\omega_j^2 - \omega_k^2)} \left. \frac{\partial^2 U(\mathbf{Q})}{\partial Q_j \partial Q_k} \right|_{\mathbf{Q}_0} \times \sum_i \frac{g_{ijk}}{M_i \omega_i^2} \left. \frac{\partial U(\mathbf{Q})}{\partial Q_i} \right|_{\mathbf{Q}_0}. \quad (61)$$

13 In practice, one might need to evaluate the general expression given in Eq. (60) and find
 14 eigenvalues of the effective Hessian matrix. Nevertheless, as long as U is computable
 15 accurately and solute-solvent separably, the vibrational frequency shifts of most of the normal
 16 modes can be expressed as an *ab initio* VSM, treating the normal modes of the solute molecule
 17 in the gas phase as the basis modes.

18 From Eq. (57), it becomes clear that the vibrational solvatochromism of IR probes
 19 relies on accurate and efficient modeling of U and its derivatives with respect to the normal
 20 coordinates, where the intermolecular interaction potential U at various intermolecular
 21 separation regimes is described in terms of well-known and intuitive physical
 22 approximations.¹⁵⁷ In the limiting case of relatively large intermolecular separation, molecular
 23 wavefunctions sense only the electrostatic potential created by the other surrounding molecules.
 24 In this case, the interaction energy equals the pseudo-classical Coulombic energy between
 25 unperturbed charge densities of the solute and solvent molecules. As the two molecules get
 26 close to each other, the electrostatic potential becomes strong enough to induce relevant
 27 changes in the wavefunctions due to the self-polarization of their charge densities. This
 28 induction process always leads to a stabilization of the system. Also, quantum effects cause
 29 electrons to correlate their movements, which exert instantaneous attractive forces known as
 30 dispersion interactions. Once the distance becomes very small enough to create a non-
 31 negligible overlap between wavefunctions, the Pauli exclusion principle causes the electrons
 32 to pull away from the overlap region, which is the underlying physics behind repulsive forces.
 33 At the same time, the indistinguishability of electrons reduces this repulsion to some extent,
 34 which is a quantum exchange effect. Furthermore, the smaller the distance is, and the larger
 35 the overlap is, the more severe electronic structure rearrangement takes place, which eventually
 36 leads to a change in a net electric charge of interacting molecules. This intermolecular charge

1 transfer is an attractive interaction and further stabilizes the system energetically. As the
2 intermolecular distance becomes smaller, the nature of the interactions becomes more
3 complicated, requiring higher-level theoretical descriptions. This, in turn, indicates that
4 vibrational solvatochromism and properties of solute or IR probe molecules in solutions do
5 result from highly complicated intermolecular interaction potential as well as intramolecular
6 anharmonicities and couplings. However, due to the linearity of the WCA expression with
7 respect to U – note that there is no second-order (in the intermolecular interaction potential)
8 term in Eq. (57), it is, in principle, legitimate to partition the vibrational solvatochromic
9 frequency shift into separate contributions originating from distinct physical approximations,
10 such as electrostatic, exchange-repulsion, induction, dispersion, and charge-transfer.
11 Sometimes, even simpler approaches utilizing a less formal but more chemically intuitive set
12 of intermolecular interaction potential descriptors such as solute and solvent polarity,
13 acidity/basicity, H-bonding strength and so on were found to be useful to interpret
14 experimentally measured spectroscopic observables such as vibrational frequency, oscillator
15 strength, linewidth, and vibrational dynamics. Therefore, as long as the degree of separability
16 between unperturbed solute and perturbing environment is acceptable, the mapping of
17 vibrational observables, e.g., frequencies, transition dipole moments, and polarizabilities, onto
18 a universal set of parameters becomes possible and can be justified theoretically. In the
19 following sections, we introduce those approaches that are based on the solute-solvent
20 separable forms of vibrational frequency maps, which served as groundworks and bases for
21 further development of the more robust empirical vibrational frequency maps later.

22

23 **3.3. Vibrational solvatochromism: Bulk phenomenological descriptions**

24 Due to an unduly complex nature of the solute-solvent intermolecular potential and associated
25 computational cost of employing full quantum mechanical calculation method for systems in
26 condensed phases, a few decades of extensive theoretical and experimental studies have been
27 performed to develop approximate, efficient, but highly accurate methods useful for
28 quantitatively describing the vibrational solvatochromism of important IR probes in terms of a
29 relatively small set of adjustable parameters. Such approaches, though often derived from first
30 principles, used a variety of fitting procedures to link general descriptors of solute/solvent
31 properties like polarity, Lewis/Brønsted acidity/basicity, and H-bond donating/accepting
32 ability with the vibrational frequency, IR absorption coefficient, and Raman scattering cross-
33 section of a given mode in a wide range of solvents.

34 It was nearly eight decades ago when Bauer and Magat noticed that the vibrational frequencies
35 of solute tend to undergo redshifts with increasing dielectric constant of the solvent.¹⁵⁸
36 According to the Kirkwood-Bauer-Magat (KBM) limiting law based on the Kirkwood-Onsager
37 continuum model of solvation,^{134,159} vibrational frequency is a linear function of the Onsager
38 factor. It is well known that the KBM law works well only for aprotic solvents and breaks down
39 when solvent's permanent dipole moment is not vanishingly small.¹⁵⁵ Later, Ben-Amotz et
40 al.¹⁶⁰ used the theory of Buckingham^{62,145,146} to study the relationship between the vibrational
41 frequency shift of acetonitrile $C\equiv N$ stretch mode and the applied pressure, and found the

1 dependence of the vibrational frequency with the bulk solvent density. Later, Fawcett et
2 al.^{161,162} expressed the solute's vibrational frequency in terms of the Gutmann solvent acceptor
3 and donor numbers¹⁶³, the solute and solvent dielectric constant and the refractive index, as
4 well as four adjustable parameters. One of the most important findings in the Ben-Amotz et
5 al.'s and Fawcett et al.'s studies is that the dispersion plays an important role in the vibrational
6 barochromism of acetonitrile C≡N stretch mode at low densities and the repulsive interaction
7 causes a strong blueshift at high densities. In addition, Fawcett et al.'s model accurately
8 predicted the peak maxima of the C≡N stretch mode of acetonitrile in a wide range of solvents.
9 In 1998, Reimers and Hall¹⁶⁴ investigated in great detail the solvation of acetonitrile based on
10 the Ben-Amotz et al.'s and Fawcett et al.'s models at ambient conditions. They considered
11 thirty-three different solvents that range from nonpolar and non-protic CCl₄, strongly polar
12 aprotic DMSO, to acidic trifluoroacetic acid (TFA). They noticed that the electrostatic non-
13 specific interactions cause much smaller redshifts than the dispersion interactions do. Note that
14 the latter cannot be correlated with solvent electrostatic potential or electric field at all. What
15 is also interesting in their work is that they reported specific (short-range) frequency blueshifts
16 that are caused by solvent molecules with H-bonding capability. The stronger the H-bond
17 between MeCN and a solvent molecule forms, the larger the blueshift is. However, since it was
18 not possible to separately calculate various short-range interaction contributions to the
19 frequency blueshift, the detailed mechanism was not entirely clear.

20 It is of great interest to elucidate the effect of H-bonding interaction on the vibrational
21 frequency because many useful IR probes act as a sensitive reporter providing information on
22 the local H-bonding environment. Boxer and coworkers^{165,166} proposed that the vibrational
23 spectroscopy of IR probes can be combined with the nuclear magnetic resonance (NMR)
24 spectroscopy to separate the frequency shifts induced by the H-bonding interaction and the
25 other interactions. Recently, Zhang et al. proposed an empirical method based on the Kamlet-
26 Taft (KT) solvent parameters, which enables one to separately estimate the solvent polarity and
27 H-bonding effects on the vibrational solvatochromism.^{167,168} They suggested that vibrational
28 frequency shift can be mapped to KT parameters as

$$\Delta\omega = A(-\alpha_{KT} + \beta_{KT} + \pi_{KT}^*) + B, \quad (62)$$

29 where the coefficients A and B are fitting parameters. Note that the solvent KT parameters were
30 originally determined from the solvatochromic shift of absorption maximum of electronic
31 chromophores in solution. Based on the analyses of different spectroscopic observables, three
32 types of KT parameters are defined and parameterized: the H-bond accepting¹⁶⁹ β_{KT} , the H-
33 bond donating¹⁷⁰ α_{KT} , and the polarity¹⁷¹ π_{KT}^* . Zhang et al. showed that their method is
34 applicable to quite complicated solute molecules like 5-cyanotryptophan dissolved in a broad
35 range of solvents, including strongly polar and protic solvent like trifluoroethanol (TFE). They
36 showed that this empirical model is especially useful for studying IR probes that can donate
37 and accept H-bonds via various functional groups.

38

39 **3.4. Onsager reaction field theory: Dipolar solute and *continuum* solvent model**

1 At the turn of the 20th century, Hush and Reimers^{172,173} and Andrews and Boxer^{174,175} studied
 2 vibrational electrochromism to quantitatively relate experimentally measured vibrational
 3 properties with an applied external electric field. This vibrational Stark effect (VSE)
 4 spectroscopy that measures field-dependent spectra for isotropic samples was thoroughly
 5 described by Liptay.¹⁷⁶ To provide a quantitative interpretation of VSEs on vibrational
 6 frequency shift and the changes in absorbance and lineshape, which has been referred to as
 7 vibrational electrochromism, it was necessary to develop a theoretical framework by treating
 8 the interaction between molecular dipole and polarizability and applied spatially uniform
 9 electric field.^{148,172-174} As a result, the vibrational frequency shift of a j th normal mode was
 10 shown to be related to the electric field as follows

$$\Delta\omega_j \approx -\Delta\mu_j \cdot \mathbf{E} - \frac{1}{2} \Delta\alpha_j: \mathbf{E} \otimes \mathbf{E}, \quad (63)$$

11 where $\Delta\mu_j$ is the vibrational Stark dipole moment and $\Delta\alpha_j$ is the vibrational Stark
 12 polarizability that accounts for the quadratic effect with respect to the electric field, \mathbf{E} . From
 13 VSE spectroscopic investigations, it was shown that this quadratic term can often be ignored
 14 because the applied electric field strength is weak. Consequently, only the first-order term in
 15 Eq. (63), which is based on the approximation that the applied electric field interacts with
 16 molecular dipoles, is important in quantitatively describing the VSE on vibrational frequency
 17 shift, i.e.,

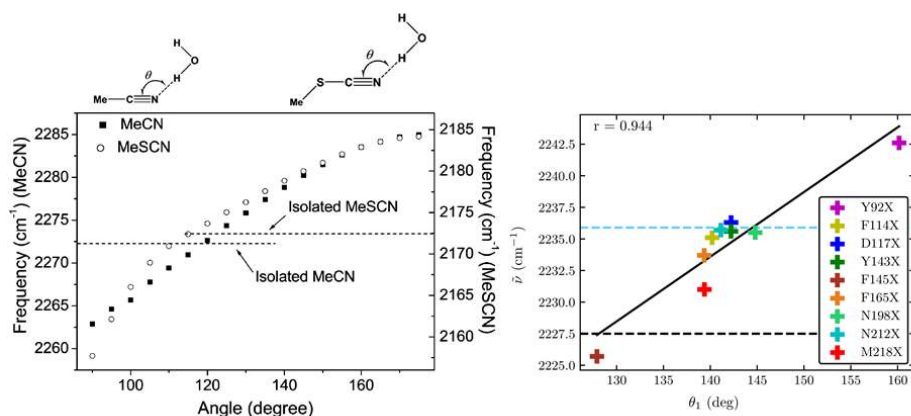
$$\Delta\omega_j \approx -\Delta\mu_j^{\text{VSE}} E_j, \quad (64)$$

18 where $\Delta\mu_j^{\text{VSE}}$ is the vibrational Stark tuning rate and E_j is the electric field component. The
 19 vibrational Stark tuning rates of a variety of IR probes were reported.^{177,178} Also, they were
 20 calculated using quantum chemistry calculation methods and found to be in quantitative
 21 agreement with experimental data.^{174,175,179} Typically, the vibrational Stark tuning rates are in
 22 a range of 0.4–1.0 $\text{cm}^{-1}/(\text{MV}/\text{cm})$. To make use of the vibrational Stark theory for
 23 quantitatively describing the vibrational frequency shift of IR probe molecule in solutions, one
 24 needs to take into consideration the fact that the effective local electric field around it differs
 25 from the applied external field. Thus, an empirical scaling factor, so-called the local field
 26 correction factor, f , was introduced to modify the VSE theory as

$$\Delta\omega_j \approx -f \Delta\mu_j^{\text{VSE}} E_j. \quad (65)$$

27 In typical solvents, the local field correction factor f is estimated to be approximately 2.¹⁸⁰⁻¹⁸²
 28 In practice, the factor f has been treated as an adjustable parameter to fit the VSE model to
 29 experimental results. Due to the simplicity of vibrational Stark effect theory for vibrational
 30 frequency shift induced by molecule-field interaction, it has been extensively used to
 31 quantitatively describe vibrational solvatochromism of IR probes in solutions. However,
 32 because the local electric field around molecules in solutions is not spatially uniform, the
 33 vibrational Stark effect theory in Eq. (65) is not quantitatively reliable even in the case that the
 34 vibrational solvatochromism is determined by the Coulomb interaction between solute and
 35 solvent molecules.^{180,181}

1 A good example of this effect is the dependence of nitrile solvatochromism by
 2 hydrogen-bonding angle. Using a density functional theory, Cho and coworkers¹⁸³ calculated
 3 the nitrile stretching frequency in acetonitrile and methyl thiocyanate in water clusters as a
 4 function of the angle (θ) between the hydrogen being donated to the nitrogen lone pair and the
 5 nitrile, shown in Figure 3. At large values of $\theta > 120^\circ$, the H-bond is accepted by the nitrile
 6 lone pairs, which sit in an antibonding orbital. This has the effect of strengthening the nitrile
 7 bond and increasing the nitrile stretching frequency. At smaller values of θ , 90-120°, the H-
 8 bond is accepted by electrons in a π bonding orbital of the nitrile triple bond. This has the effect
 9 of weakening the nitrile bond and decreasing the nitrile stretching frequency. Webb and
 10 coworkers¹⁸⁴ investigated this effect experimentally by engineering the noncanonical amino
 11 acid *p*-cyanophenylalanine into a variant of green fluorescent protein (GFP) at a variety of both
 12 solvent-accessible and solvent-excluded locations within the protein structure. Measured nitrile
 13 absorption energies from these vibrational probes could not be straightforwardly explained
 14 through the Stark effect in Eq. (65). However, MD simulations of the nitrile-containing variants
 15 revealed that the nitriles experienced a range of hydrogen bonding geometries, either to solvent
 16 or to the protein itself, based on their positions within the protein structure. As in Cho's
 17 theoretical work, the value of θ was strongly correlated to nitrile stretching frequency (Figure
 18 3), providing the first experimental demonstration of this prediction. This result serves as a
 19 warning for interpreting vibrational spectra purely in terms of electrostatic effects without other
 20 information, such as MD simulations or temperature-based experiments. It also demonstrates
 21 that in heterogeneous and complex environments, every local interaction is important in
 22 determining the vibrational spectra of many interesting probes (including the nitrile), and
 23 justifies the approach of using empirical frequency maps for calculating and interpreting
 24 spectra.



25
 26 **Figure 3.** Left: Nitrile stretching mode frequencies of acetonitrile (MeCN, closed squares) and methyl
 27 thiocyanate (MeSCN, open circles) plotted with respect to the hydrogen-bond angle, θ , between the
 28 nitrile's N atom and the hydrogen atom of the H-bonded water molecule. Reproduced from Figure 2 of
 29 Ref.¹⁸³ Copyright 2008 AIP Publishing. Right: Experimentally measured mean nitrile vibrational
 30 frequency plotted with respect to the average value of θ from MD simulations of nine variants of GFP
 31 containing *p*-cyanophenylalanine (given in the figure key). Reproduced from Figure 8(B) of Ref.¹⁸⁴
 32 Copyright 2018 The American Chemical Society.
 33

1 Instead of considering the dipole-electric field interaction only, using the more general
 2 intermolecular interaction of the solute molecule with dielectric *continuum* solvent, one can
 3 obtain the more general relationship between the vibrational frequency and intermolecular
 4 interaction potential. Invoking the WCA in Eq. (57), the first-principles formula for the
 5 vibrational frequency shift was obtained and it is given by the sum of the three contributions:
 6 (i) the Coulombic term associated with the permanent dipole moment, (ii) the induction term
 7 associated with the induced dipole moment, and (iii) the electric field-correction term,¹⁸⁵ i.e.,

$$8 \quad \Delta\omega_j(\varepsilon, a_0) = \Delta\omega_j^{\text{Coul}} + \Delta\omega_j^{\text{Ind}} + \Delta\omega_j(\mathbf{E}^{\text{Ons}}). \quad (66)$$

9 In Eq. (66), a_0 is the Onsager cavity radius, \mathbf{E}^{Ons} is the Onsager reaction field given in Eq.
 10 (35), and

$$11 \quad \Delta\omega_j^{\text{Coul}} = -\boldsymbol{\mu}_j \cdot \mathbf{E}^{\text{Ons}} \quad (67)$$

$$12 \quad \Delta\omega_j^{\text{Ind}} = -\frac{1}{2}\boldsymbol{\mu}_j^{\text{Ind}} \cdot \mathbf{E}^{\text{Ons}} - \frac{1}{2}\boldsymbol{\alpha}_j : \mathbf{E}^{\text{Ons}} \otimes \mathbf{E}^{\text{Ons}} \quad (68)$$

$$13 \quad \Delta\omega_j(\mathbf{E}^{\text{Ons}}) \approx \frac{1}{4M_j\omega_j} \sum_i \left\{ \frac{g_{ijj}}{M_i\omega_i^2} \boldsymbol{\mu}_0 - 2\delta_{ij} \left(\frac{\partial \boldsymbol{\mu}_0}{\partial Q_i} + \boldsymbol{\alpha}_0 \cdot \frac{\partial \mathbf{E}^{\text{Ons}}}{\partial Q_i} \Big|_{\mathbf{Q}_0} \right) \right\} \cdot \frac{\partial \mathbf{E}^{\text{Ons}}}{\partial Q_i} \Big|_{\mathbf{Q}_0} \quad (69)$$

14 The effective gas-phase and solvation-induced vibrational solvatochromic dipole moments are

$$15 \quad \boldsymbol{\mu}_j = \frac{1}{4M_j\omega_j} \left\{ \frac{\partial^2 \boldsymbol{\mu}_0}{\partial Q_j^2} \Big|_{\mathbf{Q}_0} - \sum_i \frac{g_{ijj}}{M_i\omega_i^2} \frac{\partial \boldsymbol{\mu}_0}{\partial Q_i} \Big|_{\mathbf{Q}_0} \right\} \quad (70)$$

$$16 \quad \boldsymbol{\mu}_j^{\text{Ind}} = \frac{1}{M_j\omega_j} \left\{ \frac{\partial \mathbf{E}^{\text{Ons}}}{\partial Q_j} \Big|_{\mathbf{Q}_0} \cdot \frac{\partial \boldsymbol{\alpha}_0}{\partial Q_j} \Big|_{\mathbf{Q}_0} - \sum_i \frac{g_{ijj}}{M_i\omega_i^2} \boldsymbol{\alpha}_0 \cdot \frac{\partial \mathbf{E}^{\text{Ons}}}{\partial Q_i} \Big|_{\mathbf{Q}_0} \right\}, \quad (71)$$

17 whereas the vibrational solvatochromic polarizability tensor is

$$18 \quad \boldsymbol{\alpha}_j = -\frac{1}{2M_j\omega_j} \sum_i \frac{g_{ijj}}{M_i\omega_i^2} \frac{\partial \boldsymbol{\alpha}_0}{\partial Q_i} \Big|_{\mathbf{Q}_0}. \quad (72)$$

19 Here, $\boldsymbol{\mu}_0$ and $\boldsymbol{\alpha}_0$ are the permanent dipole moment and the polarizability of the solute
 20 molecule, respectively. It should be noted that the electric field-correction term in Eq. (69),
 21 $\Delta\omega_j(\mathbf{E}^{\text{Ons}})$, arises from the change of the electric field along the normal coordinate.

22 Now, taking into consideration the linear terms with respect to the Onsager reaction
 23 field in Eq. (35), the frequency shift in Eq. (66) simplifies as

$$\Delta\omega_j(\varepsilon, a_0) = \left[-\boldsymbol{\mu}_j - \frac{1}{2}\boldsymbol{\mu}_j^{\text{Ind}} \right] \cdot \mathbf{E}^{\text{Ons}} + \Delta\omega_j(\mathbf{E}^{\text{Ons}}). \quad (73)$$

24 This expression can be directly compared to the empirical relationship in Eq. (89), which
 25 suggests that the local field correction could be associated with the induced solvatochromic
 26 dipole effect as well as the electric-field correction term.

27 Since Eq. (66) shows that the vibrational frequency shift is proportional to the solute's
 28 dipole moment, the dipole-approximated VSE theory has been frequently used in combination
 29 with the Onsager's solvation model. That is to say, the Onsager reaction field generated by the
 30 vibrational Stark dipole moment interacts with that dipole, which results in a simplified
 31 expression for the vibrational frequency shift given as

$$\Delta\omega_j(\varepsilon, a_0) = -\frac{2(\varepsilon-1)(n^2+2)}{3(2\varepsilon+n^2)} \frac{\mu_0}{V} \Delta\mu, \quad (74)$$

1 where V is the molecular volume.¹⁷⁸ In Eq. (74), the solvent's refractive index n is included in
 2 the reaction field to take into account the effect of solvent polarizability. This approximate
 3 theory in Eq. (74) was found to be useful to describe the vibrational solvatochromism of C=O
 4 stretching modes in ketones and amides. However, because of the approximate natures of the
 5 solute-solvent interaction potential and dielectric continuum solvent model considered, it does
 6 not provide quantitative descriptions of vibrational solvatochromism of other IR probes.
 7 Despite the limited validity, the VSE theory of vibrational solvatochromism is still often used
 8 by researchers, especially when the more refined theoretical model is challenging to implement
 9 or not available.^{186,187}

11 3.5. Electrostatic effect: Distributed multipole analysis

12 To overcome the limitations of dipole interaction-based theory for vibrational solvatochromism,
 13 one should consider local electric potential created by surrounding solvent molecules more
 14 realistically. Indeed, the solvent electric field experienced by a given solute molecule in
 15 solution is highly non-uniform in space. Assuming that the solute-solvent intermolecular
 16 interaction potential can be fully described by the distributed charges, dipoles, and high-order
 17 multipoles interacting with solvent electric potential and its linear and nonlinear gradients, it
 18 was shown that the vibrational solvatochromic frequency shift is given as¹⁴⁸

$$\Delta\omega_j = \sum_x \left\{ l_{x;j} \phi_x + \boldsymbol{\mu}_{x;j} \cdot \nabla \phi_x + \frac{1}{3} \boldsymbol{\Theta}_{x;j} : \nabla \otimes \nabla \phi_x + \frac{1}{15} \boldsymbol{\Omega}_{x;j} \right. \\ \left. : \nabla \otimes \nabla \otimes \nabla \phi_x + \dots \right\}, \quad (75)$$

19 where the vibrational solvatochromic monopole (charge; $l_{x;j}$), dipole ($\boldsymbol{\mu}_{x;j}$), quadrupole ($\boldsymbol{\Theta}_{x;j}$),
 20 and octupole ($\boldsymbol{\Omega}_{x;j}$) moments are defined as

$$l_{x,j} = \frac{1}{2M_j\omega_j} \left\{ \frac{\partial^2 q_x}{\partial Q_j^2} \Big|_{\mathbf{Q}_0} - \sum_i \frac{g_{ijj}}{M_i\omega_i^2} \frac{\partial q_x}{\partial Q_i} \Big|_{\mathbf{Q}_0} \right\} \quad (76)$$

$$\boldsymbol{\mu}_{x,j} = \frac{1}{2M_j\omega_j} \left\{ \frac{\partial^2 \boldsymbol{\mu}_x}{\partial Q_j^2} \Big|_{\mathbf{Q}_0} - \sum_i \frac{g_{ijj}}{M_i\omega_i^2} \frac{\partial \boldsymbol{\mu}_x}{\partial Q_i} \Big|_{\mathbf{Q}_0} \right\} \quad (77)$$

$$\boldsymbol{\Theta}_{x,j} = \frac{1}{2M_j\omega_j} \left\{ \frac{\partial^2 \boldsymbol{\Theta}_x}{\partial Q_j^2} \Big|_{\mathbf{Q}_0} - \sum_i \frac{g_{ijj}}{M_i\omega_i^2} \frac{\partial \boldsymbol{\Theta}_x}{\partial Q_i} \Big|_{\mathbf{Q}_0} \right\} \quad (78)$$

$$\boldsymbol{\Omega}_{x,j} = \frac{1}{2M_j\omega_j} \left\{ \frac{\partial^2 \boldsymbol{\Omega}_x}{\partial Q_j^2} \Big|_{\mathbf{Q}_0} - \sum_i \frac{g_{ijj}}{M_i\omega_i^2} \frac{\partial \boldsymbol{\Omega}_x}{\partial Q_i} \Big|_{\mathbf{Q}_0} \right\} \quad (79)$$

21 These charges and multipoles are distributed over a generalized set of centers placed on the
 22 solute molecule (typically atomic centers). They interact with the solvent electric potential

1 ϕ_x (evaluated at the x th distributed site), electric field ($\mathbf{E}_x = -\nabla\phi_x$), the gradient of electric
 2 field gradient, and so on, thus sensing the electric field created by surrounding solvent
 3 molecules. These vibrational solvatochromic charges and multipoles, i.e., q_x , $\boldsymbol{\mu}_x$, $\boldsymbol{\Theta}_x$, and
 4 $\boldsymbol{\Omega}_x$, can be calculated using the cumulative atomic multipole moment (CAMP) calculation
 5 method developed by Sokalski and Poirier or any other distributed multipole expansion
 6 method.¹⁸⁵ Eq.(72) is essentially a very general form of the electrochromic VSM.

7 In the limiting case that only one interaction site, e.g., the center of mass, of a solute
 8 molecule is considered, the vibrational solvatochromic charge is zero due to the charge
 9 conservation condition and the distributed multipole expansion form of the vibrational
 10 solvatochromic frequency shift in Eq. (75) becomes highly simplified as¹⁸⁸

$$\Delta\omega_j = -\boldsymbol{\mu}_j \cdot \mathbf{E} - \frac{1}{3}\boldsymbol{\Theta}_j : \nabla \otimes \mathbf{E} - \frac{1}{15}\boldsymbol{\Omega}_j : \nabla \otimes \nabla \otimes \mathbf{E} + \dots, \quad (80)$$

11 where the first term is nothing but the well-known VSE theory. From the quantum chemistry
 12 calculations for a few IR probes, such as C \equiv N stretches in CN $^-$, MeCN, MeSCN, *p*-tolunitrile
 13 and 4-cyanopyridine, asymmetric azido stretch in MeN $_3$, and C–F stretches in fluorobenzene
 14 and 3-fluoropyridine, it was found that the terms up to vibrational solvatochromic quadrupoles
 15 should be included to adequately describe the vibrational frequency shift.

17 **3.6. Electrostatic and non-electrostatic interactions: Effective fragment potential** 18 **approach**

19 As opposed to many studies concentrating on electrostatic interaction-induced vibrational
 20 solvatochromism,³⁸ there are just a few reports considering non-electrostatic interaction
 21 contributions to the frequency shift due to solvation. Rey and Hynes¹⁸⁹ decomposed the atomic
 22 forces obtained from classical molecular dynamics (CMD) simulations. They found that the
 23 van der Waals interaction induces a strong blueshift of the C \equiv N stretch mode in cyanide anion
 24 in solution. A similar conclusion was drawn by Morales and Thompson, who investigated
 25 MeCN/water system by using classical MD simulation methods.¹⁹⁰ There also exist other works
 26 showing the non-negligible exchange-repulsion-induced effect on vibrational frequency
 27 shifts.¹⁹¹⁻¹⁹⁶ By correlating various interaction potential components with frequency shifts, the
 28 repulsive potential was found to be responsible for vibrational frequency blueshifts.
 29 Zierkiewicz et al. studied a series of both blue- and red-shifting complexes.¹⁹³ They attributed
 30 the blueshift of vibrational frequency to a ‘repulsion wall’ caused by the Pauli exclusion
 31 principle. Furthermore, the dispersion interaction term also plays a role in causing vibrational
 32 frequency shifts. Rodziewicz et al. combined Buckingham’s theory for a diatomic molecule
 33 with SAPT and studied vibrations involving C–H or C–X stretches, where X denotes a halogen
 34 atom.¹⁹⁴ They found that the exchange-repulsion effects cause a vibrational frequency blueshift,
 35 though the underlying mechanism of these frequency shifts is very complicated. Choi et al.
 36 studied the effects of charge transfer on the vibrational frequency of ionic IR probes such as
 37 CN $^-$ or N $_3^-$ anions dissolved in water.¹⁹⁷ Although a considerable charge transfer between
 38 solute and water molecules was found, the net charge transferred appeared to be in no
 39 correlation with the vibrational frequency shifts. That led them to suggest that the charge
 40 transfer phenomenon can be neglected when considering the intermolecular interaction-

1 induced frequency shifts for the studied systems. However, recently, charge transfer was found
2 to be important in a certain case by Brinzer et al.,¹⁹⁸ where they studied CO₂ asymmetric
3 stretching (ν_3) mode as an IR probe for sensing the local molecular environments in ionic
4 liquids. Moreover, it was demonstrated recently that the solvation-induced vibrational
5 frequency shifts of pyrimidine vibrations are correlated with charge transfer between
6 pyrimidine and various polar solvents, including water, methanol, and hexylamine.¹⁹⁹ To
7 examine both electrostatic and non-electrostatic interaction-induced frequency shifts
8 theoretically, the WCA based theory combined with the hybrid variational-perturbational
9 interaction energy decomposition scheme (SolEDS) was applied to the vibrational
10 solvatochromism of amide I mode and C \equiv N stretch modes of MeSCN in various solvents. This
11 approach revealed that exchange-repulsion blueshifts and non-Coulombic redshifts due to
12 dispersion and induction interactions are equally important.^{143,154-156}

13 In order to accurately predict and simulate the non-electrostatic interaction effects on
14 the vibrational solvatochromism of IR probes, high-level quantum mechanical description of
15 the solute-solvent interaction potential is needed. To systematically study and predict the
16 electrostatic and non-electrostatic effects on the vibrational frequency shifts in condensed
17 phases directly by utilizing MD simulations of various IR probes, the optimized quantum
18 mechanics/molecular mechanics (OQM/MM) method was introduced by the Skinner group⁶⁹
19 and later further developed by the Corcelli group^{42,200,201}. In their method, the semi-empirical
20 Hamiltonian of an IR-active fragment and its bath-coupling parameters are re-parameterized
21 from the original set of parameters, e.g., PM3 minimal basis model of Hamiltonian²⁰². The
22 vibrational solvatochromism is described at a hybrid level of PM3 and classical force fields
23 with an electrostatic embedding scheme, making this approach very efficient when combined
24 with MD simulations. It was shown that OQM/MM is easily transferable to other solute and
25 solvent systems and capable of accurately simulating the IR spectra of complicated systems,
26 including proteins in water. Recently, the OQM/MM method was shown to be of limited use
27 for describing the frequency shifts of SCN probe incorporated in calmodulin. This limitation
28 is likely to originate from the electrostatic embedding approximation that has been a common
29 choice in QM/MM treatment of the interactions between QM and MM parts of the system.²⁰³
30 In general, the quantum embedding of an IR probe's Hamiltonian into QM/MM can be a
31 relatively expensive and difficult task, especially if the exchange-repulsion and dispersion
32 interactions are to be explicitly included in the system-bath interaction. To circumvent this
33 problem, one can combine the WCA theory with a quantum mechanical model for
34 intermolecular interaction potential, U .

35 Inserting the expression for the intermolecular interaction potential given in Eq. (48)
36 into the WCA expression for the vibrational frequency shift in Eq. (57), one can obtain the
37 vibrational solvatochromism theory based on the effective fragment potential theory,^{40,143,154,155}
38 which was referred to as SolIEFP. Unlike the OQM/MM model, the SolIEFP model is a VSM
39 because it is derived from the solute-solvent-separable EFP2 intermolecular potential. The
40 resultant expression for the vibrational frequency shift of a j th normal mode is given as a sum
41 of the Coulombic, exchange-repulsion, induction, and dispersion contributions, i.e.,

$$\Delta\omega_j = \Delta\omega_j^{\text{Coul}} + \Delta\omega_j^{\text{Ex-Rep}} + \Delta\omega_j^{\text{Ind}} + \Delta\omega_j^{\text{Disp}}. \quad (81)$$

1 The Coulombic term can be factorized into two components as

$$\Delta\omega_j^{\text{Coul}} = \Delta\omega_j^{\text{SolCamm}} + \Delta\Delta\omega_j^{\text{Coul}}(\phi), \quad (82)$$

2 where $\Delta\omega_j^{\text{SolCamm}}$ is the distributed multipole contribution to the vibrational frequency shift
 3 (see Eq. (75)).¹⁸⁵ The second term, $\Delta\Delta\omega_j^{\text{Coul}}(\phi)$, represents the contribution originating from
 4 the vibrational coordinate-dependence of electric potential created by surrounding solvent
 5 molecules. Usually, this secondary effect is small. Nevertheless, in practice, to estimate
 6 $\Delta\Delta\omega_j^{\text{Coul}}(\phi)$, only the monopole terms in the multipole expansion series are taken into
 7 consideration due to a convergence issue. Then, $\Delta\Delta\omega_j^{\text{Coul}}(\phi)$ is given as¹⁴³

$$8 \quad \Delta\Delta\omega_j^{\text{Coul}}(\phi) = \frac{1}{2M_j\omega_j} \sum_{x \in \text{slt}} \sum_{y \in \text{slv}} \sum_i \left\{ \frac{g_{ijj}}{M_i\omega_i^2} q_x - 2\delta_{ij} \left. \frac{\partial q_x}{\partial Q_i} \right|_{\mathbf{Q}_0} \right\} \frac{q_y}{r_{xy}^3} \mathbf{L}_x^{(i)} \cdot \mathbf{r}_{xy}, \quad (83)$$

9 where $\mathbf{L}_x^{(i)}$ is the vibrational eigenvector element associated with the x th solute's atom in the
 10 i th normal mode and the relative position vector of the y th solvent atom is defined as $\mathbf{r}_{xy} =$
 11 $\mathbf{r}_x - \mathbf{r}_y$.

12 The exchange-repulsion term in the SolEFP originates from the exchange-repulsion
 13 interaction potential obtained by Gordon and coworkers,^{204,205} where they assumed a single
 14 electron pair exchange between the unperturbed Hartree-Fock wave functions and the spherical
 15 Gaussian overlap. Under such an approximation, it was shown that

$$\Delta\omega_j^{\text{Ex-Rep}} \approx - \frac{1}{2M_j\omega_j} \sum_i \frac{g_{ijj}}{M_i\omega_i^2} \left. \frac{\partial E^{\text{Ex-Rep}}}{\partial Q_i} \right|_{\mathbf{Q}_0}, \quad (84)$$

16 when neglecting the electronic anharmonicity contribution to $\Delta\omega_j^{\text{Ex-Rep}}$. The vibrational force
 17 associated with the exchange-repulsion potential is given as

$$18 \quad \left. \frac{\partial E^{\text{Ex-Rep}}}{\partial Q_i} \right|_{\mathbf{Q}_0} = \sum_{a \in A} \sum_{b \in B} \left[4 \frac{S_{ab}}{r_{ab}} \frac{\partial S_{ab}}{\partial Q_i} \left\{ \sqrt{\frac{-1}{2\pi \ln|S_{ab}|}} - 2\sqrt{\frac{-2 \ln|S_{ab}|}{\pi}} \right\} + 4 \frac{S_{ab}^2}{r_{ab}^2} \frac{\partial r_{ab}}{\partial Q_i} \sqrt{\frac{-2 \ln|S_{ab}|}{\pi}} - \right. \\
 19 \quad 2 \frac{\partial S_{ab}}{\partial Q_i} (\sum_{c \in A} G_{ac}^A S_{cb} + \sum_{d \in B} G_{bd}^B S_{da} - 2T_{ab}) - 4S_{ab} \frac{\partial S_{ab}}{\partial Q_i} \left(\sum_{x \in A} \frac{Z_x}{r_{bx}} + \sum_{y \in B} \frac{Z_y}{r_{ay}} - \right. \\
 20 \quad \left. 2 \sum_{c \in A} \frac{1}{r_{cb}} - 2 \sum_{d \in B} \frac{1}{r_{ad}} + \frac{1}{r_{ab}} \right) - 2S_{ab} \left\{ \sum_{c \in A} \left[\frac{\partial G_{ac}^A}{\partial Q_i} S_{cb} + G_{ac}^A \frac{\partial S_{cb}}{\partial Q_i} \right] + \sum_{d \in B} G_{bd}^B \frac{\partial S_{da}}{\partial Q_i} - \right. \\
 21 \quad \left. 2 \frac{\partial T_{ab}}{\partial Q_i} \right\} + 2S_{ab}^2 \left\{ \sum_{x \in A} \frac{Z_x}{r_{bx}^2} \frac{\partial r_{xb}}{\partial Q_i} + \sum_{y \in B} \frac{Z_y}{r_{ay}^2} \frac{\partial r_{ay}}{\partial Q_i} - 2 \sum_{c \in A} \frac{1}{r_{cb}^2} \frac{\partial r_{cb}}{\partial Q_i} - 2 \sum_{d \in B} \frac{1}{r_{ad}^2} \frac{\partial r_{ad}}{\partial Q_i} + \frac{1}{r_{ab}^2} \frac{\partial r_{ab}}{\partial Q_i} \right\} \Big]. \quad (85)$$

23 here S_{ab} and T_{ab} are the one-electron overlap and kinetic integrals between the a th and b th
 24 localized molecular orbitals (LMOs), respectively, G_{ac}^X is the Fock matrix element of
 25 molecule X , and Z_x is the atomic number of the x th atom. The relative distance $r_{\alpha\beta} =$

1 $|\mathbf{r}_\alpha - \mathbf{r}_\beta|$. Here, the indices a, b, c , and d refer to LMOs located at their charge centroids of
 2 charge \mathbf{r}_α , whereas indices x and y do to atoms in molecules A (solute) and B (solvent),
 3 respectively. Because the exchange-repulsion is approximately pairwise-additive,²⁰⁶⁻²¹⁰ one
 4 can use Eq. (85) to calculate the corresponding frequency shift of an IR probe molecule even
 5 in complicated environments. Also, it is relatively easy to evaluate $\Delta\omega_j^{\text{Ex-Rep}}$ from MD
 6 simulations because the calculation requires only one-electron integrals. Although there are
 7 many derivatives to be calculated in Eq. (85), they are just the first derivatives of one-electron
 8 integrals with respect to interatomic distances, which can be computed analytically. In addition,
 9 the first derivatives of the LMO centroids and Fock matrix elements can be calculated
 10 numerically and treated as SoleFP parameters, much like the way to determine EFP2
 11 parameters.

12 The vibrational frequency shift due to the induction interaction is given as¹⁴³

$$\Delta\omega_j^{\text{Ind}} \approx -\frac{1}{2}\mathbf{a}_j \cdot \Phi - \frac{1}{2}\mathbf{A}_j : \Phi \otimes \Phi, \quad (86)$$

13 where the induced vibrational solvatochromic dipole and the permanent vibrational
 14 solvatochromic polarizability of the entire system are, respectively,

$$\mathbf{a}_j = -\frac{1}{2M_j\omega_j} \left[\sum_i \frac{g_{ijj}}{M_i\omega_i^2} \frac{\partial \Phi^T}{\partial Q_i} \Big|_{\mathbf{Q}_0} \right] \cdot [\mathbf{D}^{-1} + (\mathbf{D}^{-1})^T] \quad (87)$$

$$\mathbf{A}_j = \frac{1}{2M_j\omega_j} \mathbf{D}^{-1} \cdot \left[\sum_i \frac{g_{ijj}}{M_i\omega_i^2} \frac{\partial \mathbf{D}}{\partial Q_i} \Big|_{\mathbf{Q}_0} \right] \cdot \mathbf{D}^{-1}. \quad (88)$$

15 The generalized electric field Φ and the inverse polarizability tensor \mathbf{D} are

$$\Phi_a = \mathbf{E}(\mathbf{r}_a) \quad (89)$$

$$\mathbf{D}_{ab} = \begin{cases} \alpha_a^{-1}(0)\delta_{ab} & \text{if } a, b \text{ belong to the same molecule} \\ -\mathbf{T}_{ab}^{(2)} & \text{if } a, b \text{ belong to different molecules} \end{cases} \quad (90)$$

16 where $\alpha_a(0)$ is the distributed anisotropic polarizability tensor evaluated at zero frequency.
 17 $\alpha_a(0)$ can be calculated by using the coupled-perturbed Hartree-Fock theory and it is
 18 essentially the response of the LMOs against electric field perturbation. The derivatives of Φ
 19 and \mathbf{D} with respect to the normal coordinates are calculated with $\frac{\partial \alpha_a(0)}{\partial Q_i} \Big|_{\mathbf{Q}_0}$ pre-computed
 20 numerically and used as the SoleFP parameters.

21 The dispersion contribution to the vibrational frequency shift is given by¹⁵⁴

$$\begin{aligned}
& \Delta\omega_j^{\text{Disp}} \approx \frac{1}{4\pi M_j \omega_j} \sum_i \frac{g_{ijj}}{M_i \omega_i^2} \sum_{a \in A} \sum_{b \in B} \sum_{\alpha\beta\gamma\delta}^{x,y,z} \int_0^\infty d\xi \left\{ T_{\alpha\beta}^{(2);ab} T_{\gamma\delta}^{(2);ab} \frac{\partial \alpha_{\alpha\gamma}^{(a)}(i\xi)}{\partial Q_i} \right\}_{\mathbf{Q}_0} + \\
& \left. \frac{\partial (T_{\alpha\beta}^{(2);ab} T_{\gamma\delta}^{(2);ab})}{\partial Q_i} \right|_{\mathbf{Q}_0} \alpha_{\alpha\gamma}^{(a)}(i\xi) \left. \right\} \alpha_{\beta\delta}^{(b)}(i\xi),
\end{aligned} \tag{91}$$

where $\alpha^{(a)}(i\xi)$ is the imaginary frequency-dependent anisotropic polarizability tensor associated with the a th LMO of solute molecule. The derivatives of the product of dipole-dipole interaction tensors can be easily evaluated analytically and $\left. \frac{\partial \alpha_{\alpha\gamma}^{(a)}(i\xi)}{\partial Q_i} \right|_{\mathbf{Q}_0}$ are the numerically calculated SoleFP parameters.

Since the EFP2 model describes inherently rigid molecular fragments, SoleFP was first applied to *N*-methylacetamide (NMA) and MeSCN dissolved in solvents of varying polarity as well as in water. Recently, SoleFP was further developed to make it of use for vibrational frequency shift calculations of IR probes in proteins. This extended version of SoleFP is denoted as Bio-SoleFP. In the Bio-SoleFP method,^{155,203} the vibrational frequency shift of an IR probe is given by

$$\Delta\omega^{\text{Bio-SoleFP}} \approx \Delta\omega_{\text{NearZone:CONH}}^{\text{Coul}} + \Delta\omega_{\text{Through-bond\text{effect}}} + \Delta\omega^{\text{SoleFP}}, \tag{92}$$

where $\Delta\omega_{\text{NearZone:CONH}}^{\text{Coul}}$ accounts for the Coulombic frequency shift due to the closest peptide groups for which the superimposition of EFP2 fragments is impossible due to close contact with the IR probe's SoleFP fragment, $\Delta\omega_{\text{Through-bond\text{effect}}}$ is the constant offset due to the attachment of the IR probe to protein, and $\Delta\omega^{\text{SoleFP}}$ is the remaining contribution modeled by SoleFP. It was shown that Bio-SoleFP applied to the molecular configurations sampled from classical MD trajectories of the SCN-labeled calmodulin in water can successfully reproduce the C \equiv N stretch IR spectra of SCN groups that have different solvent environments.²⁰³ In fact, the SoleFP/MM method is of comparable cost as OQM/MM method. However, still due to a number of approximations used in SoleFP/MM method, e.g., neglecting the electric anharmonicity terms in the non-electrostatic interaction-induced frequency shift and the charge-transfer and penetration effects, SoleFP was found to suffer from systematic errors that lead to a slight overestimation of the frequency blueshift. Furthermore, the evaluation of the second derivatives of the exchange-repulsion and induction interaction potentials with respect to the normal coordinates is computationally expensive. Nonetheless, in the case of the amide I and the nitrile stretch modes, from *ab initio* calculations of such electric anharmonicity-induced frequency shifts originating from non-Coulombic interaction for a few model solute-solvent clusters, we found that they cancel out with each other to a great extent. This is indirect evidence supporting the assumption that the mechanical anharmonicity-induced frequency shifts originating from the non-Coulombic intermolecular potentials are dominant. Still, it

1 would be desirable to further develop the SolIEFP theory by including those neglected terms
2 more accurately in the near future. The SolIEFP VSM and Bio-SolIEFP are available in the
3 Solvshift quantum chemistry program at <https://globulion.github.io/slv>. Multiple IR probes as
4 well as solvent and protein fragments are parameterized at the HF/6-311++G** level of theory
5 in a fragment library, which is interfaced via the MDAnalysis^{211,212} library with popularly used
6 MD trajectory file formats such as those used by GROMACS,²¹³ AMBER²¹⁴ and NAMD²¹⁵
7 molecular dynamics software. This makes the Solvshift code easy to use even for complex
8 heterogeneous systems such as IR probes in bulk solvents and even proteins. The automatic
9 generation of custom fragment parameters is also possible.

10

11

4. Semiempirical Approaches: Vibrational Spectroscopic Maps

Several rigorous theories for vibrational solvatochromism and electrochromism based on physical approximations have been presented and discussed before, as reviewed in Sec. 3. However, those highly sophisticated models require extensive quantum chemistry calculations at high levels with a large basis set. It is not practical to use fully *ab initio* simulation methods, not only because the molecular systems of interest are complicated and heterogeneous solutions containing biomolecules, ions, and polymers, but also because they have complex molecular dynamics such as conformational transitions, protein-protein interactions, protein-ligand dynamics, and ultrafast solvation and chemical reaction dynamics. Note that the current *ab initio* MD simulation methods do not provide vibrational frequencies that can be directly compared with experimentally measured frequency shifts on the order of a few wavenumbers. Consequently, vibrational solvatochromism theory that utilizes pre-calculated parameters from high-level quantum chemistry calculations of solute molecule in the gas phase is exceptionally useful and has been shown to be capable of predicting vibrational frequencies using the configurations and structures of solute and solvent molecules from MD trajectories.

However, there is a complication that cannot be easily overcome, even with semiempirical vibrational frequency maps. A solute molecule samples an ensemble of structures in solutions that are different from the geometries optimized in the gas phase using quantum chemistry calculation methods. Thus, it is not straightforward to match *ab initio* calculated molecular structures to those from MD trajectories. This difficulty in superposing gas-phase structures onto those in solutions, which will be referred to as *geometrical superposition error* (GSE), is a complicated problem and sometimes can lead to frequency shifts that are far from the experimental results. The GSE becomes especially critical when a short-range repulsive interaction between solute and solvent molecules via H-bonding interactions plays the dominant role in vibrational solvatochromism, e.g., CN stretch frequency shift of nitrile-derivatized compounds in protic solvents. Furthermore, the gas-phase calculations often cannot accurately reproduce the anharmonic potential energy surface of the solute molecule in solution and lead to inaccurate prediction of vibrational solvatochromic parameters. The anharmonicities of the multidimensional potential energy surfaces of an ensemble of solute molecules in solution are also strongly affected by the detailed intermolecular interactions between the solute and solvent molecules. Hereafter, this difficulty will be referred to as potential anharmonicity solvatochromism problem. To overcome these major difficulties in accurately calculating vibrational solvatochromism parameters, one of the simplest ways is to use multivariate least-square fitting analyses with a sufficiently large set of training database. In the present section, we shall discuss the general theoretical background and present real applications to a variety of IR probes used over the past two decades.

4.1. General consideration and motivation: Linear combination of basis functions based on physical approximations

1 Quantum mechanics makes it feasible to quantitatively describe chemical bonds and to
 2 understand molecular structures in terms of wavefunctions of constituent particles like
 3 electrons and nuclei. However, there are only a handful of examples of which Schrödinger
 4 equations are mathematically solvable. Even the Schrödinger equation for the simplest
 5 molecule, H₂, cannot be solved analytically. However, due to the dramatic advance in
 6 computational chemistry calculation and numerical analysis methods, it becomes possible to
 7 calculate the energies of small molecules accurately. Up until now, the most successful way to
 8 obtain molecular orbitals is to write them as linear combinations of atomic orbitals (LCAO-
 9 MO). For the sake of computational convenience and efficiency, we assume the atomic orbitals
 10 of constituent atoms in a given molecule are Gaussian functions:

$$11 \quad \psi_j^{MO}(\mathbf{r}) = \sum_{k=1}^N a_{jk} \varphi_k^{AO}(\mathbf{r}). \quad (93)$$

12 Here ψ_j^{MO} is the j th molecular orbital, φ_k^{AO} is the k th atomic orbital, N is the number of
 13 atomic orbitals, and a_{jk} are the expansion coefficients. This set of mathematical functions used
 14 to construct both the atomic orbitals $\{\varphi_k^{AO}\}$ and the molecular orbitals is known as the basis
 15 set. It should be noted that the Gaussian functions in each basis set do not have to have long
 16 exponential tails like the H-atomic orbitals. However, if they are well-behaved quantum
 17 mechanically and useful for computational purposes, the lack of long radial tails of basis
 18 functions is not a serious problem. Bearing this aspect in mind, let us consider the vibrational
 19 frequency map functions developed and used over the past decade.

20 One of the early attempts is to expand the solvation-induced vibrational frequency shift
 21 in terms of the solvent electric potentials at distributed atomic sites on the target solute
 22 molecule.^{38,147} The solvent electric potentials at the solute sites are calculable by considering
 23 atomic partial charges of surrounding solvent molecules. When the solvent molecules have
 24 atomic configurations determined by \mathbf{Q} , the instantaneous frequency shift of the solute
 25 molecule, $\Delta\omega_j(\mathbf{Q})$, of the j th vibrational mode can be written as a linear combination of
 26 solvent electric potential,

$$27 \quad \Delta\omega_j(\mathbf{Q}) = \omega_j(\mathbf{Q}) - \omega_{j0} = \sum_{k=1}^N b_{jk} \phi_k(\mathbf{Q}), \quad (94)$$

28 where $\omega_j(\mathbf{Q})$ is the vibrational frequency of the j th normal mode in solution, ω_{j0} is the
 29 vibrational frequency of the same j th mode in the gas phase, N is the number of distributed
 30 sites on the molecule, $\phi_k(\mathbf{Q})$ is the solvent electric potential at the k th site of the solute
 31 molecule, and b_{jk} are the expansion coefficients. Comparing Eq. (94) for vibrational frequency
 32 shifts with Eq. (93) for LCAO-MO, one can find the analogy between the two approaches. It
 33 should be mentioned that the wavefunction in Eq. (93) enters the expectation value of quantum
 34 mechanical observables $A = \langle \psi | \hat{A} | \psi \rangle$ as in Eq. (94) quadratically. One of the critical
 35 differences between the two, aside from the observable itself and the functional forms of the

1 basis functions, lies in the way of determining the corresponding expansion coefficients. The
 2 expansion coefficients a_{jk} for an LCAO-MO are determined by applying the variation principle
 3 to the calculation of the ground state energy. On the other hand, the expansion coefficients b_{jk}
 4 for a vibrational frequency shift $\Delta\omega_j(\mathbf{Q})$ are determined by carrying out a multivariate least-
 5 square fitting analysis for a training database obtained from *ab initio* calculations of the
 6 vibrational frequency shifts of the j th mode for many clusters containing a solute and multiple
 7 solvent molecules. The number of clusters should be sufficiently larger than the number of
 8 expansion coefficients or that of distributed sites on the solute molecule.

9 The electric potential model in Eq. (94) was derived rigorously from the quantum
 10 mechanical perturbation theory with treating the associated solute-solvent interaction energy
 11 as a perturbation to the potential energy function of vibrational degrees of freedom of a given
 12 solute molecule.¹⁴⁷ The solute-solvent intermolecular interactions are assumed to be dictated
 13 by the Coulomb interactions of atomic partial charges of the solvent molecules with the
 14 distributed charges of the solute. Although the formal expression for the expansion coefficients
 15 b_{jk} was presented elsewhere¹⁴⁷ in terms of transition charges, potential anharmonic coefficients
 16 of solute molecule in the gas phase, vibrational frequencies, reduced masses, and so on, they
 17 were treated as fitting parameters for multivariate least square analyses of a set of *ab initio*
 18 calculated solute-solvent clusters. Thus, even though the solvent electric potential model in Eq.
 19 (94) is based on rigorous physical approximations, the key parameters b_{jk} were obtained in an
 20 empirical manner by fitting to the quantum chemistry calculation results for many clusters.

21 Another popular model for theoretically describing such vibrational solvatochromic
 22 frequency shifts assumes that the frequency shift can be expanded in terms of solvent electric
 23 fields at distributed sites on the target solute molecule,

$$24 \quad \Delta\omega_j(\mathbf{Q}) = \sum_{k=1}^N \boldsymbol{\mu}_{jk} \cdot \mathbf{E}_k(\mathbf{Q}) = \sum_{m=x,y,z} \sum_{k=1}^N \mu_{jk}^m E_k^m(\mathbf{Q}), \quad (95)$$

25 where $\mathbf{E}_k(\mathbf{Q})$ is the solvent electric field, or negative gradient of solvent electric potential, at
 26 the k th site on the solute molecule, $\boldsymbol{\mu}_{jk}$ is the vectorial expansion coefficients connecting
 27 $\mathbf{E}_k(\mathbf{Q})$ to $\Delta\omega_j(\mathbf{Q})$, and μ_{jk}^m and $E_k^m(\mathbf{Q})$ are the m th Cartesian components of $\boldsymbol{\mu}_{jk}$ and
 28 $\mathbf{E}_k(\mathbf{Q})$ vectors, respectively. From these two models in Eqs. (94) and (95), the vibrational
 29 frequency shift is expanded as a linear combination of the basis functions, which are either
 30 solvent electric potentials or electric fields at solute's distributed sites. The solvent electric field
 31 model in Eq. (95) assumes that the solute-solvent intermolecular interaction can be described
 32 by the sum of Coulomb interactions between distributed solute electric dipoles and solvent
 33 electric fields. Again, the expansion coefficients, μ_{jk}^m , are determined by performing a
 34 multivariate least-square fitting analysis for a set of *ab initio* calculated vibrational frequencies
 35 for a set of solute-solvent clusters with Eq. (95).

1 These two representative models assume that the solute-solvent interaction can be fully
 2 described by the Coulomb interactions between solute charges (dipoles) with solvent electric
 3 potential (field). The expansion coefficients, either b_{jk} in Eq. (94) or μ_{jk}^m in Eq. (95), are
 4 obtained from a training database from a series of quantum chemistry vibrational analyses of a
 5 large number of solute-solvent clusters. Once the set of parameters is determined, one can use
 6 the corresponding Eq. (94) or (95) to predict the frequency shift $\Delta\omega_j(\mathbf{Q})$ of the oscillator in
 7 any solutions or condensed phases by calculating the solvent electric potential or field using
 8 instantaneous solvent configurations and the corresponding partial charges described by MD
 9 force fields.

10 Considering a more sophisticated intermolecular interaction model, one can expand
 11 the set of basis functions. For instance, short-range Pauli repulsive interactions between the
 12 solute and solvent molecules cause blueshifts of the nitrile stretch frequency when the nitrile
 13 forms a strong H-bond with water or other protic solvent molecules. This leads to the
 14 development of more general approaches based on physical approximations to the solute-
 15 solvent intermolecular interaction energy. Thus, one can make a generalization of vibrational
 16 frequency as

$$17 \quad \Delta\omega_j(\mathbf{Q}) = \sum_{k=1}^N c_{jk} \chi_k(\mathbf{Q}), \quad (96)$$

18 where $\chi_k(\mathbf{Q})$ constitute the basis set of functions that can be based on physical
 19 approximations or that can adopt any arbitrary mathematical forms as long as they are well-
 20 behaved functions without singularity or divergence. Here, c_{jk} are the expansion coefficients.
 21 The most critical assumption for all the semiempirical vibrational frequency maps, which
 22 include vibrational frequency shift, vibrational transition dipole and polarizability, and
 23 vibrational coupling maps, is that the best set of parameters $\{c_{jk}\}$ are obtained by carrying out
 24 multivariate least-square fitting analysis for a training database from quantum chemistry
 25 calculation results for various clusters.

26 In this section, we shall compare theoretically developed VSMs for a variety of IR
 27 probe modes with experimental results or high-level *ab initio* calculations. Unfortunately, it is
 28 difficult to establish a simple set of criteria used to assess the validity of VSM in a quantitative
 29 manner, because the magnitudes of solvatochromic vibrational frequency shifts are in a wide
 30 range from just a few wavenumbers to hundreds of wavenumbers. However, there is an
 31 interesting paper reported by the Ge group,^{216,217} where they compared different VSMs for
 32 amide I vibration and used them to make interpretations of their 2DIR spectroscopic results
 33 (Sec. 4.3). It would be interesting to carry out benchmarking studies of various IR probes other
 34 than the most extensively studied amide I vibration in the future.

36 **4.2. General parameterization method**

37 Essentially all the VSMs proposed to date, both semiempirical and *ab initio*, can be recast in
 38 the following form,

1

$$Y = \sum_T \sum_x \sum_{R=0} \sum_{\substack{\alpha\beta\gamma\dots \\ R}} \left\{ S_{x;\alpha\beta\gamma\dots}^{T,(R)} P_{x;\alpha\beta\gamma\dots}^{T,(R)} + \sum_{R'=0} \sum_{\substack{\alpha'\beta'\gamma'\dots \\ R'}} \left\{ S_{x;\alpha\beta\gamma\dots,\alpha'\beta'\gamma'\dots}^{T,(R,R')} P_{x;\alpha\beta\gamma\dots}^{T,(R)} P_{x;\alpha\beta\gamma\dots}^{T,(R')} \right\} + \dots \right\} \quad (97)$$

3

4 where Y is the vibrational spectroscopic observable of interest, $S_{x;\alpha\beta\gamma\dots}^{T,(R)}$ and $S_{x;\alpha\beta\gamma\dots,\alpha'\beta'\gamma'\dots}^{T,(R,R')}$
5 are the associated *vibrational solvatochromic parameters* such as charges, multipoles and so
6 on, and $P_{x;\alpha\beta\gamma\dots}^{T,(R)}$ is the *conjugate field* created by the surrounding solvent molecules. Here,
7 $P_{x;\alpha\beta\gamma\dots}^{T,(R)}$ should be evaluated at the x th interaction site of the solute, that could be an atomic
8 site, an LMO centroid, or any other point within the IR probe's charge density distribution. The
9 superscript "T" denotes the type of intermolecular interaction, e.g., Coulombic, induction, etc.,
10 of rank R . For example, the rank-zero field is a scalar, and the rank-one field is a vector. The
11 Greek subscript indices in Eq. (97) represent the Cartesian coordinates. For example, $S_{x;\alpha\beta\gamma\dots}^{T,(R)}$
12 when $R=0$ could represent a vibrational Stark tuning rate. The vibrational solvatochromic
13 quadrupole is $S_{x;\alpha\beta\gamma\dots}^{T,(R)}$ with $R=2$. In the second term in the curly bracket of Eq. (97), vibrational
14 solvatochromic parameter $S_{x;\alpha\beta\gamma\dots,\alpha'\beta'\gamma'\dots}^{T,(R,R')}$ could be vibrational solvatochromic polarizability
15 when $R=R'=1$. In an extreme case, the conjugate field can adopt a very complex tensor form
16 as in, for example, the SOLEFP model, in which not only electrostatic but also wavefunction
17 overlap and dispersion effects are mapped in a way that formally fits the functional form of
18 Eq.(94). On the other hand, it is also the way the VSM is parameterized, and conjugate fields
19 are defined, which allows the explicit function in the form of Eq.(94) to be designed in a
20 relatively simpler form, allowing computationally more robust VSMs to be developed in terms
21 of semiempirical mapping procedures.

22 In Sec. 4.1, we have already reviewed two popular semiempirical vibrational
23 parameterization schemes. They are broadly referred to as the electrostatic fitting methods
24 (ESF), which correlate benchmark *ab initio* or density functional theory (DFT)-calculated
25 vibrational properties with electric potentials or electric fields on/around the IR probe in
26 condensed phases.^{66,67,111,183,188,197,218-241} The expansion sites are called the "interaction centers
27 or interaction sites", and they are chosen in a way to effectively represent the local electric
28 potential or field created by surrounding solvent molecules. The non-electrostatic interaction-
29 induced effects on the vibrational spectroscopic observables can also be taken into account
30 similarly. There are a few examples of vibrational frequency maps connecting H-bond
31 distances²⁴⁰ or van der Waals forces²⁴¹ with the vibrational frequency of the IR probe.

32 Most previous works focused on just one type of parameters, e.g. scalar vibrational
33 solvatochromic charges^{111,183,188,197,218-220,222-224,232,234,236,238,242} and vectorial vibrational
34 solvatochromic dipoles^{66,67}. However, there are also maps utilizing multiple types of
35 parameters, as well. Torii and coworkers^{237,239} considered both scalar charges and vectorial

1 dipoles as vibrational solvatochromic parameters, whereas Jansen and Knoester²³¹ and
2 Mukamel and coworkers^{227,228} considered vectorial dipoles and tensorial quadrupoles as
3 vibrational solvatochromic parameters. In order to account for the non-electrostatic effects in
4 the VSMs and intramolecular mode couplings, the van der Waals effects should be
5 parameterized by combining MD simulations with experimentally measured protein spectra as
6 reference data.^{240,241} Such an approach is specifically designed for very large systems like
7 proteins in water. In the following subsections, various vibrational spectroscopic maps
8 developed so far are reviewed.

9 10 **4.3. Amide I vibration: Frequency and coupling maps**

11 In the protein backbone, repeating units of peptide bonds link amino acids together and their
12 vibrations create a series of normal modes in the 1200 – 1800 cm⁻¹ region that are characteristic
13 of the protein structures. From higher to lower frequencies, these normal modes are called the
14 amide I, II and III modes. (please cite reference 233) The amide I mode is the most extensively
15 studied vibration in protein spectroscopy, and we will use Sections 4.3 and 4.4 to summarize
16 the theoretical methods to model its vibrational features and demonstrate how it can be
17 combined with isotope labeling to reveal site-specific information. We will then discuss the
18 amide II and III bands in Section 4.5.

19 The amide I band, which appears in the 1600 – 1800 cm⁻¹ spectral region, arises mainly
20 from the peptide bond C=O stretch with minor contributions from the amide C-N stretch and
21 C_α-C-N deformation. It shows distinctive features for different secondary structures in
22 polypeptide chains and thus has been widely used in linear and nonlinear vibrational
23 spectroscopies to detect the structures and dynamics of polypeptides and proteins.^{25,111,139,242-}
24 ²⁵⁴ These spectroscopy experiments in the amide I region are particularly useful for systems
25 that are not easily studied using standard techniques of protein structural analysis such as NMR
26 and X-ray scattering, including membrane proteins, intrinsically disordered peptides, and
27 systems undergoing triggered folding or unfolding. For example, 2D IR spectroscopy has been
28 applied to monitor the conformational dynamics in the folding and unfolding of proteins,
29 revealing the gating mechanism and water dynamics of transmembrane proton channels, and
30 uncovering the structures and aggregation pathways of amyloid proteins.^{75,83,106,107,255,256} The
31 intrinsic ultrafast time scale of the amide I vibration (~20 fs) makes amide I spectroscopy much
32 less susceptible to the motional narrowing difficulties encountered in NMR spectroscopy.

33 To quantitatively relate the amide I spectral features with the structures and dynamics
34 of proteins, researchers often use a mixed quantum mechanical/classical mechanical approach
35 that treats all the amide I vibrations in a protein quantum mechanically and the low-frequency
36 degrees of freedom (such as those along main-chain dihedral angles) classically.^{124,127,257} If a
37 protein contains N amide I modes, the single-quantum vibrational Hamiltonian is a $N \times N$
38 matrix, in which the diagonal terms are the site frequencies of each chromophore and the off-
39 diagonal terms are the couplings between them. In principle, one can obtain the vibrational
40 Hamiltonian from quantum chemical (such as DFT) calculations. However, it is impractical to
41 perform high-level quantum chemical calculations on large proteins in the condensed phases,²⁵⁸
42 particularly if we want to follow the time course of structures along the dynamics of the proteins.

1 Alternatively, researchers have designed a variety of frequency and coupling maps for the
2 amide I vibrations so that one can efficiently compute the elements of the vibrational
3 Hamiltonian based on the time series of structures obtained from MD simulations.²⁵⁹

4 Among other factors, electrostatic interactions play a major role in determining the
5 shifts in vibrational frequencies and the coupling between peptide chromophores in the amide
6 I vibrational chromophores. In particular, inhomogeneous and fluctuating electrostatic
7 environment around the vibrational chromophores alters their site frequencies and broadens the
8 absorption bands. The VSMs developed so far for the amide I mode relate the site frequencies
9 to the electrostatic potentials and/or electric fields (and electric field gradients in some cases)
10 on the atomic sites (and some other points, such as bond centers, if needed) in the peptide
11 group.^{67,217,219-221,225,228,231,233,235,237,238,260-263} They often take the form of Eq. (94) or (95) and
12 are based on *N*-methylacetamide (NMA) as a model compound to mimic the most typical
13 peptide groups, i.e., the secondary amide groups, of the protein backbone. The parameters in
14 the frequency maps are determined by referring to the results of quantum chemical calculations,
15 or in a few cases, directly to the experimental spectral features.^{233,240,260,261,264} For example,
16 Cho and coworkers developed the first amide I frequency map by considering a series of NMA-
17 D₂O complexes and carrying out *ab initio* quantum chemical calculations to obtain their amide
18 I frequencies. They then used Eq. (94) and obtained the linear combination coefficients from
19 multivariate least-squares fitting analysis to the quantum chemical results.²²⁰ Taking a similar
20 approach, Skinner and coworkers examined deuterated NMA/water clusters and provided the
21 first electric field-based amide I frequency map.⁶⁷ While most of the frequency maps developed
22 so far employ the electrostatic potentials *or* the electric fields on the atomic sites to represent
23 the electrostatic environment,²⁶⁰ it has also been shown^{237,238} that both the electrostatic
24 potentials *and* the electric fields on those sites can be essential in describing the inhomogeneity
25 of the electrostatic environment. To account for the electrostatic effects in various solvent
26 environments, Jansen and Knoester embedded deuterated NMA in 75 charge environments and
27 developed a frequency map that incorporates the electric field and its gradient on the C, O, N
28 and D atoms of the chromophore and demonstrated its transferability in common organic
29 solvents²³¹ and need to include multipole and polarizability in solvents like chloroform.²⁶⁵
30 Skinner and coworkers have also adopted an empirical approach by optimizing the coefficients
31 against experimental spectra of deuterated NMA in D₂O, DMSO, and chloroform and designed
32 a frequency map that is transferrable to different electrostatic environments.²⁶¹ A similar
33 approach has been adopted by the Tokmakoff group, who have developed an extensive set of
34 experimental standards (including 28 model dipeptides and 5 isotope-edited protein constructs)
35 that can be used to test and refine vibrational frequency maps.^{45,260,264} These frequency maps
36 have been extensively tested and applied to predict the linear and 2D IR spectra of polypeptides
37 and proteins.^{217,259,266}

38 In most cases, one can apply an amide I frequency map to all peptide bonds, regardless
39 of its composition of amino acids. A notable exception is the peptide bond involving the N
40 atom of a proline residue, i.e., the peptide bond of the form Xxx-Pro, where Xxx represents
41 any amino acid. Typically, the amide I mode of this tertiary amide group is shifted strongly
42 (~35 cm⁻¹) to the red in comparison to that of a secondary amide. Thus, it must be treated

1 separately either by adding an overall shift to the standard map or through a separate
 2 parameterization.^{235,260,267} In the latter case, *N,N*-dimethylacetamide has been chosen as the
 3 model compound for the map parametrization. Due to the large redshift, peptides containing
 4 the Xxx-Pro amide bonds show an amide I absorption peak well separated from the main band
 5 in the IR spectrum, which provides a unique and excellent probe for investigating local structural
 6 and dynamical changes in proline-rich proteins such as collagen and elastin. In addition to
 7 modeling the backbone amide I chromophores, vibrational frequency maps have also been
 8 developed for the side chains of asparagine and glutamine, which contain primary amide
 9 groups.²⁶¹

10 Although electrostatic interactions strongly shift the site frequencies of the amide I
 11 mode in the condensed phases, it has been shown that special treatment is needed to account
 12 for the nearest neighbor (NN) effects on the frequencies. Accordingly, DFT-based maps for
 13 NN-induced frequency shifts^{230,268,269} have been developed. The site frequency of an amide I
 14 vibration is given by

$$15 \quad \omega = \omega_{elst} + \Delta\omega_N(\phi_{i,i-1}, \psi_{i,i-1}) + \Delta\omega_C(\phi_{i,i+1}, \psi_{i,i+1}) \quad (98)$$

16 where ω_{elst} is the frequency derived from an electrostatic frequency map, and $\Delta\omega_N$ and
 17 $\Delta\omega_C$ are the frequency shifts affected by the nearest neighbors of the vibrational chromophore
 18 on the N- and C-terminus sides of the chromophore, respectively. $\Delta\omega_N$ and $\Delta\omega_C$ depend
 19 on the ϕ and ψ dihedral angles in the protein backbone as used in the Ramachandran plot.
 20 The method of deriving those DFT-based maps will be discussed later, together with the NN
 21 vibrational coupling maps.

22 The electrostatic interactions also play an important role in determining the vibrational
 23 couplings between the amide I vibrations of peptide groups. The simplest model in describing
 24 these couplings is the transition dipole coupling (TDC) model.^{139,270-274} Here, each amide I
 25 chromophore is treated as a transition dipole moment and their couplings F_{ij} are given by

$$26 \quad F_{ij} = \frac{A(\vec{m}_i \cdot \vec{m}_j) - 3(\vec{m}_i \cdot \hat{n}_{ij})(\vec{m}_j \cdot \hat{n}_{ij})}{\epsilon r_{ij}^3} \quad (99)$$

27 In this equation, \vec{m}_i and \vec{m}_j are the transition dipoles of the *i*th and *j*th vibrational
 28 chromophores in the unit of D Å⁻¹ amu^{-1/2}. r_{ij} is the distance between the two vibrational
 29 chromophores and \hat{n}_{ij} is the unit vector that connects them. The dielectric constant ϵ is
 30 usually taken to be 1. The conversion factor *A* is 0.1 if F_{ij} is represented in units of mdyne Å⁻¹
 31 amu⁻¹. It is possible to convert it to the coupling in units of cm⁻¹ by assuming the “central
 32 frequency” of 1650 cm⁻¹ and multiplying further by 848619/1650 (i.e., using $A = 0.1 \times 848619$
 33 / 1650).^{139,273} Parameters in the TDC model include the location, orientation, and magnitude of
 34 the transition dipoles, and are determined by fitting to experimental peak splitting or *ab initio*
 35 quantum chemical calculation results.^{270,271} To go beyond the dipole approximation,
 36 researchers have also developed models such as the transition charge coupling (TCC)
 37 method^{230,272} and the transition density derivative distribution method.²⁷⁵

1 Despite the success of the TDC model in predicting long-range interactions between
 2 the amide I chromophores, it is not sufficient to describe the couplings between adjacent or
 3 nearest neighbor peptide groups.^{271,272} To overcome this situation, NN coupling maps have
 4 been developed for the amide I mode based on quantum chemical
 5 calculations.^{230,268,269,271,272,276} In deriving those maps, *ab initio* MO or DFT calculations were
 6 carried out for peptide dimers with the ϕ and ψ dihedral angles of the main chain being
 7 varied for all possible ranges of values at appropriate intervals. The calculated force constant
 8 matrix was then size-contracted to the vibrational subspace of the amide I mode by using, for
 9 example, the Hessian Matrix Reconstruction (HMR) method²⁷⁷ to obtain the site frequencies
 10 (for the maps of NN-induced frequency shifts) and the coupling constants for each particular
 11 set of ϕ and ψ . The maps were made by collecting those site frequencies and coupling
 12 constants, represented by the diagonal and off-diagonal terms of the size-contracted matrix, as
 13 functions of ϕ and ψ . In using those maps, one can estimate the site frequencies and coupling
 14 constants for any set of ϕ and ψ by interpolation. In contrast, the TDC model is sufficiently
 15 accurate when modeling the couplings between the amide I modes of the peptide groups that
 16 are not nearest neighbors.

17 Vibrational frequency maps that further include non-electrostatic perturbations have
 18 been presented as well for the amide I local mode frequencies.^{240,241,278} For example, in the
 19 vibrational frequency map developed by Malolepsza et al.,²⁴¹ the corresponding vibrational
 20 frequency shift is computed using two independent sets of distributed vectorial parameters: the
 21 first describes the usual vibrational response of the amide I mode to the solvent electric field
 22 (\mathbf{E}_i) and the second is associated with van der Waals force ($\mathbf{F}_i^{\text{vdW}}$) exerted to each atom in a
 23 given peptide, i.e.,

$$24 \quad \omega^{\text{Amide I}} = \omega_{\text{NMA}}^{\text{Gas phase}} + \sum_i \{ \mathbf{c}_i \cdot \mathbf{E}_i + \mathbf{d}_i \cdot \mathbf{F}_i^{\text{vdW}} \}, \quad (100)$$

25 where i runs over atoms in the peptide CONH group. It was shown that the map, initially
 26 optimized for NMA in three different solvents, is accurate enough to model the amide I IR
 27 spectra of a few different proteins that include ubiquitin, ribonuclease, myoglobin, and
 28 concanavalin. In other works,^{240,278} the vibrational solvatochromism maps for amide I
 29 vibrations of proteins were developed by considering their backbone structures and H-bonding
 30 environment only. More specifically, the vibrational frequency shift of the amide I mode of a
 31 given peptide in a protein is assumed to be^{240,278}

$$32 \quad \omega^{\text{Amide I}} = \omega_{\text{NMA}}^{\text{Gas phase}} + \Delta\omega(\phi, \psi) + \Delta\omega^{\text{H-bond(solvent)}} + \Delta\omega^{\text{H-bond(Interpeptide)}}. \quad (101)$$

33 The backbone structure of the peptide group is determined by the two Ramachandran angles
 34 so that the frequency shift depends on its backbone structure, which is described by the term
 35 $\Delta\omega(\phi, \psi)$ in Eq. (101) (see also Eq. (98)). The vibrational frequency shift due to its H-
 36 bonding interaction with surrounding solvent molecules is described by the term
 37 $\Delta\omega^{\text{H-bond(solvent)}}$ which is mainly determined by the extent of water exposure, i.e., solvent
 38 accessible surface area, of the CONH unit. The effect of interpeptide H-bonds on the
 39 vibrational frequency shift, $\Delta\omega^{\text{H-bond(Interpeptide)}}$, is assumed to be proportional to the Kabsch-

1 Sander bonding energy,²⁷⁹ which is determined by the H-bond length and angle between the
 2 amide CO group (H-bond acceptor) and the amide NH group (H-bond donor) in the same
 3 protein. To determine these parameters, they used forty-four experimentally measured IR
 4 absorption spectra of protein systems in water.²⁴⁰

5 All these frequency maps are typically validated against experimental data for NMA
 6 in different solvents.^{226,228,235,241,260,261,264,280} Validation of the coupling maps proves more
 7 challenging, because it is difficult to thoroughly sample the flexible structures of small peptides
 8 in simulations and it is challenging to extract useful information from the broad and congested
 9 IR absorption bands of large proteins with well-defined structures. 2D IR spectra are more
 10 sensitive to couplings, although they are time-consuming to calculate for full proteins.²⁸¹
 11 Despite these computational challenges, Jansen and coworkers have calculated the 2D IR
 12 spectra of a selection of proteins and compared the theoretical spectra using different
 13 mappings^{266,282} with the experimental ones.²⁸³ Among the methods tested, they have
 14 concluded¹⁵⁴ that the electrostatic frequency map of Skinner²⁶¹ combined with the OPLS/AA
 15 force field,²⁸⁴ the TDC map of Torii and Tasumi²⁷¹ and the NN maps of Jansen²³⁰ have the best
 16 performance. Spectral simulations of liquid NMA²⁸⁵ and its mixtures with water²⁸⁶ provided a
 17 further benchmark suggesting that the long-range TCC model possibly overestimates the
 18 coupling constants.

19 One thing that is counter-intuitive in the electrostatic frequency map of Skinner²⁶¹ is
 20 that the electrostatic situation of O atom of the peptide group, which acts as an H-bond acceptor
 21 and vibrates with large amplitude in the amide I mode, is not involved in calculating the
 22 frequency shift of the amide I mode. It was shown that this is because of the mutual cancellation
 23 between the effects of electrostatic potential and the electric field on the frequency shift, and is
 24 related to a general property of H-bond accepting stretching modes.^{237,238}

25 Other localized coordinate approaches have also been recently developed for use in *ab*
 26 *initio* anharmonic vibrational frequency calculations, where the anharmonicity is calculated
 27 explicitly.²⁸⁷⁻²⁹⁶ In a similar way, site-specific frequencies, NN coupling terms, and non-nearest
 28 neighbor coupling terms can be determined directly from harmonic vibrational calculations on
 29 molecules of (in principle) any size, using the technique put forward by Hanson-Heine et al.²⁹⁷
 30 In this technique a subset of the normal coordinate eigenvectors from a harmonic frequency
 31 calculation are rotated by applying a unitary transformation that maximizes one of the objective
 32 functions proposed by Jacob and Reiher,²⁹⁸ where the transformation either maximizes the sum
 33 of the squares of the atomic contributions to the normal modes,

$$\xi_{at} = \sum_{\mu} \sum_i^M \left(\sum_{\alpha=x,y,z} (Q_{i\alpha,\mu})^2 \right)^2, \quad (102)$$

34 where μ and i are normal modes and nuclei, respectively, and M is the total number of nuclei,
 35 or the transformation maximizes the distance between the centers of the modes,

$$\xi_{dist} = \sum_{\mu} \left(\sum_i^M \sum_{\alpha=x,y,z} (Q_{i\alpha,\mu})^2 \mathbf{R}_i \right)^2, \quad (103)$$

36 where \mathbf{R}_i is the position vector of each nucleus in the molecular coordinate system. If an
 37 appropriately localized subset of normal coordinates is chosen, such as the amide I manifold,

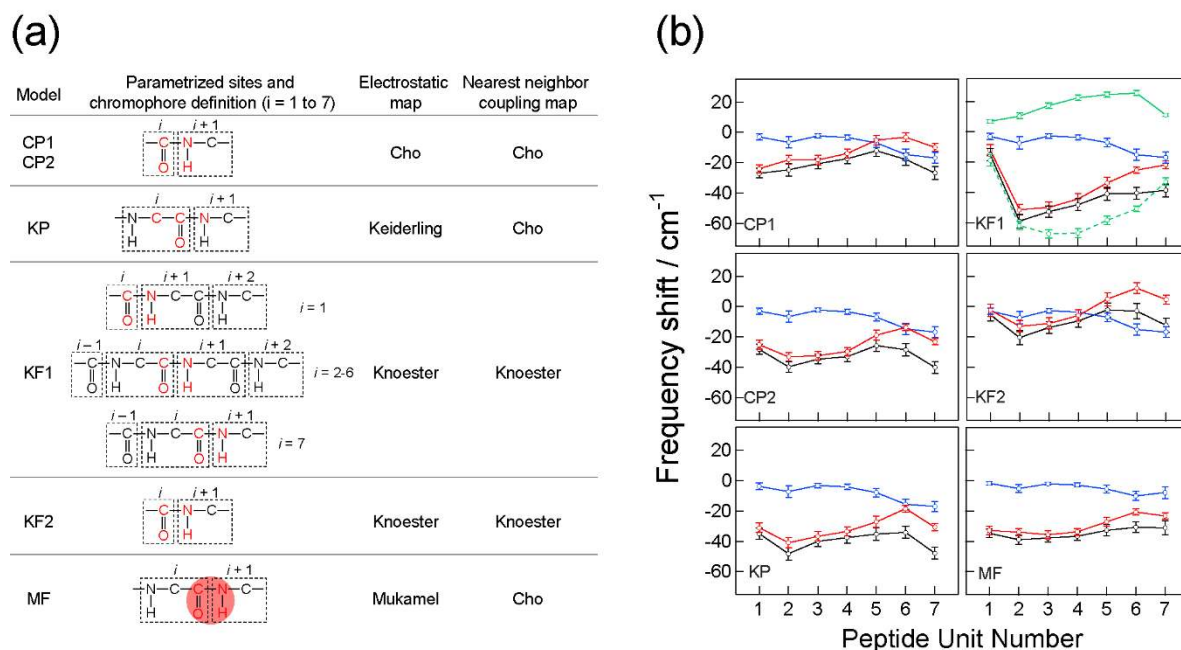
1 then site-specific frequencies and coupling terms can be derived from the diagonal and off-
2 diagonal elements of the mass-weighted Hessian matrix in the newly transformed coordinates.

3 This approach has been successfully applied to vibrational exciton calculations of 2D
4 IR spectra for the amide I band of a range of dipeptides and the hexapeptide Z-Aib-L-Leu-
5 (Aib)₂-Gly-Aib-OtBu. However, the approach is not specific to the amide I mode and can, in
6 principle, be applied to any system for which the localized modes have an appropriate form.
7 Semiempirical maps of site-specific frequencies and NN couplings across different ϕ and ψ
8 angles can be obtained by considering small model systems. The newly created local
9 coordinates are also not localized on to a subset of atoms chosen *a priori*, leading to amide I
10 modes that contained significant motion of the nitrogen atom for the species originally tested,
11 which is consistent with the true nature of the amide I mode. However, care should be taken
12 when selecting the subset of coordinates to be transformed, so that the automatically generated
13 coordinates remain correct.

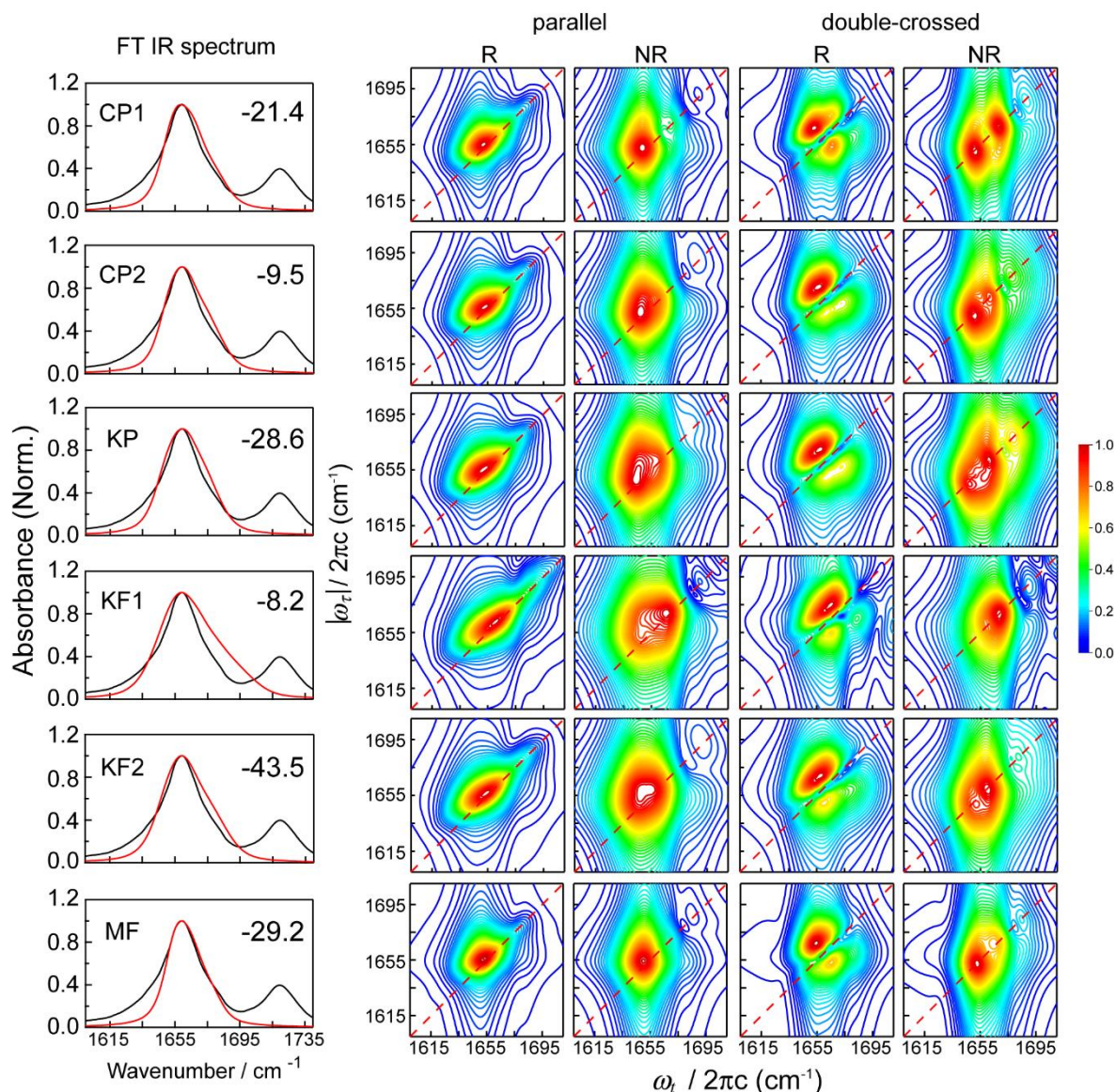
14 To test the validity of the frequency and vibrational coupling map of amide I mode,
15 one should consider peptides with relatively rigid structures to avoid the need for statistical
16 averaging of multiple backbone conformations in MD simulations. One particularly good
17 system for such a test, as demonstrated by the Ge group, is a peptide with C^α-alkylated amino
18 acid residues, such as Aib (C^α-dimethylglycine) and (αMe)Val (C^α-methyl valine). Because
19 of the steric hindrance caused by the alkyl side chains, these unnatural residues restrict the
20 available dihedral angles in the Ramachandran plot and hence can dictate a peptide to fold into
21 a well-defined conformation. Ge and coworkers measured polarization-dependent 2D IR
22 rephasing and non-rephasing spectra of a capped octapeptide Z-[L-(αMe)Val]₈-OtBu (Z,
23 benzyloxycarbonyl; OtBu: tert-butoxy) in deuterated chloroform (CDCl₃), and used the amide
24 I spectral signatures to judge spectra calculated based on MD trajectories and six different
25 combinations of electrostatic frequency maps and NN coupling maps.²¹⁶ The main differences
26 in the frequency maps are the parameterized sites in a peptide unit, whether the amide I
27 frequency fluctuation is estimated from electric potentials or electric fields and field-gradients
28 on the sites, whether the partial charges are taken from an MD force field or from the frequency
29 map parametrization, whether nearest-neighbor frequency shift (NNFS) map is used, and the
30 gas-phase frequency origin (Figure 4a). The chromophore definition in each model is chosen
31 to ensure charge neutrality within the chromophore.

32 On the basis of the number of peaks, relative peak positions and intensities in the
33 computed linear and 2D IR spectra, especially the cross-peak patterns obtained from the
34 double-crossed polarizations, it was determined that the potential-based model (CP2: Cho-
35 Potential 2) developed by Cho and coworkers²⁶² and the field-based model (MF) in the
36 computation package SPECTRON created by Mukamel and coworkers^{228,273} performed the
37 best and similarly reproduced the measured spectra (Figure 5) when using an MD trajectory
38 with the peptide dihedral angles restrained near the crystal structure values. Structural
39 ensembles sampled from unrestrained MD simulations are too broad. Comparing the different
40 models, the solvent contributions to the total frequency shifts are very similar in the magnitude
41 and the variations across the peptide backbone, whereas the peptide contributions exhibit more
42 differences (Figure 4b). The widths of calculated spectra are dominated by the relative spread

1 of the frequency shifts. All models require a redshift of simulated spectra by 10-40 cm^{-1} . This
 2 is most likely because the frequency maps were computed for *N*-methylacetamide solvated
 3 with water molecules whereas the experimental spectra were acquired for the octapeptide in
 4 CDCl_3 . A model that takes into account strong dispersion forces may be more suitable for a
 5 better agreement between experiment and calculation.²⁶⁵ This study demonstrates that 2D IR
 6 can provide a large set of spectral constraints that are useful for further refining classical force
 7 fields and testing theoretical models. In particular, the double-crossed polarization
 8 nonrephasing spectrum exhibits the highest sensitivity to structural ensembles and models.
 9



10 **Figure 4.** (a) Summary of the models used for spectral calculations. Parametrized sites are shown in red. The red shading in the MF model schematically indicates the transition charge region for sampling. Cho-Potential model 1 (CP1) utilized parametrized partial charges whereas other models utilize partial charges defined in MD simulations. Knoester-Field model 1 (KF1) utilized NNFS maps. (b) The amide-I local mode frequency shifts calculated with the six models for the restrained trajectory. Blue circles: solvent contributions ($\overline{\delta\omega_{i,s}}$); red circles: peptide backbone and side-chain contributions ($\overline{\delta\omega_{i,p}}$); black circles: total shifts ($\overline{\delta\omega_i}$). The vertical bars indicate the range enclosed by \pm one standard deviation (σ_i). Green symbols with solid and dash lines in KF1 are the NNFS and electrostatic contributions in $\overline{\delta\omega_{i,p}}$, respectively. Reproduced from Table 1 and Figure 8 of Ref.²¹⁶ Copyright 2009 The American Chemical Society.



1
 2
 3 **Figure 5.** The linear and 2D IR spectra calculated with the CP1, CP2, KP, KF1, KF2, and MF models
 4 for the restrained trajectory. The number in the upper right corner of the FT IR spectrum panel indicates
 5 the frequency shift (in cm^{-1}) applied to the calculated spectra. Red and black lines in the linear spectra
 6 correspond to the simulated and experimental data, respectively. Reproduced from Figure 7 of Ref.²¹⁶.
 7 Copyright 2009 The American Chemical Society.
 8

9 **4.4. Amide I vibration: Isotope-labeled proteins**

10 While the amide I band provides key information on the structural arrangements and
 11 conformational dynamics of proteins in the condensed phase, the relatively short vibrational
 12 lifetime of the amide I mode (around 1 ps in aqueous systems), together with a relatively narrow
 13 frequency range (typically $1600 - 1700 \text{ cm}^{-1}$) and a large number of amide bonds in typical
 14 polypeptides and proteins, often leads to considerable congestion in the measured spectra. This
 15 issue obscures the information content of label-free amide I spectra and makes it difficult to
 16 disentangle the vibrational patterns of each chromophore.

1 Combining vibrational spectroscopy in the amide I region and the isotope labeling
2 technique provides an effective way to reveal site-specific information in complex protein
3 systems. For example, replacing ^{12}C with ^{13}C or ^{16}O with ^{18}O in a C=O group reduces its stretch
4 frequency by about 40 cm^{-1} ,^{299,300} thus shifting its vibrational absorption out of the main amide
5 I band. The frequency changes due to the presence of a C or O isotope can be estimated by
6 treating the C=O stretch as a harmonic oscillator whose angular frequency is $\omega_{CO} = \sqrt{k/\mu}$.

7 Here k and μ are the force constant and reduced mass of the harmonic oscillator, $\mu = \frac{m_C m_O}{m_C + m_O}$

8 where m_C and m_O are the masses of the C and O atoms, respectively. As isotope labeling
9 introduces a minor perturbation to the molecular vibration, one can assume that the force
10 constant of the C=O group remains the same. Replacing ^{12}C with ^{13}C thus changes the
11 frequency of the chromophore by

$$\frac{\omega_{^{13}\text{CO}}}{\omega_{\text{CO}}} = \sqrt{\frac{m_C (m_{^{13}\text{C}} + m_O)}{m_{^{12}\text{C}} (m_C + m_O)}} = 0.978. \quad (104)$$

13 After its first development in 1991,²⁹⁹ the ^{13}C labeling technique has enabled researchers to
14 probe the secondary structures of polypeptides and amyloid fibrils with residue-specific
15 resolution using linear and 2D IR spectroscopy.^{43,255,299-303} In addition, Chen and coworkers
16 have demonstrated that the ^{13}C -isotope labels can be combined with the vibrational sum-
17 frequency generation (SFG) spectroscopy in the amide I region to detect the structures and
18 orientations of surface-bound peptides at the single residue level.³⁰⁴ Despite these advances,
19 the ^{13}C -isotope editing method has two main drawbacks. First, the isotopically labeled
20 vibrational modes are often not well resolved in the vibrational spectra and appear as shoulders
21 on the broad amide I band. Second, the natural abundance of ^{13}C is 1.1%, and thus proteins
22 containing 90 or more amino acids would possibly exhibit IR signals from non-labeled $^{13}\text{C}=\text{O}$
23 groups and complicate the spectra.^{277,304,305}

24 To overcome these issues, researchers have designed the $^{13}\text{C}=\text{O}$ isotope label, which
25 redshifts the absorption frequency of a C=O group by about 65 cm^{-1} and spectroscopically
26 isolates the vibrational mode from the rest of the protein. For example, Arkin and coworkers
27 have utilized isotope-edited IR spectroscopy to measure the conformations and orientations of
28 membrane proteins at a variety of residue positions.^{300,305,306} By incorporating the $^{13}\text{C}=\text{O}$ label
29 on 11 amino acids, one at a time, along the transmembrane helical bundle of the CD3 ζ peptide,
30 Zanni and coworkers have measured the homogeneous and inhomogeneous line widths of the
31 2D IR spectra and revealed the structural distributions and dynamics of the protein.⁸⁶
32 Furthermore, they have conducted a series of 2D IR experiments with isotope labeling to
33 elucidate the pathway and inhibition of the amyloid formation of human amyloid polypeptide
34 (hIAPP), which is closely related to type 2 diabetes.³⁰⁷⁻³¹⁰ As demonstrated in Figure 6,
35 Buchanan et al. have placed a series of $^{13}\text{C}=\text{O}$ labels in the β -sheet and loop region of hIAPP
36 and measured their 2D IR spectra in both the lag phase and equilibrium phase of the
37 aggregation.³⁰⁷ The $^{13}\text{C}=\text{O}$ signal of V17 in Figures 6C and 6D shows that the residue changes
38 from a disordered region to a β -sheet structure upon fibril formation. In contrast, Figures 6D

1 and 2F suggest that residue F23 undergoes the opposite conformational change. By detecting
 2 the 2D IR spectra of all the isotope labels, as highlighted in Figures 6A and 6B, they could
 3 monitor the structural evolution of hIAPP in the aggregation process with residue-specific
 4 resolution and identify the structural features of the oligomeric intermediate in the lag phase.³⁰⁷

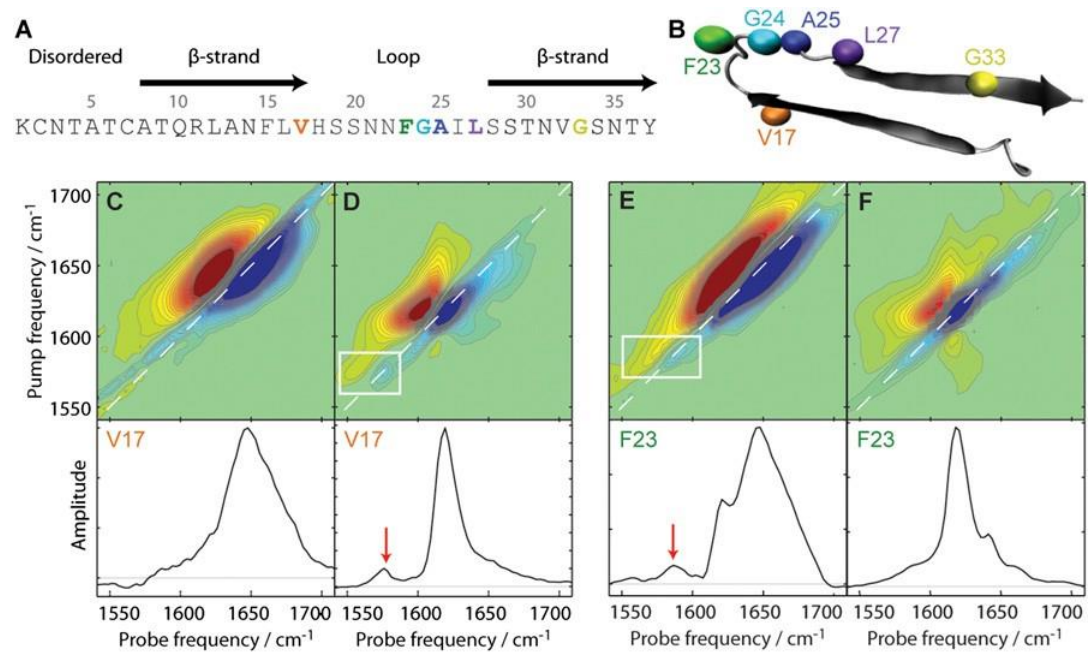
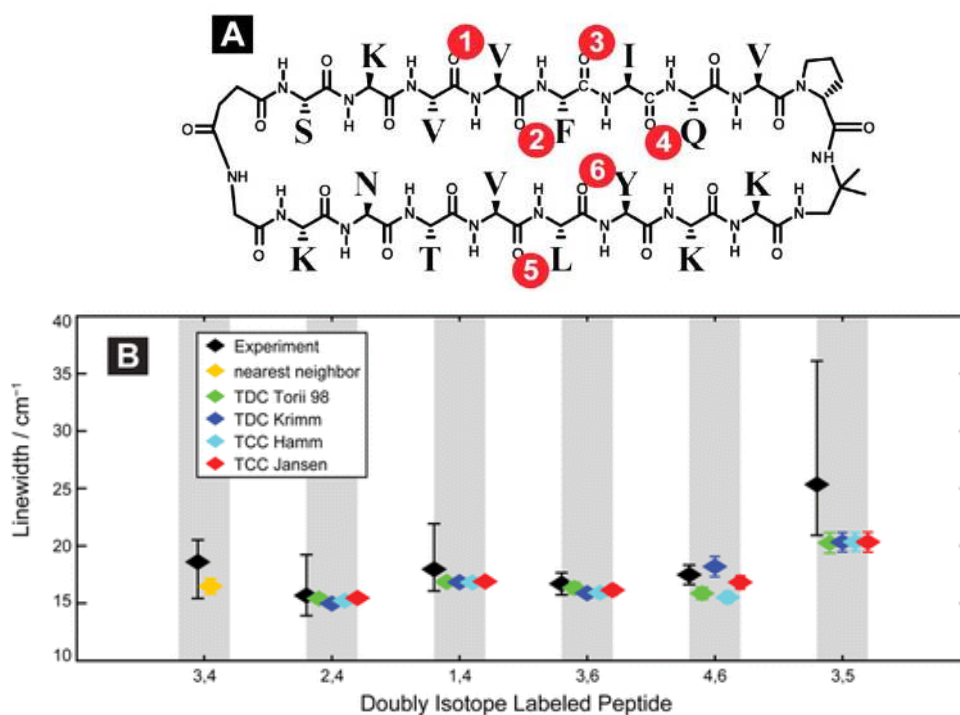


Figure 6. Structure and 2D IR spectra of isotope-labeled hIAPP from reference ³⁰⁷. The sequence (A) and structural model (B) of hIAPP with the ¹³C=¹⁸O isotope labels highlighted. 2D IR spectra and the diagonal intensity slices of the lag-phase and equilibrium phase V17 (C and D) and F23 (E and F) labeled proteins. The boxes and arrows indicate the ¹³C=¹⁸O labeled modes. Reproduced from Figure 1 of Ref.³⁰⁷ Copyright 2013 the National Academy of Sciences of the United States of America.

By combining isotope-edited vibrational spectroscopy and theoretical spectroscopy modeling, researchers have successfully probed the vibrational Hamiltonian in the amide I region and revealed the conformations and dynamics of peptides and proteins with residue-specific resolution. Combining the theoretical vibrational spectroscopic maps and the 2D IR spectroscopy experiments with the ¹⁸O or ¹³C=¹⁸O isotope labels, researchers have determined the site frequencies of individual amino acids, which constitute the diagonal elements of the vibrational Hamiltonian matrix. They have further used the sensitivity of these site frequencies to the interactions between amino acids and their nearby biological and solvent molecules to elucidate the site-specific structural fluctuations of peptides in a heterogeneous environment, the location and orientation of an antimicrobial peptide in lipid bilayers, and the conformational transformations of a β -hairpin peptide in the melting process.^{44,100,233,259,311,312}

In addition, one can utilize multiple isotope-labeled IR probes in the 2D IR measurements to characterize the interactions between the amide chromophores. For example, Hochstrasser and coworkers incorporated ¹³C and ¹³C=¹⁸O labels on alanine residues that are separated by 1, 2 or 3 amino acids and determined the magnitude and sign of the coupling constants in an α -helical peptide.^{91,301} Zanni and coworkers performed 2D IR measurements on a macrocycle that adopts a parallel β -sheet conformation and labeled several pairs of residues

1 with $^{13}\text{C}=^{18}\text{O}$, as demonstrated in Figure 7.³¹³ They then calculated the 2D IR spectra using a
 2 vibrational frequency map²⁶¹ and a variety of coupling schemes, including the through-bond
 3 nearest-neighbor couplings method²³⁰ and the through-space TDC and TCC
 4 models.^{230,271,272,314} As shown in Figure 7B, the theoretical approaches can predict the 2D IR
 5 line widths that are in quantitative agreement with experiments.³¹³ More recently, Tokmakoff
 6 and coworkers combined IR spectroscopy and ^{13}C and $^{13}\text{C}=^{18}\text{O}$ isotope labeling to
 7 systematically evaluate the performance of the vibrational frequency maps and the vibrational
 8 coupling models in the amide I region, providing a benchmark for the theoretical developments
 9 in the field.⁴⁵ In addition to probing the couplings between amide I modes, Ge and coworkers
 10 utilized a combination of $^{13}\text{C}=^{18}\text{O}$ and ^{15}N labels to reveal the interactions between the amide
 11 I and II modes.⁷⁷ With quantum chemistry calculations and the TCC model, they determined
 12 the coupling constants and their dependence on the three-dimensional peptide structure. All of
 13 these examples demonstrate that a close collaboration between theoretical and experimental
 14 spectroscopy methods, in conjunction with the isotope labeling technique, provides a powerful
 15 way to reveal the vibrational Hamiltonian and detect the structure and dynamics of peptides
 16 and proteins.
 17



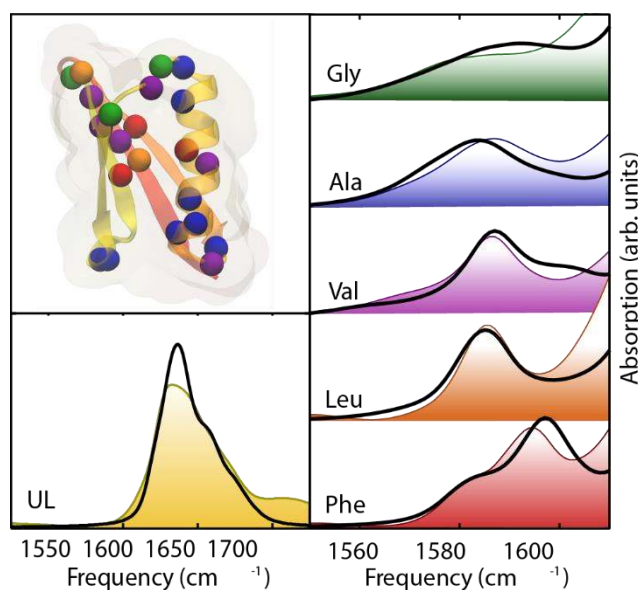
18 **Figure 7.** (A) Sequence of the macrocycle with the isotope labeled positions highlighted. (B)
 19 Comparison of experimental and theoretical 2D IR line widths. The theoretical spectra are calculated
 20 using various coupling schemes. Reproduced from Figure 1A and Figure 6 of Ref.³¹³ Copyright 2012
 21 American Chemical Society.

22
 23 It is still challenging to use the amide I maps to predict the amide I spectra that are in
 24 quantitative agreement with experiments.^{45,261,266,282} A major issue is the accuracy of the
 25 models used, such as the quantum chemistry methods chosen for the map developments and
 26 the sampling of conformational distribution using MD simulations. Therefore, it is desirable to

1 have reliable experimental standards so that researchers can develop or evaluate a vibrational
2 frequency map directly and systematically. While isotope labeling isolates a C=O from the
3 other amide I vibrations and offers a unique opportunity to examine the frequency map
4 predictions, preparing isotope-edited protein standards often falls into a dilemma between
5 synthetic difficulty and reliability of the underlying protein conformation.⁴⁵ For example,
6 isotope-labeled short peptides can be obtained using a standard peptide synthesis approach, but
7 these peptides are usually conformationally disordered. It has been shown that even the well-
8 studied tripeptide Ala–Ala–Ala exhibits conformational heterogeneity and the current protein
9 force fields cannot correctly predict the conformational distribution.^{74,315} On the other hand,
10 larger proteins usually have well-folded conformations, but synthesis with site-specific
11 isotope-labeling is almost prohibitive.

12 To develop experimental standards, the Tokmakoff group used isotope-enriched
13 protein expression to produce residue-specific isotope-edited NuG2b protein, which has
14 strong structural stability to mitigate the issue of conformational disorder for short peptides.⁴⁵
15 From the direct evaluation of vibrational frequency maps against experiments, they found that
16 the empirical one-site field map parameterized against dipeptide set failed to qualitatively
17 describe some of the isotope-labeled spectra, although the map had a good performance for the
18 dipeptide set. They also showed that representative sampling of the N–H electrostatics were
19 required to obtain qualitative agreement since hydrogen bonding interactions around the N–H
20 group can affect the amide I frequency.²²⁰ In addition, the predicted peak frequencies of the
21 labeled C=O chromophore depend strongly on the force field employed in the spectroscopic
22 simulations,^{260,267} which creates issues of the transferability of the frequency maps across
23 different force fields and their ability to quantitatively predict the amide I spectra. The
24 Tokmakoff group later developed an empirically optimized four-site potential map against the
25 IR spectra of the isotope-edited NuG2b proteins, which related the amide I frequency to the
26 electrostatic potential evaluated at the C, O, N, and D atoms.²⁶⁴ The map quantitatively
27 described the isotope-labeled spectral features (Figure 8) and achieved ~ 2 cm⁻¹ frequency error
28 against the dipeptide spectra. From these examples, new experimental data are imperative to
29 evaluate and refine the existing frequency maps so that they can be applied to crucial biological
30 problems such as determining conformational ensemble and interconversion dynamics of
31 intrinsically disordered peptides and proteins.^{74,266,267,282}

1



2

3 **Figure 8.** (Taken from Figure 8 of Ref²⁵⁹) Comparison of the frequencies, line widths, and intensities
 4 of experimental spectra with simulated spectra starting from MD simulations of the crystal structure of
 5 the protein G mutant NuG2b.⁴⁵ Copyright 2016 Annual Reviews.

6

7 **4.5. Amide II and III vibrations**

8 The amide II and III modes are the out-of-phase and in-phase combinations of N-H in-plane
 9 bend and C-N stretch of the peptide bonds, respectively. In addition to the amide I band, the
 10 peak positions and lineshapes of these modes are highly sensitive to the secondary structure of
 11 polypeptides and proteins. Given the high computational cost for performing *ab initio*
 12 vibrational analyses of proteins in the condensed phase, researchers have developed the
 13 vibrational coupled oscillator model and the fragmentation approach so that one only needs to
 14 consider the vibrational properties of a single unit, e.g., amide I, II, and III local mode
 15 frequencies, and the vibrational couplings between adjacent amide local modes. One of such
 16 methods is HMR, which requires quantum chemistry calculation of a chosen spectroscopic unit
 17 and fragmentation analysis of a polypeptide.

18 In the HMR method, one first divide a polypeptide consisting of N amino acids into N
 19 fragments. For example, it is natural to consider a dipeptide as a two-fragment system with
 20 peptides 1 and 2, as shown in Figure 9. Then, the full Hessian matrix of the dipeptide is
 21 rearranged such that the sub-matrix 1, $\bar{F}^{(1)}$, corresponds to the Hessian matrix associated with
 22 the atoms of peptide 1 and similarly the sub-matrix, $\bar{F}^{(2)}$, to those associated with the atoms
 23 constituting peptide 2. For these two sub-Hessian matrices, one can find eigenvector matrices
 24 $\bar{u}^{(1)}$ and $\bar{u}^{(2)}$ that diagonalize them, respectively. From the eigenvectors of the vibrational
 25 modes localized in peptides 1 and 2, one can identify the amide I, II, and III local modes and
 26 obtain their frequencies. In addition, the off-diagonal matrix elements correspond to the
 27 vibrational coupling force constants. For instance, considering the amide I, II, and III vibrations
 28 of a given dipeptide, one can obtain the reconstructed Hessian matrix by using the following

1 similarity transformation method:

$$2 \quad \begin{bmatrix} \bar{\mathbf{u}}^{(1)} & \mathbf{0} \\ \mathbf{0} & \bar{\mathbf{u}}^{(2)} \end{bmatrix}^T \begin{bmatrix} \bar{\mathbf{F}}^{(1)} & \dots \\ \dots & \bar{\mathbf{F}}^{(2)} \end{bmatrix} \begin{bmatrix} \bar{\mathbf{u}}^{(1)} & \mathbf{0} \\ \mathbf{0} & \bar{\mathbf{u}}^{(2)} \end{bmatrix} = \begin{bmatrix} F_{11} & F_{12} & \dots & \cdot \\ F_{12} & F_{22} & \dots & \cdot \\ \vdots & \vdots & \ddots & \vdots \\ \cdot & \cdot & \dots & F_{66} \end{bmatrix}. \quad (105)$$

3 Here, the diagonal elements $F_{11} - F_{33}$ ($F_{44} - F_{66}$) are the force constants of the amide I, II, and
 4 III local modes of peptide 1 (2). Once the reconstructed Hessian matrix in the basis set of local
 5 modes is determined, its diagonalization provides both the delocalized normal mode
 6 frequencies and corresponding eigenvectors. After obtaining the transition dipole moment or
 7 polarizability of a given peptide unit from high-level *ab initio* calculations, one can write the
 8 transition dipole moments or polarizabilities of the normal modes as linear combinations of
 9 those local modes, where the weighting coefficients are the associated eigenvector elements.

10 For example, Cho and coworkers used the HMR method to calculate the IR and
 11 vibrational circular dichroism (VCD) spectra of a model dipeptide and compared them to the
 12 spectra obtained from DFT calculations.³¹⁶ For the right-handed helix (RHH: $\phi = -57^\circ$ and ψ
 13 $= -47^\circ$) and polyproline II (P_{II}: $\phi = -78^\circ$ and $\psi = 149^\circ$) conformations of the dipeptide, the IR
 14 and VCD spectra agreed quantitatively between the two methods, as shown in Figure 9. The
 15 VCD spectra of the amide modes are critically dependent on the backbone conformation, and
 16 thus the spectral features of the amide I, II, and III modes are considerably different for the
 17 RHH and P_{II} configurations (Figure 9). Specifically, the amide II mode of the helical structure
 18 RHH displays a negative peak in the VCD spectrum, while the extended structure P_{II} exhibits
 19 a positive peak pattern. These are consistent with the experimental results of polypeptide with
 20 helical or extended β -sheet secondary structures. The good agreement between the HMR
 21 method and DFT calculations demonstrates that the fragment approximation method can be
 22 used to numerically simulate the vibrational spectra of large polymer systems consisting of
 23 repeating monomer units such as proteins, nucleic acids, and sugars.

24

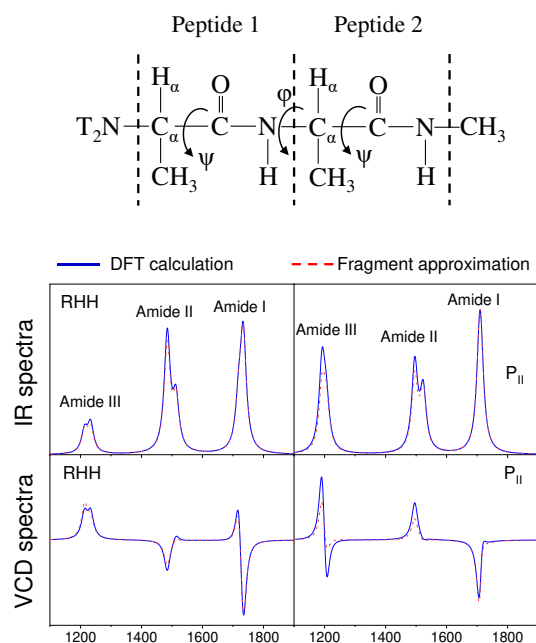


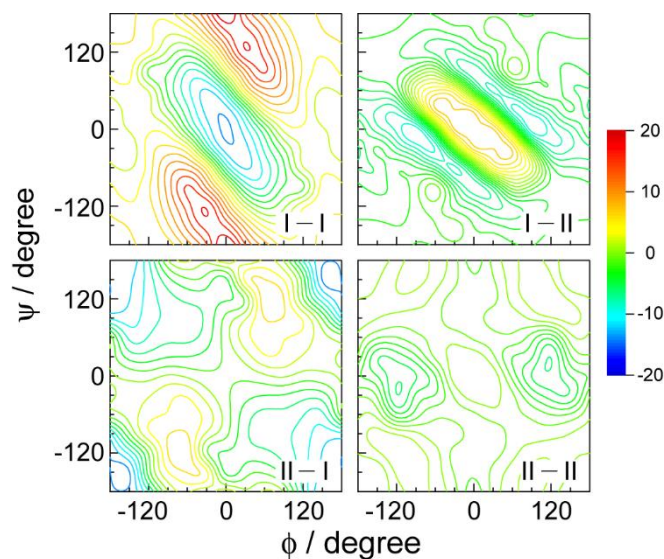
Figure 9. Molecular structures of alanine dipeptide in the upper panel. IR and VCD spectra of amide I, II, and III modes are displayed for its RHH and P_{II} conformations in the bottom panel. The blue solid and red dashed lines correspond to the simulated spectra obtained from DFT calculation and the fragment approximation, respectively. Reproduced from Figures 1, 3, and 4 of Ref.³¹⁶. Copyright 2009 Elsevier.

While most simulations of amide I modes are performed assuming these modes are independent of other vibrations, 2D IR spectra of amide groups in solutions exhibit cross peaks between the amide I and II modes even at short waiting times.^{85,317} This observation indicates that these modes are coupled to each other. In this representation, these basis states interact through harmonic coupling terms and all of the Hamiltonian elements fluctuate in aqueous solutions. Frequency maps that describe the fluctuations of the amide I and amide II energies and the amide I – amide II harmonic couplings were developed.³¹⁸ The dependencies of these quantities as well as the coupling between neighboring peptide units on dihedral angles were also parameterized by using the HMR method.³¹⁹ Simulations that employ these maps can be used to investigate vibrational relaxation and the origin of the short lifetime of the amide I vibration.³¹⁸

The amide II mode has been used to study the structural stability of biological macromolecules, hydrogen-deuterium exchange kinetics, and molecular conformation by linear IR and vibrational circular dichroism spectroscopy. In the past decade, 2D IR experiments have been performed on the amide II modes of NMA,^{78,320} small peptides^{78,321-323} and proteins^{85,324,325}, and thereby theoretical efforts have been made to compute the diagonal peaks of the amide II modes and their cross-peaks with the amide I modes.^{319,326}

Several groups have mapped out the NN couplings of not only amide I/amide I but also amide I/amide II and amide II/amide II based on quantum mechanical calculation for *N*-acetyl-glycine *N*'-methylamide (AcGlyNHMe)^{78,319,327} Hayashi and Mukamel obtained

1 couplings of the amide modes between neighboring peptide units using the anharmonic
2 vibrational Hamiltonian from the DFT calculation at the BPW91/6-31G(d,p) level.³²⁷ They
3 reported the NN amide II/II and II/I coupling maps, but not the amide I/II coupling map. It is
4 expected that the amide I/II and amide II/I coupling maps are different because of the
5 asymmetric arrangement of the amide I and amide II modes in the two peptide units. Ge and
6 coworkers carried out DFT calculations at the B3LYP/6-31+G(d) level for a complete mapping
7 of the amide I/I, I/II, II/I and II/II coupling strengths, and the reported amide I/II and II/I maps
8 showed distinct dihedral angle dependence of coupling strength (Figure 10).⁷⁸ Choi and Cho
9 developed a computational procedure of generalized HMR and estimated the NN amide
10 couplings, including amide II modes, for six pairs of dihedral angles for representative protein
11 secondary structures.³¹⁶ Knoester and coworkers performed a HMR calculation based on
12 writing the eigenmodes of a dipeptide, which they obtained from DFT calculations with the
13 ADF TZ2P basis set and the RPBE exchange-correlation functional, as a linear superposition
14 of the eigenmodes in two NMA-d₇ molecules.³¹⁹ While the amide I/II, II/I, II/II coupling maps
15 created from different protocols have qualitatively similar patterns, their ϕ - ψ dependences have
16 quantitative differences and more work in this field is required to produce a universal coupling
17 scheme.
18

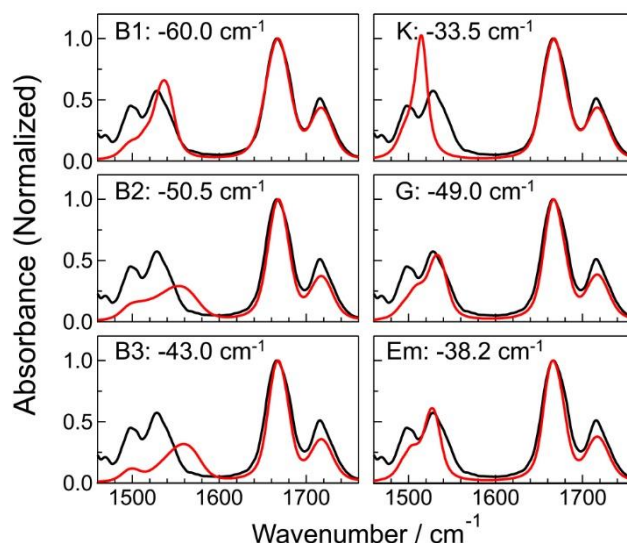


19
20 **Figure 10.** Nearest-neighbor amide I/I, I/II, II/I, and II/II coupling maps calculated for AcGlyNHMe at
21 the B3LYP/6-31+G(d) level with fixed dihedral angles. All four maps are plotted in a single color scale
22 and the unit of couplings is cm⁻¹. Reproduced from Figure 8 of Ref.⁷⁸. Copyright 2009 The American
23 Chemical Society.
24

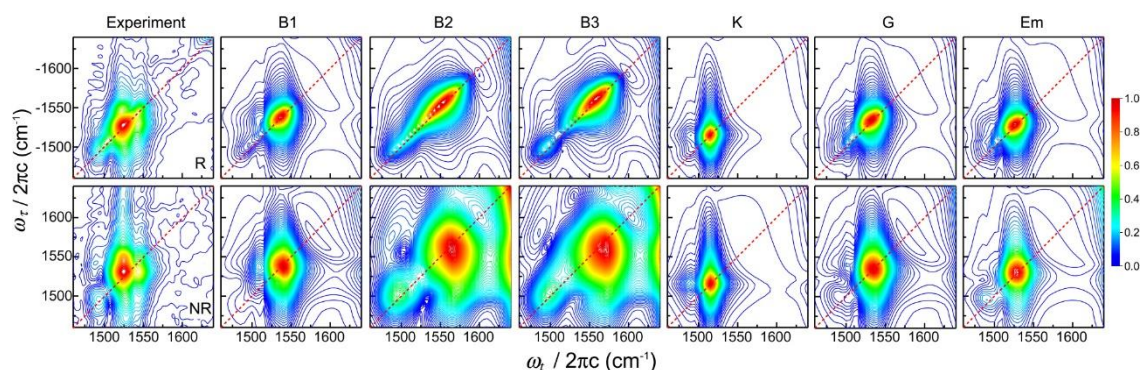
25 The NN couplings between proline and other amino acids are likely to be different
26 from those modeled by AcGlyNHMe, because the unique five-membered ring of the proline
27 residue imposes spatial constraints on the peptide structure. Sul et al. performed DFT
28 calculations and normal-mode analyses on the *trans* conformer of a model dipeptide, *N*-acetyl-
29 L-prolinamide (AcProNH₂), in vacuo at the B3LYP/6-31+G(d,p) level, and calculated the NN
30 amide I/I and I/II coupling maps by extending the HMR method, carbonyl population
31 analysis,³²⁸ to include the amide II mode.³²⁹

1 In addition to the NN couplings, the bilinear amide I/II coupling in the same peptide
2 unit is also important for calculating the amide I and II spectra of oligo- and longer peptides.
3 This coupling strength is about 27-39 cm⁻¹ as obtained experimentally from the 2D IR spectra
4 of NMA,³²⁰ NMA-d₇,^{78,317} and AcProNH₂.³³⁰ As its magnitude is much larger than the other
5 inter-unit amide couplings, it is useful to know how this amide I/II intrapeptide-unit coupling
6 depends on the dihedral angles of a polypeptide and the surrounding environment. From DFT
7 calculations at the B3LYP/6-31+G(d) level in vacuo, Ge and coworkers found the coupling
8 constant to be ±33 cm⁻¹ for AcGlyNHMe.⁷⁸ They further found the couplings to be ±23.8 cm⁻¹
9 for the *trans*-C₇ conformer and ±30.6 cm⁻¹ for the *cis* conformer of AcProNH₂ in chloroform
10 based on DFT calculations at the B3LYP/6-311++G(d,p) level and a self-consistent reaction
11 field polarizable continuum model.³²⁹ In addition to calculating the coupling constants for two
12 specific conformations,³²⁹ they also mapped out the coupling constant as well as the angle
13 between the amide I and II transition dipoles for the *trans* AcProNH₂ at 105 different dihedral
14 angles in vacuo at the B3LYP/6-31+G(d,p) level. While it is often assumed that this angle is
15 independent of the peptide conformations, their study demonstrated the variations of this angle
16 and provided an additional constraint to narrow down the allowed conformational space for the
17 structural determinations of polypeptides. Besides these studies on dipeptides, Knoester and
18 coworkers also parameterized the electrostatic effects on the intra-site coupling between the
19 amide I and II modes of NMA-d₇ and their transition dipole moments.³¹⁹

20 To establish a relationship between the amide II local mode frequency and the
21 electrostatic properties around the peptide unit, several groups carried out theoretical studies
22 on NMA and parameterized frequency maps for the amide II mode based on electric
23 potential^{217,229} or electric field and gradient.^{228,318,319} To evaluate the amide I and II maps,
24 Maekawa and Ge carried out MD simulations of a 3₁₀-helical hexapeptide Z-Aib-L-Leu-(Aib)₂-
25 Gly-OrBu and compared the calculated spectra with the experimental linear and 2D IR
26 spectra.²¹⁷ As shown in Figures 11 and 12, different models predict vastly different amide II
27 spectral signatures, while the amide I band profiles show less variations. Interestingly even
28 though the amide II mode is more delocalized than the amide I mode, the simulation results
29 show that it does not necessarily require a multi-site model that is more spatially spread to
30 correlate its frequency with the electrostatic properties: A simple model involving four atom
31 sites on a peptide unit performs quite well. Also, DFT calculations with a larger basis set do
32 not necessarily improve the agreement between the simulated and experimental peaks of the
33 amide II modes. Moreover, it has been shown that a simple semiempirical model works equally
34 well as the best performing four-site potential model. This semi-empirical model considers the
35 intramolecular C=O···H-N H-bonding as the only contribution from the peptide to the amide I
36 and II frequency shifts. The frequency shifts were parameterized based on the H-bond energies
37 calculated at the C=O and N-H sites.⁷⁸ Similar comparative studies are required to further test
38 the validity of the amide II frequency and coupling maps.



1
2 **Figure 11.** Experimental (black) and simulated (red) linear IR spectra of a 3_{10} -helical hexapeptide Z-Aib-L-Leu-(Aib)₂-Gly-O*t*Bu in CDCl₃ in the amide I and II regions.²¹⁷ B1, B2, and B3 are six-site potential
3 models,²²⁹ K is a four-site field/gradient model,³¹⁸ G is a four-site potential model,²¹⁷ and Em is a
4 semiempirical model.⁷⁸ The local amide I frequency was shifted from the gas phase value by the value
5 reported in each panel. Reproduced from Figure 8 of Ref.²¹⁷. Copyright 2010 The American Chemical
6 Society.
7
8



9
10 **Figure 12.** Experimental and simulated absolute 2D IR rephasing (top) and nonrephasing (bottom)
11 spectra of a 3_{10} -helical hexapeptide Z-Aib-L-Leu-(Aib)₂-Gly-O*t*Bu in the amide II frequency region. Each
12 spectrum is normalized by the peak intensity of the diagonal amide II band.²¹⁷ Reproduced from Figure
13 10 of Ref.²¹⁷. Copyright 2010 The American Chemical Society.
14
15

16 The application of VSMs of amide modes is not limited to polypeptides and proteins
17 composed of α -amino acids. Recently, Wang and coworkers theoretically determined the
18 coefficients to calculate the amide I frequency of *N*-ethylpropionamide (NEPA), a model
19 compound of β -amino acid, based on electrostatic potentials on the N, H, C and O atoms of the
20 peptide unit,³³¹ and the calculated linear spectra of NEPA in three different solvents were in
21 reasonable agreement with the experimental results. They also computed the coupling strengths
22 of the amide I and II modes for five helical β -peptide conformers,^{332,333} and showed that the
23 coupling strengths for shorter inter-amide distances cannot be described well by the TDC
24 model. It thus will be useful to obtain NN coupling maps as a function of dihedral angles for

1 the β -dipeptides, and including an additional pair of ϕ and ψ around the β -carbon in the
2 parameterization.

3 Researchers have also reported other empirical relationships between the amide I and
4 II local mode frequencies and H-bond energy^{76,78,278}:

$$\omega_p^{0,I(II)} = \omega_0^{I(II)} - \delta\omega_{\text{solvent}}^{I(II)} - \delta\omega_{\text{CO}}^{I(II)} - \delta\omega_{\text{NH}}^{I(II)}$$

$$\delta\omega_{\text{CO}}^I = -0.42 \text{ cm}^{-1} \text{ mol/kJ} \times E_{\text{KS}}$$

$$\delta\omega_{\text{NH}}^I = -0.96 \text{ cm}^{-1} \text{ mol/kJ} \times E_{\text{KS}}$$

$$\delta\omega_{\text{CO}}^{II} = 0.7 \text{ cm}^{-1} \text{ mol/kJ} \times E_{\text{KS}}$$

$$\delta\omega_{\text{NH}}^{II} = 2.9 \text{ cm}^{-1} \text{ mol/kJ} \times E_{\text{KS}}, \quad (106)$$

11 where $\delta\omega_{\text{CO(NH)}}^I$ and $\delta\omega_{\text{CO(NH)}}^{II}$ are the frequency shifts of the amide I and II modes due to the
12 presence of H-bond at the C=O (N–H) group, respectively. The frequency shifts were found to
13 be in good correlation with the electrostatic energy of the intramolecularly hydrogen-bonded
14 C=O \cdots H–N groups, denoted as E_{KS} .²⁷⁹ By matching the model frequency shift to the results
15 obtained from quantum mechanical calculations of NMA-water clusters,³³⁴ the correlation
16 coefficients in the above equations were obtained.^{78,278} In addition to the intramolecular H-
17 bonding effects, if the C=O or N–H group is exposed to solvent, it is necessary to consider an
18 additional decrease (increase) of the amide I (II) mode frequency due to the effect of solvation
19 ($\delta\omega_{\text{solvent}}$). The latter was empirically included as a constant shift of $\delta\omega_{\text{solvent}}^I = 10\text{--}20 \text{ cm}^{-1}$ and
20 $\delta\omega_{\text{solvent}}^{II} = -5 \text{ cm}^{-1}$ by the Ge group. Such semiempirical models have been successfully applied
21 to calculate the 2D IR spectra in the amide I region for 3_{10} - and α -helical peptides,²⁷⁸ their chain
22 length dependence,⁷⁶ as well as the amide II spectra and their cross-peaks with the amide I
23 modes.^{78,217}

24 25 **4.6. Nitrile stretch**

26 The nitrile stretching mode at around 2260 cm^{-1} has the advantage of not overlapping the
27 frequency regions of the water bending and stretching modes and is known as an important
28 compact IR probe that can be inserted into peptides and proteins to sensitively measure the
29 local electrostatic environment of the peptide and protein active sites. Specifically, as the nitrile
30 group forms an H-bond with the surrounding water, the stretch mode frequency of the molecule
31 undergoes a significant blue shift of $\sim 10 \text{ cm}^{-1}$, and the spectral bandwidth increases. Due to the
32 sensitivity of the nitrile stretch mode as a reporter sensing the local electric field, this IR probe
33 has been critically used to explore the solvation dynamics as well as the protein active-site
34 structures. 2D IR vibrational spectroscopic measurements of the CN stretch mode of cyano-
35 phenylalanine in the villin headpiece (HP35) protein revealed that the solvent-exposed nitrile
36 group exhibited a blue shifting behavior compared to other CN groups in the hydrophobic
37 environments. Furthermore, Chung et al.⁸⁴ showed through 2D IR vibrational spectroscopic
38 experiments on the HP35 protein that the spectral diffusion of unfolded peptides is much faster
39 than that of folded peptides and is very similar to that of PheCN, meaning that the solvent

1 molecules make significant contributions to frequency fluctuation and dephasing process the
2 dynamics probed by the CN stretch. Vibrational Stark Effect Spectroscopy has been
3 extensively applied to nitrile-incorporated chemical systems and measures the local electric
4 field around the IR probe using a vibrational Stark tuning rate (see Eq. (64)) of a nitrile of about
5 0.4 to 1.1 $\text{cm}^{-1}/(\text{MV}/\text{cm})$. However, the linear Stark theory considering only the electric field
6 parallel to the CN bond fails to predict the vibrational frequency shift of the nitrile in a strong
7 H-bonding system such as aqueous solutions, whereas using six electric field vectors located
8 at two atoms of the CN bond leads to a reasonable calculation of the frequency shift in the
9 CH_3CN -water solution. Boxer's group, who recently performed IR and NMR spectroscopic
10 measurements, showed that H-bonding interactions with IR probes should be considered
11 differently compared to nonspecific electrostatic interactions.¹⁸² The Thielges group has
12 introduced PheCN at multiple sites in several proteins for linear and 2D IR spectroscopy, but
13 report limited success in applying a linear Stark model.^{46,87,88} In addition, Gai and coworkers
14 showed that the vibrational frequency of the nitrile stretch mode of 5-cyanotryptophan can be
15 determined by the linear relationship of the Kamlet-Taft solvent parameters, including solvent
16 polarity and H-bonding accepting or donating capability, while the individual parameters do
17 not correlate with the nitrile stretching mode frequency. Bredenbeck and coworkers³³⁵ have
18 shown that the solvatochromic properties of cyanotryptophan depend on the position of the
19 nitrile on the ring, with 4-cyanotryptophan being more sensitive to solvent polarity than 5-
20 cyanotryptophane. Due to their short CN stretch vibrational lifetime of 1.5 ps or less, however,
21 cyanotryptophans are mainly attractive because they can serve as a combined label for linear
22 IR spectroscopy and fluorescence spectroscopy and not so much for 2D IR spectroscopy. To
23 take into account the effect of an H-bond between OH group and nitrile N atom to the
24 vibrational solvatochromism in an *ad hoc* manner, Biava et al. modified the vibrational Stark
25 effect theory considering two different CN groups, i.e., non-H-bonded and H-bonded
26 nitriles.³³⁶ They are then treated differently so that the net vibrational frequency shift of the CN
27 stretch mode is expressed as a function of the fraction of the H-bonded species, X_{HB} , i.e.,

$$28 \quad \Delta\omega = \left[(1 - X_{\text{HB}}) \Delta\mu_{\text{non}} + X_{\text{HB}} k_{\text{HB}} \right] E_{f,s} - X_{\text{HB}} (1 - X_{\text{HB}}) (\Delta\mu_{\text{non}} - k_{\text{HB}}) E_{\text{CN-H}} + X_{\text{HB}} (\omega_{0,\text{HB}} - \omega_{0,\text{non}}), \quad (107)$$

29 where $\omega_{0,\text{non}}$ is the unperturbed vibrational frequency, $\Delta\mu_{\text{non}}$ the vibrational Stark tuning
30 rate, X_{HB} is the mole fraction of the H-bonded nitrile, and $E_{f,s}$ is the average solvent electric
31 field on the CN group, k_{HB} is the vibrational Stark tuning rate for H-bonded species, $\omega_{0,\text{HB}}$
32 is the zero-field vibrational frequency of H-bonded species, and $E_{\text{CN-H}}$ is the effective average
33 solvent electric field for H-bonded species. Since this phenomenological model involves
34 calculations of the ensemble-averaged solvent electric field from molecular dynamics
35 simulations, they can only be used to estimate the average vibrational frequency shift, $\Delta\omega$,
36 not fluctuating instantaneous vibrational frequency, $\delta\omega(t)$ (see Eq.(10) in Section 2.2) that is

1 necessary to simulate linear and nonlinear vibrational spectra of molecular systems in
2 condensed phases.

3 The above results and failures in developing a rigorous and systematic theory for
4 vibrational solvatochromism of CN stretching vibration in solutions suggest that the vibrational
5 solvatochromic frequency shifts of the nitrile stretching mode result from various contributions
6 from quadrupole and higher-order multipole terms and non-Coulomb interactions in addition
7 to the dipolar term. By employing the Bio-SoleEFP method for the vibrational frequency shift
8 of the IR probe, Błasiak et al. demonstrated that the nitrile stretching frequency shift due to H-
9 bonding interaction with surrounding water molecules is determined not only by the
10 contribution of Coulomb interactions but also by the dispersion interactions and the exchange-
11 repulsion contributions.^{40,155} Despite the success of the Bio-SoleEFP method and the modified
12 linear Stark theory to calculate the vibrational frequency of the nitrile stretching mode in
13 aqueous solution, a semiempirical approach using vibrational frequency maps is still useful in
14 consideration of reasonable computational cost and high accuracy in simulating the linear and
15 nonlinear vibrational spectra of nitrile-inserted chemical systems.

16 To estimate the solvation-induced vibrational frequency shift of various IR probes such
17 as nitrile and thiocyanate quantitatively, and azido moieties, the multivariate linear relationship
18 between the IR frequency shift and electrostatic potentials around the IR probe has been
19 established. That is, the solvatochromic vibrational mode frequency shift of the IR probe is
20 assumed to be described by electrochromic relationships involving electric field or electrostatic
21 potential evaluated at various points within the IR probe. For instance, the simplest map of this
22 kind is the dipolar map that can be recast in the following form,^{183,337}

$$23 \quad \Delta\omega = \sum_i \{ \mathbf{C} \cdot \mathbf{E}_C + \mathbf{N} \cdot \mathbf{E}_N \}, \quad (108)$$

24 where \mathbf{E}_X denotes the electric field at the X atom of CN and \mathbf{C} and \mathbf{N} are the vectorial
25 parameters. Another frequency map is the so-called antenna model for the vibrational
26 solvatochromism, where the frequency shift in wavenumber is described as a sum of products
27 of vibrational solvatochromic charge and solvent electric potential at the interaction site of the
28 solute molecule, i.e.,

$$29 \quad \delta\nu = \sum_{a=1}^n l_a \phi_a^{water}. \quad (109)$$

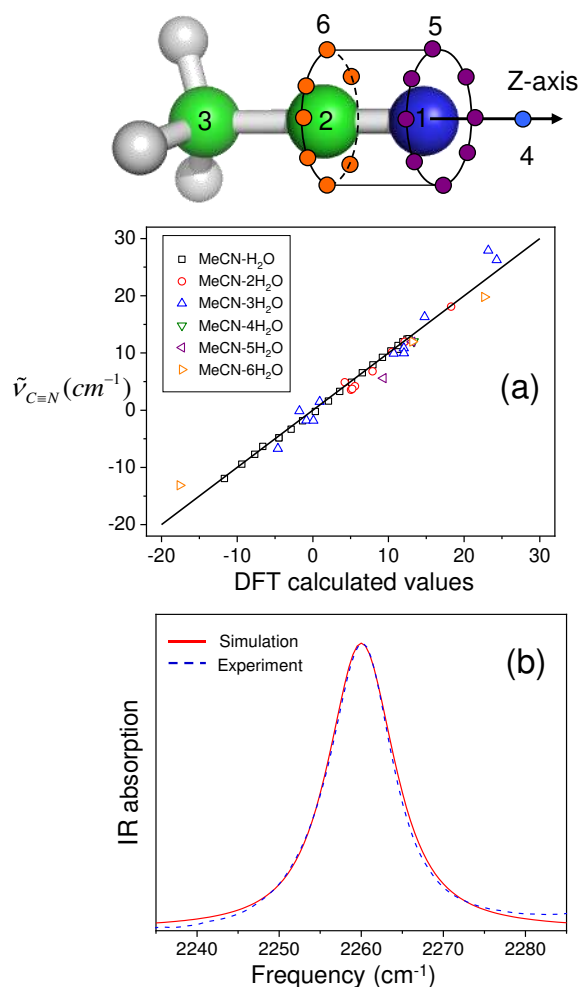
30 Here, ϕ_a^{water} and l_a are the Coulomb electrostatic potential created from water molecules at
31 the a th site of the IR probe group and the vibrational solvatochromic charge at the site,
32 respectively. The C≡N group has two different H-bonding interactions with neighboring water
33 molecules, one is the H-bonding interaction between the lone pair orbital of the nitrogen atom
34 and a hydrogen atom of a water molecule (σ -H-bonding), and the other is the H-bonding
35 interaction between the CN π -orbitals and a hydrogen atom of a water molecule (π -H-bonding).
36 In a previous study to describe the vibrational frequency shift of the nitrile stretch mode, a
37 solvatochromic dipole vector model was employed, but the use of only the dipole interaction
38 term is inappropriate for describing these complicated two interactions including the σ -H-
39 bonding causing the blue-shifting behavior of the CN stretch mode and the π -H-bonding

1 inducing the red-shift of the frequency.

2 A crucial step in evaluating the solvatochromic frequency shift arising from these two
3 competing interactions is to introduce a set of distributed interaction sites around the IR probe
4 and determine the solvatochromic charges using quantum chemical calculations. In the case of
5 MeCN in Figure 13, a total of 20 sites are considered describing the lone pair of the N atom
6 and the CN π bonding orbitals where the number of independent coefficients is 5 because of
7 the charge neutrality condition, that is, $\sum_{a=1}^n l_a = 0$.

8 The solvatochromic charges l_a were determined by a multivariate least-squares fitting
9 procedure by performing DFT calculations on numerous CH₃CN-water complexes and the
10 vibrational frequency shifts obtained from Eq. (109) were found to be in good agreement with
11 the results of DFT calculations in Figure 13(a). By performing MD simulations for an aqueous
12 MeCN solution, the time-varying frequency shift of the CN stretch mode was evaluated from
13 the MD trajectory using Eq. (109). The average CN frequency shift is 9.0 cm⁻¹, indicating a
14 blue-shift, which is consistent with the experimental result of 7.9 cm⁻¹ compared to the gas
15 phase frequency and mainly resulted from the σ -H-bonding interaction between CN and water.
16 The numerically simulated IR spectrum using the Fourier transform procedure was found to be
17 consistent with the experimentally measured band shape (Figure 13(b)). Thus, the hybrid
18 method using the frequency map and MD simulations is confirmed to be useful for obtaining
19 information on the structures and dynamics near the IR probe in proteins.

20 Another approach to incorporating the two competing interactions is to take both the
21 electrostatic potentials and the electric fields on the atomic sites in the electrostatic frequency
22 map.^{239,338} It has been shown that the frequency blue-shift of the nitrile CN stretch due to σ -H-
23 bonding arises from the spatially inhomogeneous nature of the electrostatic environment
24 generated by the H-bond donating group (such as the OH group in water).³³⁸ The vector
25 component, representing the vibrational response to the electric field, on the nitrile N atom is
26 responsible for the blue-shift due to the σ -H-bonding (with a large electric field on the N atom
27 along the CN bond direction), which is counteracted by the scalar component, representing the
28 vibrational response to the electrostatic potential, which is effective in both the σ - and π -H-
29 bonding and lowers the frequency (Note that the electric field on the N atom along the CN
30 bond direction is smaller in π -H-bonding). The difference between the cases of the uniform
31 electric field (employed in the vibrational Stark effect experiment) and the H-bonding
32 environment is the uniform/non-uniform nature of the local electric field, which causes a
33 change in the relative weights of the vibrational response parameters on the nitrile N and C
34 atoms in calculating the frequency shifts.

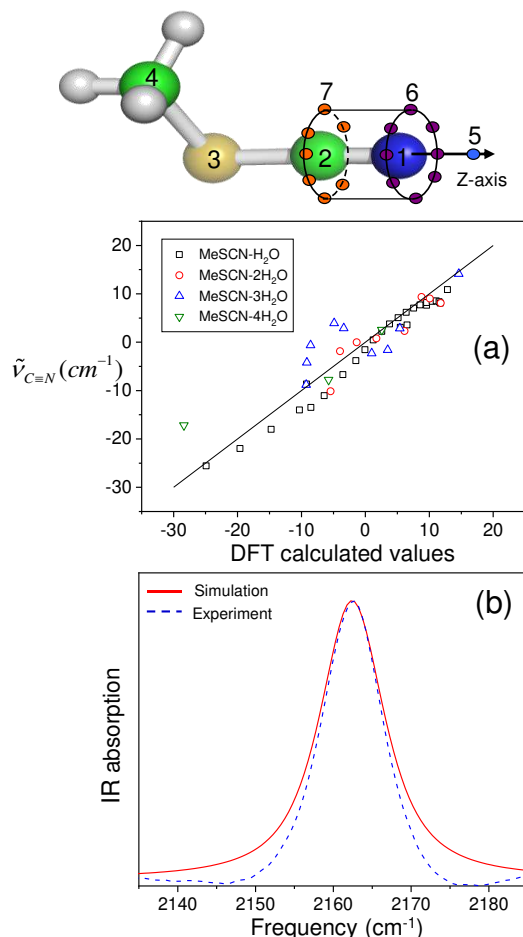


1
 2 **Figure 13.** Solvatochromic charge model with distributed interaction sites for MeCN in the upper panel.
 3 The calculated nitrile stretching mode frequency shift using Eq. (109) is directly compared to the DFT
 4 calculation results in (a). The numerically simulated IR spectrum of the CN stretch mode (red solid line)
 5 is plotted with the experimentally measured result (blue dashed line) in (b). The figure of the interaction
 6 sites and (a) is reproduced from Figure 5(a) Ref.¹⁸³ and (b) is reproduced from Figure 10(a) of Ref.²¹⁸.
 7 Copyright 2008 AIP Publishing.

9 4.7. Thiocyanato stretch

10 The vibrational properties of thiocyanato stretch mode are quite similar to that of the nitrile
 11 mode in that the SCN frequency shift and band shape depend on the extent of exposure to
 12 surrounding water molecules. Quantum chemistry calculations on various CH₃SCN-water
 13 complexes were performed to determine the solvatochromic charge parameters l_a of MeSCN
 14 in Eq. (109). A total of 21 sites were considered for MeSCN (Figure 14), where the number of
 15 independent coefficients to be determined is just six. The vibrational frequency shifts
 16 calculated with Eq. (109) with pre-determined solvatochromic charges, l_a , are found to be in
 17 excellent agreement with the DFT calculation results (Figure 14(a)). The average frequency
 18 shift of thiocyanato stretch mode calculated with Eq. (109) and MD trajectory is 1.9 cm⁻¹ for
 19 MeSCN, and it is close to the experimental result of 5.5 cm⁻¹. The main contribution results

1 from the linear H-bond between the N atom of SCN and the H atom of water. The numerically
 2 simulated IR spectrum was shown to be in good agreement with the experimentally measured
 3 spectrum (see Figure 14(b)).



4
 5 **Figure 14.** Solvatochromic charge model with distributed interaction sites for MeSCN in the upper panel.
 6 The y-axis in (a) corresponds to the thiocyanato stretch mode frequency obtained with Eq. (109) and
 7 the x-axis to the DFT calculated results. The numerically simulated IR spectrum of the SCN stretch
 8 mode (red solid line) is plotted with the experimentally measured result (blue dashed line) in (b). The
 9 figure of the interaction sites and (a) is reproduced from Figure 5(b) of Ref.¹⁸³ and (b) is reproduced
 10 from Figure 10(b) of Ref.²¹⁸. Copyright 2008 AIP Publishing.

11
 12 Maienschein-Cline and Londergan investigated the IR absorption spectra of methyl
 13 thiocyanate in various solvent environments and showed that SCN stretch mode can be used
 14 as an excellent reporter for specific H-bonding and local dynamics around the IR probe by
 15 observing the temperature dependence of the peak position and shape of the SCN stretch
 16 mode.³³⁹ A later solvatochromic study showed that the peak position depends on not only the
 17 H-bonding but also solvent polarity.^{48,340} While H-bonding causes a blue-shift, increasing
 18 polarity leads to a red-shift. Consequently, the two effects can compensate each other. For
 19 example, the SCN band in the nonpolar and aprotic perchloroethylene has almost the same
 20 wavenumber as in the polar and protic water. Methyl thiocyanate lifetimes of up to 150 ps have
 21 been observed, rendering the SCN stretch a very interesting label for probing protein dynamics

1 by 2D IR despite its low transition dipole moment. Furthermore, cyanylation of cysteine in the
2 target protein enables the site-specific insertion of the label without synthesizing the entire
3 protein. Various processes in proteins have been studied by observing the change of the
4 vibrational frequency in the SCN stretch mode, such as inhibitor binding to an enzyme in the
5 case of ketosteroid isomerase,³⁴¹ or conformational changes during the photocycle of the
6 photoreceptor PYP.³⁴² Londergan and his coworkers employed cyanylated cysteine
7 incorporated to a peptide of calmodulin (CaM)-binding domain to examine the binding affinity
8 of CaM to the target protein of skeletal muscle myosin light chain kinase and showed the use
9 of SCN probe allows monitoring of site-specific changes in the CaM-peptide complex without
10 any perturbation.⁴⁷ Recently, Bredenbeck and his coworkers performed time-resolved 2D IR
11 spectroscopic measurements of the SCN stretch mode of cyanylated cysteine in the bovine
12 hemoglobin protein and demonstrated that the isotope-labeled S¹³C¹⁵N incorporated into
13 protein could be critically used as a reporter for probing local structural dynamics around the
14 IR probe.⁴⁸ More recently, it was shown that the vibrational lifetime of the SCN label,
15 incorporated into the photoreceptor protein PYP, is a very reliable probe for bulk solvent
16 exposure. As the lifetime notably differs between H₂O and D₂O buffer for a solvent-exposed
17 label, comparison of the lifetimes in H₂O and D₂O measurements allows determination of the
18 solvent accessibility of the SCN label in proteins.³⁴³ Schmidt-Engler et al. showed that the long
19 vibrational lifetime of the -SCN label in proteins allows to track spectral diffusion up to 120 ps
20 in 2D IR spectra and applied the label to look at ion- and ligand-binding in calmodulin.⁸⁹

21 In addition to various experimental measurements on SCN stretch mode, there have
22 been theoretical attempts to establish a relationship between electric field nearby IR probe and
23 the vibrational frequency shift based on the linear vibrational Stark theory. To overcome the
24 inability of the vibrational Stark effect to predict the SCN stretch mode frequency in an H-
25 bonding system, Bagchi and his coworkers showed the correlation of the local electrostatic
26 field around the IR probe with the SCN frequency in various solvents, taking into account
27 specific H-bonding interactions and nonspecific electrostatic interactions differently.³⁴⁴
28 Furthermore, using QM/MM MD simulation with reparametrized PM3 potential, Layfield and
29 Hammes-Schiffer successfully described the vibrational line shape of the SCN group inserted
30 to protein active site.³⁴⁵ However this semiempirical approach has difficulties in transferring
31 force field parameters to various chemical systems, Błasiak et al. recently developed an
32 effective fragment potential approach taking into account the contribution of dispersion and
33 exchange repulsion to SCN stretch mode frequency calculation, as well as electrostatic
34 contribution. The combination of QM/MM MD and the SoleFP approach was shown to
35 successfully reproduce the vibrational spectrum of the SCN group incorporated into the target
36 peptide of the CaM-peptide complex while QM/MM calculation without the SoleFP method
37 fails in predicting experimental result.²⁰³ Although the semi-experimental approach using a
38 vibration frequency map is based on electrostatic interaction between the IR probe and the
39 adjacent environment without considering dispersion and exchange repulsion, multivariate
40 least-squares fitting analysis of Eq. (94) on the DFT results works properly when simulating
41 the vibration spectrum of the SCN stretch mode in various chemical systems.

42 The solvatochromic charge model with distributed interaction sites have also been

1 applied to SCN⁻ anion³⁴⁶ and 2-nitro-5-thiocyanate benzoic acid (NTBA) in water⁴⁹ by
2 Tominaga and co-workers. The SCN frequency shifts are described by using 28 and 35
3 interaction sites for SCN⁻ and NTBA, respectively. The solvatochromic charge model can
4 reproduce experimental blue shifts of the SCN frequencies of SCN⁻ and NTBA in water. It was
5 found that the calculated FFCFs of SCN⁻ and NTBA in water are fitted by a double exponential
6 function and that the slow component with the time scale of ~1 ps arises from the H-bond
7 network rearrangements around the solute molecules. By examining the spatially-resolved
8 SCN frequency fluctuation, Okuda et al., showed that the SCN frequency fluctuation of SCN⁻
9 is mainly determined by water molecules in the first hydration shell, i.e., within ~3.5 Å from
10 the SCN⁻ molecule, whereas that of NTBA is affected by water molecules in more extended
11 region, i.e., within ~7 Å from the NTBA molecule.

12 13 **4.8. Selenothiocyanato stretch**

14
15 CN stretch mode in SeCN group is a valuable IR probe because it has a significantly longer
16 vibrational lifetime as compared to the CN stretch modes in SCN or CN groups.³⁴⁷ Yet, it is
17 similarly sensitive to the environment as all other nitrile-containing groups. The electrochromic
18 map developed by Yamada, Thompson, and Fayer for SeCN⁻ anion was used to study the
19 dynamics of the H-bonding network in water.³⁴⁸ In their map, they addressed not only the
20 vibrational frequency corresponding to the fundamental transition, but also the first vibrational
21 excited state absorption frequency, transition dipole moment derivative of the fundamental
22 transition as well as the anharmonicity constants. In their map, the magnitude of the solvent
23 electric field along the SeCN⁻ molecular axis evaluated on the carbon atom, E_C , is assumed to
24 be the sole perturbation inducing changes in the vibrational properties, i.e.,

$$25 \quad x = A_x + B_x E_C \quad (110)$$

26 where x is one of the vibrational spectroscopic quantities, and A_x and B_x are the fit
27 parameters. Considering various SeCN⁻-(D₂O)_{*n*} clusters sampled from MD trajectories and
28 carrying out DFT calculations at B3LYP/aug-cc-pVDZ level, they constructed a set of data for
29 obtaining the optimized parameters. To better describe the long-range intermolecular
30 interaction effect on the vibrational solvatochromism of SeCN⁻ while preserving computational
31 efficiency, the first nine nearest water molecules relative to the anion's center of mass are
32 treated quantum mechanically at the DFT level, whereas the other water molecules beyond the
33 cutoff distance of 10 Å from the center of mass of SeCN⁻ are represented by the corresponding
34 atomic point charges. The linear relationships between the electric field and spectroscopic
35 properties are used to calculate the 1D and 2D IR spectra for the sake of comparisons with their
36 experimental results. Furthermore, their model was found to be useful for explaining the
37 anisotropy decay of the IR PP signal and the time-dependent decay of the CLS of SeCN⁻ in
38 D₂O. They argue that SeCN⁻ is an excellent IR probe to study the H-bond reorganization
39 dynamics even though it is not a neutral molecule and its size is large as compared to the OD
40 stretch of HOD that has been used routinely in various studies of water H-bonding network
41 structure and dynamics.

4.9. Azido stretch

The azido-incorporated amino acids have been applied to study different conformational states of the rhodopsin and to investigate the structural change in the protein folding-unfolding process through monitoring the peak position and lineshape of azido stretch mode. Genetically incorporating p-azido-phenylalanine into CaM protein, Creon et al. showed that azido stretch mode is a sensitive IR probe for investigating the electrostatic environment around the azido group in the CaM-CaM binding domain complex.³⁴⁹ Performing 2D IR spectroscopic measurements on azido stretch mode with the incorporation of azido group into the specific residue of protein, Fayer and his coworkers demonstrated that the N_3 IR probe is of critical use for probing protein dynamics in MbCO active site by analyzing FFCF extracted from 2D IR measurements.³⁵⁰ Interpretation of the dynamic line shape of aromatic azides, such as p-azido-phenylalanine can be complicated by Fermi resonance.³⁵¹⁻³⁵³ However, the azido stretch mode has an increased sensitivity advantage over other IR probes such as the -CN and -SCN groups due to its large transition dipole moment, which makes it the probe of choice for vibrational energy transfer experiments in proteins.³⁵⁴ To describe the vibrational absorption spectrum of the azido stretch mode, the semiempirical approach was successfully used in terms of the electrostatic potential at distributed sites, while the vibrational stark theory does not work properly due to the significant contribution of quadrupole term to the solvatochromic frequency shift. The distributed interaction site model for azido stretch mode is shown in Figure 15, where 29 sites serve as an antenna sensing the local electrostatic potential around the IR probe.²³² The azido stretch mode frequency is predicted with Eq. (94), where the b_{jk} coefficients are determined by using multivariate least square fitting method and quantum mechanical calculations for various methyl azide-water complexes.

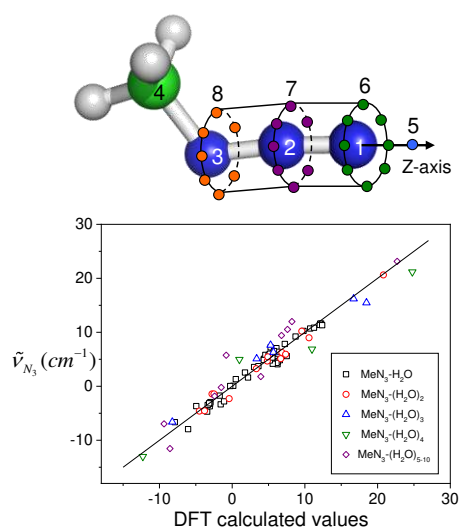
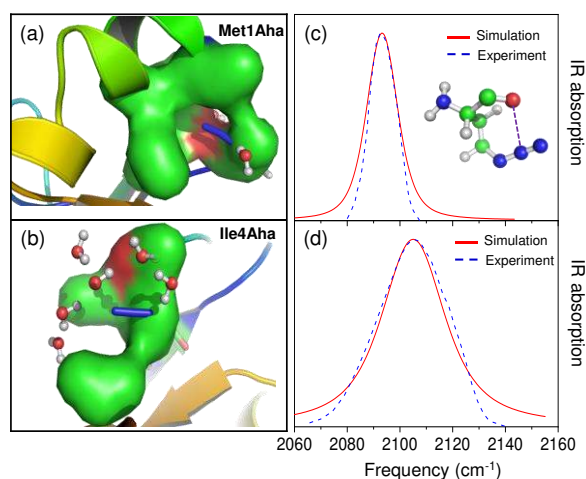


Figure 15. Solvatochromic charge model with distributed interaction sites for MeN_3 in the upper panel. The y-axis in the bottom panel represents the azido stretch mode frequency obtained with Eq. (109) and the x-axis to the DFT calculated results. Reproduced from Figures 4(b) and 5 of Ref.²³². Copyright 2008 AIP Publishing.

1 The semiempirical approach of describing the frequency shift of the azido stretch
2 mode was used to examine the electrostatic environment of the azidohomoalanine-incorporated
3 NTL9 protein that is the N-terminal domain of the ribosome protein. Taskent-Sezgin et al.³⁵⁵
4 measured the IR spectra of two mutants of NTL9, Met1Aha and NTL9-Ile4Aha. The showed
5 that the azido IR probes in the two mutants are exposed to different local electrostatic
6 environments, that is, hydrophobic pocket (Figure 16(a)) and solvent water (Figure 16(b)).
7 Quantitative analyses of the IR spectra for these two mutants were made by performing
8 QM/MM MD simulations of aqueous NTL9 mutant solutions and estimating the fluctuating
9 frequency shift of the azido stretch mode with Eq. (94).²³⁶ For the azido frequency shift of
10 Met1Aha, the contribution from the peptide backbone is 12.5 cm^{-1} , and this large blue shift
11 results from the electrostatic interaction of carbonyl oxygen atom of Met1 with middle N-atom
12 of azido group (see the inset of Figure 16(c)). Surrounding water molecules cause a red-shift
13 of -6.9 cm^{-1} , indicating that the presence of hydrophobic pocket in Met1Aha prevents water
14 molecules from making linear H-bonds with the azido group. Since the azido group of Ile4Aha
15 in Figure 16(b) is fully exposed to the solvent, water molecules can form a linear H-bonding
16 interaction with the terminal N-atom of N_3 and causes a large blue shift of 8.4 cm^{-1} whereas
17 the contribution of neighboring peptides is relatively small, exhibiting a blue-shift of 1.3 cm^{-1} .
18 Although the total frequency shift difference of about 4 cm^{-1} in the N_3 mode between Met1Aha
19 and Ile4Aha is smaller than that of experimentally measured value of 11 cm^{-1} , the blue-shifting
20 pattern is clearly reproduced by considering two contributions from water and neighboring
21 peptide backbone atoms. The calculated spectral lineshapes of the azido stretch mode for both
22 mutants were found to be consistent with the experimental results (Figures 16(c) and 16(d)). In
23 short, the combination of QM/MM MD with vibrational frequency maps is successful in
24 reproducing the IR spectrum of azido-homoalanine and in extracting the critical information
25 on the native protein structure and the solvent effect on the IR probe.



26
27 **Figure 16.** (a) Azido group in the hydrophobic pocket of Met1Aha NTL9 mutant (b) fully hydrated azido
28 group of Ile4Aha NTL9 mutant. The numerically calculated IR spectra of the azido stretch mode (solid
29 red line) of Met1Aha in (c) and Ile4Aha in (d) are displayed with the experimental results (blue dashed
30 line). Reproduced from Figures 1 and 4 of Ref.²³⁶. Copyright 2011 The American Chemical Society.

31

1 More recently, Zanobini et al.⁵⁰ employed the frequency map developed by Choi et al.
2 to estimate vibrational frequency shifts caused by changes in the electrostatic environment of
3 the azidohomoalanine (Aha) incorporated in the vicinity of the binding groove of the PDZ2
4 domain in the study of protein-ligand interactions of the K38Aha mutant of apo-PDZ2.
5

6 **4.10. Carbonmonoxy stretch**

7 When CO is bound to a heme group in proteins, the CO stretch transition dipole moment is
8 enhanced; the vibrational Stark tuning rate of the CO stretch mode for CO bound to a heme
9 group was estimated to be $2.4/f \text{ cm}^{-1}/(\text{MV}/\text{cm}^{-1})$ with the local field correction factor f . In
10 contrast, the free CO in an organic solvent solution has a smaller value of $\sim 0.7/f \text{ cm}^{-1}/(\text{MV}/\text{cm}^{-1})$.³⁵⁶ Thus, the CO stretch mode of proteins containing heme groups such as myoglobin and
11 hemoglobin can be used as an excellent IR probe to study the electrostatic environment in the
12 protein active sites. When CO binds to the heme of myoglobin, the CO stretch mode shows
13 two distinct peaks in the vibrational absorption spectrum, which were assigned to the
14 vibrational sub-state of A_1 at $\sim 1944 \text{ cm}^{-1}$ and to A_3 at $\sim 1932 \text{ cm}^{-1}$. Recently, the Fayer group
15 performed linear and 2D IR spectroscopic measurements of the wild-type and double mutant,
16 T67R/S92D, myoglobins, where such site-specific mutations significantly enhance the
17 catalytic activity of peroxidase compared to wild-type myoglobin. They found that the
18 chemical exchange rates between the conformational states of A_1 and A_3 are significantly
19 different from each other. Upon visible light illumination, CO is cleaved from the heme iron
20 and populates the so-called docking state in the vicinity of the heme within a few picoseconds,
21 producing the so-called B-states in the IR spectrum.³⁵⁷ Using triggered 2D-IR exchange
22 spectroscopy, Bredenbeck et al.⁹³ established the relationships between the bound states A_1 and
23 A_3 and the different B states at the docking site, which have been the target of detailed
24 theoretical investigations as well.
25

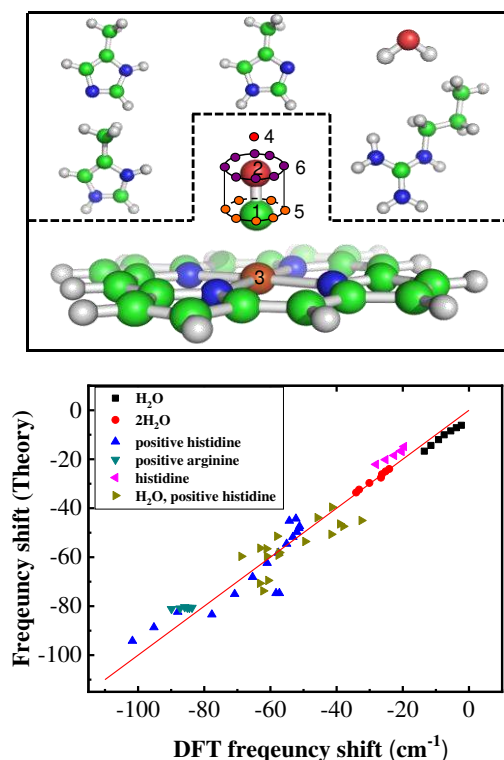
26 Along with numerous experimental works of vibrational spectroscopic measurements
27 to explore the active site structures and dynamics of CO-bound heme proteins, theoretical
28 attempts have been made to simulate the CO stretch spectra of MbCO and to directly compare
29 them with the experimental data, both, for the heme-bound CO in the A-states and the CO at
30 the docking site (B-states). To describe the vibrational spectrum of the CO stretch mode in the
31 CO bound heme associated with the B_1 and B_2 states corresponding to the two orientations of
32 CO at the docking site, that is, CO pointing either with its O or C atom towards its former
33 binding site of the Fe atom, respectively, Anselmi et al. carried out MD simulations of CO-
34 bound Mb and numerically simulated the CO stretch IR spectrum of the CO ligand within the
35 heme distal pocket using the perturbed matrix method to describe the vibrationally excited
36 states of a given molecule. In direct comparison with the experimental vibrational spectra of
37 the CO stretch mode of the complex of heme and CO, the simulated CO stretch IR spectrum
38 exhibits two distinct peaks that are assigned to the vibrational spectroscopic states of B_1 and
39 B_2 ,³⁵⁸ confirming the assignment proposed by Lim et al.³⁵⁷ Recently, to describe the vibrational
40 frequency shift of the CO stretch mode caused by swapping the CO orientation in the docking
41 site, Wang et al. successfully described the CO stretch IR spectrum associated with the B_1 and
42 B_2 states with a match between the theoretical result of 13.1 cm^{-1} and the experimentally

1 measured value of 11.5 cm^{-1} .³⁵⁹ On the other hand, to estimate the vibrational frequency shift
2 of the CO stretch mode in the A-states, where CO is bound to the iron atom, in consideration
3 of the H-bonding interaction between the oxygen atom of CO and the hydrogen atom of the
4 neighboring His 64 residue, the semiempirical approach of Eq. (94) was used with the treatment
5 of electrostatic potential generated from water solvents and neighboring peptides.³⁶⁰ The
6 distributed solvatochromic charge model was used to estimate the CO stretch frequency shift
7 of MbCO, reflecting the change in the electrostatic potential on the CO ligand. Note that the
8 IR probe is not an isolated CO but is the CO-heme complex, where the CO ligand forms a
9 strong $d-\pi^*$ back bonding interaction with the iron atom. Since the heme pocket contains not
10 only water but also various residues such as arginine and histidine, DFT calculations were
11 performed on various heme-CO complexes to determine the solvatochromic charge parameters
12 l_a in Eq. (94). As can be seen in Figure 17, the VSM model for predicting the CO stretch
13 frequency shift is suitable for reproducing the DFT calculation results. Using the MD
14 simulation and the multivariate equation with Eq. (94), the numerically simulated IR spectra
15 of the two mutants are shown to be consistent with those of the experiments (Figure 18). The
16 relative decrease in the A_3 peak intensity in the double mutant could be attributed to the
17 rotational restriction of the imidazole ring and an increase in the H-bonding interaction of the
18 CO ligand with the N_ϵ -H of imidazole.

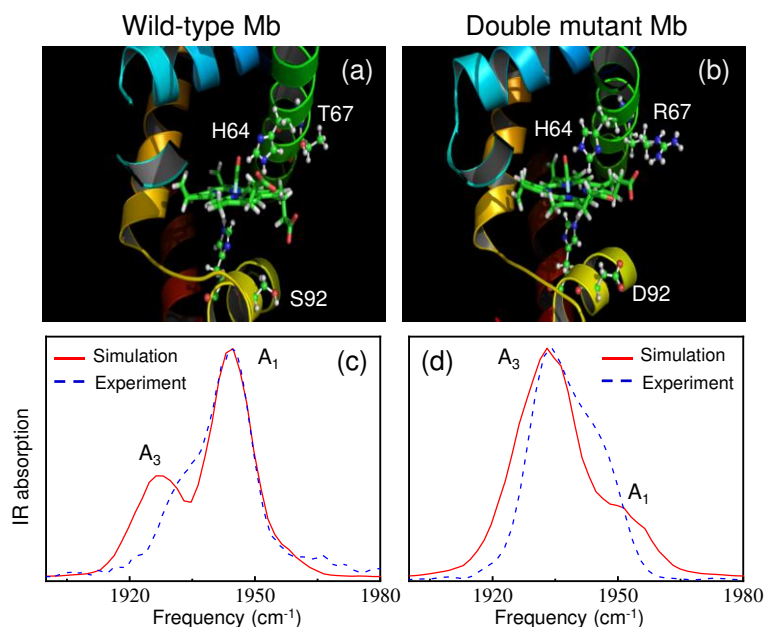
19 By calculating the nonlinear response functions directly, Choi et al. obtain numerically
20 simulated 2D IR spectra of the double mutant T67R/S92D, which appear to be significantly
21 different from that of the wild-type MbCO.

22 In addition to CO, nitric oxide (NO) and the cyanide anion (CN^-) also work as ligands
23 to the heme and are sensitive to the electrostatic environment around them.^{179,361} Electrostatic
24 frequency maps that encompass both the dipolar solvation cases and the hydrogen-bonding
25 cases (with rather uniform and significantly non-uniform electric field environment,
26 respectively) have been developed for the heme (Fe^{II})...CO, heme (Fe^{II})... CN^- , and heme
27 (Fe^{III})... CN^- complexes, which have been shown to demonstrate rather linear dependence of the
28 stretching frequency to the electric field.^{238,362}

29



1
 2 **Figure 17.** The heme-CO complex, a distributed solvatochromic charge model of the top panel, is
 3 shown along with model compounds such as neutral histidine, positively charged histidine protonated
 4 at the atom of N ϵ or N δ , positively charged arginine and water molecules. In the bottom panel, the
 5 frequency shift of the CO stretch mode theoretically obtained from the Eq. (109) is compared with the
 6 DFT calculation result. Reproduced from Figures 1 and 2 of Ref.³⁶⁰. Copyright 2013 The American
 7 Chemical Society.
 8



9
 10 **Figure 18.** (a) Protein structures obtained from MD simulation of native MbCO in (a) and the double
 11 mutant MbCO in (b). The double mutant has two substituted residues of Arg67 (R67) and Asp92 (D92)
 12 instead of Thr67 (T67) and Ser92 (S92) in the wild type. The numerically calculated IR spectra of the
 13 CO stretch mode (solid red line) of native MbCO in (c) and the double mutant in (d) are displayed with

1 the experimental results (blue dashed line). Reproduced from Figures 4 and 9 of Ref.³⁶⁰. Copyright 2013
2 The American Chemical Society.

4 **4.11. Ester carbonyl stretch**

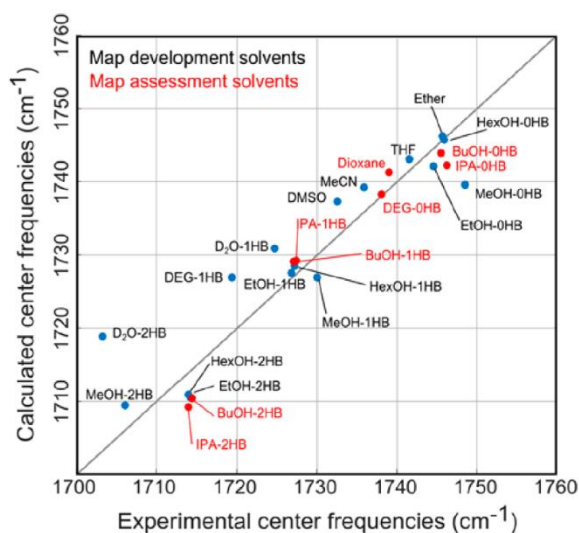
5 Ester carbonyls are intrinsic probes of biological membranes and are also common features in
6 industrial biofuels and surfactants. In lipid membranes, ester carbonyls are positioned precisely
7 at the ~1 nm interface between hydrophobic and hydrophilic regions, making them ideal
8 reporters of interfacial hydration, heterogeneity, and water penetration into the lipid
9 bilayer.^{363,364} The spectral properties of ester carbonyls are similar to the amide I vibrations in
10 amino acids; however, vibrational maps of these modes have only been developed recently.

11 Ester carbonyls are especially useful reporters of hydrogen-bonding in protic solvents
12 such as aqueous solutions. The ester C=O frequency exhibits an approximate red-shift of 15
13 cm^{-1} per hydrogen bond, similar to amides.³⁶⁵ Gai and coworkers measured the center
14 frequencies of methyl acetate and methyl propionate in different solvents and found a simple
15 Stark shift with a tuning rate of $1.3 \text{ cm}^{-1}/(\text{MV}/\text{cm})$.⁵¹ Building on this work, Baiz and coworkers
16 developed an electric-field map that semi-quantitatively reproduces the absorption lineshapes
17 of ethyl acetate in eight different solvents spanning a wide polarity range.³⁶⁶ This electrostatic
18 map consists of six electric field parameters computed at the positions of the three atoms that
19 compose the ester group, O-C=O.

20 The parameters were directly optimized against the experiment by minimizing the
21 differences between calculated and measured absorption spectra in eight common solvents.
22 Combining the Baiz frequency map and MD simulations, Yu and Shi have simulated the IR
23 absorption spectra of [6,6]-phenyl-C₆₁-butyric acid methyl ester, an organic semiconducting
24 material widely used in photovoltaic devices, in a set of organic solvents and revealed how its
25 solvatochromic shifts arise from specific interactions between the ester carbonyl group and the
26 solvent molecules.³⁶⁷ More recently, Wang and coworkers have applied this combined
27 approach to study the structure, dynamics, and IR spectra of omega-3 fatty acids that are widely
28 used in dietary supplements. These calculations elucidate the packing and dynamical
29 fluctuations of these polyunsaturated fatty acids in the liquid phase and uncover how the
30 conformations and intermolecular interactions of these molecules result in distinct IR spectral
31 features of their ethyl esters and triglycerides.³⁶⁸

32 Despite the success of the Baiz frequency map, one outstanding challenge is that its
33 parameterization against the experiment relies on the MD simulations sampling the correct H-
34 bond ensemble populations; as such, force fields are usually modified to produce accurate H-
35 bond populations prior to parameterizing the maps. Alternatively, when peaks are well-
36 separated, individual H-bond populations can be treated independently in the simulation and
37 experiment. Figure 19 shows the performance of the map in which the average frequencies of
38 individual H-bond populations in protic solvents are plotted.

1



2

3 **Figure 19.** Comparison between computed and experimental CO center frequencies and line widths in
 4 all solvents. Solvents used to parametrize the map are indicated in blue, and solvents used to evaluate
 5 the map performance are shown in red. The solvents are labeled Ether = diethyl ether, THF =
 6 tetrahydrofuran, MeCN = acetonitrile, HexOH = hexanol, EtOH = ethanol, MeOH = methanol, BuOH =
 7 butanol, IPA = isopropanol, and DEG = diethylene glycol. Reproduced from Figure 7 of Ref.³⁶⁶.
 8 Copyright 2016 The American Chemical Society.

9

10 To overcome this problem, Zhuang and coworkers have parameterized an *ab initio*
 11 map for methyl acetate.³⁶⁹ This map contains 20 parameters, which include electrostatic
 12 potential, electric fields and gradients at the C, and terminal and bridging O sites. Together
 13 these models have become useful in mapping the frequency-frequency correlation functions of
 14 carbonyls in interfacial environments, producing frequency fluctuation correlation functions
 15 that are in a near-quantitative agreement with experiments.³⁷⁰

16 Using 2D IR spectroscopy, Chutonov and coworkers recently observed H-bond-
 17 dependent Fermi resonances induced by intermolecular interactions.³⁷¹ These effects are most
 18 prevalent in small molecules, such as methyl acetate, but are lifted in larger molecules. Thus,
 19 future parameterizations must account for potential Fermi resonances to more accurately
 20 predict the H-bond populations of ester carbonyls in protic solvents.

21

22 4.12. Carbonate carbonyl stretch

23 Carbonyl stretch mode in amide, ester, and ketone compounds has a very large transition dipole
 24 moment, and its frequency appears to be highly sensitive to local H-bonding interaction with
 25 H-bond donating solvent molecules in solutions or neighboring peptide residues in proteins.
 26 Therefore, modeling the C=O stretch frequency maps has been an important research subject
 27 in the field. Recently, the C=O stretch mode of carbonate attracted a great deal of attention
 28 because a variety of carbonate molecules have been used in the electrolytes of lithium-ion
 29 batteries (LIB) that are commercially available and used extensively in portable electronic

1 devices, electric cars, and mobile vehicles. However, still, the relationship between
2 microscopic solvent dynamics and macroscopic ion conductivity in carbonate electrolytes with
3 a high concentration of lithium-ion has not been elucidated yet.

4 Improving the performance of LIB requires understanding the lithium-ion mobility
5 mechanism in mixed carbonate solutions.³⁷² Linear and cyclic carbonates are usually used as a
6 mixture for the electrolyte in LIB, and they are assumed to have different roles. More
7 specifically, cyclic carbonates such as propylene carbonate (PC) and ethylene carbonate (EC)
8 have larger dipole moments and more polar than linear carbonates. Therefore, those cyclic
9 carbonates have been used as the principal solvent dissolving and solvating lithium ions and
10 they tend to hinder any formation of ion pairs between lithium cation and counter anions. In
11 contrast, the linear carbonates like diethyl carbonate (DEC) and dimethyl carbonate (DMC) act
12 as a medium facilitating the transport of ion-solvent complexes, e.g., lithium-ion solvated by
13 mainly cyclic carbonates. This hypothesis about the different roles of the cyclic and linear
14 carbonates has been considered to be reasonable because of the differences in their polarities
15 and viscosities. However, recent linear and 2D IR experiments of the carbonyl stretch mode of
16 carbonates in LiPF₆/carbonate solutions revealed interesting structure and dynamics of lithium
17 ion-solvent complexation in linear and cyclic carbonate solvents.^{101,373-377} To extract
18 quantitative information about the solvation structure and chemical exchange dynamics from
19 the experimental results, it is necessary to numerically simulate the steady-state and time-
20 resolved IR spectra using the vibrational frequency map of the carbonate CO stretching mode
21 and carrying out numerical calculation of the vibrational Schrödinger equation.¹¹⁰ Liang et
22 al.³⁷⁵ employed the electric field vectors located at the carbonate group to estimate the time-
23 varying frequency and transition dipole moment, which were then used to simulate the carbonyl
24 stretch IR spectra and the time-resolved 2D IR spectra of various lithium salt/carbonate
25 solutions. They showed that the increasing cross-peak in the 2D IR spectra mainly originates
26 from the chemical exchange process between free carbonate and lithium-ion bound carbonate
27 molecules in the LiPF₆/carbonate solutions. Also, by examining the waiting-time dependent
28 2D IR spectra, the solvation dynamics associated with the formation and dissociation process
29 of the lithium-ion-carbonate³⁷⁸ complexes were found to be faster in cyclic carbonate solvent
30 compared to the linear carbonate solvent.³⁷⁵ This is an excellent example showing that the
31 marriage of vibrational frequency maps of critical IR probe modes and the state-of-the-art 2D
32 IR spectroscopic techniques is capable of providing unique piece of information about the
33 detailed ultrafast solvent dynamics as well as the specific roles of different carbonate molecules
34 in LIB electrolytes containing a mixture of both cyclic and linear carbonate solvents.

35 36 **4.13. Water OH and OD stretch modes: Frequency map, non-Condon effect, and** 37 **anharmonicity**

38
39 Spectroscopic maps have been considered essential tools for understanding the IR absorption
40 and 2D IR spectroscopy of liquid water. The first IR photon echo experiments on the OH stretch
41 vibration of HOD in D₂O were reported by Stenger et al.³⁷⁹⁻³⁸¹ and Yeremenko et al.³⁸²
42 Tokmakoff and coworkers reported the measurement of the spectral diffusion dynamics of the

1 OH stretch of dilute HOD in D₂O.¹⁰⁴ Soon thereafter, Fayer and coworkers reported the same
2 for dilute HOD in H₂O.^{383,384} The experimental and theoretical advantage of studying HOD in
3 D₂O is to isolate the OH stretch vibrational frequency of the HOD solute from the myriad of
4 OD stretches in surrounding D₂O solvent. Studies of HOD in H₂O isolate the OH stretch of
5 HOD. In their study of HOD in D₂O, Fecko et al. assumed that the shift of the OH stretch
6 vibrational frequency of HOD from its value in the gas-phase could be modeled as a linear
7 Stark effect, where the electric field along the OH bond of HOD was computed from a classical
8 MD simulation and the Stark tuning rate was calculated with first-order perturbation theory.¹⁰⁴
9 Similar perturbative approaches were utilized previously by Hynes and coworkers³⁸⁵ and by
10 Lawrence and Skinner.³⁸⁶ However, the formula employed by Fecko et al. to compute the OH
11 stretch vibrational frequencies of HOD was, in essence, a spectroscopic map that assumed a
12 causal relationship between the value of the electric field from the solvent and the vibrational
13 frequency. Calculations of the normalized frequency correlation function of the OH stretch of
14 HOD in D₂O were in good agreement with experiment with a long-time decay (600 fs) that
15 was about a factor of two faster than in the experiment. Later, the discrepancy between the
16 calculated long-time frequency fluctuation dynamics with the experiment was found to be
17 typical of nonpolarizable water models.^{387,388}

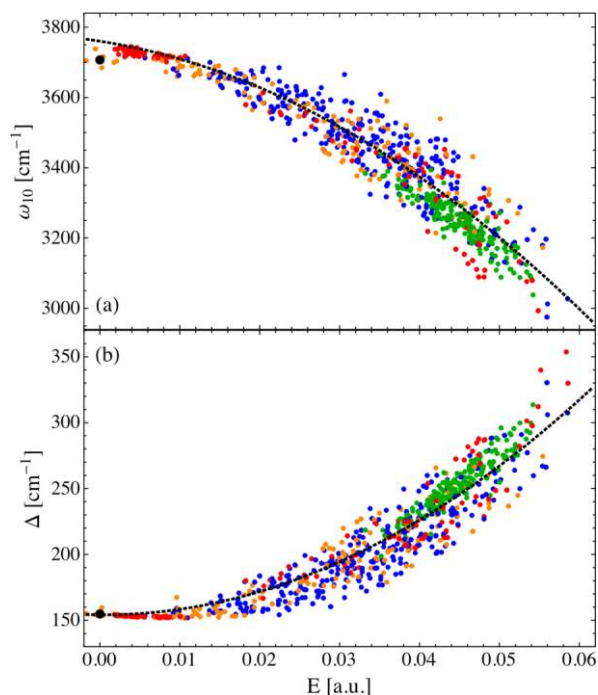
18 In 2004, Corcelli, Lawrence, and Skinner developed the first empirical DFT-based
19 spectroscopic map for the OH and OD vibrations of dilute HOD in water.⁶⁶ Their approach was
20 to harvest 100 statistically independent clusters from an MD simulation containing HOD with
21 4 – 9 water molecules. The OH or OD stretch vibrational frequency of interest was calculated
22 by first computing the one-dimensional potential energy curve moving only the H or D atom
23 along its OH or OD bond. The potential energy curve was then fit to a Morse oscillator whose
24 fully-anharmonic vibrational frequencies are known analytically. The 100 vibrational
25 frequencies were fit to a linear function of the electric field due to the solvent projected along
26 the OH or OD bond. The spectroscopic map developed by Skinner and coworkers did not
27 assume a causal relationship between the electric field and vibrational frequency. Instead, the
28 map exploited the electric field as a descriptor of the solvent environment that correlates with
29 the vibrational frequency of the OH or OD stretch of interest.

30 In later studies by Skinner and coworkers, the approach for developing spectroscopic
31 maps for the OH and OD vibrations of HOD was refined. Vibrational frequencies were
32 computed from the one-dimensional potential energy curves with the more efficient and
33 accurate Colbert-Miller discrete variable representation (DVR)³⁸⁹ method. Collecting more
34 snapshots from the MD simulations for DFT analysis showed that the vibrational frequencies
35 were better correlated to a quadratic function of the electric field.³⁹⁰ Alternate strategies for
36 constructing OH and OD frequency maps were developed by other groups. For example,
37 Mukamel and coworkers developed a map using electronic structure calculations of HOD in
38 uniform and spatially varying electric fields.^{130,227,391} The resulting map required the electric
39 field and its gradients from an MD simulation at the atomic sites of the HOD molecule. OH
40 and OD frequency maps have been applied to water in a variety of contexts, for example,
41 aqueous electrolyte solutions,³⁹² as a solute in ionic liquids,³⁹³ air-water interfaces,³⁹⁴⁻⁴⁰⁰ gas-
42 phase water clusters,^{401,402} near lipid bilayers,⁴⁰³⁻⁴⁰⁷ in reverse micelles,^{408,409} and ice.^{378,410-412}

1 The transferability of the maps is noteworthy. Figure 20 shows that the same spectroscopic
2 map can be used to describe the OH vibrational frequency and anharmonicity for HOD isolated
3 in the gas-phase, embedded in a water hexamer at 80 K, in liquid water, in ice I_h at 100 K, and
4 at the vacuum/water interface.⁴¹³ In 2019, Skinner and coworkers utilized a machine learning
5 approach, whereby a neural network is trained on DFT-computed vibrational frequencies, to
6 study the vibrational spectroscopy of HOD in water.⁴¹⁴

7 In 2005, Skinner and coworkers reported on the importance of non-Condon effects in
8 describing the vibrational spectroscopy of HOD in water.^{68,415} Non-Condon effects refer to the
9 dependence of the transition dipole moment of a vibration on its solvation environment. These
10 studies found that the transition dipole moment of the OH or OD vibration of HOD in water
11 can vary by a factor of five across its IR absorption band.⁴¹⁵ High frequency OH vibrations
12 were found to have small transition dipole moments, whereas lower frequency vibrations have
13 large transition dipole moments. Remarkably, the magnitude of the transition dipole moment
14 is linearly related to the electric field along the OH bond.^{390,415} Because the IR absorption
15 depends on the transition dipole moment squared, the non-Condon effects have profound
16 implications for the calculation of the IR absorption line shape. In contrast, the transition
17 polarizability, which is relevant for Raman spectroscopy, does not display significant non-
18 Condon effects. Corcelli and Skinner showed that the differences in non-Condon effects are
19 directly related to the differences in the IR and Raman spectra of HOD in water.⁴¹⁵ Schmidt, et
20 al. showed that the non-Condon effects play a significant role in the calculation and
21 interpretation of 2D IR spectra, which depend on the fourth power of the transition dipole
22 moment.⁶⁸

23 The spectroscopic maps for the OH and OD vibrations of HOD in water are a starting
24 point for understanding the vibrational spectroscopy of liquid water. The complication of
25 moving from HOD to pure water is that the nearly resonant OH vibrations can couple.⁴¹⁶⁻⁴¹⁸
26 Auer and Skinner developed maps for both the intra- and intermolecular coupling of OH
27 vibrations in water. These maps facilitated the theoretical study of the vibrational spectroscopy
28 of water.⁴¹⁹ They also formed a basis to study the SFG spectroscopy of the vacuum/water
29 interface of liquid water.^{395-398,400} Several groups have developed causal spectroscopic maps
30 for OH vibrational frequencies, transition moments, and couplings in liquid water. Utilizing
31 the work of Hush and Reimers on describing the vibrational Stark effect,¹⁷² in 2006, Torii
32 investigated the vibrational spectroscopy of water, including the role of coupling but without
33 incorporating non-Condon effects, although the paper did acknowledge that such effects might
34 be relevant.⁴²⁰ In 2013, Choi and Cho utilized a HMR approach to describe the frequencies,
35 transition dipole moments, and coupling constants of OH vibrations in water in terms of the
36 local environment and electrostatics.⁴²¹



1
2 **Figure 20.** Reproduced with permission from Figure 2 of Ref. ⁴¹³. (a) DFT calculations of the OH stretch
3 vibrational frequency, ω_{10} , of HOD in various environments, including (black) a gas-phase monomer,
4 (red) a water hexamer at 80 K, (blue) liquid water, (green) ice I_h at 100 K, and (orange) the water/vacuum
5 interface. The dashed line is a spectroscopic map in terms of the electric field, E , along the OH bond
6 evaluated at the site of the H atom. (b) Calculated anharmonicity, Δ , of the OH vibration. Copyright
7 2013 The American Chemical Society.
8

9 Isotopically diluted OH or OD stretch modes are vastly used as perfect sensors of the
10 local environment to study the dynamics of the H-bond network in aqueous systems including
11 liquid water, ice, and heterogeneous systems such as hydrated lipid multi-bilayers.⁴¹³ Due to
12 the fact that the OH (OD) stretch mode is highly anharmonic, the vibrational frequency maps
13 need to parameterize the changes of anharmonicity due to the molecular surroundings. The first
14 group of vibrational maps, developed by Skinner group, are effectively electrochromic and
15 choose only a single collective variable – electric field evaluated at the location of the water
16 hydrogen atom along the direction of the OH (OD) bond.^{378,400,404,410,411,419,422} For each
17 configuration of water molecules, the electric field is computed from the point charges utilized
18 in the molecular dynamics forcefield. The quadratic form of the fitting functional is usually
19 chosen according to

$$20 \quad x = A_x + B_x \frac{E_O}{D} + C_x \frac{E_O^2}{D} \quad (111)$$

21 where x can be the absorption frequency ω_{nm} , dipole moment derivative with respect to the
22 OH (OD) normal coordinate μ' , position matrix elements $x_{nm} \equiv m \left| \hat{Q} - Q_{OH/OD,eq} \right| n$ or
23 momentum matrix elements $p_{nm} \equiv m \left| \hat{P} - P_{OH/OD,eq} \right| n$. It was reported that the higher-order
24 polynomial functionals do not improve the performance of the vibrational maps for OH/OD
25 stretch mode. In most of the applications, only the fundamental and first excited state

1 absorption transitions are considered. To fit the parameters A_x , B_x and C_x , one can follow
 2 the standard procedure based on collecting anharmonic analysis results from small molecular
 3 clusters at the DFT level and performing the least-squares multivariate analysis. Another
 4 approach was used based on adjusting to the correct distribution of DFT frequencies, $p(\omega)$,
 5 given the distribution of electric fields $p(E)$ in the liquid-state simulation, i.e.,⁴¹⁰

$$6 \quad \int_{\omega(E)}^{\infty} p(\omega') d\omega' = \int_{-\infty}^E p(E') dE' \quad (112)$$

7 referred sometimes as the ‘cumulative vibrational mapping. For this, standard water forcefields
 8 such as SPC/E^{390,419} and TIP4P^{378,410} were used to run MD simulations and generate the
 9 ensemble of configurations and distributions of the electric field. Intramolecular coupling
 10 matrix elements were also parameterized according to the functional form,^{378,411}

$$11 \quad \omega_{jk}^{intra} = \left[a + b(E_{OH/OD,j} - E_{OH/OD,k}) \right] x_{01,j} x_{01,k} + c p_{01,j} p_{01,k} \quad (113)$$

12 where the j and k indices refer to the coupled vibrational chromophores and a , b and c are
 13 adjustable parameters.
 14

15 Another class of vibrational solvatochromism maps was developed by Tokmakoff and
 16 coworkers⁴²³ that is applicable for OH/OD stretches with much larger anharmonicity such as
 17 excess proton in hydronium cations. They initially maintained the electrochromic form of the
 18 map for the dipole moment derivatives (with the quadratic functional of the electric field) but
 19 used the solvation coordinate as a conjugate perturbation to describe the vibrational transition
 20 frequencies, i.e.,

$$21 \quad \omega_{mn} = A |\Delta E_{DFT}|^4 + B |\Delta E_{DFT}|^3 + C |\Delta E_{DFT}|^2 + D |\Delta E_{DFT}| + E, \quad (114)$$

22 where ΔE is defined as the difference in potential energy at appropriately selected two
 23 reference points along OH bond in question. They also found that correlating the dipole
 24 derivatives with the transition frequencies

$$25 \quad |\mu_{mn}| = a \omega_{mn}^3 + b \omega_{mn}^2 + c \omega_{mn} + d \quad (115)$$

26 results in better agreement with the benchmark DFT data, as compared to the electrochromic
 27 maps. To translate the DFT solvation energy onto the molecular mechanics level, the auxiliary
 28 mapping was established

$$29 \quad \Delta E_{DFT} = a' \Delta E_{EVB} + b', \quad (116)$$

30 where ΔE_{EVB} is the solvation energy from the multi-state empirical valence bond (MS-EVB)
 31 simulation,¹⁰⁵ computed as the difference between the EVB potential energy of solvated
 32 hydronium ion with OH bond length set to be 1.0 Å (equilibrium bond length in bulk water)
 33 and that with OH bond length set to be 1.4 Å (position of the second minimum of the double-
 34 well potential of $D_2O \cdots H \cdots OD_2$ complex). The benchmark data for parameterizing the maps
 35 were obtained from the database of the MS-EVB water clusters analyzed by using the
 36 B3LYP/6-311G++** method and concomitant anharmonic analysis yielding the reference
 37 transition frequencies and dipole moment derivatives up until the 4th vibrational excited state.

1 The simulated excess proton spectral response of OH stretch in bulk D₂O qualitatively captures
2 the experimental features for isotopically dilute excess protons. The model was also used to
3 decompose IR spectra into contributions from different aqueous proton configurations.

4 5 **4.14. Strongly correlated OH stretch modes: Local mode or collective mode**

6 Understanding the vibrational dynamics in bulk^{424,425} and confined water⁴²⁶⁻⁴²⁸ is a challenging
7 task. The OH-stretch vibrations within a water molecule are strongly coupled, leading to
8 symmetric and asymmetric stretch modes in the gas phase. The hydrogen bond distance in
9 water is so short that the coupling between OH-stretch vibrations on different water molecules
10 can be expected to be comparable to the intra-molecular coupling in size. A good way of
11 disentangling these effects is the study of isolated water molecules in hydrophilic solvents as
12 acetonitrile.^{120,429} Two-dimensional infrared experiments of this system reveal strong but
13 imperfect coupling of the intermolecular OH-stretches, which make the low-frequency
14 eigenstate a mixture between symmetric state and a state of the strongest H-bonded OH-stretch
15 vibration.¹²⁰ The eigenstates, thus, rapidly scramble within the individual water molecule. As
16 intermolecular couplings are included, the vibrational dynamics further speed-up one broad
17 spectral feature is formed, which contains states with continuously changing identity across the
18 line.^{69,430} Water confined in reverse micelles exhibit contributions from bulk-like water and
19 surface water where the latter behaves more like the isolated water in acetonitrile.^{408,409}

20 As water is frozen forming ice, the OH-stretch peaks get sharper, and distinct peaks
21 arise due to different vibrational symmetries imposed by the oxygen ordering in the I_h phase of
22 ice.⁴³¹ This behavior is well described with the mappings developed for bulk water.^{378,390,412,419}
23 The distinct peaks appearing in the hydrogen order ice II phase are also well described,¹²⁸ while
24 more complex high-density ices still pose a challenge.

25 The behavior of water near heterogeneous liquid interfaces is complex and different
26 from water in bulk and at less-complex air-water interfaces. To capture the sole effects of local
27 structures and dynamics on the water spectra for such complex interfaces, Skinner and
28 coworkers focused on investigating local mode vibrations of water using computational
29 spectroscopy.^{400,406,407} They considered a series of lipid- and surfactant-water interfaces with
30 different local interfacial curvatures and chemical structures. For example, their computed
31 vibrational sum-frequency generation (VSFG) spectra of water at flat cationic or anionic lipid
32 or surfactant interfaces showed the existence of water molecules that have OH chromophores
33 pointing away from the interface (indicated by negative peaks) or pointing towards the interface
34 (indicated by positive peaks) while forming hydrogen bonds with the lipid or surfactant
35 headgroups. Interestingly, the coexistence of these two types of interfacial water molecules is
36 observed near interfaces between water and mixtures of cationic and anionic lipids, as revealed
37 by the presence of both negative and positive VSFG peaks. In the case of zwitterionic lipid
38 interfaces, OH orientation is toward the interface on the average, resulting in positive VSFG
39 peaks.

40 The two-dimensional variants of VSFG, namely 2DSFG, enable characterization of
41 the dynamics of interfacial water at the flat interfaces. 2DSFG could distinguish the dynamics
42 of interfacial water as a function of the lipid charge and headgroup-water chemistry. It was

1 shown that the orientational relaxation of interfacial water is much slower compared to the bulk
2 water due to conformational constraints imposed by strong headgroup-water H-bonding and
3 electrostatics. Computation of H-bonding and rotational correlation functions revealed that the
4 separation of interfacial water from the bulk water in terms of water dynamics is possible,
5 which occurs about 7 Å away from the interface. Note that Tahara and coworkers performed a
6 series of VSFG and 2DSFG experiments on different lipid/surfactant-water interfaces; their
7 findings were in good agreement with this computational work.^{99,432-435}

8 In addition to studying flat interfaces, investigating the structure and dynamics of water
9 near concave and convex surfaces is necessary to complete the picture about the effects of
10 membrane surface geometry on the behavior of interfacial water molecules. Skinner and
11 coworkers investigated H-bonding dynamics of interfacial water within a normal (Type I)
12 lyotropic gyroid phase formed by a gemini dicarboxylate surfactant self-assembly using a
13 combination of 2D IR spectroscopy and MD simulations.⁴³⁶ This phase has convex surfactant
14 headgroup-water interfaces. It was found that the dynamics of water near the convex surfaces
15 is slower than bulk water dynamics. However, the dynamics of water near convex surfaces are
16 faster than those of water confined in a reverse spherical micelle of sulfonate surfactants that
17 form the concave surfactant headgroup-water interface, given that the water pool in the reverse
18 micelle and the water pore in the gyroid phase have roughly the same diameters. This difference
19 in confined water dynamics likely arises from the significantly reduced curvature-induced
20 frustration at the convex interfaces of the normal gyroid, as compared to the concave interfaces
21 of a reverse spherical micelle.⁴³⁶

22 23 **4.15. C-D stretch: Non-perturbative IR probe**

24 Like the nitrile and azido vibrations, carbon-deuterium vibrations have been explored for the
25 characterization of specific sites in proteins. The substitution of hydrogen for deuterium shifts
26 the vibrational frequencies to the transparent frequency window of the protein IR spectrum,
27 enabling single absorptions to be discerned apart from the spectral congestion arising from the
28 multitude of native protein vibrations. The advantage of C-D bonds is that they do not introduce
29 unnatural moieties into the protein and thus are virtually non-perturbative. In addition to
30 reporting on their surrounding environment, C-D vibrations enable probing the structure of the
31 protein itself. While less utilized than the nitrile or azido probes, a few research groups have
32 been applying C-D bonds for the study of proteins and peptides. C-D probes have provided
33 insight into protein folding, molecular recognition, and catalysis.⁴³⁷⁻⁴⁴³ However, their
34 widespread adoption likely has been hindered by their weak absorptions due to the small
35 transition dipole strengths. High (mM) protein concentrations are typically required, and
36 discerning the absorption bands requires careful matching of reference and sample transmission
37 spectra to achieve flat background absorbance. Nonetheless, some delicate protein regions,
38 such as surrounding redox centers, are likely to be perturbed by the introduction of the other
39 non-native transparent window probes. For such regions, C-D bonds may be the only probes
40 that can be introduced while preserving native function.

41 As their applications, efforts at the theoretical description of C-D probes are less
42 developed compared to nitriles and azido groups. However, DFT calculations of vibrational

1 frequencies have been reported for many C-D labeled amino acids, including glycine, alanine,
2 proline, methionine, lysine, and histidine.^{441,444-448} For backbone C α -D bonds and the γ -
3 methylene CD₂ of proline, the calculated frequencies show dependence on amino acid
4 conformation and therefore have been proposed as a way to measure local protein or peptide
5 structure. Many experimental studies have taken advantage of the sensitivity to learn about
6 protein or peptide conformational ensembles.^{441,443,448-451} An extensive QM/MM study reported
7 by Corcelli and coworkers has aimed to account for the absorption lineshape of C α -D backbone
8 deuterated *d*₁-alanine in aqueous solution; the power spectrum of the fluctuating electric dipole
9 moment was determined from PM3 calculations of snapshots along a classical MD
10 simulation.⁴⁵²

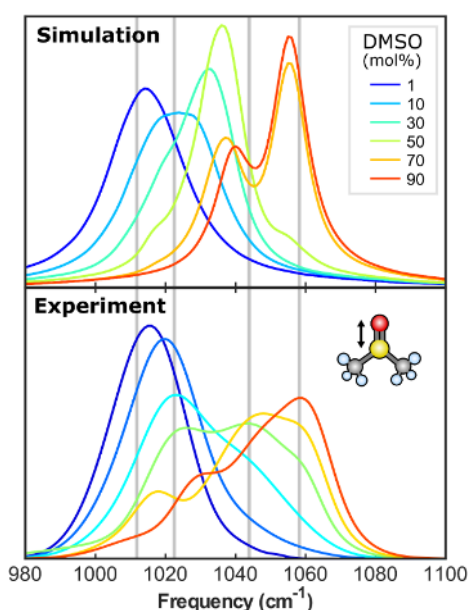
11 In addition to investigating backbone structure, C-D probes have been introduced at side
12 chains of amino acids to take advantage of their sensitivity to their local protein environment.
13 In many cases, C-D probes have been employed simply as qualitative reporters that a specific
14 residue of a protein contributes to a functional process, such as folding or recognition.^{450,453,454}
15 The influence of the local reaction field on C-D vibrations has been more quantitatively
16 considered for methyl-*d*₃-methionine by DFT calculations of the amino acid in the presence of
17 varying external field.⁴³⁹ However, in addition to the local field, H-bonding by water molecules
18 to the adjacent sulfur was found to impact the C-D frequency substantially. When installed
19 as a ligand to the copper center of plastocyanin, the C-D vibrations of methyl-*d*₃-methionine
20 were found by DFT calculations to be primarily sensitive to interaction of the sulfur orbitals
21 and charged metal. Specific water H-bonding likewise affects the vibrational frequencies of
22 C α -D bonds of alanine peptides.⁴⁵⁵ Thus, a theoretical description of C-D bonds, like the other
23 transparent window probes, must account for multiple contributions, including local potential
24 and specific local interactions with the environment. Future extension of the Bio-SolEFP
25 approach for C-D probes should assist in more rigorously understanding their spectroscopy to
26 fully exploit them for investigating the complex environments of proteins in the future.

27 28 **4.16. S=O stretch**

29 The sulfinyl (S=O) group is common in a wide range of compounds such as dimethyl sulfoxide
30 (DMSO), one of the most routinely used solvents in many areas of chemistry. In biology,
31 DMSO is commonly used as a cryopreservation agent. The S=O group interacts strongly with
32 water and prevents toxic ice-crystal growth in cells and tissues.⁴⁵⁶ The large dipole moment
33 and the polarizability of the S=O group are responsible for DMSO's amphiphilic behavior,
34 which produces abnormal bulk properties in aqueous mixtures.⁴⁵⁷

35 The S=O stretch is characterized by a strong solvatochromic shift, from 1071 cm⁻¹ in
36 non-polar solvents to approximately 1016 cm⁻¹ in water.⁴⁵⁸ Hydrogen-bonding environments
37 can be directly quantified from the IR absorption lineshapes. In water, a single H-bond induces
38 a red-shift of the S=O stretch frequency by approximately 20 cm⁻¹. The S=O stretch oscillator
39 strength is dependent on its substituents; for the case of DMSO in water, the transition dipole
40 moment is 0.14 D, approximately half that of the C=O stretch.^{458,459} Together, the strong
41 solvatochromism and relatively large oscillator strength make the S=O stretch an attractive IR
42 probe for nonlinear spectroscopy. However, ultrafast measurements on the S=O stretch remain
43 scarce due to the experimental challenges of operating in the fingerprint region.⁴⁶⁰

1 Torii and Noge used density functional theory (DFT) calculations to quantify the
2 dependence of the S=O stretch frequency on some structural parameters, i.e., the S=O bond
3 length, the O...H hydrogen-bond distance, and the S=O...H angle.²³⁹ Strong dependence of
4 the S=O stretch frequency on the S=O...H angle was obtained with larger red-shifts being
5 correlated with larger bent angles along rather isotopically around the S=O bond axis. These
6 frequency shifts were parameterized using a combination of electric fields at the S and O atoms
7 projected along the S=O bond axis, together with the electrostatic potentials at the S, O, and C
8 atoms. Building on the work by Torii, recently, Baiz and coworkers have parameterized a fully
9 empirical S=O stretch frequency map using the IR absorption spectra of DMSO in water as a
10 reference. The parameterization is able to semi-quantitatively reproduce the S=O lineshape
11 over a wide range of concentrations of the DMSO/water mixtures and has also been
12 benchmarked against experimental 2D IR spectra (Figure 21).⁴⁶¹



13
14 **Figure 21.** Experimental and computed IR absorption spectra of the S=O stretching mode at different
15 concentrations in binary DMSO/water mixtures. Computed spectra were obtained using the map of Oh
16 and Baiz. Vertical bars represent the average experimental frequencies of the four DMSO species
17 present in solution: singly hydrogen-bonded (1HB), doubly-hydrogen bonded (2HB), Aggregate (Agg),
18 and non-hydrogen bonded (Free) from low to high frequency respectively. Adapted from Figure 1 of
19 Ref.⁴⁶¹ Copyright 2019 AIP Publishing.

20

21 **4.17. Phosphate modes**

22 Phosphate groups are ubiquitous in biological molecules, including DNA, RNA, ADP, ATP,
23 *etc.* Phosphate group vibrations involving the PO₂⁻ moiety consist of a symmetric stretch
24 vibration at about 1100 cm⁻¹ and an antisymmetric stretch around 1250 cm⁻¹. Phosphate
25 vibrations have been extensively applied as a probe to understand enzymatic hydrolysis of ATP
26 and GTP using time-resolved IR spectroscopy.⁴⁶²⁻⁴⁶⁴ Phosphate vibrations have also revealed
27 insights about DNA hydration.⁴⁶⁵ The antisymmetric PO₂⁻ stretch exhibits a red frequency shift
28 with an increased relative humidity of DNA from about 0% to 92%, which is intimately related
29 to the local hydration environment around PO₂⁻.^{466,467} The symmetric stretch, however, exhibits
30 only a slight blue shift with increasing hydration.⁴⁶⁷ Because of the sensitivity to local hydration

1 environment, 2D IR spectroscopy has been used to study the spectral diffusion dynamics of
2 phosphate vibrations, showing a fast component (~0.3 ps) of local structural fluctuations
3 around the phosphate group, and a slow component (>10 ps) accounting for the persistence of
4 water-phosphate hydrogen bond.⁴⁶⁸

5 Levinson et al. utilized vibrational Stark spectroscopy on phospholipids to investigate
6 the electric field dependence of the phosphate stretch vibrations.⁴⁶⁷ Their experiments
7 demonstrated that the frequency shifts of the symmetric stretch and the asymmetric stretch
8 could be described as a linear Stark effect, with the Stark tuning rates of 0.54 ± 0.02 and 1.35
9 ± 0.02 $\text{cm}^{-1}/(\text{MV}/\text{cm})$, respectively.⁴⁶⁷ DFT calculations on dimethyl phosphate as a model
10 system shows that the Stark tuning rates result from the component of the electric field along
11 the C_2 axis of the PO_2^- group, while the electric field dependence along O–O axis is quadratic
12 and results in only modest frequency shifts. The DFT-based calculation thus established a
13 spectroscopic map for phosphate group vibrations.

14 Corcelli and co-workers applied this spectroscopic map of the asymmetric phosphate
15 stretch to the DNA hydration environment, showing that the frequency shift is not a monotonic
16 red-shift with increasing water solvation and distance from the phosphate group.⁴⁶⁹ The closest
17 four water molecules around the phosphate group induce a red frequency shift of -34.6 cm^{-1} to
18 the asymmetric phosphate stretch due to direct H-bond to the oxygen atoms of the PO_2^- group.
19 In contrast, the fifth and sixth water molecules induce a blue-shift of 9.0 cm^{-1} , which comes
20 from interacting with the oxygen atoms covalently linked to the PO_2^- . Frequency time
21 correlation functions showed a qualitative agreement with the experimental 2D IR result.⁴⁶⁸
22 This phosphate spectroscopic map shows an almost quantitative agreement to the experimental
23 frequency shift as a function of relative humidity, assuming that there is a residual water
24 molecule per phosphate group at 0 % relative humidity, which is also suggested
25 experimentally.^{465,470}

26 In recent papers by Elsaesser and coworkers,^{381,471,472} the interaction of phosphate
27 groups with alkali and alkaline earth ions in water has been studied by using the linear and
28 femtosecond 2D IR spectroscopy. The 2D IR spectra of the prototypical system dimethyl
29 phosphate in water with an excess concentration of Mg^{2+} display two distinct and uncoupled
30 vibrational bands due to phosphate groups with and without an Mg^{2+} ion in close contact, and
31 the band of the contact ion pairs exhibits a frequency blue-shift. Fingerhut et al. calculated the
32 fluctuating electric force exerted on the $(\text{PO}_2)^-$ moiety by the ab initio based effective fragment
33 potential approach to establish a linear relation for the solvent field-induced solvatochromic
34 shift.⁴⁷²

36 **4.18. Nucleic acid base modes**

37 The vibrational modes of DNA bases that absorb in the frequency range of $1400\text{-}1800$ cm^{-1} are
38 strongly IR-active and highly sensitive to DNA structures such as the base pairing and helical
39 geometries in the A, B, and Z forms. These vibrational marker bands are mainly composed of
40 the in-plane carbonyl stretch mode and the NH_2 or N-H bending modes of the bases, and have
41 been used to extract critical information on the H-bonding interactions between base pairs, as
42 well as the melting processes and structural transitions of DNA. For example, Polyanichko et

1 al. investigated the effect of the transition metal ion Mn^{2+} on the DNA structure by analyzing
2 the IR absorption and vibrational CD spectra of the marker bands and showed that the observed
3 B- to C-form conformational transition arisen due to the interaction of Mn^{2+} with the bases of
4 DNA.⁴⁷³ Furthermore, Krummel et al. carried out 2D IR spectroscopic measurement to
5 investigate the carbonyl stretch modes of the guanine and cytosine bases in dG_5dC_5 and $d(GC)_8$
6 double helices in D_2O . Combining 2D IR measurements and numerical simulations, they
7 showed that the base pairs that are held together by H-bonds are strongly coupled.⁴⁷⁴

8 In conjunction with the experimental spectroscopy measurements, theoretical spectral
9 simulations based upon vibrational normal mode analysis have provided crucial insights into
10 DNA structural properties and the vibrational properties of delocalized excitons in the bases.
11 Note that it is impractical to perform *ab initio* vibrational analysis of the nucleic acids because
12 they have large system sizes and complicated interactions with the solvent water molecules.
13 As a natural extension of the HMR method, which has been successfully applied to
14 polypeptides,^{277,475} the extended HMR method was developed to analyze the vibrational mode
15 characteristics of base pairs and to simulate the vibrational spectra of various DNA
16 oligomers.⁴⁷⁶⁻⁴⁷⁹ It was found that the vibrational coupling constants are strongly dependent on
17 H-bonding interactions between nucleobases. The IR spectra of a few different DNA model
18 systems in D_2O were simulated and compared with the experimentally measured spectra. These
19 calculations reveal that the hydration effects, which lead to solvatochromic frequency shifts of
20 the basis modes, are important for quantitative descriptions of the IR absorption spectra of
21 DNA molecules.^{476,477}

22 The 2D IR spectra of $dG_n:dC_n$ and $dA_n:dT_n$ double helices were simulated by using the
23 basis mode frequencies and vibrational coupling constants. The vibrational anharmonicities of
24 the basis modes were estimated with DFT calculation method, and the conformational
25 inhomogeneity and solvation dynamics were examined by analyzing classical MD
26 trajectories.^{478,479} The simulation results for the 2D IR spectra of double-helical DNAs
27 showed a weak correlation between the IR spectra and the number of base pairs, which is
28 consistent with the previous experimental observations. From quantum chemistry calculations
29 of A-, B-, and Z-form DNAs, the vibrational coupling constants were shown to be strongly
30 dependent on the DNA conformation. In particular, the coupling constants between base modes
31 in the Z-DNA are fairly small, causing localization of vibrational modes. In contrast, those in
32 A-DNA are large, leading to delocalized vibrational modes.

33 Among the base vibrational modes, the carbonyl stretch modes are particularly
34 sensitive to the H-bonding patterns and base stacking configurations in nucleic acids.^{94-97,474,480-}
35 ⁴⁸³ For example, pioneering 2D IR experiments focusing on the C=O vibrations have revealed
36 the inter- and intrastrand couplings in model A- and B-form DNA and elucidated the
37 dissociation pathway of DNA duplexes.^{94,96,97,474}

38 To facilitate the interpretation of the vibrational spectroscopy experiments, Jiang and
39 Wang have recently developed two vibrational frequency maps to describe the C=O stretch
40 mode in nucleobases and a C=C frequency map to account for the interactions between the
41 C=O and C=C vibrations in pyrimidine bases.⁴⁸⁴ These frequency maps are developed using
42 nucleoside 5'-monophosphates (NMPs) as model systems and take the form of

$$\omega_{map} = \omega_0 + \sum_{im} c_{im} E_{im} \quad (117)$$

In the C=O frequency map, i indexes C, O, and N atoms, and m represents the x, y and z directions as defined in Figure 22a. For the C=C frequency map, i indexes the C5 and C6 atoms in pyrimidine bases and the coordinate system is shown in Figure 22b. E_{im} is the electric field on atom i in direction m , which is exerted by all the solvent molecules and counterions around the solute molecules. The intercept ω_0 and the coefficients c_{im} are determined by minimizing the differences in vibrational frequencies as predicted from the maps and DFT calculations on 1200 NMP-water clusters.⁴⁸⁴

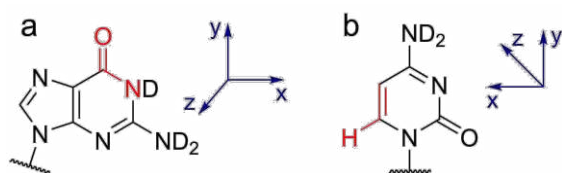
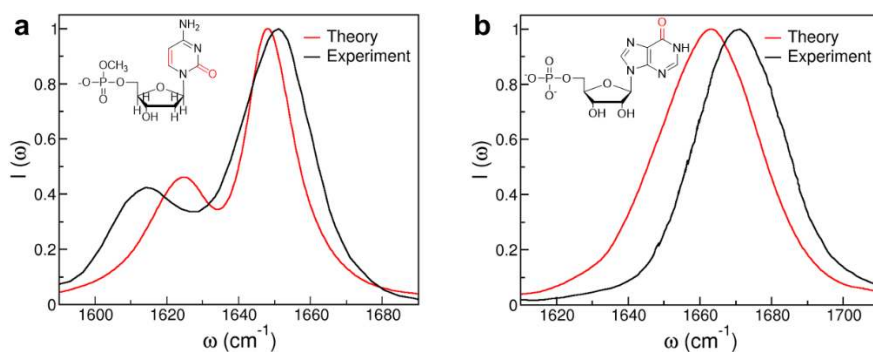


Figure 22. Coordinate systems of the (a) C=O and (b) C=C vibrational frequency maps. The atoms used to define the axes are shown in red.⁴⁸⁴ Reproduced from Figure 4 of Ref.⁴⁸⁴. Copyright 2019 The American Chemical Society.

The C=O and C=C frequency maps provide an efficient way to calculate the vibrational frequencies of nucleobases directly from MD simulations. Jiang and Wang have shown that one can combine the frequency maps with a mixed quantum/classical treatment of the line shape theory and capture the IR spectra of NMP in aqueous solutions.⁴⁸⁴ They have further demonstrated that the frequency maps are applicable to nucleobase derivatives and are transferrable in different solvents. For example, Figure 23a shows that the calculations correctly predict a two-peak feature in the IR spectrum of deoxycytidine 5'-monophosphate in D₂O, which comes from the coupled vibrations of the C=O and C=C group in the cytosine base. In contrast, the predicted IR spectrum of inosine 5'-monophosphate, a nucleobase derivative, contains a single peak at 1663 cm⁻¹. As shown in Figure 23b, the theoretical and experimental⁴⁸⁵ IR line shapes agree well with each other, and their peak positions differ by only 7 cm⁻¹.⁴⁸⁴ The C=O and C=C frequency maps can thus be readily applied to model the linear and 2D IR spectra of nucleic acids in the carbonyl stretch region and elucidate the molecular origin of the experimental spectra.



1 **Figure 23.** Theoretical and experimental^{6,11} IR spectra of (a) deoxycytidine 5'-monophosphate and (b)
2 inosine 5'-monophosphate in D₂O. The chemical structures of the molecules are shown in the insets
3 with their chromophores highlighted in red.⁴⁸⁴ Reproduced from Figure 7 and Figure 9 of Ref.⁴⁸⁴.
4 Copyright 2019 The American Chemical Society.
5

6 **4.19. Other vibrational frequency maps**

7

8 The alcohol OH-stretch mode was treated quite successfully^{486,487}, assuming that the frequency
9 and dipole fluctuations are similar to those found in water and that the water map³⁹⁰ is a good
10 approximation apart from an overall frequency shift. A mapping was developed for the OD-
11 stretch of methanol in carbon tetrachloride^{488,489} using the electric field on deuterium, DFT
12 frequencies, and a polarizable MD approach.
13

14 **4.19.1. Alcohols**

15 Semiempirical maps for the OH and OD stretching vibrations in alcohols were developed
16 primarily in the electrochromic formulation with the electric field as a conjugate vibrational
17 perturbation. In the map proposed by Mosele and Thompson,⁴⁹⁰ the relevant spectroscopic
18 quantities are expressed in terms of the electric field exerted on the OH (or OD) group hydrogen
19 atom by the surrounding neat liquid. Due to the substantial anharmonicity of the OH (OD)
20 stretch vibration, anharmonic constants as well as the vibrationally excited state absorption
21 frequency were parameterized with the functional form identical to the one in Eq. (109).
22 Benchmark data were obtained by using the discrete variable representation (DVR) method for
23 one-dimensional vibrational potential energy curves along OH (OD) stretch normal coordinate,
24 obtained at the B3LYP/6-311++G** level of DFT approximation. It was found, by examining
25 methanol, ethanol, *n*-propanol, and *n*-butanol, that the derived map is transferable and quite
26 independent of the alkyl groups. IR Absorption spectra and reorientation time calculated for
27 the isotopically diluted deuterated alcohols agreed well with experiment (FTIR and NMR data,
28 respectively), in contrast to the 2D-IR photo echo spectra, in which the time scales of the
29 spectral diffusion were overestimated.
30

31 **4.19.2. Water bending mode**

32 In addition to the water OH or OD stretch modes, the other water vibrational mode whose
33 frequency is also sensitive to local H-bonding environment is the HOH bending vibration.<sup>491-
34 504</sup> Vibrational spectroscopy of the water bending mode has also been performed to establish
35 the relationship between the lineshape of water bend and the H-bonding network structure of
36 water in solution.⁴⁹²⁻⁵⁰¹ Ni and Skinner, using a hybrid quantum/classical MD simulation
37 method, calculated the theoretical IR and sum-frequency generation spectra of the HOH bend
38 in liquid water as well as at the water liquid/vapor interface. They carried out classical MD
39 simulation and took into consideration the three-body interactions to describe the air-water
40 interface. Ni and Skinner developed the maps for water bend transition frequency, dipole,

1 polarizability, and intermolecular coupling. The good agreement between their calculated IR
2 and SFG spectra and the experimental measurements indicate the validity of their vibrational
3 spectroscopic maps.

4 5 **4.19.3. Mapping of strongly coupled vibrations**

6 As has been discussed in detail above, vibrational frequency mapping approaches work best
7 for localized modes that have relatively weak coupling to both the environments and to other
8 local modes. In addition to water (both H₂O and D₂O), there are useful vibrational transitions
9 where the spectroscopic modes are delocalized over many atoms, such as phosphate (—
10 OPO₂O—) and carboxylate (—COO⁻) organic species, as well as numerous organometallic
11 complexes containing transition metal carbonyls, cyanides, and nitrosyls. Mapping approaches
12 for these systems are much less advanced and need developments. A key step in that direction
13 has been the detailed decomposition of the delocalized anharmonic modes into local modes,
14 which are more physically amenable to electrostatic mapping procedures. Baiz et al.,⁵⁰⁵
15 computed anharmonic vibrational modes of two transition metal complexes,
16 rhodium(acetylacetonato)dicarbonyl (RDC) and dimanganese decacarbonyl (DMDC). These
17 anharmonic modes were recast in a basis of local modes described as Morse oscillators, with
18 only bilinear coupling among these local modes. The advantage of this method is that the
19 vibrational anharmonicity for the coupled states is obtained automatically. Explicitly including
20 the effects of H-bonding by treating clusters containing methanol, it was possible to deduce
21 that the H-bonding effects are additive, though their impact is delocalized within the coupled
22 modes. These kinds of considerations will be important not only for solvation probes but also
23 for using MD simulations to help interpret reactive motions that induce spectral diffusion,^{506,507}
24 as well as to establish links between environmental factors and intramolecular vibrational
25 energy redistribution,^{507,508} and coherence transfer dynamics.⁵⁰⁹⁻⁵¹¹ The extension of frequency
26 mapping to strongly coupled vibrations will enable a more broad adoption of these methods to
27 widely used chemical probes such as methyl groups and aromatic rings.

28

5. Repository, Perspective, and a few Concluding Remarks

5.1. Vibrational frequency map repository

Because of the rapidly growing number of vibrational frequency maps reported in the literature, it is desirable and useful to collect all those maps and make them available to everyone interested in utilizing them for their researches. Therefore, we have created a repository internet site, <http://frequencymap.org/>, for voluntary deposition of vibrational frequency map files by the developers themselves and for downloading of those files by the users. In addition to free deposition and downloading of vibrational frequency map files, this site can be considered as an internet forum for discussing and updating recent developments and news in this research field. Any map file that is to be uploaded should contain information on the vibrational mode, such as CO stretch or HOH bending, in addition to the parameters constituting the map. Users have free access to those deposited files.

5.2. Format of the deposited map file

Various research groups developing vibrational frequency maps tend to use their style of data files. To make the repository site useful among the researchers in this field, however, it is necessary to have a common standard format for all the deposited files. In addition to vibrational frequencies, some maps have also been developed for other vibrational properties, such as vibrational transition dipoles and polarizabilities, or coupling between two neighboring local vibrations. Therefore, each map file should essentially contain the following three elements: (i) the identity of the molecule, the vibrational mode, and its property, e.g., frequency shift, for which the map is developed, (ii) the structural information on the molecule concerned and the interaction sites (the number of those sites and their locations) at which perturbations should be calculated, and (iii) the parameter values for mapping those perturbations to the properties. Each map file is a plain text file with the extension '.vbm' denoting a 'vibration map'. It consists of sections whose titles start with the '%' character. The details of the format defined for each of the three elements of the vbm file are explained in Supporting Information.

5.3. New approaches based on genetic algorithm, neural network, and machine learning

In recent publications in the field of chemistry, we observe an increasing number of reports employing machine learning approaches in calculating energy and other physicochemical properties of molecular systems. The total number of possible small organic molecules that populate 'chemical space' has been estimated to exceed 10^{60} .⁵¹² To find or design molecules or materials having desired quantum mechanical properties, machine learning approaches have been actively employed to avoid computationally demanding methods of electronic structure calculations. Recently, Faber et al.⁵¹³ assessed performances of various machine learning methods such as Bayesian ridge regression, elastic net regularization,⁵¹⁴ kernel ridge regression,⁵¹⁵ graph convolution,⁵¹⁶ and gated graph neural networks⁵¹⁷ in modeling electronic ground-state properties of organic molecules such as free

1 energies and enthalpies of atomization, HOMO/LUMO gap, dipole moment, static
2 polarizability, zero-point vibrational energy, heat capacity, and highest fundamental vibrational
3 frequency. Their work shows numerical evidence that, even though there is no single machine
4 learning model that works superbly for all the considered cases, the best machine learning
5 model for each considered property reaches the accuracy of density functional theory at the
6 B3LYP level.

7 Another active area in which machine learning methodology has been receiving
8 considerable attention is the computational study using MD simulation methods. Classical MD
9 uses MM force fields to calculate the energies and forces for a large number of atomic
10 configurations, but the results of the MD simulations depend greatly on the accuracy of the
11 molecular potentials and their parameters. Employing electronic structure calculations in *ab*
12 *initio* MD simulation can remove the force field dependence of the simulation results, but
13 considerably reduce the size and time of the simulation. Machine learning models of potential
14 energy surface of molecular or solid-state systems can achieve the accuracy of the electronic
15 structure method with the efficiency of the classical force fields MD. The conventional force
16 fields in MD simulations have limitations in treating reactive events of breaking and forming
17 of chemical bonds due to the fixed functional forms employed in the MM force fields. Even
18 for the cases of simulating nonreactive dynamics, the classical force fields having the potential
19 energy functions constructed under various physical approximations have difficulties in
20 treating the polarization and charge transfer effects. Machine learning methods make it possible
21 to construct potential energy surfaces that are not restricted by any functional form based on
22 physical approximations and can describe polarization, charge transfer, and reactive processes
23 with accuracy approaching that of electronic structure calculations.

24 Highly reliable potential energy surfaces are also an essential prerequisite for obtaining
25 accurate values of vibrational frequency shifts. Methods using vibrational frequency map to
26 calculate the frequency shifts assume a specific functional form to relate the geometrical
27 configurations of the solute-solvent system to the vibrational frequency shifts. The parameters
28 in functions of fixed form are obtained by fitting to electronic structure calculations or
29 experimental spectra. Although the information of the multidimensional potential energy
30 surfaces can be incorporated in the process of constructing the frequency maps by the fitting
31 procedure, these maps are limited by the assumptions on the dominating factors among various
32 types of interatomic interactions. Machine learning approaches can provide the possibility of
33 constructing mappings from geometry to vibrational frequency shifts incorporating the
34 information of the potential energy surfaces without the limit of preassigned functional
35 dependences.

36 In this regard, it is pertinent, as the first step toward machine learning schemes for
37 vibrational frequency shifts, to try to develop a model of vibrational frequency shifts, which is
38 not constrained by any preliminary set of assumptions about the physical nature of the factors
39 inducing the frequency shifts. Recently, Kwac and Cho showed that a differential evolution
40 algorithm approach, which is one of the genetic algorithms for global optimization, is useful
41 for describing vibrational solvatochromism.⁵¹⁸ In their model, the solvation-induced
42 vibrational frequency shifts are expressed as a polynomial function expanded by the inverse
43 power of interatomic distances.

$$\Delta\omega = \sum_{n=1}^M \sum_A \sum_B a_n^{A,B} \sum_{i=1}^W \left(\frac{1}{r_{AB_i}} \right)^n, \quad (118)$$

where A and B denote the interaction sites of the solute and solvent molecules, respectively. M is the order of the polynomial, W is the number of solvent molecules for each configuration of the solute-solvent clusters. We obtain the coefficients $a_n^{A,B}$ using the frequency shifts calculated by quantum chemistry methods for a set of clusters of a solute molecule surrounded by solvent molecules, where the set of clusters can be considered as a training data set. The crucial step in this model is to represent the frequency shift $\Delta\omega$ by a sum of the contribution $\Delta\omega_n$ which is due to the $1/r^n$ interaction term only so that

$$\Delta\omega = \sum_{n=1}^M \Delta\omega_n. \quad (119)$$

$$\Delta\omega_n = c_n \Delta\omega \quad (n = 1, \dots, M), \quad (120)$$

where $0 \leq c_n \leq 1$ and $\sum_{n=1}^M c_n = 1$. Then for a given set of values $\{c_1, \dots, c_M\}$, we solve the following M equations for $\Delta\omega_n$ by singular value decomposition

$$\Delta\omega_n = \sum_A \sum_B a_n^{A,B} \sum_{i=1}^W \left(\frac{1}{r_{AB_i}} \right)^n \quad (n = 1, \dots, M). \quad (121)$$

We use thus obtained coefficients $a_n^{A,B}$ to calculate the root mean square error (RMSE) defined as

$$d_{RMSE} = \frac{1}{S} \sqrt{\sum_{k=1}^S [\Delta\omega^{predict}(k) - \Delta\omega^{QM}(k)]^2}, \quad (122)$$

where S is the number of configurations. $\Delta\omega^{predict}(k)$ is the frequency shift calculated by Eq. (118) for the k th configuration. $\Delta\omega^{QM}(k)$ is the frequency shift calculated by quantum chemistry calculation methods. The whole process from the selection of $\{c_1, \dots, c_M\}$ to the calculation of d_{RMSE} in Eq. (121) can be regarded as a function H whose input is $\{c_1, \dots, c_M\}$ and the output is d_{RMSE} such that

$$d_{RMSE} = H(c_1, \dots, c_M). \quad (123)$$

This procedure is schematically shown in Figure 24.

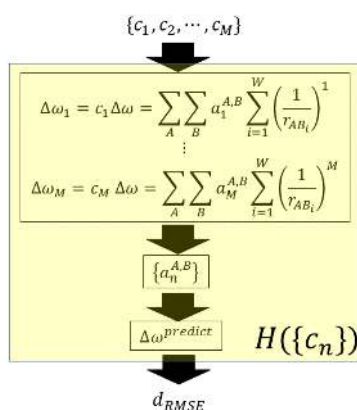


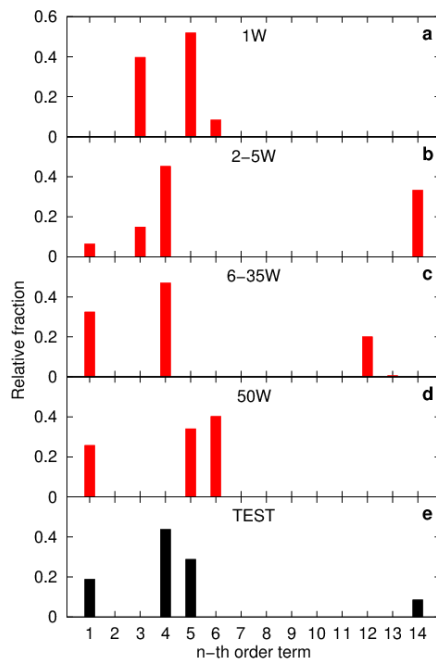
Figure 24. Schematic diagram of the procedure from the relative contributions c_n to the RMSE value, d_{RMSE} .

We employ a differential evolution algorithm (DEA)^{519,520} to optimize the function H with respect to $\{c_1, \dots, c_M\}$, thereby we obtain the coefficients $a_n^{A,B}$ that minimize the value of d_{RMSE} . Differential evolution algorithm is one of the genetic algorithms that have been developed to solve optimization problems by employing an evolutionary mechanism in biology. In the differential evolution approach, one generation evolves into the next generation by mutation, crossover, and survival of the fittest. This evolutionary mechanism tries to find the optimum partitioning of the contributing terms in the model to reproduce as closely as possible the vibrational frequency shifts of the configurations in the training set that plays a role much like an environment inducing evolutionary development in biology. This differential evolution algorithm has been applied to the vibrational frequency shifts of the amide I and II modes of NMA in water and the CN stretch mode of MeCN in water using a 14-order polynomial ($M = 14$) and considering about five hundred configurations of the solute-solvent system as a training set. The results of optimization with the differential evolution algorithm are such that only a few selected orders of terms dominate the contribution to the frequency shifts and the remaining terms are virtually zero. The dominating orders of the terms in the polynomial are different depending on the vibration mode of interest. The dominating orders of the terms are also susceptible to the size of the configurations used in the training set, as shown in Figure 25 where ‘1W’, ‘2-5W’, ‘6-35W’, and ‘50W’ denote the configurations having one water, 2-5 water molecules, 6-35 water molecules and 50 water molecules, respectively. The fifth panel in Figure 25 shows the relative contributions $\{c_n\}$ when all the four types of configurations are used in the training set. Since the genetic algorithm employed in this work is not based on any physical assumption, we could not interpret each nominating terms as originating from a specific type of physical interaction. However, regardless of the sensitive change according to the type of the training set, a general trend is observed that only two to four selected orders are the dominating ones, and these dominating orders are distributed so that usually one order occurs in each of low range, middle range, and high range orders in all cases of vibration mode considered in this work.

The observation that only a few orders of the terms in the polynomial model dominate

1 the contribution to the frequency shift while the other terms with different orders are nearly
 2 zero can be understood from the viewpoint of the complexity of the model. Having a larger
 3 number of parameters in a model is equivalent to having a more complex model. The
 4 complexity resulting from the differential evolution algorithm corresponds to the four
 5 dominating orders terms in the polynomial in the case of the amide I mode of NMA in water,
 6 which is very similar in complexity to the result obtained by a rigorous first-principles
 7 theory.¹⁵⁴ In the previous studies on the vibrational frequency shifts based on various physical
 8 assumptions, the complexity of the model was prefixed by assuming that specific types of
 9 interactions such as electrostatic, dispersion, or repulsion are the origins of the vibrational
 10 frequency shift. In the paper by Kwac and Cho who applied the DEA to the development of
 11 vibrational solvatochromism theory, both the complexity of the model and the parameters
 12 therein are optimized simultaneously, and this is one of the most significant differences from
 13 the previous studies that are strictly based on various prefixed physical approximations. We
 14 anticipate that this work can be a first step toward further developing different genetic
 15 algorithms and machine learning schemes for applying to vibrational spectroscopic studies.

16



17 **Figure 25.** (a-d) Magnitude of relative contributions c_i when we use as a training set (a) 1W, (b) 2-
 18 5W, (c) 6-35W, and (d) 50W set. (e) Relative contributions c_i for the training set of the study in Ref.⁵¹⁸
 19 Reproduced from Figure 10 of Ref.⁵¹⁸. Copyright 2019 AIP Publishing.

20

21 In a recent paper by Kananenka et al.,⁴¹⁴ an attempt to go beyond the spectroscopic maps
 22 in modeling spectroscopic properties of a vibrational mode was made by adapting machine
 23 learning methodologies called the Gaussian process regression⁵²¹ and Δ -machine learning.⁵²²
 24 In their approach, a property $P[\{Q\}]$ of a vibrational mode, such as the vibrational frequency
 25 or transition dipole, dependent of the local chemical environment Q , is provided by

$$P[\{Q\}] = P_b[\{Q\}] + M[\{Q\}], \quad (124)$$

where $P_b[\{Q\}]$ is the baseline estimate of $P[\{Q\}]$ provided the already established vibrational frequency maps, and $M[\{Q\}]$ is a correction modeled using an ML method. Specifically, in their work, OH-stretch frequencies and transition dipoles of water were considered by describing the local chemical environment Q using the atom-centered symmetry functions.^{523,524} They prepared a data set consisting of 40000 configurations of water molecules and corresponding OH stretch frequencies and transition dipoles obtained by DFT calculations on the grids of varied OH bond lengths. The production of this large-sized data set was possible because they reduced the number of necessary grid points for DFT calculation by interpolating the potential energy surface using the method of Gaussian process regression. The correction term $M[\{Q\}]$ in Eq. (124) is estimated by training the feed-forward artificial neural network (ANN) with one hidden layer containing 100 nodes. The results are summarized in Figure 26. The resulting root mean square errors in transition frequency of the OH-stretch local mode is improved from 63.4 cm^{-1} of the spectroscopic maps to about 35 cm^{-1} by employing the Δ -machine learning approach. The RMSE of 0.0730 a.u. of the dipole derivative of the OH-stretch mode by the spectroscopic maps is reduced to as low as 0.0283 a.u. by the Δ -machine learning approach. We anticipate that the genetic algorithm and machine learning approaches will be useful for developing novel computational methods to calculate various vibrational spectroscopic properties.

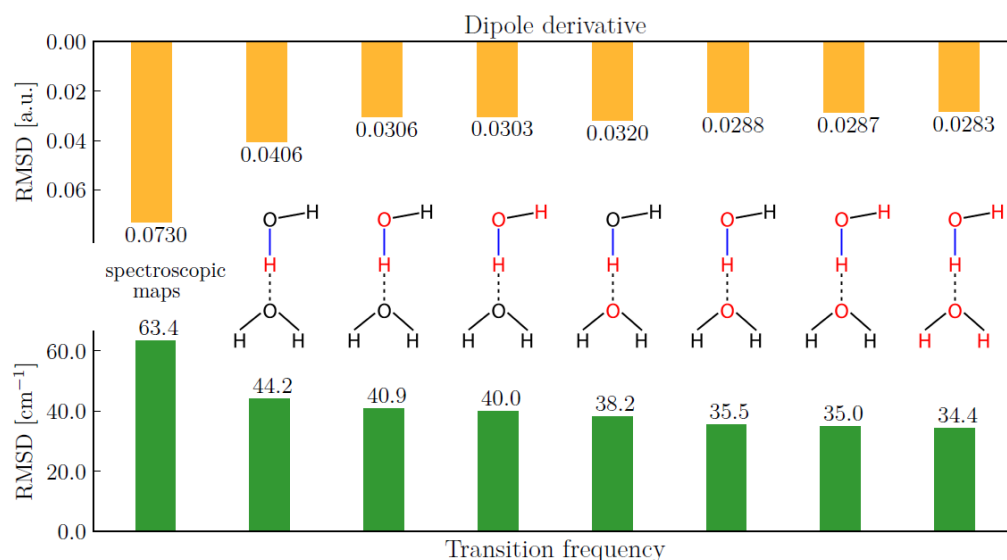


Figure 26. RMSE in transition frequency and dipole derivative of the OH-stretch (blue line) local mode depending on which atoms' local chemical environment is used as an input to ANN (marked in red). The leftmost set of bars corresponds to RMSEs of the spectroscopic maps developed in Ref.⁴¹³, all others correspond to the Δ -ML approach of ref. (Adapted from Figure 2 of Ref.⁴¹⁴) Copyright 2019 The American Chemical Society.

1 In a recently published paper by Kwac and Cho,⁵²⁵ the authors tried to directly apply
 2 machine learning approaches in describing vibrational solvatochromism without employing
 3 any established vibrational frequency maps. In that work, the authors employed the feed-
 4 forward and the convolutional neural networks to describe the frequency shifts of the amide I
 5 mode vibration of NMA in water and assessed the performance of neural network models by
 6 comparing the results with those of the differential evolution algorithm approach using the
 7 same data sets. The data sets contain snapshots of molecular dynamics simulation trajectories
 8 where a single NMA molecule is surrounded by more than a thousand of water molecules. The
 9 corresponding frequency of the amide I mode of NMA for each configuration is calculated by
 10 a QM/MM method treating a selected number of nearest water molecules to the NMA molecule
 11 with QM method and the remaining water molecules by classical force fields.

12 In applying ML methods to describe vibrational solvatochromism, it is important to
 13 employ a suitable set of descriptors that properly represent the configuration of the solute and
 14 solvent molecules and simultaneously satisfy translation, rotation, and permutation symmetry.
 15 In that work, the authors tried two different representations of configurations of NMA in water:
 16 one is the atom centered symmetry functions (ACSF),^{523,524} which have been successfully
 17 employed in previous ML molecular dynamics simulations, and the other is the terms of a
 18 polynomial function of the inverse of interatomic distances already used in the DEA approach.

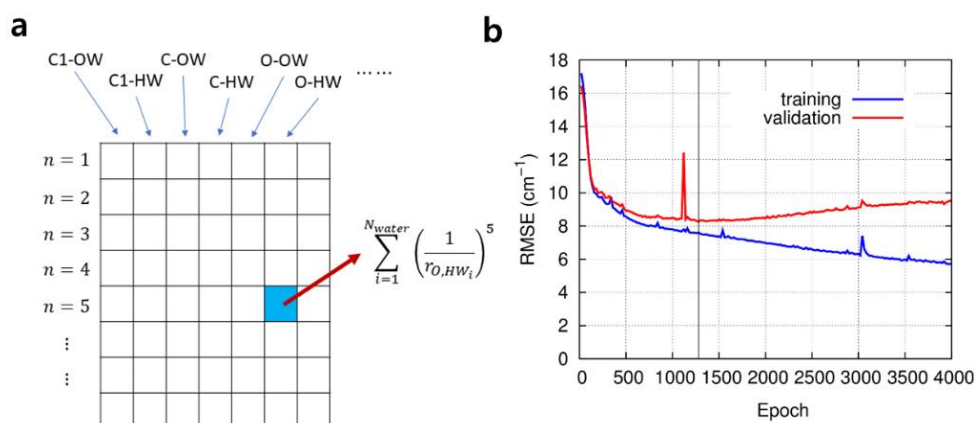
19 The ACSFs consist of two-body radial and three-body angular symmetry functions
 20 whose distance dependence is described by a Gaussian function. In that work, two sets of
 21 ACSFs, denoted as ACSF-I and ACSF-II, which have different parametrization so that the
 22 position and width of the Gaussian functions, the behavior of decay to zero, the angular
 23 resolution and the position of the extrema are different between the two sets. When feed-
 24 forward neural networks having one or two hidden layers are employed to describe the amide
 25 I mode vibrational frequency shifts of NMA in water using the carbonyl C atom of NMA and
 26 the O atom of water as the interaction sites, any noticeable difference in the performance is not
 27 observed between the ACSF-I and ACSF-II symmetry functions. In both cases, the obtained
 28 test RMSE value is about 18 cm^{-1} . In contrast, a significant improvement is observed by
 29 considering more of the interaction sites on the NMA and water molecules. If we consider 6
 30 sites (two methyl carbon and the C, O, N, H atom of the amide bond) on NMA with the oxygen
 31 and hydrogen sites of water, the test RMSE values are 11.8 and 11.1 cm^{-1} for ACSF-I and
 32 ACSF-II, respectively.

33 Next, the authors in that paper considered the terms of the polynomial function as
 34 descriptors to be input to the feed-forward neural network. By considering the six sites on NMA,
 35 two sites, O and H atoms, on water, and up to 14-order terms of the polynomial functions, each
 36 of which has a form of

$$37 \quad f_{A,B_i}^n = \sum_{i=1}^{N_{\text{water}}} \left(\frac{1}{r_{A,B_i}} \right)^n \quad (125)$$

38 where A represents one of the six sites of NMA and B_i does O or H atom of i th water molecule,
 39 r_{A,B_i} is the distance between A and B_i , and n is an integer between 1 and 14, the authors

1 obtained the optimized parameters of the feed forward neural network to give the test RMSE
 2 of 8.91 cm^{-1} , which is an improved result compared to the atom centered symmetry functions,
 3 ACSF-I and ACSF-II, employed in that work. In addition to the feed forward neural network,
 4 the authors in that paper also tried the convolutional neural network (CNN),⁵²⁶ which has been
 5 successfully applied to image processing. They prepared the input of the CNN as a form of
 6 matrix or third-rank tensor with the third dimension to be unity using the terms of the
 7 polynomial function, as shown in Figure 27(a). Figure 27(b) shows the process of the training
 8 of the neural networks using a plot of the training and the validation RMSE as a function of the
 9 elapse of epochs where one epoch corresponds to one cycle of processing all the data in the
 10 training set to update the parameters of the network. The optimized parameters at the epoch of
 11 the minimum validation RMSE give the test RMSE of 8.56 cm^{-1} , which is an improved result
 12 compared to the differential evolution algorithm result. Thus it is shown that the neural network
 13 models for vibrational solvatochromism can work better than the DEA method for the case of



14 the amide I mode of NMA in water.

15 **Figure 27.** The plot of the training and the validation RMSE values as a function of elapsed
 16 epochs in the training of the feed forward neural network model with the unscaled terms of the
 17 polynomial function. Adapted from Figures 7 and 8(a) of Ref.⁵²⁵ Copyright 2020 AIP Publishing.

18

19 5.4. Perspective

20 In solutions, the spectator molecule in question is often solvated by a relatively small number
 21 of polar solvent molecules that create varying electrostatic potential.^{188,221,233} The perturbing
 22 fields can also be applied in many directions.^{227-231,235} It is also possible to account for
 23 molecular anharmonicity when the model gas-phase Hamiltonian with a polynomial expansion
 24 of anharmonic potential is used and perturbed by external electric fields.²³¹ Subsequent
 25 multivariate least-square analyses of these model systems are then performed to obtain the
 26 vibrational solvatochromic parameters (or maps) for a given IR probe molecule, from which
 27 the benchmark results could be reproduced. There are a few reports showing that the vibrational
 28 map parameters associated with the electrostatic potential or electric field can achieve a high
 29 degree of transferability between solvent or even solute molecules, without the need of
 30 additional re-parameterization.^{111,226,231,236} However, it is not clear to what extent the
 31 universality is preserved, especially when the change of environment is drastic. For example,

1 put a probe in a completely non-polar solvent such as CCl_4 that has no net molecular dipole
2 moment. Since CCl_4 molecules are rather unlikely to exert strong electrostatic fields around the
3 IR probe one might expect very small frequency shifts. But the examples of MeCN and MeSCN
4 probes dissolved in this solvent show very pronounced frequency redshifts that are roughly –
5 10 cm^{-1} relative to that in the gas phase, which is, in magnitude, comparable to frequency shifts
6 in water. This is just one example showing the limitation of current approaches based on
7 physical approximations. Although electrostatic maps have proven to be a powerful and
8 efficient way to simulate IR spectra of various IR probes in solutions and highly heterogeneous
9 environments like proteins or nucleic acids, still it is necessary to refine theoretical models that
10 are capable of describing vibrational spectroscopic properties and dynamics of complex
11 molecules accurately.

12 Artificial intelligence (AI) and machine learning (ML) approaches^{527,528} can be
13 employed in developing more accurate models of vibrational solvatochromism with similar
14 advantages as the differential evolution algorithm since those ML methods are free from any
15 preliminary physical assumptions. Another advantage of the ML approach is the flexibility in
16 that we model the molecular interactions in a non-analytical form so that the functional form
17 of the model is also optimized. One challenging question is how to control or optimize the
18 complexity of models as in the differential evolution algorithm to avoid the pitfall of overfitting
19 in ML approach to model vibrational solvatochromism. Another challenge is about how to
20 reduce the size of the training data set since the necessary number of sample configurations in
21 ML approaches can be significantly larger than that in the previous studies of frequency maps
22 obtained using physical approximations. One of the other possibilities employing ML is not
23 directly modeling the vibrational frequency shifts, but modeling the closely related quantities
24 such as molecular dipole or polarizability using ML approach and calculate the vibrational
25 spectrum from these quantities.⁵²⁹ Finally, there is an issue about how and what kind of
26 physical insights we can extract from such ML models of vibrational solvatochromism, even
27 though the procedures of the ML approach are driven solely by data in training sets without
28 any physical assumptions.

29

30 **5.5. Summary and a few concluding remarks**

31 In the present article, we have reviewed both the theoretical and experimental works on
32 vibrational solvatochromism, vibrational spectroscopy, and their relations with intermolecular
33 interactions. Over the past two decades, technological developments in coherent nonlinear
34 vibrational spectroscopy such as multidimensional electronic, IR, THz, IR-Raman, IR-vis, vis-
35 IR, and THz-Raman measurement methods have enabled to extract solvation-induced
36 frequency shifts and time-correlation of fluctuating frequencies of IR probes that are site-
37 specifically incorporated into a variety of chemical, biological, and material systems. Due to
38 the increased number of IR probes and time-resolved vibrational spectroscopic data sets,
39 interpretive methods with atom-level chemical accuracy have been needed and developed.
40 Some of them are based on physical approximations, but more recent works show that using a
41 genetic algorithm, vibrational solvatochromism can be described without relying on physical
42 approximations.

1 One of the most successful approaches to quantitatively describing vibrational
2 solvatochromic effects on molecular spectra is to use a vibrational frequency map for a specific
3 IR probe of interest, which is a semiempirical model using a set of *ab initio* calculations results
4 or spectroscopic data. Recently, a website (<http://frequencymap.org>) has been created as a
5 repository site for vibrational frequency maps that have been successfully used to quantitatively
6 describe vibrational frequency shifts and fluctuations of various peptide modes, small IR probe
7 oscillators incorporated into proteins and functional materials, and so on. Although the
8 theoretical development of various vibrational frequency map approaches is mainly motivated
9 by experimental needs, rapid developments of vibrational frequency maps of localized modes
10 of molecules in condensed phases, vibrational coupling maps for interacting vibrational modes,
11 and vibrational transition dipole/polarizability maps for determining the corresponding
12 IR/Raman transition amplitudes developed over the past decades have been found to be
13 amazing. There is no doubt that judicious use of vibrational frequency map approaches with
14 state-of-the-art coherent multidimensional vibrational spectroscopy will be one of the most
15 useful methods for studying structure and dynamics of chemical, biological, and functional
16 molecular systems in the future.

17
18
19
20
21

1 **6. Glossary of Acronyms**

2		
3	1D	one-dimensional
4	2D	two-dimensional
5	2D IR	two-dimensional infrared
6	2D SFG	two-dimensional sum-frequency generation
7	AcGlyNHMe	N-acetyl-glycine N'-methylamide
8	AcProNH ₂	N-acetyl-L-prolinamide
9	AI	artificial intelligence
10	ANN	artificial neural network
11	AO-MO	atomic orbital-molecular orbital
12	BP	Buckingham potential
13	CaM	calmodulin
14	CAMM	cumulative atomic multipole moment
15	CDCl ₃	deuterated chloroform
16	CLS	center line slope
17	CMD	classical molecular dynamics
18	COSMO	conductor-like screening model
19	CP1	Cho-Potential model 1
20	CP2	Cho-Potential model 2
21	DCBS	dimer-centered basis set
22	DEA	differential evolution algorithm
23	DEC	diethyl carbonate
24	DFT	density functional theory
25	DMC	dimethyl carbonate
26	DMDC	dimanganese decacarbonyl
27	DMSO	dimethyl sulfoxide
28	DNA	deoxyribonucleic acid
29	EA	excited state absorption
30	EC	ethylene carbonate

1	EFP	effective fragment potential
2	ESF	electrostatic fitting
3	FFCF	frequency-frequency correlation function
4	FWHM	full width at half maximum
5	GB	ground state bleaching
6	GFP	green fluorescent protein
7	GSE	geometrical superposition error
8	H-bond	hydrogen-bond
9	HF	Hartree-Fock
10	hIAPP	human amyloid polypeptide
11	HMR	Hessian matrix reconstruction
12	HP35	villin headpiece protein
13	IR-Raman	infrared-Raman
14	IR-vis	infrared-visible
15	IR	infrared
16	KBM	Kirkwood-Bauer-Magat
17	KF1	Knoester-Field model 1
18	KF2	Knoester-Field model 2
19	KT	Kamlet-Taft
20	LCAO-MO	linear combinations of atomic orbitals
21	LIB	lithium ion battery
22	LJ	Lennard-Jones
23	LMO	localized molecular orbital
24	MCBS	monomer-centered basis set
25	MD	molecular dynamics
26	MeCN	acetonitrile
27	MeSCN	methyl thiocyanate
28	ML	machine learning
29	MM	molecular mechanics
30	MS-EVB	multi-state empirical valence bond

1	NEP	non-linear exciton propagation
2	NEPA	N-ethylpropionamide
3	NISE	numerical integration of the Schrödinger equation
4	NLS	nodal line slope
5	NMA	<i>N</i> -methylacetamide
6	NMA-d ₇	deuterated <i>N</i> -methylacetamide
7	NMP	nucleoside 5'-monophosphate
8	NMR	nuclear magnetic resonance
9	NN	nearest neighbor
10	NNFS	nearest neighbor frequency shift
11	NTBA	2-nitro-5-thiocyanate benzoic acid
12	OQM/MM	optimized quantum mechanics/molecular mechanics
13	PC	propylene carbonate
14	PCM	polarizable continuum model
15	PE	photon echo
16	PEPS	photon echo peak shift
17	PheCN	cyanophenylalanine
18	P _{II}	polyproline II
19	PM3	Parametric Method 3
20	PP	pump-probe
21	QM	quantum mechanics
22	RDC	rhodium(acetylacetonato)dicarbonyl
23	RHH	right-handed helix
24	RMSE	root mean squared error
25	RNA	ribonucleic acid
26	SAPT	symmetry adapted perturbation theory
27	SE	stimulated emission
28	SFG	sum-frequency-generation
29	SoIEDS	hybrid variational-perturbational interaction energy decomposition scheme
30	SoIEFP	vibrational solvatochromism theory based on the effective fragment potential

1		theory
2	TCC	transition charge coupling
3	TDC	transition dipole coupling
4	TFA	trifluoroacetic acid
5	TFE	trifluoroethanol
6	THz-Raman	terahertz-Raman
7	THz	terahertz
8	T_w	waiting time
9	VCD	vibrational circular dichroism
10	vdW	van der Waals
11	vis-IR	visible-infrared
12	VSE	vibrational Stark effect
13	VSFG	vibrational sum-frequency generation
14	VSM	vibrational solvatochromic maps
15	WCA	weak-coupling approximation
16		
17		
18		

1 AUTHOR INFORMATION

3 Corresponding Author

4 *E-mail: mcho@korea.ac.kr (MC)

6 ORCID

7 Carlos R. Baiz: 0000-0003-0699-8468

8 Bartosz Błasiak: 0000-0003-1968-3465

9 Jens Bredenbeck: 0000-0003-1929-9092

10 Minhaeng Cho: 0000-0003-1618-1056

11 Steven A. Corcelli: 0000-0001-6451-4447

12 Arend G. Dijkstra: 0000-0003-2298-4736

13 Chi-Jui Feng: 0000-0002-4006-9489

14 Sean Garrett-Roe: 0000-0001-6199-8773

15 Thomas L.C. Jansen: 0000-0001-6066-6080

16 Magnus Hanson-Heine: 0000-0002-6709-297X

17 Hiroaki Maekawa: 0000-0003-0782-4486

18 Santanu Roy: 0000-0001-6991-8205

19 Shinji Saito: 0000-0003-4982-4820

20 James L. Skinner: 0000-0001-6939-9759

21 Megan C. Thielges: 0000-0002-4520-6673

22 Hajime Torii: 0000-0002-6061-9599

23 Lu Wang: 0000-0001-6230-1835

25 Notes

26 The authors declare no competing financial interest.

28 Biographies

29
30 Carlos R. Baiz is a faculty member at the University of Texas at Austin. His lab studies the
31 biophysics of complex systems such as heterogeneous lipid membranes and membrane proteins
32 using ultrafast two-dimensional infrared spectroscopy and molecular dynamics simulations.
33 His group also develops vibrational models, including frequency maps to connect experiments
34 with simulations. He has a Ph.D. in Chemistry from the University of Michigan where he
35 worked in the lab of Prof. Kevin Kubarych and postdoctoral training at MIT and University of
36 Chicago with Prof. Andrei Tokmakoff.

37
38 Bartosz Błasiak was born in Oleśnica, Poland in 1988. In 2012, he received his M.S. in
39 chemistry from Wrocław University of Technology in Wrocław, Poland. He did his PhD
40 studies at Korea University, Seoul, Korea, which he graduated in August 2016. In 2017, he was
41 a post-doctoral fellow in Institute for Biophysics at Goethe University Frankfurt. Currently, he
42 is an assistant professor in the Department of Physical and Quantum Chemistry at Wrocław
43 University of Science and Technology, Poland. He is interested in developing quantum
44 chemistry and theoretical methods for the description of extended molecular aggregates and
45 molecular spectroscopy.

1
2 Jens Bredenbeck obtained his Diploma in chemistry in 2000 with Reinhard Schinke (MPI for
3 Flow Research, Göttingen) and his Dr. sc. nat. in 2005 with Peter Hamm (Max Born Institute
4 of Nonlinear Optics, Berlin, and University of Zurich). After postdoctoral research with Mischa
5 Bonn (AMOLF, Amsterdam) he received the Sofja-Kovalevskaja Award of the Humboldt-
6 Foundation and established his group at Goethe University, Frankfurt, in 2007. Since 2010 he
7 is a full professor of Experimental Biophysics and Chemical Physics at the Institute of
8 Biophysics of Goethe University. His research explores molecular structure and dynamics over
9 a wide range of time scales and the development of nonlinear vibrational spectroscopies and
10 spectroscopic probes.

11
12 Minhaeng Cho is the director of the IBS Center for Molecular Spectroscopy and Dynamics,
13 established in Dec. 2014 and Professor of Chemistry at Korea University, Seoul, Korea, since
14 1996. He grew up in Seoul, where he attended the public schools. He received his B.S. and
15 M.S. from Seoul National University in 1987 and 1989, respectively, before studying in the
16 U.S. A. where he received his Ph.D. in 1993 from the University of Chicago. He returned to
17 Korea in 1996 as an Assistant Professor at the Korea University after a two-year post-doctoral
18 research experience at MIT, Cambridge, USA. He became a full Professor at the Korea
19 University in 2003 before his directorship with IBS in 2014. IBS Center for Molecular
20 Spectroscopy and Dynamics (CMSD), located in the Seoul campus of Korea University,
21 emphasizes developments of novel time- and space-resolved spectroscopy techniques and their
22 applications to chemically reactive and biologically important systems. He is a member of the
23 Korean Academy of Science and Technology (KAST) and received numerous awards given by
24 the American Chemical Society, National Science Foundation in Korea, KAST, Kyung-Am
25 Science Foundation, and National Academy of Science in Korea.

26
27 Jun-Ho Choi has been on the faculty of Gwangju Institute of Science and Technology since
28 2018. He received a B.S., M.S., and Ph.D. in chemistry from Seoul National University in 1990,
29 1992 and 1996 and worked as a research professor at the IBS Center for Molecular
30 Spectroscopy and Dynamics from 2014 to 2018. His research interests are computational
31 spectroscopy and computer-aided molecular design.

32
33 Steven A. Corcelli is a theoretical chemist whose research focuses on the structure, dynamics,
34 and spectroscopy of molecular and biomolecular solutes in solution. He graduated from Brown
35 University in 1997 (Sc.B. in Chemistry). In 2002, he was awarded a Ph.D. from Yale University
36 where he trained with Dr. John Tully. From 2002 – 2005, he was a postdoctoral scholar with
37 Dr. Jim Skinner at the University of Wisconsin-Madison. Dr. Corcelli began his independent
38 academic career in 2005 at the University of Notre Dame, where he has been the grateful
39 recipient of several awards, including the Camille and Henry Dreyfus New Faculty Award, an
40 NSF CAREER Award, a Sloan Research Fellowship, and twice the Rev. Edmund P. Joyce,
41 C.S.C. Award for Excellence in Undergraduate Teaching.

42
43 Arend G. Dijkstra received his Ph.D. from the University of Groningen in the Netherlands,
44 where he worked on nonlinear vibrational spectroscopy of peptides supervised by Profs Jasper
45 Knoester and Thomas la Cour Jansen. He then performed postdoctoral work with Profs
46 Yoshitaka Tanimura in Kyoto, Jianshu Cao at MIT and R. J. Dwayne Miller in Hamburg,
47 before starting his group as a University Academic Fellow at the University of Leeds. His work
48 has focused on the theoretical description of light-induced ultrafast processes in large
49 molecules and materials.

1
2 Chi-Jui Feng received a B.Sc. in chemistry from National Taiwan University in 2013, working
3 on structure-based modeling of excitation energy transfer dynamics in pigment-protein
4 complexes, under the supervision of Prof. Yuan-Chung Cheng. He is a Ph.D. candidate from
5 University of Chicago under the supervision of Prof. Andrei Tokmakoff, working on dynamics
6 of coupled folding and binding processes in protein recognition using two-dimensional infrared
7 spectroscopy and amide I computational spectroscopy.

8
9 Sean Garrett-Roe received his B.S in Chemistry from Princeton University (1999) and his Ph.D.
10 from the University of California, Berkeley (2005). From 2006 to 2011, he was a postdoctoral
11 scientist at the University of Zurich with Prof. Peter Hamm. Sean joined the chemistry
12 department of the University of Pittsburgh as an assistant professor in 2011 and was promoted
13 to associate professor with tenure in 2018. At Pitt, his research has focused on ultrafast
14 vibrational spectroscopy (2D-IR) of ionic liquids. He has published over 40 peer reviewed
15 journal papers. He was awarded the Chancellor's Distinguished Teaching Award (2017).

16
17 Nien-Hui Ge is a Professor of Chemistry at the University of California at Irvine. She received
18 her B.S. and M.S. from National Taiwan University, working on NMR spectroscopy of
19 quadrupolar nuclei. She received her Ph.D. from the University of California at Berkeley in the
20 group of Prof. Charles Harris in 1998, focusing on two-photoemission spectroscopy of metal-
21 dielectric interfaces. During her post-doctoral research in the Robin Hochstrasser group at the
22 University of Pennsylvania, she was involved with the development of coherent two-
23 dimensional infrared spectroscopy. She joined UC Irvine in 2002 and received National
24 Science Foundation CAREER award in 2005. Her current research focuses on the study of
25 chemical, biological, and material processes using a combination of ultrafast spectroscopy and
26 microscopy (2D IR, SFG, s-SNOM) and plasmonics.

27
28 Magnus Hanson-Heine is a research fellow working in quantum chemistry at the University of
29 Nottingham, where he received his Ph.D. in 2010. His research interests include method
30 development for modeling molecular spectroscopy and vibrational dynamics, modeling
31 molecular excited state behavior using DFT, and work simulating catalytic reaction pathways.

32
33 Jonathan Hirst is a Professor of Computational Chemistry at the University of Nottingham,
34 where he has been since 1999. He received a BA from the University of Oxford in 1990 and
35 was awarded a Ph.D. in 1993 from the University of London, based on his research conducted
36 at the Imperial Cancer Research Fund. He moved to the USA in 1993, first to Carnegie Mellon
37 University and then, with a Human Frontiers Science Programme Fellowship, to The Scripps
38 Research Institute, La Jolla, becoming Assistant Professor in 1996. In 1999, he returned to the
39 UK, to the University of Nottingham, becoming full Professor in 2004. He served as Head of
40 the School of Chemistry from 2013 to 2017. His ongoing research includes applications of
41 computational chemistry to the study of the structure, dynamics and spectroscopy of biological
42 molecules and the development and application of computer-aided molecular design.

43
44 Thomas L.C. Jansen is working in the Zernike Institute for Advanced Materials at the
45 University of Groningen, Groningen, the Netherlands since 2005. He grew up in Denmark and
46 received his B.S. and M.S. in Chemistry from the University of Copenhagen in 1996 and 1998,
47 respectively. He then moved to The Netherlands, where he received his Ph.D. degree *cum laude*
48 from the University of Groningen in 2002. He then moved to University of Rochester, New
49 York, United States, to work with Professor Shaul Mukamel. In 2003, he moved with the

1 Mukamel group to the University of California at Irvine, Irvine, California. In 2005, he returned
2 to the University of Groningen on a Dutch VENI grant and in 2008 he received a VIDI grant
3 to continue his research then focused on the theory of infrared spectroscopy of proteins. His
4 current research extends to the study of electronic spectroscopy and transport properties of
5 biological and artificial systems with an emphasis on real-time dynamics and method
6 development.

7
8 Kevin J. Kubarych is Professor of Chemistry and of Biophysics at the University of Michigan.
9 Kevin has spent his scientific career developing and using multidimensional spectroscopy,
10 starting with graduate research using 2D fifth-order Raman spectroscopy at the University of
11 Toronto working with R. J. Dwayne Miller. After graduating in 2003, Kevin was a Human
12 Frontier Science Program postdoctoral fellow at the CNRS Laboratoire d'Optique et
13 Biosciences at Ecole Polytechnique where he worked with Manuel Joffre to develop
14 upconversion IR detection and pulse-shaping based nonlinear spectroscopy. Since 2005,
15 Kevin's independent research group at the University of Michigan has used 2D-IR
16 spectroscopy to study chemical dynamics in a variety of contexts, ranging from
17 photocatalysis to interfacial protein hydration. He was a recipient of an NSF CAREER award
18 and the Camille Dreyfus Teacher-Scholar award.

19
20 Kijeong Kwac received his B.S in chemistry education in 1992 and his M.S. and Ph. D. in
21 chemistry from Seoul National University in 1994 and 2001, respectively. He worked as a
22 postdoctoral researcher at universities in South Korea and the United States. He is a research
23 professor at the IBS Center for Molecular Spectroscopy and Dynamics since 2018.

24
25 Casey H. Londergan is Chair and Associate Professor of Chemistry at Haverford College. He
26 received his B.S. in Chemistry in 1997 from Williams College and his M.S. and Ph.D. in
27 Chemistry in 2000 and 2003, respectively, from University of California, San Diego. He was
28 a NRSA Kirschstein postdoctoral fellow and received Henry Dreyfus Teacher-Scholar award,
29 Cottrell College Science award, and NSF-CAREER Early Career Development award. He is a
30 member of ACS, Sigma Xi, Biophysical Society, and Protein Society.

31
32 Hiroaki Maekawa was born in Osaka, Japan, and graduated from Kobe university with B.Sc.
33 (1999) and M. Sc. (2001) degrees. He received his Ph.D. in 2004 from the same university
34 under the supervision of Prof. Keisuke Tominaga. He is currently working as an associate
35 specialist of Prof. Nien-Hui Ge's group at the University of California, Irvine. His research
36 interests include mid-infrared nonlinear spectroscopy, microscopy, and nanoscopy.

37
38 Mike Reppert received his BSc from Kansas State University in 2009. After a year as a
39 Fulbright scholar at the Polish Academy of Sciences, he studied amide I two-dimensional
40 spectroscopy under Andrei Tokmakoff at the Massachusetts Institute of Technology,
41 completing his PhD in 2016. As a Banting postdoctoral fellow in the Chemical Physics Theory
42 Group at the University of Toronto, he then worked with Paul Brumer to probe the similarities
43 and distinctions between quantum and classical dynamics in ultrafast spectroscopy. He is
44 currently an Assistant Professor of Chemistry at Purdue University, where his group develops
45 new experimental and computational approaches to describing the optical and infrared
46 properties of proteins and pigment/protein complexes.

47
48 Santanu Roy is a postdoctoral research associate in the Chemical Separations Group, Chemical
49 Sciences Division, Oak Ridge National Laboratory (ORNL). He received his Ph.D. in Natural

1 Sciences from the Center for Theoretical Physics, Zernike Institute for Advanced Materials,
2 University of Groningen, The Netherlands in 2012. He was a postdoctoral research associate
3 in the Department of Chemistry, University of Wisconsin at Madison (2012–2014) and at
4 Pacific Northwest National Laboratory (2014–2017) before joining ORNL. His research
5 expertise includes ab initio and force field-based molecular dynamics (MD) simulations,
6 development of reaction rate theory, and modeling and simulation of different molecular
7 spectroscopic measurements including two-dimensional infrared/sum-frequency generation,
8 X-ray scattering/absorption, and neutron scattering for condensed phase systems. His
9 experience and interests lie in a wide variety of research problems, including protein
10 folding/misfolding, structures of elastic biopolymers, clean water and water in energy,
11 mechanisms of ion-pairing, solvation, and chemical separation, molecular self-assembly,
12 recovery of rare-earth minerals, and chemistry of molten salts.

13
14 Shinji Saito received his Ph.D. from The Graduate University for Advanced Studies in 1995.
15 He worked at Nagoya University as Research Associate and Associate Professor for about 12
16 years. Since 2005, he has been Professor at Institute for Molecular Science. He has worked on
17 dynamical and thermodynamic aspects in condensed phases theoretically and computationally.
18 More specifically, he has been interested in spatiotemporally heterogeneous dynamics in
19 (supercooled) water and reaction dynamics and functions in biomolecules.

20
21 James L. Skinner is the Crown Family Professor and Deputy Dean for Faculty Affairs at the
22 Pritzker School of Molecular Engineering at the University of Chicago. He received his Ph.D.
23 in Chemical Physics from Harvard in 1979, and started his academic career as an Assistant
24 Professor at Columbia University in 1981. In 1990 he moved to the University of Wisconsin
25 as the Joseph O. Hirschfelder Professor of Chemistry, and in 2017 he moved to his current
26 position at the University of Chicago. He served for a decade as Associate and then Deputy
27 Editor of the Journal of Chemical Physics, and was President of the Telluride Science Research
28 Center in 2018. He was elected to the National Academy of Sciences in 2012 and has served
29 on the Scientific Advisory Board of the Welch Foundation since 2015.

30
31 Gerhard Stock studied Physics at the Technical University of Munich (TUM) and got his
32 doctorate 1990 with Professor Wolfgang Domcke. He spent 1991/1992 at the University of
33 California, Berkeley with Professor William H. Miller as a postdoctoral fellow of the Deutsche
34 Forschungsgemeinschaft (DFG). Back at the TUM, he worked as a DFG Habilitation fellow
35 and obtained his Habilitation in 1996. From 1997 to 2000 he was a Heisenberg Professor at the
36 Department of Physics at the University of Freiburg, before he moved to the Goethe University
37 in Frankfurt am Main, where he held a full professorship in Theoretical Chemistry. Since 2009,
38 he holds a Chair of Theoretical Physics (successor of John Briggs) at the University of Freiburg.
39 His 'Biomolecular Dynamics group' aims to develop new theoretical and computational
40 methods to model the dynamics and spectroscopy of complex molecular systems.

41
42 John E. Straub is Professor of Chemistry at Boston University. He received his B.S. in
43 Chemistry in 1982 from the University of Maryland at College Park, where he worked with
44 Millard Alexander on quantum scattering theory, and his Ph.D. in Chemical Physics in 1987
45 from Columbia University, where he worked with Bruce Berne on chemical research rate
46 theory and simulation. He was a NIH Postdoctoral Fellow at Harvard University, where he
47 worked with Martin Karplus on theory and simulation of protein dynamics, before joining the
48 faculty of Boston University in 1990. His research explores the dynamics and thermodynamics
49 of proteins, membrane, and complex molecular assemblies, as well as algorithmic development

1 for optimization, enhanced sampling, and long-time dynamics. He has served as President of
2 the Telluride Science Research Center (TSRC), Phi Beta Kappa National Visiting Scholar, and
3 is an Associate Editor of The Journal of Chemical Physics.

4
5 Megan C. Thielges received her Ph.D. in biophysics at The Scripps Research Institute (La Jolla,
6 CA) in 2009 and completed postdoctoral studies in multidimensional IR spectroscopy at
7 Stanford University. In 2012, she joined the faculty at Indiana University and became an
8 associate professor in 2018. Her primary research interests center around elucidating the
9 conformations and dynamics of proteins and understanding how they are involved in
10 function. In support of these goals, her research program aims to advance experimental
11 methods of site-specific linear and multidimensional infrared spectroscopy for characterizing
12 protein dynamics with high spatial and temporal detail.

13
14 Andrei Tokmakoff earned his B.S. in Chemistry from California State University in 1988. He
15 went on to earn an M.S. and Ph.D., both in Chemistry and from Stanford University, in 1991
16 and 1995. He became an Alexander von Humboldt Research Fellow at Technical University
17 Munich from 1995-96. Then, he was a National Science Foundation Postdoctoral Research
18 Fellow at the University of Chicago, University of California Berkeley, and the Lawrence
19 Berkeley National Laboratory. In 1998, he became a professor at MIT, eventually becoming
20 Robert T. Haslam and Bradley Dewey Professor of Chemistry in 2012. He now serves as Henry
21 G. Dale Distinguished Service Professor at the University of Chicago. He has received many
22 awards, including the Coblentz Award, the National Fresenius Award, the Earle K. Plyler Prize
23 for Molecular Spectroscopy & Dynamics, and the 2014 Ellis R. Lippincott Award from OSA.

24
25 Keisuke Tominaga received a B.Sc. (Kyoto University, 1985), M.Sc. (Kyoto University, 1987),
26 and D.Sc. (Kyoto University, 1990). He was a postdoctoral fellow at the University of
27 Minnesota (1990), a research associate at the Institute for Molecular Science (1992), an
28 associate professor at Kobe University (1998), and a professor at the Molecular Photoscience
29 Research Center, Kobe University (2001). His research focuses on time-resolved spectroscopy
30 of condensed phases.

31
32 Hajime Torii is a professor at the Department of Applied Chemistry and Biochemical
33 Engineering, Faculty of Engineering, and Department of Optoelectronics and Nanostructure
34 Science, Graduate School of Science and Technology, Shizuoka University. He received his
35 Ph.D. from the University of Tokyo in 1992. After working as a research associate at the
36 University of Tokyo, he moved to Shizuoka University in 2001 as an associate professor (PI),
37 and was promoted to a professor in 2008. He had been the chair of the Japanese Molecular
38 Liquids Group (JMLG) from 2010 to 2019. His present research interests focus on theories and
39 computations on intermolecular interactions, structures, dynamics, and spectroscopic
40 properties (including IR, THz, 2D-IR, and Raman) of liquids and biomolecules.

41
42 Lu Wang is an assistant professor in the Department of Chemistry and Chemical Biology at
43 Rutgers University. She received her Ph.D. degree in Physical Chemistry from the University
44 of Wisconsin-Madison under the supervision of Professor Jim Skinner. She then worked as a
45 postdoctoral fellow with Professor Tom Markland at Stanford University before starting her
46 independent career in 2016. Her research uses theoretical and computational tools to elucidate
47 the structure and dynamics of condensed phase systems, with a particular emphasis on the
48 vibrational spectroscopy and quantum effects of biological macromolecules.

1 Lauren J. Webb is an associate professor of chemistry at The University of Texas at Austin.
2 She obtained her A.B. in chemistry (music minor) from Bowdoin College in 2000. She entered
3 graduate school at the California Institute of Technology and earned her Ph.D. in chemistry
4 in 2005. From 2005 to 2008 she was a postdoctoral fellow in the laboratory of Dr. Steven Boxer
5 in the Department of Chemistry at Stanford University. Her research focused on quantifying
6 electrostatic fields in proteins using vibrational Stark effect spectroscopy. Dr. Webb moved to
7 UT-Austin in 2008, where she has developed a research program based on her training in both
8 surface and biological chemistry. Her research interests are centered on understanding and
9 manipulating the mechanisms of interaction, organization, and self- assembly of biological
10 macromolecules in both natural and artificial environments.

11
12 Martin T. Zanni is the Meloche-Bascom Professor of Chemistry at the University of
13 Wisconsin-Madison. He is one of the early pioneers of 2D IR spectroscopy and has made many
14 technological innovations that has broadened the capabilities and scope for a wide range of
15 multidimensional spectroscopies and microscopies. He utilizes these new techniques to study
16 topics in biophysics, chemical physics, photovoltaics, and surfaces. He has received many
17 accolades for his research and was recently elected to the American Academy of Arts and
18 Sciences. He founded PhaseTech Spectroscopy Inc., which is the first company to
19 commercialize ultrafast 2D spectroscopy.

20 21 22 **SUPPORTING INFORMATION**

23 Detailed format of the deposited map file.
24

25 **ACKNOWLEDGMENTS**

26
27 This work was supported by IBS-R023-D1 (MC). BB wishes to thank the European Union's
28 Horizon 2020 under the Marie Skłodowska-Curie Grant Agreement No. 665778, as well as the
29 National Science Centre, Poland (grant no. 2016/23/P/ST4/01720). CRB acknowledges
30 generous support from the National Science Foundation (CHE-1847199, BIO-1815354), the
31 National Institutes of Health (R35GM133359), and the Welch Foundation (F-1891). MWDH-
32 H and JDH thank the University of Nottingham, Green Chemicals Beacon for funding toward
33 this research. MCT acknowledges support from Department of Energy (DE-SC0018983),
34 National Science Foundation (1552996), and National Institutes of Health (GM114500). AGD
35 would like to thank Prof Andrei Tokmakoff for discussing amide modes when he was a PhD
36 student. LW acknowledges the support from the National Institutes of Health through Award
37 R01GM130697. SAC acknowledges support from National Science Foundation (CHE-
38 1565471)
39

References

- (1) Herzberg, G. *Molecular Spectra and Molecular Structure I: Spectra of Diatomic Molecules*; Van Nostrand, 1950.
- (2) Herzberg, G. *Molecular Spectra and Molecular Structure II: Infrared and Raman of Polyatomic Molecules*; Van Nostrand, 1956.
- (3) Mukamel, S. *Principles of Nonlinear Optical Spectroscopy*; Oxford University Press: Oxford, 1995.
- (4) Cho, M. *Two-Dimensional Optical Spectroscopy*; CRC Press: Boca Raton, 2009.
- (5) Hamm, P.; Zanni, M. T. *Concepts and Methods of 2D Infrared Spectroscopy*; Cambridge University Press: New York, 2011.
- (6) Mukamel, S. Multidimensional Femtosecond Correlation Spectroscopies of Electronic and Vibrational Excitations. *Annu. Rev. Phys. Chem.* **2000**, *51*, 691-729.
- (7) Cho, M. Coherent Two-Dimensional Optical Spectroscopy. *Chem. Rev.* **2008**, *108*, 1331-1418.
- (8) Jonas, D. M. Vibrational and Nonadiabatic Coherence in 2D Electronic Spectroscopy, the Jahn–Teller Effect, and Energy Transfer. *Annu. Rev. Phys. Chem.* **2016**, *69*, 327-352.
- (9) Nihonyanagi, S.; Mondal, J. A.; Yamaguchi, S.; Tahara, T. Structure and Dynamics of Interfacial Water Studied by Heterodyne-Detected Vibrational Sum-Frequency Generation. *Annu. Rev. Phys. Chem.* **2013**, *64*, 579-603.
- (10) Tanimura, Y.; Mukamel, S. Two-Dimensional Femtosecond Vibrational Spectroscopy of Liquids. *J. Chem. Phys.* **1993**, *99*, 9496-9511.
- (11) Cho, M.; Fleming, G. R. Fifth-Order Three-Pulse Scattering Spectroscopy: Can We Separate Homogeneous and Inhomogeneous Contributions to Optical Spectra? *J. Phys. Chem.* **1994**, *98*, 3478-3485.
- (12) Park, K.; Cho, M. Time- and Frequency-Resolved Coherent Two-Dimensional IR Spectroscopy: Its Complementary Relationship with the Coherent Two-Dimensional Raman Scattering Spectroscopy. *J. Chem. Phys.* **1998**, *109*, 10559-10569.
- (13) Hybl, J. D.; Albrecht, A. W.; Gallagher Faeder, S. M.; Jonas, D. M. Two-Dimensional Electronic Spectroscopy. *Chem. Phys. Lett.* **1998**, *297*, 307-313.
- (14) Zhao, W.; Wright, J. C. Spectral Simplification in Vibrational Spectroscopy Using Doubly Vibrationally Enhanced Infrared Four Wave Mixing. *J. Am. Chem. Soc.* **1999**, *121*, 10994-10998.
- (15) Savolainen, J.; Ahmed, S.; Hamm, P. Two-Dimensional Raman-Terahertz Spectroscopy of Water. *Proc. Natl. Acad. Sci. U.S.A.* **2013**, *110*, 20402.
- (16) Elsaesser, T.; Reimann, K.; Woerner, M. Focus: Phase-Resolved Nonlinear Terahertz Spectroscopy—from Charge Dynamics in Solids to Molecular Excitations in Liquids. *J. Chem. Phys.* **2015**, *142*, 212301.
- (17) Shalit, A.; Ahmed, S.; Savolainen, J.; Hamm, P. Terahertz Echoes Reveal the Inhomogeneity of Aqueous Salt Solutions. *Nature Chemistry* **2016**, *9*, 273.
- (18) Courtney, T. L.; Fox, Z. W.; Slenkamp, K. M.; Khalil, M. Two-Dimensional Vibrational-Electronic Spectroscopy. *J. Chem. Phys.* **2015**, *143*, 154201.
- (19) Courtney, T. L.; Fox, Z. W.; Estergreen, L.; Khalil, M. Measuring Coherently Coupled Intramolecular Vibrational and Charge-Transfer Dynamics with Two-Dimensional Vibrational–Electronic Spectroscopy. *J. Phys. Chem. Lett.* **2015**, *6*, 1286-1292.

- 1 (20) Lewis, N. H. C.; Dong, H.; Oliver, T. A. A.; Fleming, G. R. Measuring Correlated
2 Electronic and Vibrational Spectral Dynamics Using Line Shapes in Two-Dimensional
3 Electronic-Vibrational Spectroscopy. *J. Chem. Phys.* **2015**, *142*, 174202.
- 4 (21) Oliver, T. A. A.; Lewis, N. H. C.; Fleming, G. R. Correlating the Motion of Electrons
5 and Nuclei with Two-Dimensional Electronic-Vibrational Spectroscopy. *Proc. Natl.*
6 *Acad. Sci. U.S.A.* **2014**, *111*, 10061-10066.
- 7 (22) Cyran, J. D.; Backus, E. H. G.; Nagata, Y.; Bonn, M. Structure from Dynamics:
8 Vibrational Dynamics of Interfacial Water as a Probe of Aqueous Heterogeneity. *J.*
9 *Phys. Chem. B* **2018**, *122*, 3667-3679.
- 10 (23) Zhang, Z.; Piatkowski, L.; Bakker, H. J.; Bonn, M. Ultrafast Vibrational Energy
11 Transfer at the Water/Air Interface Revealed by Two-Dimensional Surface Vibrational
12 Spectroscopy. *Nature Chemistry* **2011**, *3*, 888-893.
- 13 (24) Matsuzaki, K.; Kusaka, R.; Nihonyanagi, S.; Yamaguchi, S.; Nagata, T.; Tahara, T.
14 Partially Hydrated Electrons at the Air/Water Interface Observed by UV-Excited Time-
15 Resolved Heterodyne-Detected Vibrational Sum Frequency Generation Spectroscopy.
16 *J. Am. Chem. Soc.* **2016**, *138*, 7551-7557.
- 17 (25) Hamm, P.; Lim, M.; Hochstrasser, R. M. Structure of the Amide I Band of Peptides
18 Measured by Femtosecond Nonlinear-Infrared Spectroscopy. *J. Phys. Chem. B* **1998**,
19 *102*, 6123-6138.
- 20 (26) Cho, M. In *Advances in Multi-Photon Processes and Spectroscopy*; Lin, S. H.; Villaeys,
21 A. A.; Fujimura, Y., Eds.; World Scientific: Singapore, 1999; Vol. 12.
- 22 (27) Hahn, S.; Park, K.; Cho, M. Two-Dimensional Vibrational Spectroscopy. I. Theoretical
23 Calculation of the Nonlinear Raman Response Function of CHCl_3 . *J. Chem. Phys.* **1999**,
24 *111*, 4121-4130.
- 25 (28) Park, K.; Cho, M.; Hahn, S.; Kim, D. Two-Dimensional Vibrational Spectroscopy. II.
26 Ab Initio Calculation of the Coherent 2D Infrared Response Function of CHCl_3 and
27 Comparison with the 2D Raman Response Function. *J. Chem. Phys.* **1999**, *111*, 4131-
28 4139.
- 29 (29) Cho, M. Two-Dimensional Vibrational Spectroscopy. III. Theoretical Description of
30 the Coherent Two-Dimensional IR-Raman Spectroscopy for the Investigation of the
31 Coupling between Both IR- and Raman-Active Vibrational Modes. *J. Chem. Phys.*
32 **1999**, *111*, 4140-4147.
- 33 (30) Hahn, S.; Kwak, K.; Cho, M. Two-Dimensional Vibrational Spectroscopy. IV.
34 Relationship between through-Space Vibrational Coupling and Intermolecular
35 Distance. *J. Chem. Phys.* **2000**, *112*, 4553-4556.
- 36 (31) Cho, M. Two-Dimensional Vibrational Spectroscopy. V. Novel 2-Dimensional Surface
37 Vibrational Spectroscopies of Adsorbed Molecules on Surfaces or at Interfaces. *J.*
38 *Chem. Phys.* **2000**, *112*, 9978-9985.
- 39 (32) Park, K.; Cho, M. Two-Dimensional Vibrational Spectroscopy. Vi. Higher-Order
40 Contributions to the Two-Dimensional Vibrational Response Functions. *J. Chem. Phys.*
41 **2000**, *112*, 10496-10509.
- 42 (33) Cho, M. Two-Dimensional Vibrational Spectroscopy. Vii. Investigation of the Vibronic
43 and Vibrational Couplings by Using Novel Triply Resonant Two-Dimensional
44 Vibrational Spectroscopies. *J. Chem. Phys.* **2000**, *113*, 7746-7755.
- 45 (34) Bonn, M.; Hess, C.; Miners, J. H.; Heinz, T. F.; Bakker, H. J.; Cho, M. Novel Surface
46 Vibrational Spectroscopy: Infrared-Infrared-Visible Sum-Frequency Generation. *Phys.*
47 *Rev. Lett.* **2001**, *86*, 1566-1569.

- 1 (35) Cho, M. Two-Dimensional Vibrational Spectroscopy. Viii. Infrared Optical Kerr Effect
2 and Two-Color Infrared Pump–Probe Measurements. *J. Chem. Phys.* **2001**, *114*, 9982-
3 9992.
- 4 (36) Cho, M. Ultrafast Vibrational Spectroscopy in Condensed Phases. *PhysChemComm*
5 **2002**, *5*, 40-58.
- 6 (37) van Wilderen, L. J. G. W.; Bredenbeck, J. From Ultrafast Structure Determination to
7 Steering Reactions: Mixed IR/Non-IR Multidimensional Vibrational Spectroscopies.
8 *Angew. Chem. Int. Ed.* **2015**, *54*, 11624-11640.
- 9 (38) Kim, H.; Cho, M. Infrared Probes for Studying the Structure and Dynamics of
10 Biomolecules. *Chem. Rev.* **2013**, *113*, 5817-5847.
- 11 (39) Ma, J.; Pazos, I. M.; Zhang, W.; Culik, R. M.; Gai, F. Site-Specific Infrared Probes of
12 Proteins. *Annu. Rev. Phys. Chem.* **2015**, *66*, 357-377.
- 13 (40) Błasiak, B.; Londergan, C. H.; Webb, L. J.; Cho, M. Vibrational Probes: From Small
14 Molecule Solvatochromism Theory and Experiments to Applications in Complex
15 Systems. *Acc. Chem. Res.* **2017**, *50*, 968-976.
- 16 (41) Adhikary, R.; Zimmermann, J.; Romesberg, F. E. Transparent Window Vibrational
17 Probes for the Characterization of Proteins with High Structural and Temporal
18 Resolution. *Chem. Rev.* **2017**, *117*, 1927-1969.
- 19 (42) Lindquist, B. A.; Furse, K. E.; Corcelli, S. A. Nitrile Groups as Vibrational Probes of
20 Biomolecular Structure and Dynamics: An Overview. *Phys. Chem. Chem. Phys.* **2009**,
21 *11*, 8119-8132.
- 22 (43) Moran, S. D.; Woys, A. M.; Buchanan, L. E.; Bixby, E.; Decatur, S. M.; Zanni, M. T.
23 Two-Dimensional IR Spectroscopy and Segmental ¹³C Labeling Reveals the Domain
24 Structure of Human γ D-Crystallin Amyloid Fibrils. *Proc. Natl. Acad. Sci. U.S.A.* **2012**,
25 *109*, 3329.
- 26 (44) Baiz, Carlos R.; Tokmakoff, A. Structural Disorder of Folded Proteins: Isotope-Edited
27 2D IR Spectroscopy and Markov State Modeling. *Biophys. J.* **2015**, *108*, 1747-1757.
- 28 (45) Reppert, M.; Roy, A. R.; Tokmakoff, A. Isotope-Enriched Protein Standards for
29 Computational Amide I Spectroscopy. *J. Chem. Phys.* **2015**, *142*, 125104.
- 30 (46) Basom, E. J.; Maj, M.; Cho, M.; Thielges, M. C. Site-Specific Characterization of
31 Cytochrome P450cam Conformations by Infrared Spectroscopy. *Anal. Chem.* **2016**, *88*,
32 6598-6606.
- 33 (47) Dalton, S. R.; Vienneau, A. R.; Burstein, S. R.; Xu, R. J.; Linse, S.; Londergan, C. H.
34 Cyanylated Cysteine Reports Site-Specific Changes at Protein–Protein-Binding
35 Interfaces without Perturbation. *Biochemistry* **2018**, *57*, 3702-3712.
- 36 (48) van Wilderen, L. J. G. W.; Kern-Michler, D.; Müller-Werkmeister, H. M.; Bredenbeck,
37 J. Vibrational Dynamics and Solvatochromism of the Label SCN in Various Solvents
38 and Hemoglobin by Time Dependent IR and 2D-IR Spectroscopy. *Phys. Chem. Chem.*
39 *Phys.* **2014**, *16*, 19643-19653.
- 40 (49) Okuda, M.; Higashi, M.; Ohta, K.; Saito, S.; Tominaga, K. Theoretical Investigation on
41 Vibrational Frequency Fluctuations of SCN-Derivatized Vibrational Probe Molecule in
42 Water. *Chem. Phys.* **2018**, *512*, 82-87.
- 43 (50) Zanobini, C.; Bozovic, O.; Jankovic, B.; Koziol, K. L.; Johnson, P. J. M.; Hamm, P.;
44 Gulzar, A.; Wolf, S.; Stock, G. Azidohomoalanine: A Minimally Invasive, Versatile,
45 and Sensitive Infrared Label in Proteins to Study Ligand Binding. *J. Phys. Chem. B*
46 **2018**, *122*, 10118-10125.
- 47 (51) Pazos, I. M.; Ghosh, A.; Tucker, M. J.; Gai, F. Ester Carbonyl Vibration as a Sensitive
48 Probe of Protein Local Electric Field. *Angew. Chem. Int. Ed.* **2014**, *53*, 6080-6084.
- 49 (52) Stone, A. J. *The Theory of Intermolecular Forces*; Clarendon Press, Oxford, 1996.

- 1 (53) Buckingham, A. D. Molecular Quadrupole Moments. *Quarterly Reviews, Chemical*
2 *Society* **1959**, *13*, 183-214.
- 3 (54) Ritchie, J. P.; Copenhaver, A. S. Comparison of Potential-Derived Charge and Atomic
4 Multipole Models in Calculating Electrostatic Potentials and Energies of Some Nucleic
5 Acid Bases and Pairs. *J. Comput. Chem.* **1995**, *16*, 777-789.
- 6 (55) Buckingham, A. D.; Fowler, P. W. Do Electrostatic Interactions Predict Structures of
7 van der Waals Molecules? *J. Chem. Phys.* **1983**, *79*, 6426-6428.
- 8 (56) Koch, U.; Popelier, P. L. A.; Stone, A. J. Conformational Dependence of Atomic
9 Multipole Moments. *Chem. Phys. Lett.* **1995**, *238*, 253-260.
- 10 (57) Price, S. L.; Stone, A. J. The Electrostatic Interactions in van der Waals Complexes
11 Involving Aromatic Molecules. *J. Chem. Phys.* **1987**, *86*, 2859-2868.
- 12 (58) Koch, U.; Stone, A. J. Conformational Dependence of the Molecular Charge
13 Distribution and Its Influence on Intermolecular Interactions. *J. Chem. Soc., Faraday*
14 *Trans.* **1996**, *92*, 1701-1708.
- 15 (59) Price, S. L.; Stone, A. J. Electrostatic Models for Polypeptides: Can We Assume
16 Transferability? *J. Chem. Soc., Faraday Trans.* **1992**, *88*, 1755-1763.
- 17 (60) Longuet-Higgins, H. C.; Coulson, C. A. The Electronic States of Composite Systems.
18 *Proceedings of the Royal Society of London. Series A. Mathematical and Physical*
19 *Sciences* **1956**, *235*, 537-543.
- 20 (61) Longuet-Higgins, H. C. Spiers Memorial Lecture. Intermolecular Forces. *Discuss.*
21 *Faraday Soc.* **1965**, *40*, 7-18.
- 22 (62) Buckingham, A. D. Solvent Effects in Vibrational Spectroscopy. *Trans. Faraday*
23 *Society* **1960**, *56*, 753-760.
- 24 (63) Gordon, M. S.; Slipchenko, L.; Li, H.; Jensen, J. H. In *Annual Reports in Computational*
25 *Chemistry*; Spellmeyer, D. C.; Wheeler, R., Eds.; Elsevier, 2007; Vol. 3.
- 26 (64) Gordon, M. S.; Smith, Q. A.; Xu, P.; Slipchenko, L. V. Accurate First Principles Model
27 Potentials for Intermolecular Interactions. *Annu. Rev. Phys. Chem.* **2013**, *64*, 553-578.
- 28 (65) Gordon, M. S.; Fedorov, D. G.; Pruitt, S. R.; Slipchenko, L. V. Fragmentation Methods:
29 A Route to Accurate Calculations on Large Systems. *Chem. Rev.* **2012**, *112*, 632-672.
- 30 (66) Corcelli, S. A.; Lawrence, C. P.; Skinner, J. L. Combined Electronic
31 Structure/Molecular Dynamics Approach for Ultrafast Infrared Spectroscopy of Dilute
32 HOD in Liquid H₂O and D₂O. *J. Chem. Phys.* **2004**, *120*, 8107-8117.
- 33 (67) Schmidt, J. R.; Corcelli, S. A.; Skinner, J. L. Ultrafast Vibrational Spectroscopy of
34 Water and Aqueous N-Methylacetamide: Comparison of Different Electronic
35 Structure/Molecular Dynamics Approaches. *J. Chem. Phys.* **2004**, *121*, 8887-8896.
- 36 (68) Schmidt, J. R.; Corcelli, S. A.; Skinner, J. L. Pronounced Non-Condon Effects in the
37 Ultrafast Infrared Spectroscopy of Water. *J. Chem. Phys.* **2005**, *123*, 044513.
- 38 (69) Li, S.; Schmidt, J. R.; Corcelli, S. A.; Lawrence, C. P.; Skinner, J. L. Approaches for
39 the Calculation of Vibrational Frequencies in Liquids: Comparison to Benchmarks for
40 Azide/Water Clusters. *J. Chem. Phys.* **2006**, *124*, 204110.
- 41 (70) Cho, M. *Coherent Multidimensional Spectroscopy*; Springer Nature, 2019.
- 42 (71) Ernst, R. R.; Bodenhausen, G.; Wokaun, A. *Principles of Nuclear Magnetic Resonance*
43 *in One and Two Dimensions*; Clarendon Press: New York, 1987.
- 44 (72) Wüthrich, K. *NMR of Proteins and Nucleic Acids*; Wiley, 1991.
- 45 (73) Kwac, K.; Cho, M. Two-Color Pump-Probe Spectroscopies of Two- and Three-Level
46 Systems: 2-Dimensional Line Shapes and Solvation Dynamics. *J. Phys. Chem. A* **2003**,
47 *107*, 5903-5912.

- 1 (74) Feng, C.-J.; Dhayalan, B.; Tokmakoff, A. Refinement of Peptide Conformational
2 Ensembles by 2D IR Spectroscopy: Application to Ala-Ala-Ala. *Biophys. J.* **2018**, *114*,
3 2820-2832.
- 4 (75) Jones, K. C.; Peng, C. S.; Tokmakoff, A. Folding of a Heterogeneous β -Hairpin Peptide
5 from Temperature-Jump 2D IR Spectroscopy. *Proc. Natl. Acad. Sci. U.S.A.* **2013**, *110*,
6 2828.
- 7 (76) Maekawa, H.; Formaggio, F.; Toniolo, C.; Ge, N.-H. Onset of 3_{10} -Helical Secondary
8 Structure in Aib Oligopeptides Probed by Coherent 2D IR Spectroscopy. *J. Am. Chem.*
9 *Soc.* **2008**, *130*, 6556-6566.
- 10 (77) Maekawa, H.; Ballano, G.; Formaggio, F.; Toniolo, C.; Ge, N.-H. $^{13}\text{C}=\text{}^{18}\text{O}/^{15}\text{N}$ Isotope
11 Dependence of the Amide-I/II 2D IR Cross Peaks for the Fully Extended Peptides. *J.*
12 *Phys. Chem. C* **2014**, *118*, 29448-29457.
- 13 (78) Maekawa, H.; Poli, M. D.; Moretto, A.; Toniolo, C.; Ge, N.-H. Toward Detecting the
14 Formation of a Single Helical Turn by 2D IR Cross Peaks between the Amide-I and -II
15 Modes. *J. Phys. Chem. B* **2009**, *113*, 11775-11786.
- 16 (79) Hamm, P.; Lim, M.; DeGrado, W. F.; Hochstrasser, R. M. Pump/Probe Self
17 Heterodyned 2D Spectroscopy of Vibrational Transitions of a Small Globular Peptide.
18 *J. Chem. Phys.* **2000**, *112*, 1907-1916.
- 19 (80) Wang, J.; Zhuang, W.; Mukamel, S.; Hochstrasser, R. Two-Dimensional Infrared
20 Spectroscopy as a Probe of the Solvent Electrostatic Field for a Twelve Residue Peptide.
21 *J. Phys. Chem. B* **2008**, *112*, 5930-5937.
- 22 (81) Selig, O.; Cunha, A. V.; van Eldijk, M. B.; van Hest, J. C. M.; Jansen, T. L. C.; Bakker,
23 H. J.; Rezus, Y. L. A. Temperature-Induced Collapse of Elastin-Like Peptides Studied
24 by 2DIR Spectroscopy. *J. Phys. Chem. B* **2018**, *122*, 8243-8254.
- 25 (82) Huerta-Viga, A.; Domingos, S. R.; Amirjalayer, S.; Woutersen, S. A Salt-Bridge
26 Structure in Solution Revealed by 2D-IR Spectroscopy. *Phys. Chem. Chem. Phys.* **2014**,
27 *16*, 15784-15786.
- 28 (83) Chung, H. S.; Ganim, Z.; Jones, K. C.; Tokmakoff, A. Transient 2D IR Spectroscopy
29 of Ubiquitin Unfolding Dynamics. *Proc. Natl. Acad. Sci. U.S.A.* **2007**, *104*, 14237.
- 30 (84) Chung, J. K.; Thielges, M. C.; Fayer, M. D. Dynamics of the Folded and Unfolded
31 Villin Headpiece (Hp35) Measured with Ultrafast 2D IR Vibrational Echo
32 Spectroscopy. *Proc. Natl. Acad. Sci. U.S.A.* **2011**, *108*, 3578.
- 33 (85) DeFlores, L. P.; Ganim, Z.; Nicodemus, R. A.; Tokmakoff, A. Amide I'-II' 2D IR
34 Spectroscopy Provides Enhanced Protein Secondary Structural Sensitivity. *J. Am.*
35 *Chem. Soc.* **2009**, *131*, 3385-3391.
- 36 (86) Mukherjee, P.; Kass, I.; Arkin, I. T.; Zanni, M. T. Picosecond Dynamics of a Membrane
37 Protein Revealed by 2D IR. *Proc. Natl. Acad. Sci. U.S.A.* **2006**, *103*, 3528.
- 38 (87) Ramos, S.; Horness, R. E.; Collins, J. A.; Haak, D.; Thielges, M. C. Site-Specific 2D
39 IR Spectroscopy: A General Approach for the Characterization of Protein Dynamics
40 with High Spatial and Temporal Resolution. *Phys. Chem. Chem. Phys.* **2019**, *21*, 780-
41 788.
- 42 (88) Ramos, S.; Le Sueur, A. L.; Horness, R. E.; Specker, J. T.; Collins, J. A.; Thibodeau,
43 K. E.; Thielges, M. C. Heterogeneous and Highly Dynamic Interface in Plastocyanin-
44 Cytochrome F Complex Revealed by Site-Specific 2D-IR Spectroscopy. *J. Phys. Chem.*
45 *B* **2019**, *123*, 2114-2122.
- 46 (89) Schmidt-Engler, J. M.; Zangl, R.; Guldán, P.; Morgner, N.; Bredenbeck, J. Exploring
47 the 2D-IR Repertoire of the -SCN Label to Study Site-Resolved Dynamics and
48 Solvation in the Calcium Sensor Protein Calmodulin. *Phys. Chem. Chem. Phys.* **2020**,
49 *22*, 5463-5475.

- 1 (90) Woutersen, S.; Hamm, P. Time-Resolved Two-Dimensional Vibrational Spectroscopy
2 of a Short A-Helix in Water. *J. Chem. Phys.* **2001**, *115*, 7737-7743.
- 3 (91) Fang, C.; Wang, J.; Kim, Y. S.; Charnley, A. K.; Barber-Armstrong, W.; Smith, A. B.;
4 Decatur, S. M.; Hochstrasser, R. M. Two-Dimensional Infrared Spectroscopy of
5 Isotopomers of an Alanine Rich α -Helix. *J. Phys. Chem. B* **2004**, *108*, 10415-10427.
- 6 (92) King, J. T.; Arthur, E. J.; Brooks, C. L.; Kubarych, K. J. Site-Specific Hydration
7 Dynamics of Globular Proteins and the Role of Constrained Water in Solvent Exchange
8 with Amphiphilic Cosolvents. *J. Phys. Chem. B* **2012**, *116*, 5604-5611.
- 9 (93) Bredenbeck, J.; Helbing, J.; Nienhaus, K.; Nienhaus, G. U.; Hamm, P. Protein Ligand
10 Migration Mapped by Nonequilibrium 2D-IR Exchange Spectroscopy. *Proc. Natl.*
11 *Acad. Sci. U.S.A.* **2007**, *104*, 14243.
- 12 (94) Krummel, A. T.; Mukherjee, P.; Zanni, M. T. Inter and Intrastrand Vibrational
13 Coupling in DNA Studied with Heterodyned 2D-IR Spectroscopy. *J. Phys. Chem. B*
14 **2003**, *107*, 9165-9169.
- 15 (95) Ramakers, L. A. I.; Hithell, G.; May, J. J.; Greetham, G. M.; Donaldson, P. M.; Towrie,
16 M.; Parker, A. W.; Burley, G. A.; Hunt, N. T. 2D-IR Spectroscopy Shows That
17 Optimized DNA Minor Groove Binding of Hoechst33258 Follows an Induced Fit
18 Model. *J. Phys. Chem. B* **2017**, *121*, 1295-1303.
- 19 (96) Sanstead, P. J.; Stevenson, P.; Tokmakoff, A. Sequence-Dependent Mechanism of
20 DNA Oligonucleotide Dehybridization Resolved through Infrared Spectroscopy. *J. Am.*
21 *Chem. Soc.* **2016**, *138*, 11792-11801.
- 22 (97) Sanstead, P. J.; Tokmakoff, A. Direct Observation of Activated Kinetics and Downhill
23 Dynamics in DNA Dehybridization. *J. Phys. Chem. B* **2018**, *122*, 3088-3100.
- 24 (98) Bruening, E. M.; Schauss, J.; Siebert, T.; Fingerhut, B. P.; Elsaesser, T. Vibrational
25 Dynamics and Couplings of the Hydrated Rna Backbone: A Two-Dimensional Infrared
26 Study. *J. Phys. Chem. Lett.* **2018**, *9*, 583-587.
- 27 (99) Singh, P. C.; Inoue, K.; Nihonyanagi, S.; Yamaguchi, S.; Tahara, T. Femtosecond
28 Hydrogen Bond Dynamics of Bulk-Like and Bound Water at Positively and Negatively
29 Charged Lipid Interfaces Revealed by 2D Hd-Vsfg Spectroscopy. *Angew. Chem. Int.*
30 *Ed. Engl.* **2016**, *55*, 10621-10625.
- 31 (100) Woys, A. M.; Lin, Y.-S.; Reddy, A. S.; Xiong, W.; de Pablo, J. J.; Skinner, J. L.; Zanni,
32 M. T. 2D IR Line Shapes Probe Ovispirin Peptide Conformation and Depth in Lipid
33 Bilayers. *J. Am. Chem. Soc.* **2010**, *132*, 2832-2838.
- 34 (101) Fulfer, K. D.; Kuroda, D. G. A Comparison of the Solvation Structure and Dynamics
35 of the Lithium Ion in Linear Organic Carbonates with Different Alkyl Chain Lengths.
36 *Phys. Chem. Chem. Phys.* **2017**, *19*, 25140-25150.
- 37 (102) Kurochkin, D. V.; Naraharisetty, S. R. G.; Rubtsov, I. V. A Relaxation-Assisted 2D IR
38 Spectroscopy Method. *Proc. Natl. Acad. Sci. U.S.A.* **2007**, *104*, 14209.
- 39 (103) Lin, Z.; Rubtsov, I. V. Constant-Speed Vibrational Signaling Along Polyethyleneglycol
40 Chain up to 60-Å Distance. *Proc. Natl. Acad. Sci. U.S.A.* **2012**, *109*, 1413.
- 41 (104) Fecko, C. J.; Eaves, J. D.; Loparo, J. J.; Tokmakoff, A.; Geissler, P. L. Ultrafast
42 Hydrogen-Bond Dynamics in the Infrared Spectroscopy of Water. *Science* **2003**, *301*,
43 1698-1702.
- 44 (105) Roberts, S. T.; Petersen, P. B.; Ramasesha, K.; Tokmakoff, A.; Ufimtsev, I. S.;
45 Martinez, T. J. Observation of a Zundel-Like Transition State During Proton Transfer
46 in Aqueous Hydroxide Solutions. *Proc. Natl. Acad. Sci. U.S.A.* **2009**, *106*, 15154.
- 47 (106) Ghosh, A.; Qiu, J.; DeGrado, W. F.; Hochstrasser, R. M. Tidal Surge in the M2 Proton
48 Channel, Sensed by 2D IR Spectroscopy. *Proc. Natl. Acad. Sci. U.S.A.* **2011**, *108*, 6115.

- 1 (107) Manor, J.; Mukherjee, P.; Lin, Y.-S.; Leonov, H.; Skinner, J. L.; Zanni, M. T.; Arkin,
2 I. T. Gating Mechanism of the Influenza a M2 Channel Revealed by 1D and 2D IR
3 Spectroscopies. *Structure* **2009**, *17*, 247-254.
- 4 (108) Pensack, R. D.; Banyas, K. M.; Barbour, L. W.; Hegadorn, M.; Asbury, J. B. Ultrafast
5 Vibrational Spectroscopy of Charge-Carrier Dynamics in Organic Photovoltaic
6 Materials. *Phys. Chem. Chem. Phys.* **2009**, *11*, 2575-2591.
- 7 (109) Mukamel, S. Nonimpact Unified Theory of Four-Wave Mixing and Two-Photon
8 Processes. *Phys. Rev. A* **1983**, *28*, 3480-3492.
- 9 (110) Jansen, T. L. C.; Saito, S.; Jeon, J.; Cho, M. Theory of Coherent Two-Dimensional
10 Vibrational Spectroscopy. *J. Chem. Phys.* **2019**, *150*, 100901.
- 11 (111) Kwac, K.; Lee, H.; Cho, M. Non-Gaussian Statistics of Amide I Mode Frequency
12 Fluctuation of N-Methylacetamide in Methanol Solution: Linear and Nonlinear
13 Vibrational Spectra. *J. Chem. Phys.* **2004**, *120*, 1477-1490.
- 14 (112) Roy, S.; Pshenichnikov, M. S.; Jansen, T. L. C. Analysis of 2D Cs Spectra for Systems
15 with Non-Gaussian Dynamics. *J. Phys. Chem. B* **2011**, *115*, 5431-5440.
- 16 (113) Dinpajoo, M.; Matyushov, D. V. Non-Gaussian Lineshapes and Dynamics of Time-
17 Resolved Linear and Nonlinear (Correlation) Spectra. *J. Phys. Chem. B* **2014**, *118*,
18 7925-7936.
- 19 (114) Woutersen, S.; Mu, Y.; Stock, G.; Hamm, P. Hydrogen-Bond Lifetime Measured by
20 Time-Resolved 2D-IR Spectroscopy: N-Methylacetamide in Methanol. *Chem. Phys.*
21 **2001**, *266*, 137-147.
- 22 (115) Kim, Y. S.; Hochstrasser, R. M. Chemical Exchange 2D IR of Hydrogen-Bond Making
23 and Breaking. *Proc. Natl. Acad. Sci. U.S.A.* **2005**, *102*, 11185.
- 24 (116) Šanda, F.; Mukamel, S. Stochastic Simulation of Chemical Exchange in Two
25 Dimensional Infrared Spectroscopy. *J. Chem. Phys.* **2006**, *125*, 014507.
- 26 (117) Kwak, K.; Zheng, J.; Cang, H.; Fayer, M. D. Ultrafast Two-Dimensional Infrared
27 Vibrational Echo Chemical Exchange Experiments and Theory. *J. Phys. Chem. B* **2006**,
28 *110*, 19998-20013.
- 29 (118) Jansen, T. L. C.; Knoester, J. Calculation of Two-Dimensional Infrared Spectra of
30 Ultrafast Chemical Exchange with Numerical Langevin Simulations. *J. Chem. Phys.*
31 **2007**, *127*, 234502.
- 32 (119) Farag, M. H.; Hoenders, B. J.; Knoester, J.; Jansen, T. L. C. Spectral Line Shapes in
33 Linear Absorption and Two-Dimensional Spectroscopy with Skewed Frequency
34 Distributions. *J. Chem. Phys.* **2017**, *146*, 234201.
- 35 (120) Jansen, T. L. C.; Cringus, D.; Pshenichnikov, M. S. Dissimilar Dynamics of Coupled
36 Water Vibrations. *J. Phys. Chem. A* **2009**, *113*, 6260-6265.
- 37 (121) Liang, C.; Jansen, T. L. C. An Efficient N^3 -Scaling Propagation Scheme for Simulating
38 Two-Dimensional Infrared and Visible Spectra. *J. Chem. Theory Comput.* **2012**, *8*,
39 1706-1713.
- 40 (122) Falvo, C.; Palmieri, B.; Mukamel, S. Coherent Infrared Multidimensional Spectra of
41 the OH Stretching Band in Liquid Water Simulated by Direct Nonlinear Exciton
42 Propagation. *J. Chem. Phys.* **2009**, *130*, 184501.
- 43 (123) Fleming, G. R.; Cho, M. Chromophore-Solvent Dynamics. *Annu. Rev. Phys. Chem.*
44 **1996**, *47*, 109-134.
- 45 (124) Jansen, T. L. C.; Knoester, J. Nonadiabatic Effects in the Two-Dimensional Infrared
46 Spectra of Peptides: Application to Alanine Dipeptide. *J. Phys. Chem. B* **2006**, *110*,
47 22910-22916.
- 48 (125) <https://mukamel.ps.uci.edu/software.html>.
- 49 (126) https://github.com/GHlacour/NISE_2015.

- 1 (127) Torii, H. Time-Domain Calculations of the Polarized Raman and Two-Dimensional
2 Infrared Spectra of Liquid N,N-Dimethylformamide. *Chem. Phys. Lett.* **2005**, *414*, 417-
3 422.
- 4 (128) Tran, H.; Cunha, A. V.; Shephard, J. J.; Shalit, A.; Hamm, P.; Jansen, T. L. C.;
5 Salzmann, C. G. 2D IR Spectroscopy of High-Pressure Phases of Ice. *J. Chem. Phys.*
6 **2017**, *147*, 144501.
- 7 (129) Kobus, M.; Gorbunov, R. D.; Nguyen, P. H.; Stock, G. Nonadiabatic Vibrational
8 Dynamics and Spectroscopy of Peptides: A Quantum-Classical Description. *Chem.*
9 *Phys.* **2008**, *347*, 208-217.
- 10 (130) Paarmann, A.; Hayashi, T.; Mukamel, S.; Miller, R. J. D. Probing Intermolecular
11 Couplings in Liquid Water with Two-Dimensional Infrared Photon Echo Spectroscopy.
12 *J. Chem. Phys.* **2008**, *128*, 191103.
- 13 (131) Tomasi, J.; Mennucci, B.; Cammi, R. Quantum Mechanical Continuum Solvation
14 Models. *Chem. Rev.* **2005**, *105*, 2999-3094.
- 15 (132) Kirkwood, J. G. On the Theory of Strong Electrolyte Solutions. *J. Chem. Phys.* **1934**,
16 *2*, 767-781.
- 17 (133) Kirkwood, J. G. The Dielectric Polarization of Polar Liquids. *J. Chem. Phys.* **1939**, *7*,
18 911-919.
- 19 (134) Onsager, L. Electric Moments of Molecules in Liquid. *J. Am. Chem. Soc.* **1936**, *58*,
20 1486-1493.
- 21 (135) Rivail, J.-L.; Rinaldi, D. A Quantum Chemical Approach to Dielectric Solvent Effects
22 in Molecular Liquids. *Chem. Phys.* **1976**, *18*, 233-242.
- 23 (136) Cammi, R.; Tomasi, J. Remarks on the Use of the Apparent Surface Charges (ASC)
24 Methods in Solvation Problems: Iterative Versus Matrix-Inversion Procedures and the
25 Renormalization of the Apparent Charges. *J. Comput. Chem.* **1995**, *16*, 1449-1458.
- 26 (137) Miertuš, S.; Scrocco, E.; Tomasi, J. Electrostatic Interaction of a Solute with a
27 Continuum. A Direct Utilizaion of Ab Initio Molecular Potentials for the Prevision of
28 Solvent Effects. *Chem. Phys.* **1981**, *55*, 117-129.
- 29 (138) Klamt, A.; Schüürmann, G. Cosmo: A New Approach to Dielectric Screening in
30 Solvents with Explicit Expressions for the Screening Energy and Its Gradient. *J. Chem.*
31 *Soc. Perkin Trans. 2* **1993**, 799-805.
- 32 (139) Krimm, S.; Bandekar, J. In *Adv. Protein Chem.*; Anfinsen, C. B.; Edsall, J. T.; Richards,
33 F. M., Eds.; Academic Press, 1986; Vol. 38.
- 34 (140) Hobza, P.; Zahradnik, R. Intermolecular Interactions between Medium-Sized Systems.
35 Nonempirical and Empirical Calculations of Interaction Energies. Successes and
36 Failures. *Chem. Rev.* **1988**, *88*, 871-897.
- 37 (141) Jeziorski, B.; Moszynski, R.; Szalewicz, K. Perturbation-Theory Approach to
38 Intermolecular Potential-Energy Surfaces of van der Waals Complexes. *Chem. Rev.*
39 **1994**, *94*, 1887-1930.
- 40 (142) Kitaura, K.; Morokuma, K. A New Energy Decomposition Scheme for Molecular
41 Interactions within the Hartree-Fock Approximation. *Int. J. Quantum Chem* **1976**, *10*,
42 325-340.
- 43 (143) Błasiak, B.; Cho, M. Vibrational Solvatochromism. II. A First-Principle Theory of
44 Solvation-Induced Vibrational Frequency Shift Based on Effective Fragment Potential
45 Method. *J. Chem. Phys.* **2014**, *140*, 164107.
- 46 (144) Li, H.; Gordon, M. S.; Jensen, J. H. Charge Transfer Interaction in the Effective
47 Fragment Potential Method. *J. Chem. Phys.* **2006**, *124*, 214108.
- 48 (145) Buckingham, A. D. Solvent Effects in Infra-Red Spectroscopy. *Proc. R. Soc. London*,
49 *Ser. A* **1958**, *248*, 169-182.

- 1 (146) Buckingham, A. D.; Sutherland, G. B. B. M.; Pople, J. A.; Pullin, A. D. E.; Thompson,
2 H. W. A Theory of Frequency, Intensity and Band-Width Changes Due to Solvents in
3 Infra-Red Spectroscopy. *Proceedings of the Royal Society of London. Series A.*
4 *Mathematical and Physical Sciences* **1960**, *255*, 32-39.
- 5 (147) Cho, M. Correlation between Electronic and Molecular Structure Distortions and
6 Vibrational Properties. I. Adiabatic Approximations. *J. Chem. Phys.* **2003**, *118*, 3480-
7 3490.
- 8 (148) Cho, M. Vibrational Solvatochromism and Electrochromism: Coarse-Grained Models
9 and Their Relationships. *J. Chem. Phys.* **2009**, *130*, 094505.
- 10 (149) McDowell, S. A. C.; Buckingham, A. D. A Theory of Vibrational Frequency Shifts
11 Revisited: Application to Dimers of LiH with the Inert Gases He, Ne, Ar and Kr. *Mol.*
12 *Phys.* **2005**, *103*, 257-262.
- 13 (150) McDowell, S. A. C.; Buckingham, A. D. On the Correlation between Bond-Length
14 Change and Vibrational Frequency Shift in Hydrogen-Bonded Complexes: A
15 Computational Study of Y...HCl Dimers (Y = N₂, CO, BF). *J. Am. Chem. Soc.* **2005**,
16 *127*, 15515-15520.
- 17 (151) McDowell, S. A. C.; Buckingham, A. D. Comparison of Some Vibrational Features of
18 FARH...Rg and FH...Rg Complexes (Rg=He, Ne, Ar, Kr). *Spectrochimica Acta Part A:*
19 *Molecular and Biomolecular Spectroscopy* **2005**, *61*, 1603-1609.
- 20 (152) Buckingham, A. D.; Del Bene, J. E.; McDowell, S. A. C. The Hydrogen Bond. *Chem.*
21 *Phys. Lett.* **2008**, *463*, 1-10.
- 22 (153) Herrebout, W. A.; Delanoye, S. N.; van der Veken, B. J. Blue-Shifting or Red-Shifting
23 Hydrogen Bonding? Predictions for Haloform Complexes with Dimethyl Ether on the
24 Basis of Perturbation Theory. *J. Phys. Chem. A* **2004**, *108*, 6059-6064.
- 25 (154) Błasiak, B.; Cho, M. Vibrational Solvatochromism. III. Rigorous Treatment of the
26 Dispersion Interaction Contribution. *J. Chem. Phys.* **2015**, *143*, 164111.
- 27 (155) Błasiak, B.; Ritchie, A. W.; Webb, L. J.; Cho, M. Vibrational Solvatochromism of
28 Nitrile Infrared Probes: Beyond the Vibrational Stark Dipole Approach. *Phys. Chem.*
29 *Chem. Phys.* **2016**, *18*, 18094-18111.
- 30 (156) Maj, M.; Ahn, C.; Błasiak, B.; Kwak, K.; Han, H.; Cho, M. Isonitrile as an
31 Ultrasensitive Infrared Reporter of Hydrogen-Bonding Structure and Dynamics. *J.*
32 *Phys. Chem. B* **2016**, *120*, 10167-10180.
- 33 (157) Mandado, M.; Hermida-Ramón, J. M. Electron Density Based Partitioning Scheme of
34 Interaction Energies. *J. Chem. Theory Comput.* **2011**, *7*, 633-641.
- 35 (158) Bauer, E.; Magat, M. Sur La Déformation Des Molécules En Phase Condensée Et La «
36 Liaison Hydrogène ». *J. Phys. Radium* **1938**, *9*, 319-330.
- 37 (159) Kirkwood, J. G. Theory of Solutions of Molecules Containing Widely Separated
38 Charges with Special Application to Zwitterions. *J. Chem. Phys.* **1934**, *2*, 351-361.
- 39 (160) Ben-Amotz, D.; Lee, M. R.; Cho, S. Y.; List, D. J. Solvent and Pressure-Induced
40 Perturbations of the Vibrational Potential Surface of Acetonitrile. *J. Chem. Phys.* **1992**,
41 *96*, 8781-8792.
- 42 (161) Fawcett, W. R.; Liu, G.; Kessler, T. E. Solvent-Induced Frequency Shifts in the Infrared
43 Spectrum of Acetonitrile in Organic Solvents. *J. Phys. Chem.* **1993**, *97*, 9293-9298.
- 44 (162) Fawcett, W. R.; Kloss, A. A. Solvent-Induced Frequency Shifts in the Infrared
45 Spectrum of Dimethyl Sulfoxide in Organic Solvents. *J. Phys. Chem.* **1996**, *100*, 2019-
46 2024.
- 47 (163) Gutmann, V.; Resch, G.; Linert, W. Structural Variability in Solutions. *Coord. Chem.*
48 *Rev.* **1982**, *43*, 133-164.

- 1 (164) Reimers, J. R.; Hall, L. E. The Solvation of Acetonitrile. *J. Am. Chem. Soc.* **1999**, *121*,
2 3730-3744.
- 3 (165) Fafarman, A. T.; Sigala, P. A.; Herschlag, D.; Boxer, S. G. Decomposition of
4 Vibrational Shifts of Nitriles into Electrostatic and Hydrogen-Bonding Effects. *J. Am.*
5 *Chem. Soc.* **2010**, *132*, 12811-12813.
- 6 (166) Bagchi, S.; Fried, S. D.; Boxer, S. G. A Solvatochromic Model Calibrates Nitriles'
7 Vibrational Frequencies to Electrostatic Fields. *J. Am. Chem. Soc.* **2012**, *134*, 10373-
8 10376.
- 9 (167) Zhang, W.; Markiewicz, B. N.; Doerksen, R. S.; Smith, I. I. I. A. B.; Gai, F. C≡N
10 Stretching Vibration of 5-Cyanotryptophan as an Infrared Probe of Protein Local
11 Environment: What Determines Its Frequency? *Phys. Chem. Chem. Phys.* **2016**, *18*,
12 7027-7034.
- 13 (168) Rodgers, J. M.; Abaskharon, R. M.; Ding, B.; Chen, J.; Zhang, W.; Gai, F. Fermi
14 Resonance as a Means to Determine the Hydrogen-Bonding Status of Two Infrared
15 Probes. *Phys. Chem. Chem. Phys.* **2017**, *19*, 16144-16150.
- 16 (169) Kamlet, M. J.; Taft, R. W. The Solvatochromic Comparison Method. I. The β-Scale of
17 Solvent Hydrogen-Bond Acceptor (HBA) Basicities. *J. Am. Chem. Soc.* **1976**, *98*, 377-
18 383.
- 19 (170) Taft, R. W.; Kamlet, M. J. The Solvatochromic Comparison Method. 2. The α-Scale of
20 Solvent Hydrogen-Bond Donor (HBD) Acidities. *J. Am. Chem. Soc.* **1976**, *98*, 2886-
21 2894.
- 22 (171) Kamlet, M. J.; Abboud, J. L.; Taft, R. W. The Solvatochromic Comparison Method. 6.
23 The π* Scale of Solvent Polarities. *J. Am. Chem. Soc.* **1977**, *99*, 6027-6038.
- 24 (172) Hush, N. S.; Reimers, J. R. Vibrational Stark Spectroscopy. 1. Basic Theory and
25 Application to the CO Stretch. *J. Phys. Chem.* **1995**, *99*, 15798-15805.
- 26 (173) Reimers, J. R.; Zeng, J.; Hush, N. S. Vibrational Stark Spectroscopy. 2. Application to
27 the CN Stretch in Hcn and Acetonitrile. *J. Phys. Chem.* **1996**, *100*, 1498-1504.
- 28 (174) Andrews, S. S.; Boxer, S. G. Vibrational Stark Effects of Nitriles II. Physical Origins
29 of Stark Effects from Experiment and Perturbation Models. *J. Phys. Chem. A* **2002**, *106*,
30 469-477.
- 31 (175) Andrews, S. S.; Boxer, S. G. Vibrational Stark Effects of Nitriles I. Methods and
32 Experimental Results. *J. Phys. Chem. A* **2000**, *104*, 11853-11863.
- 33 (176) Liptay, W. Electrochromism and Solvatochromism. *Angewandte Chemie International*
34 *Edition in English* **1969**, *8*, 177-188.
- 35 (177) Suydam, I. T.; Boxer, S. G. Vibrational Stark Effects Calibrate the Sensitivity of
36 Vibrational Probes for Electric Fields in Proteins. *Biochemistry* **2003**, *42*, 12050-12055.
- 37 (178) Levinson, N. M.; Fried, S. D.; Boxer, S. G. Solvent-Induced Infrared Frequency Shifts
38 in Aromatic Nitriles Are Quantitatively Described by the Vibrational Stark Effect. *J.*
39 *Phys. Chem. B* **2012**, *116*, 10470-10476.
- 40 (179) Dalosto, S. D.; Vanderkooi, J. M.; Sharp, K. A. Vibrational Stark Effects on Carbonyl,
41 Nitrile, and Nitrosyl Compounds Including Heme Ligands, CO, CN, and NO, Studied
42 with Density Functional Theory. *J. Phys. Chem. B* **2004**, *108*, 6450-6457.
- 43 (180) Bublitz, G. U.; Boxer, S. G. Stark Spectroscopy: Applications in Chemistry, Biology,
44 and Materials Science. *Annu. Rev. Phys. Chem.* **1997**, *48*, 213-242.
- 45 (181) Wortmann, R.; Bishop, D. M. Effective Polarizabilities and Local Field Corrections for
46 Nonlinear Optical Experiments in Condensed Media. *J. Chem. Phys.* **1998**, *108*, 1001-
47 1007.

- 1 (182) Fried, S. D.; Boxer, S. G. Measuring Electric Fields and Noncovalent Interactions
2 Using the Vibrational Stark Effect. *Acc. Chem. Res.* **2015**, *48*, 998-1006.
- 3 (183) Choi, J.-H.; Oh, K.-I.; Lee, H.; Lee, C.; Cho, M. Nitrile and Thiocyanate IR Probes:
4 Quantum Chemistry Calculation Studies and Multivariate Least-Square Fitting
5 Analysis. *J. Chem. Phys.* **2008**, *128*, 134506.
- 6 (184) First, J. T.; Slocum, J. D.; Webb, L. J. Quantifying the Effects of Hydrogen Bonding
7 on Nitrile Frequencies in GFP: Beyond Solvent Exposure. *J. Phys. Chem. B* **2018**, *122*,
8 6733-6743.
- 9 (185) Błasiak, B.; Lee, H.; Cho, M. Vibrational Solvatochromism: Towards Systematic
10 Approach to Modeling Solvation Phenomena. *J. Chem. Phys.* **2013**, *139*, 044111.
- 11 (186) Schkolnik, G.; Utesch, T.; Salewski, J.; Tenger, K.; Millo, D.; Kranich, A.; Zebger, I.;
12 Schulz, C.; Zimányi, L.; Rákhely, G. et al. Mapping Local Electric Fields in Proteins at
13 Biomimetic Interfaces. *Chem. Commun.* **2012**, *48*, 70-72.
- 14 (187) Oklejas, V.; Sjostrom, C.; Harris, J. M. Surface-Enhanced Raman Scattering Based
15 Vibrational Stark Effect as a Spatial Probe of Interfacial Electric Fields in the Diffuse
16 Double Layer. *J. Phys. Chem. B* **2003**, *107*, 7788-7794.
- 17 (188) Lee, H.; Choi, J.-H.; Cho, M. Vibrational Solvatochromism and Electrochromism. II.
18 Multipole Analysis. *J. Chem. Phys.* **2012**, *137*, 114307.
- 19 (189) Rey, R.; Hynes, J. T. Vibrational Phase and Energy Relaxation of CN⁻ in Water. *J.*
20 *Chem. Phys.* **1998**, *108*, 142-153.
- 21 (190) Morales, C. M.; Thompson, W. H. Molecular-Level Mechanisms of Vibrational
22 Frequency Shifts in a Polar Liquid. *J. Phys. Chem. B* **2011**, *115*, 7597-7605.
- 23 (191) Li, X.; Liu, L.; Schlegel, H. B. On the Physical Origin of Blue-Shifted Hydrogen Bonds.
24 *J. Am. Chem. Soc.* **2002**, *124*, 9639-9647.
- 25 (192) Delanoye, S. N.; Herrebut, W. A.; van der Veken, B. J. Blue Shifting Hydrogen
26 Bonding in the Complexes of Chlorofluoro Haloforms with Acetone-*d*₆ and Oxirane-*d*₄.
27 *J. Am. Chem. Soc.* **2002**, *124*, 11854-11855.
- 28 (193) Zierkiewicz, W.; Jurečka, P.; Hobza, P. On Differences between Hydrogen Bonding
29 and Improper Blue-Shifting Hydrogen Bonding. *ChemPhysChem* **2005**, *6*, 609-617.
- 30 (194) Rodziewicz, P.; Rutkowski, K. S.; Melikova, S. M.; Koll, A. Ab Initio Studies of
31 Electron Acceptor–Donor Interactions with Blue- and Red-Shifted Hydrogen Bonds.
32 *ChemPhysChem* **2005**, *6*, 1282-1292.
- 33 (195) Zhou, P.-P.; Qiu, W.-Y. Red-Shifted Hydrogen Bonds and Blue-Shifted van der Waals
34 Contact in the Standard Watson–Crick Adenine–Thymine Base Pair. *J. Phys. Chem. A*
35 **2009**, *113*, 10306-10320.
- 36 (196) Mo, Y.; Wang, C.; Guan, L.; Braïda, B.; Hiberty, P. C.; Wu, W. On the Nature of
37 Blueshifting Hydrogen Bonds. *Chem. Eur. J.* **2014**, *20*, 8444-8452.
- 38 (197) Lee, H.; Choi, J.-H.; Cho, M. Vibrational Solvatochromism and Electrochromism of
39 Cyanide, Thiocyanate, and Azide Anions in Water. *Phys. Chem. Chem. Phys.* **2010**, *12*,
40 12658-12669.
- 41 (198) Brinzer, T.; Berquist, E. J.; Ren, Z.; Dutta, S.; Johnson, C. A.; Krisher, C. S.; Lambrecht,
42 D. S.; Garrett-Roe, S. Ultrafast Vibrational Spectroscopy (2D-IR) of CO₂ in Ionic
43 Liquids: Carbon Capture from Carbon Dioxide’s Point of View. *J. Chem. Phys.* **2015**,
44 *142*, 212425.
- 45 (199) Wright, A. M.; Howard, A. A.; Howard, J. C.; Tschumper, G. S.; Hammer, N. I. Charge
46 Transfer and Blue Shifting of Vibrational Frequencies in a Hydrogen Bond Acceptor.
47 *J. Phys. Chem. A* **2013**, *117*, 5435-5446.

- 1 (200) Lindquist, B. A.; Corcelli, S. A. Nitrile Groups as Vibrational Probes: Calculations of
2 the C≡N Infrared Absorption Line Shape of Acetonitrile in Water and Tetrahydrofuran.
3 *J. Phys. Chem. B* **2008**, *112*, 6301-6303.
- 4 (201) Lindquist, B. A.; Haws, R. T.; Corcelli, S. A. Optimized Quantum
5 Mechanics/Molecular Mechanics Strategies for Nitrile Vibrational Probes: Acetonitrile
6 and *para*-Tolunitrile in Water and Tetrahydrofuran. *J. Phys. Chem. B* **2008**, *112*, 13991-
7 14001.
- 8 (202) Stewart, J. J. P. Optimization of Parameters for Semiempirical Methods II. Applications.
9 *J. Comput. Chem.* **1989**, *10*, 221-264.
- 10 (203) Xu, R. J.; Błasiak, B.; Cho, M.; Layfield, J. P.; Londergan, C. H. A Direct, Quantitative
11 Connection between Molecular Dynamics Simulations and Vibrational Probe Line
12 Shapes. *J. Phys. Chem. Lett.* **2018**, *9*, 2560-2567.
- 13 (204) Jensen, J. H.; Gordon, M. S. An Approximate Formula for the Intermolecular Pauli
14 Repulsion between Closed Shell Molecules. II. Application to the Effective Fragment
15 Potential Method. *J. Chem. Phys.* **1998**, *108*, 4772-4782.
- 16 (205) Jensen, J. H.; Gordon, M. S. An Approximate Formula for the Intermolecular Pauli
17 Repulsion between Closed Shell Molecules. *Mol. Phys.* **1996**, *89*, 1313-1325.
- 18 (206) Chen, Y.; Li, H. Intermolecular Interaction in Water Hexamer. *J. Phys. Chem. A* **2010**,
19 *114*, 11719-11724.
- 20 (207) Chen, W.; Gordon, M. S. Energy Decomposition Analyses for Many-Body Interaction
21 and Applications to Water Complexes. *J. Phys. Chem.* **1996**, *100*, 14316-14328.
- 22 (208) Antony, J.; Brüske, B.; Grimme, S. Cooperativity in Noncovalent Interactions of
23 Biologically Relevant Molecules. *Phys. Chem. Chem. Phys.* **2009**, *11*, 8440-8447.
- 24 (209) Gora, R. W.; Sokalski, W. A.; Leszczynski, J.; Pett, V. B. The Nature of Interactions in
25 the Ionic Crystal of 3-Pentenenitrile, 2-Nitro-5-oxo, Ion(-1), Sodium. *J. Phys. Chem.*
26 *B* **2005**, *109*, 2027-2033.
- 27 (210) Chaudret, R.; Gresh, N.; Parisel, O.; Piquemal, J.-P. Many-Body Exchange-Repulsion
28 in Polarizable Molecular Mechanics. I. Orbital-Based Approximations and
29 Applications to Hydrated Metal Cation Complexes. *J. Comput. Chem.* **2011**, *32*, 2949-
30 2957.
- 31 (211) Michaud-Agrawal, N.; Denning, E. J.; Woolf, T. B.; Beckstein, O. Mdanalysis: A
32 Toolkit for the Analysis of Molecular Dynamics Simulations. *J. Comput. Chem.* **2011**,
33 *32*, 2319-2327.
- 34 (212) Gowers, R. J.; Linke, M.; Barnoud, J.; Reddy, T. y. J. E.; Melo, M. N.; Seyler, S. L.;
35 Domanski, J.; Dotson, D. L.; Buchoux, S.; Kenney, I. M. et al. In *Proceedings of the*
36 *15th Python in Science Conference*; Benthall, S.; Rostrup, S., Eds., 2016.
- 37 (213) Abraham, M. J.; Murtola, T.; Schulz, R.; Páll, S.; Smith, J. C.; Hess, B.; Lindahl, E.
38 Gromacs: High Performance Molecular Simulations through Multi-Level Parallelism
39 from Laptops to Supercomputers. *SoftwareX* **2015**, *1-2*, 19-25.
- 40 (214) Case, D. A.; Ben-Shalom, I. Y.; Brozell, S. R.; Cerutti, D. S.; T.E. Cheatham, I.;
41 Cruzeiro, V. W. D.; Darden, T. A.; Duke, R. E.; Ghoreishi, D.; Gilson, M. K. et al.
42 *Amber 2018*; University of California: San Francisco, 2018.
- 43 (215) Phillips, J. C.; Braun, R.; Wang, W.; Gumbart, J.; Tajkhorshid, E.; Villa, E.; Chipot, C.;
44 Skeel, R. D.; Kalé, L.; Schulten, K. Scalable Molecular Dynamics with NAMD. *J.*
45 *Comput. Chem.* **2005**, *26*, 1781-1802.
- 46 (216) Sengupta, N.; Maekawa, H.; Zhuang, W.; Toniolo, C.; Mukamel, S.; Tobias, D. J.; Ge,
47 N.-H. Sensitivity of 2D IR Spectra to Peptide Helicity: A Concerted Experimental and
48 Simulation Study of an Octapeptide. *J. Phys. Chem. B* **2009**, *113*, 12037-12049.

- 1 (217) Maekawa, H.; Ge, N.-H. Comparative Study of Electrostatic Models for the Amide-I
2 and -II Modes: Linear and Two-Dimensional Infrared Spectra. *J. Phys. Chem. B* **2010**,
3 *114*, 1434-1446.
- 4 (218) Oh, K.-I.; Choi, J.-H.; Lee, J.-H.; Han, J.-B.; Lee, H.; Cho, M. Nitrile and Thiocyanate
5 IR Probes: Molecular Dynamics Simulation Studies. *J. Chem. Phys.* **2008**, *128*, 154504.
- 6 (219) Kwac, K.; Cho, M. Molecular Dynamics Simulation Study of N-Methylacetamide in
7 Water. I. Amide I Mode Frequency Fluctuation. *J. Chem. Phys.* **2003**, *119*, 2247-2255.
- 8 (220) Ham, S.; Kim, J.-H.; Lee, H.; Cho, M. Correlation between Electronic and Molecular
9 Structure Distortions and Vibrational Properties. II. Amide I Modes of NMA-nD₂O
10 Complexes. *J. Chem. Phys.* **2003**, *118*, 3491-3498.
- 11 (221) Bouř, P.; Keiderling, T. A. Empirical Modeling of the Peptide Amide I Band IR
12 Intensity in Water Solution. *J. Chem. Phys.* **2003**, *119*, 11253-11262.
- 13 (222) Hahn, S.; Lee, H.; Cho, M. Theoretical Calculations of Infrared Absorption, Vibrational
14 Circular Dichroism, and Two-Dimensional Vibrational Spectra of Acetylproline in
15 Liquids Water and Chloroform. *J. Chem. Phys.* **2004**, *121*, 1849-1865.
- 16 (223) Choi, J.-H.; Hahn, S.; Cho, M. Amide I IR, VCD, and 2d IR Spectra of Isotope-Labeled
17 α -Helix in Liquid Water: Numerical Simulation Studies. *Int. J. Quantum Chem* **2005**,
18 *104*, 616-634.
- 19 (224) Kwac, K.; Cho, M. Hydrogen Bonding Dynamics and Two-Dimensional Vibrational
20 Spectroscopy: N-Methylacetamide in Liquid Methanol. *J. Raman Spectrosc.* **2005**, *36*,
21 326-336.
- 22 (225) Watson, T. M.; Hirst, J. D. Theoretical Studies of the Amide I Vibrational Frequencies
23 of [Leu]-Enkephalin. *Mol. Phys.* **2005**, *103*, 1531-1546.
- 24 (226) DeCamp, M. F.; DeFlores, L.; McCracken, J. M.; Tokmakoff, A.; Kwac, K.; Cho, M.
25 Amide I Vibrational Dynamics of N-Methylacetamide in Polar Solvents: The Role of
26 Electrostatic Interactions. *J. Phys. Chem. B* **2005**, *109*, 11016-11026.
- 27 (227) Hayashi, T.; Jansen, T. L. C.; Zhuang, W.; Mukamel, S. Collective Solvent Coordinates
28 for the Infrared Spectrum of HOD in D₂O Based on an ab initio Electrostatic Map. *J.*
29 *Phys. Chem. A* **2005**, *109*, 64-82.
- 30 (228) Hayashi, T.; Zhuang, W.; Mukamel, S. Electrostatic DFT Map for the Complete
31 Vibrational Amide Band of NMA. *J. Phys. Chem. A* **2005**, *109*, 9747-9759.
- 32 (229) Bouř, P.; Michalík, D.; Kapitán, J. Empirical Solvent Correction for Multiple Amide
33 Group Vibrational Modes. *J. Chem. Phys.* **2005**, *122*, 144501.
- 34 (230) Jansen, T. L. C.; Dijkstra, A. G.; Watson, T. M.; Hirst, J. D.; Knoester, J. Modeling the
35 Amide I Bands of Small Peptides. *J. Chem. Phys.* **2006**, *125*, 044312.
- 36 (231) Jansen, T. L. C.; Knoester, J. A Transferable Electrostatic Map for Solvation Effects on
37 Amide I Vibrations and Its Application to Linear and Two-Dimensional Spectroscopy.
38 *J. Chem. Phys.* **2006**, *124*, 044502.
- 39 (232) Choi, J.-H.; Oh, K.-I.; Cho, M. Azido-Derivatized Compounds as IR Probes of Local
40 Electrostatic Environment: Theoretical Studies. *J. Chem. Phys.* **2008**, *129*, 174512.
- 41 (233) Lin, Y. S.; Shorb, J. M.; Mukherjee, P.; Zanni, M. T.; Skinner, J. L. Empirical Amide I
42 Vibrational Frequency Map: Application to 2D-IR Line Shapes for Isotope-Edited
43 Membrane Peptide Bundles. *J. Phys. Chem. B* **2009**, *113*, 592-602.
- 44 (234) Choi, J.-H.; Cho, M. Vibrational Solvatochromism and Electrochromism of Infrared
45 Probe Molecules Containing C=O, C≡N, C=O, or C-F Vibrational Chromophore. *J.*
46 *Chem. Phys.* **2011**, *134*, 154513.
- 47 (235) Roy, S.; Lessing, J.; Meisl, G.; Ganim, Z.; Tokmakoff, A.; Knoester, J.; Jansen, T. L.
48 C. Solvent and Conformation Dependence of Amide I Vibrations in Peptides and
49 Proteins Containing Proline. *J. Chem. Phys.* **2011**, *135*, 234507.

- 1 (236) Choi, J.-H.; Raleigh, D.; Cho, M. Azido Homocysteine Is a Useful Infrared Probe for
2 Monitoring Local Electrostatics and Side-Chain Solvation in Proteins. *J. Phys. Chem.*
3 *Lett.* **2011**, *2*, 2158-2162.
- 4 (237) Torii, H. Amide I Vibrational Properties Affected by Hydrogen Bonding Out-of-Plane
5 of the Peptide Group. *J. Phys. Chem. Lett.* **2015**, *6*, 727-733.
- 6 (238) Torii, H. Strategy for Modeling the Electrostatic Responses of the Spectroscopic
7 Properties of Proteins. *J. Phys. Chem. B* **2018**, *122*, 154-164.
- 8 (239) Torii, H.; Noge, S. Roles of the Scalar and Vector Components of the Solvation Effects
9 on the Vibrational Properties of Hydrogen- or Halogen-Bond Accepting Stretching
10 Modes. *Phys. Chem. Chem. Phys.* **2016**, *18*, 10081-10096.
- 11 (240) Karjalainen, E.-L.; Ersmark, T.; Barth, A. Optimization of Model Parameters for
12 Describing the Amide I Spectrum of a Large Set of Proteins. *J. Phys. Chem. B* **2012**,
13 *116*, 4831-4842.
- 14 (241) Małolepsza, E.; Straub, J. E. Empirical Maps for the Calculation of Amide I Vibrational
15 Spectra of Proteins from Classical Molecular Dynamics Simulations. *J. Phys. Chem. B*
16 **2014**, *118*, 7848-7855.
- 17 (242) Miyazawa, T.; Blout, E. R. The Infrared Spectra of Polypeptides in Various
18 Conformations: Amide I and II Bands. *J. Am. Chem. Soc.* **1961**, *83*, 712-719.
- 19 (243) Ganim, Z.; Chung, H. S.; Smith, A. W.; DeFlores, L. P.; Jones, K. C.; Tokmakoff, A.
20 Amide I Two-Dimensional Infrared Spectroscopy of Proteins. *Acc. Chem. Res.* **2008**,
21 *41*, 432-441.
- 22 (244) Ghosh, A.; Ostrander, J. S.; Zanni, M. T. Watching Proteins Wiggle: Mapping
23 Structures with Two-Dimensional Infrared Spectroscopy. *Chem. Rev.* **2017**, *117*,
24 10726-10759.
- 25 (245) Byler, D. M.; Susi, H. Examination of the Secondary Structure of Proteins by
26 Deconvolved FTIR Spectra. *Biopolymers* **1986**, *25*, 469-487.
- 27 (246) Miyazawa, T. Perturbation Treatment of the Characteristic Vibrations of Polypeptide
28 Chains in Various Configurations. *J. Chem. Phys.* **1960**, *32*, 1647-1652.
- 29 (247) Mantsch, H. H.; Casal, H. L.; Jones, R. N. In *Spectroscopy of Biological Systems*; Clark,
30 R. J. H.; Hester, R. E., Eds.; Wiley: New York, 1986; Vol. 13.
- 31 (248) Surewicz, W. K.; Mantsch, H. H.; Chapman, D. Determination of Protein Secondary
32 Structure by Fourier Transform Infrared Spectroscopy: A Critical Assessment.
33 *Biochemistry* **1993**, *32*, 389-394.
- 34 (249) Torii, H.; Tasumi, M. In *Infrared Spectroscopy of Biomolecules*; Mantsch, H. H.;
35 Chapman, D., Eds.; Wiley-Liss: New York, 1996.
- 36 (250) Barth, A. Infrared Spectroscopy of Proteins. *Biochim. Biophys. Acta, Bioenerg.* **2007**,
37 *1767*, 1073-1101.
- 38 (251) Schweitzer-Stenner, R. Visible and UV-Resonance Raman Spectroscopy of Model
39 Peptides. *J. Raman Spectrosc.* **2001**, *32*, 711-732.
- 40 (252) Brauner, J. W.; Flach, C. R.; Mendelsohn, R. A Quantitative Reconstruction of the
41 Amide I Contour in the IR Spectra of Globular Proteins: From Structure to Spectrum.
42 *J. Am. Chem. Soc.* **2005**, *127*, 100-109.
- 43 (253) Chen, X. G.; Schweitzer-Stenner, R.; Krimm, S.; Mirkin, N. G.; Asher, S. A. N-
44 Methylacetamide and Its Hydrogen-Bonded Water Molecules Are Vibrationally
45 Coupled. *J. Am. Chem. Soc.* **1994**, *116*, 11141-11142.
- 46 (254) Hamm, P.; Lim, M.; DeGrado, W. F.; Hochstrasser, R. M. The Two-Dimensional IR
47 Nonlinear Spectroscopy of a Cyclic Penta-Peptide in Relation to Its Three-Dimensional
48 Structure. *Proc. Natl. Acad. Sci. U.S.A.* **1999**, *96*, 2036.

- 1 (255) Buchanan, L. E.; Carr, J. K.; Fluit, A. M.; Hoganson, A. J.; Moran, S. D.; de Pablo, J.
2 J.; Skinner, J. L.; Zanni, M. T. Structural Motif of Polyglutamine Amyloid Fibrils
3 Discerned with Mixed-Isotope Infrared Spectroscopy. *Proc. Natl. Acad. Sci. U.S.A.*
4 **2014**, *111*, 5796.
- 5 (256) Serrano, A. L.; Lomont, J. P.; Tu, L.-H.; Raleigh, D. P.; Zanni, M. T. A Free Energy
6 Barrier Caused by the Refolding of an Oligomeric Intermediate Controls the Lag Time
7 of Amyloid Formation by hIAPP. *J. Am. Chem. Soc.* **2017**, *139*, 16748-16758.
- 8 (257) Torii, H. Effects of Intermolecular Vibrational Coupling and Liquid Dynamics on the
9 Polarized Raman and Two-Dimensional Infrared Spectral Profiles of Liquid N,N-
10 Dimethylformamide Analyzed with a Time-Domain Computational Method. *J. Phys.*
11 *Chem. A* **2006**, *110*, 4822-4832.
- 12 (258) Torii, H. Electrostatic Origin of the Cooperative Effect on the CO Bond Lengths and
13 the Amide I Vibrational Frequencies of the N-Methylacetamide Oligomers. *J. Mol.*
14 *Struct.* **2005**, *735-736*, 21-26.
- 15 (259) Reppert, M.; Tokmakoff, A. Computational Amide I 2D IR Spectroscopy as a Probe of
16 Protein Structure and Dynamics. *Annu. Rev. Phys. Chem.* **2016**, *67*, 359-386.
- 17 (260) Reppert, M.; Tokmakoff, A. Electrostatic Frequency Shifts in Amide I Vibrational
18 Spectra: Direct Parameterization Against Experiment. *J. Chem. Phys.* **2013**, *138*,
19 134116.
- 20 (261) Wang, L.; Middleton, C. T.; Zanni, M. T.; Skinner, J. L. Development and Validation
21 of Transferable Amide I Vibrational Frequency Maps for Peptides. *J. Phys. Chem. B*
22 **2011**, *115*, 3713-3724.
- 23 (262) Ham, S.; Cho, M. Amide I Modes in the N-Methylacetamide Dimer and Glycine
24 Dipeptide Analog: Diagonal Force Constants. *J. Chem. Phys.* **2003**, *118*, 6915-6922.
- 25 (263) Andrushchenko, V.; Matějka, P.; Anderson, D. T.; Kaminský, J.; Horníček, J.; Paulson,
26 L. O.; Bouř, P. Solvent Dependence of the N-Methylacetamide Structure and Force
27 Field. *J. Phys. Chem. A* **2009**, *113*, 9727-9736.
- 28 (264) Reppert, M.; Tokmakoff, A. Communication: Quantitative Multi-Site Frequency Maps
29 for Amide I Vibrational Spectroscopy. *J. Chem. Phys.* **2015**, *143*, 061102.
- 30 (265) Jansen, T. L. C. Linear Absorption and Two-Dimensional Infrared Spectra of N-
31 Methylacetamide in Chloroform Revisited: Polarizability and Multipole Effects. *J.*
32 *Phys. Chem. B* **2014**, *118*, 8162-8169.
- 33 (266) Bondarenko, A. S.; Jansen, T. L. C. Application of Two-Dimensional Infrared
34 Spectroscopy to Benchmark Models for the Amide I Band of Proteins. *J. Chem. Phys.*
35 **2015**, *142*, 212437.
- 36 (267) Reppert, M.; Roy, A. R.; Tempkin, J. O. B.; Dinner, A. R.; Tokmakoff, A. Refining
37 Disordered Peptide Ensembles with Computational Amide I Spectroscopy: Application
38 to Elastin-Like Peptides. *J. Phys. Chem. B* **2016**, *120*, 11395-11404.
- 39 (268) Jansen, T. L. C.; Dijkstra, A. G.; Watson, T. M.; Hirst, J. D.; Knoester, J. Erratum:
40 "Modeling the Amide I Bands of Small Peptides" [*J. Chem. Phys.* 125, 044312 (2006)].
41 *J. Chem. Phys.* **2012**, *136*, 209901.
- 42 (269) Gorbunov, R. D.; Kosov, D. S.; Stock, G. Ab Initio-Based Exciton Model of Amide I
43 Vibrations in Peptides: Definition, Conformational Dependence, and Transferability. *J.*
44 *Chem. Phys.* **2005**, *122*, 224904.
- 45 (270) Moore, W. H.; Krimm, S. Transition Dipole Coupling in Amide I Modes of β
46 Polypeptides. *Proc. Natl. Acad. Sci. U.S.A.* **1975**, *72*, 4933.
- 47 (271) Torii, H.; Tasumi, M. Ab Initio Molecular Orbital Study of the Amide I Vibrational
48 Interactions between the Peptide Groups in Di- and Tripeptides and Considerations on
49 the Conformation of the Extended Helix. *J. Raman Spectrosc.* **1998**, *29*, 81-86.

- 1 (272) Hamm, P.; Woutersen, S. Coupling of the Amide I Modes of the Glycine Dipeptide.
2 *Bull. Chem. Soc. Jpn.* **2002**, *75*, 985-988.
- 3 (273) Zhuang, W.; Abramavicius, D.; Hayashi, T.; Mukamel, S. Simulation Protocols for
4 Coherent Femtosecond Vibrational Spectra of Peptides. *J. Phys. Chem. B* **2006**, *110*,
5 3362-3374.
- 6 (274) Torii, H.; Tasumi, M. Model Calculations on the Amide-I Infrared Bands of Globular
7 Proteins. *J. Chem. Phys.* **1992**, *96*, 3379-3387.
- 8 (275) Moran, A.; Mukamel, S. The Origin of Vibrational Mode Couplings in Various
9 Secondary Structural Motifs of Polypeptides. *Proc. Natl. Acad. Sci. U.S.A.* **2004**, *101*,
10 506.
- 11 (276) Gorbunov, R. D.; Stock, G. Ab Initio Based Building Block Model of Amide I
12 Vibrations in Peptides. *Chem. Phys. Lett.* **2007**, *437*, 272-276.
- 13 (277) Ham, S.; Cha, S.; Choi, J.-H.; Cho, M. Amide I Modes of Tripeptides: Hessian Matrix
14 Reconstruction and Isotope Effects. *J. Chem. Phys.* **2003**, *119*, 1451-1461.
- 15 (278) Maekawa, H.; Toniolo, C.; Broxterman, Q. B.; Ge, N.-H. Two-Dimensional Infrared
16 Spectral Signatures of 3_{10} - and α -Helical Peptides. *J. Phys. Chem. B* **2007**, *111*, 3222-
17 3235.
- 18 (279) Kabsch, W.; Sander, C. Dictionary of Protein Secondary Structure: Pattern Recognition
19 of Hydrogen-Bonded and Geometrical Features. *Biopolymers* **1983**, *22*, 2577-2637.
- 20 (280) Cai, K.; Han, C.; Wang, J. Molecular Mechanics Force Field-Based Map for Peptide
21 Amide-I Mode in Solution and Its Application to Alanine Di- and Tripeptides. *Phys.*
22 *Chem. Chem. Phys.* **2009**, *11*, 9149-9159.
- 23 (281) Choi, J.-H.; Lee, H.; Lee, K.-K.; Hahn, S.; Cho, M. Computational Spectroscopy of
24 Ubiquitin: Comparison between Theory and Experiments. *J. Chem. Phys.* **2007**, *126*,
25 045102.
- 26 (282) Cunha, A. V.; Bondarenko, A. S.; Jansen, T. L. C. Assessing Spectral Simulation
27 Protocols for the Amide I Band of Proteins. *J. Chem. Theory Comput.* **2016**, *12*, 3982-
28 3992.
- 29 (283) Baiz, C. R.; Peng, C. S.; Reppert, M. E.; Jones, K. C.; Tokmakoff, A. Coherent Two-
30 Dimensional Infrared Spectroscopy: Quantitative Analysis of Protein Secondary
31 Structure in Solution. *Analyst* **2012**, *137*, 1793-1799.
- 32 (284) Jorgensen, W. L.; Tirado-Rives, J. Potential Energy Functions for Atomic-Level
33 Simulations of Water and Organic and Biomolecular Systems. *Proc. Natl. Acad. Sci.*
34 *U.S.A.* **2005**, *102*, 6665.
- 35 (285) Cunha, A. V.; Salamatova, E.; Bloem, R.; Roeters, S. J.; Woutersen, S.; Pshenichnikov,
36 M. S.; Jansen, T. L. C. Interplay between Hydrogen Bonding and Vibrational Coupling
37 in Liquid N-Methylacetamide. *J. Phys. Chem. Lett.* **2017**, *8*, 2438-2444.
- 38 (286) Salamatova, E.; Cunha, A. V.; Bloem, R.; Roeters, S. J.; Woutersen, S.; Jansen, T. L.
39 C.; Pshenichnikov, M. S. Hydrophobic Collapse in N-Methylacetamide-Water
40 Mixtures. *J. Phys. Chem. A* **2018**, *122*, 2468-2478.
- 41 (287) Cheng, X.; Steele, R. P. Efficient Anharmonic Vibrational Spectroscopy for Large
42 Molecules Using Local-Mode Coordinates. *J. Chem. Phys.* **2014**, *141*, 104105.
- 43 (288) Panek, P. T.; Jacob, C. R. Efficient Calculation of Anharmonic Vibrational Spectra of
44 Large Molecules with Localized Modes. *ChemPhysChem* **2014**, *15*, 3365-3377.
- 45 (289) Hanson-Heine, M. W. D. Examining the Impact of Harmonic Correlation on
46 Vibrational Frequencies Calculated in Localized Coordinates. *J. Chem. Phys.* **2015**, *143*,
47 164104.

- 1 (290) Molina, A.; Smereka, P.; Zimmerman, P. M. Exploring the Relationship between
2 Vibrational Mode Locality and Coupling Using Constrained Optimization. *J. Chem.*
3 *Phys.* **2016**, *144*, 124111.
- 4 (291) Zimmerman, P. M.; Smereka, P. Optimizing Vibrational Coordinates to Modulate
5 Intermode Coupling. *J. Chem. Theory Comput.* **2016**, *12*, 1883-1891.
- 6 (292) Hanson-Heine, M. W. D. Intermediate Vibrational Coordinate Localization with
7 Harmonic Coupling Constraints. *J. Chem. Phys.* **2016**, *144*, 204116.
- 8 (293) Panek, P. T.; Jacob, C. R. Anharmonic Theoretical Vibrational Spectroscopy of
9 Polypeptides. *J. Phys. Chem. Lett.* **2016**, *7*, 3084-3090.
- 10 (294) Panek, P. T.; Jacob, C. R. On the Benefits of Localized Modes in Anharmonic
11 Vibrational Calculations for Small Molecules. *J. Chem. Phys.* **2016**, *144*, 164111.
- 12 (295) Hanson-Heine, M. W. D. Reduced Basis Set Dependence in Anharmonic Frequency
13 Calculations Involving Localized Coordinates. *J. Chem. Theory Comput.* **2018**, *14*,
14 1277-1285.
- 15 (296) Panek, P. T.; Hoeske, A. A.; Jacob, C. R. On the Choice of Coordinates in Anharmonic
16 Theoretical Vibrational Spectroscopy: Harmonic vs. Anharmonic Coupling in
17 Vibrational Configuration Interaction. *J. Chem. Phys.* **2019**, *150*, 054107.
- 18 (297) Hanson-Heine, M. W. D.; Hussein, F. S.; Hirst, J. D.; Besley, N. A. Simulation of Two-
19 Dimensional Infrared Spectroscopy of Peptides Using Localized Normal Modes. *J.*
20 *Chem. Theory Comput.* **2016**, *12*, 1905-1918.
- 21 (298) Jacob, C. R.; Reiher, M. Localizing Normal Modes in Large Molecules. *J. Chem. Phys.*
22 **2009**, *130*, 084106.
- 23 (299) Tadesse, L.; Nazarbaghi, R.; Walters, L. Isotopically Enhanced Infrared Spectroscopy:
24 A Novel Method for Examining Secondary Structure at Specific Sites in
25 Conformationally Heterogeneous Peptides. *J. Am. Chem. Soc.* **1991**, *113*, 7036-7037.
- 26 (300) Arkin, I. T. Isotope-Edited IR Spectroscopy for the Study of Membrane Proteins. *Curr.*
27 *Opin. Chem. Biol.* **2006**, *10*, 394-401.
- 28 (301) Fang, C.; Wang, J.; Charnley, A. K.; Barber-Armstrong, W.; Smith III, A. B.; Decatur,
29 S. M.; Hochstrasser, R. M. Two-Dimensional Infrared Measurements of the Coupling
30 between Amide Modes of an α -Helix. *Chem. Phys. Lett.* **2003**, *382*, 586-592.
- 31 (302) Moran, S. D.; Decatur, S. M.; Zanni, M. T. Structural and Sequence Analysis of the
32 Human γ D-Crystallin Amyloid Fibril Core Using 2D IR Spectroscopy, Segmental ^{13}C
33 Labeling, and Mass Spectrometry. *J. Am. Chem. Soc.* **2012**, *134*, 18410-18416.
- 34 (303) Huang, R.; Kubelka, J.; Barber-Armstrong, W.; Silva, R. A. G. D.; Decatur, S. M.;
35 Keiderling, T. A. Nature of Vibrational Coupling in Helical Peptides: An Isotopic
36 Labeling Study. *J. Am. Chem. Soc.* **2004**, *126*, 2346-2354.
- 37 (304) Ding, B.; Laaser, J. E.; Liu, Y.; Wang, P.; Zanni, M. T.; Chen, Z. Site-Specific
38 Orientation of an α -Helical Peptide Ovispirin-1 from Isotope-Labeled SFG
39 Spectroscopy. *J. Phys. Chem. B* **2013**, *117*, 14625-14634.
- 40 (305) Manor, J.; Arkin, I. T. Gaining Insight into Membrane Protein Structure Using Isotope-
41 Edited FTIR. *Biochimica et Biophysica Acta (BBA) - Biomembranes* **2013**, *1828*, 2256-
42 2264.
- 43 (306) Manor, J.; Arbely, E.; Beerlink, A.; Akkawi, M.; Arkin, I. T. Use of Isotope-Edited
44 FTIR to Derive a Backbone Structure of a Transmembrane Protein. *J. Phys. Chem. Lett.*
45 **2014**, *5*, 2573-2579.
- 46 (307) Buchanan, L. E.; Dunkelberger, E. B.; Tran, H. Q.; Cheng, P.-N.; Chiu, C.-C.; Cao, P.;
47 Raleigh, D. P.; de Pablo, J. J.; Nowick, J. S.; Zanni, M. T. Mechanism of IAPP Amyloid

- 1 Fibril Formation Involves an Intermediate with a Transient β -Sheet. *Proc. Natl. Acad. Sci. U.S.A.* **2013**, *110*, 19285.
- 2
- 3 (308) Shim, S.-H.; Gupta, R.; Ling, Y. L.; Strasfeld, D. B.; Raleigh, D. P.; Zanni, M. T. Two-
4 Dimensional IR Spectroscopy and Isotope Labeling Defines the Pathway of Amyloid
5 Formation with Residue-Specific Resolution. *Proc. Natl. Acad. Sci. U.S.A.* **2009**, *106*,
6 6614.
- 7 (309) Middleton, C. T.; Marek, P.; Cao, P.; Chiu, C.-c.; Singh, S.; Woys, A. M.; de Pablo, J.
8 J.; Raleigh, D. P.; Zanni, M. T. Two-Dimensional Infrared Spectroscopy Reveals the
9 Complex Behaviour of an Amyloid Fibril Inhibitor. *Nature Chemistry* **2012**, *4*, 355-
10 360.
- 11 (310) Dunkelberger, E. B.; Buchanan, L. E.; Marek, P.; Cao, P.; Raleigh, D. P.; Zanni, M. T.
12 Deamidation Accelerates Amyloid Formation and Alters Amylin Fiber Structure. *J. Am.*
13 *Chem. Soc.* **2012**, *134*, 12658-12667.
- 14 (311) Smith, A. W.; Lessing, J.; Ganim, Z.; Peng, C. S.; Tokmakoff, A.; Roy, S.; Jansen, T.
15 L. C.; Knoester, J. Melting of a β -Hairpin Peptide Using Isotope-Edited 2D IR
16 Spectroscopy and Simulations. *J. Phys. Chem. B* **2010**, *114*, 10913-10924.
- 17 (312) Wang, L.; Middleton, C. T.; Singh, S.; Reddy, A. S.; Woys, A. M.; Strasfeld, D. B.;
18 Marek, P.; Raleigh, D. P.; de Pablo, J. J.; Zanni, M. T. et al. 2DIR Spectroscopy of
19 Human Amylin Fibrils Reflects Stable β -Sheet Structure. *J. Am. Chem. Soc.* **2011**, *133*,
20 16062-16071.
- 21 (313) Woys, A. M.; Almeida, A. M.; Wang, L.; Chiu, C.-C.; McGovern, M.; de Pablo, J. J.;
22 Skinner, J. L.; Gellman, S. H.; Zanni, M. T. Parallel β -Sheet Vibrational Couplings
23 Revealed by 2D IR Spectroscopy of an Isotopically Labeled Macrocyclic: Quantitative
24 Benchmark for the Interpretation of Amyloid and Protein Infrared Spectra. *J. Am. Chem.*
25 *Soc.* **2012**, *134*, 19118-19128.
- 26 (314) Moore, W. H.; Krimm, S. Vibrational Analysis of Peptides, Polypeptides, and Proteins.
27 I. Polyglycine I. *Biopolymers* **1976**, *15*, 2439-2464.
- 28 (315) Woutersen, S.; Pfister, R.; Hamm, P.; Mu, Y.; Kosov, D. S.; Stock, G. Peptide
29 Conformational Heterogeneity Revealed from Nonlinear Vibrational Spectroscopy and
30 Molecular-Dynamics Simulations. *J. Chem. Phys.* **2002**, *117*, 6833-6840.
- 31 (316) Choi, J.-H.; Cho, M. Calculations of Intermode Coupling Constants and Simulations of
32 Amide I, II, and III Vibrational Spectra of Dipeptides. *Chem. Phys.* **2009**, *361*, 168-175.
- 33 (317) DeFlores, L. P.; Ganim, Z.; Ackley, S. F.; Chung, H. S.; Tokmakoff, A. The
34 Anharmonic Vibrational Potential and Relaxation Pathways of the Amide I and II
35 Modes of N-Methylacetamide. *J. Phys. Chem. B* **2006**, *110*, 18973-18980.
- 36 (318) Bloem, R.; Dijkstra, A. G.; Jansen, T. L. C.; Knoester, J. Simulation of Vibrational
37 Energy Transfer in Two-Dimensional Infrared Spectroscopy of Amide I and Amide II
38 Modes in Solution. *J. Chem. Phys.* **2008**, *129*, 055101.
- 39 (319) Dijkstra, A. G.; Jansen, T. L. C.; Knoester, J. Modeling the Vibrational Dynamics and
40 Nonlinear Infrared Spectra of Coupled Amide I and II Modes in Peptides. *J. Phys. Chem.*
41 *B* **2011**, *115*, 5392-5401.
- 42 (320) Rubtsov, I. V.; Wang, J.; Hochstrasser, R. M. Dual-Frequency 2D-IR Spectroscopy
43 Heterodyned Photon Echo of the Peptide Bond. *Proc. Natl. Acad. Sci. U.S.A.* **2003**, *100*,
44 5601.
- 45 (321) Maekawa, H.; Ballano, G.; Toniolo, C.; Ge, N.-H. Linear and Two-Dimensional
46 Infrared Spectroscopic Study of the Amide I and II Modes in Fully Extended Peptide
47 Chains. *J. Phys. Chem. B* **2011**, *115*, 5168-5182.

- 1 (322) Maekawa, H.; De Poli, M.; Toniolo, C.; Ge, N.-H. Couplings between Peptide Linkages
2 across a 3_{10} -Helical Hydrogen Bond Revealed by Two-Dimensional Infrared
3 Spectroscopy. *J. Am. Chem. Soc.* **2009**, *131*, 2042-2043.
- 4 (323) Dunkelberger, E. B.; Woys, A. M.; Zanni, M. T. 2D IR Cross Peaks Reveal Hydrogen–
5 Deuterium Exchange with Single Residue Specificity. *J. Phys. Chem. B* **2013**, *117*,
6 15297-15305.
- 7 (324) DeFlores, L. P.; Tokmakoff, A. Water Penetration into Protein Secondary Structure
8 Revealed by Hydrogen–Deuterium Exchange Two-Dimensional Infrared Spectroscopy.
9 *J. Am. Chem. Soc.* **2006**, *128*, 16520-16521.
- 10 (325) Giubertoni, G.; Meister, K.; DeVries, A. L.; Bakker, H. J. Determination of the Solution
11 Structure of Antifreeze Glycoproteins Using Two-Dimensional Infrared Spectroscopy.
12 *J. Phys. Chem. Lett.* **2019**, *10*, 352-357.
- 13 (326) Hayashi, T.; Mukamel, S. Two-Dimensional Vibrational Lineshapes of Amide III, II, I
14 and a Bands in a Helical Peptide. *J. Mol. Liq.* **2008**, *141*, 149-154.
- 15 (327) Hayashi, T.; Mukamel, S. Vibrational–Exciton Couplings for the Amide I, II, III, and
16 a Modes of Peptides. *J. Phys. Chem. B* **2007**, *111*, 11032-11046.
- 17 (328) Harms, G. S.; Pauls, S. W.; Hedstrom, J. F.; Johnson, C. K. Tyrosyl Fluorescence
18 Decays and Rotational Dynamics in Tyrosine Monomers and in Dipeptides. *Journal of*
19 *Fluorescence* **1997**, *7*, 273-282.
- 20 (329) Sul, S.; Feng, Y.; Le, U.; Tobias, D. J.; Ge, N.-H. Interactions of Tyrosine in Leu-
21 Enkephalin at a Membrane–Water Interface: An Ultrafast Two-Dimensional Infrared
22 Study Combined with Density Functional Calculations and Molecular Dynamics
23 Simulations. *J. Phys. Chem. B* **2010**, *114*, 1180-1190.
- 24 (330) Rubtsov, I. V.; Hochstrasser, R. M. Vibrational Dynamics, Mode Coupling, and
25 Structural Constraints for Acetylproline-NH₂. *J. Phys. Chem. B* **2002**, *106*, 9165-9171.
- 26 (331) Cai, K.; Du, F.; Zheng, X.; Liu, J.; Zheng, R.; Zhao, J.; Wang, J. General Applicable
27 Frequency Map for the Amide-I Mode in β -Peptides. *J. Phys. Chem. B* **2016**, *120*, 1069-
28 1079.
- 29 (332) Zhao, J.; Wang, J. Understanding the Amide-II Vibrations in β -Peptides. *J. Phys. Chem.*
30 *B* **2015**, *119*, 14831-14839.
- 31 (333) Zhao, J.; Wang, J. Dissecting Amide-I Vibration in β -Peptide Helices. *J. Phys. Chem.*
32 *B* **2015**, *119*, 3387-3397.
- 33 (334) Kim, J.-H.; Cho, M. Interplay of the Intramolecular Water Vibrations and Hydrogen
34 Bond in N-Methylacetamide-Water Complexes: Ab Initio Calculation Studies *Bull.*
35 *Korean Chem. Soc.* **2003**, *24*, 1061.
- 36 (335) van Wilderen, L. J. G. W.; Brunst, H.; Gustmann, H.; Wachtveitl, J.; Broos, J.;
37 Bredenbeck, J. Cyano-Tryptophans as Dual Infrared and Fluorescence Spectroscopic
38 Labels to Assess Structural Dynamics in Proteins. *Phys. Chem. Chem. Phys.* **2018**, *20*,
39 19906-19915.
- 40 (336) Biava, H.; Schreiber, T.; Katz, S.; Völler, J.-S.; Stolarski, M.; Schulz, C.; Michael, N.;
41 Budisa, N.; Kozuch, J.; Utesch, T. et al. Long-Range Modulations of Electric Fields in
42 Proteins. *J. Phys. Chem. B* **2018**, *122*, 8330-8342.
- 43 (337) Devereux, C. J.; Fulfer, K. D.; Zhang, X.; Kuroda, D. G. Vibrational Spectroscopy
44 Modeling of a Drug in Molecular Solvents and Enzymes. *Chem. Phys.* **2017**, *495*, 1-9.
- 45 (338) Torii, H. Unified Electrostatic Understanding on the Solvation-Induced Changes in the
46 CN Stretching Frequency and the NMR Chemical Shifts of a Nitrile. *J. Phys. Chem. A*
47 **2016**, *120*, 7137-7144.

- 1 (339) Maienschein-Cline, M. G.; Londergan, C. H. The CN Stretching Band of Aliphatic
2 Thiocyanate Is Sensitive to Solvent Dynamics and Specific Solvation. *J. Phys. Chem.*
3 *A* **2007**, *111*, 10020-10025.
- 4 (340) van Wilderen, L. J. G. W.; Kern-Michler, D.; Müller-Werkmeister, H. M.; Bredenbeck,
5 J. Correction: Vibrational Dynamics and Solvatochromism of the Label SCN in Various
6 Solvents and Hemoglobin by Time Dependent IR and 2D-IR Spectroscopy. *Phys. Chem.*
7 *Chem. Phys.* **2017**, *19*, 9676-9678.
- 8 (341) Sigala, P. A.; Fafarman, A. T.; Bogard, P. E.; Boxer, S. G.; Herschlag, D. Do Ligand
9 Binding and Solvent Exclusion Alter the Electrostatic Character within the Oxyanion
10 Hole of an Enzymatic Active Site? *J. Am. Chem. Soc.* **2007**, *129*, 12104-12105.
- 11 (342) Blankenburg, L.; Schroeder, L.; Habenstein, F.; Błasiak, B.; Kottke, T.; Bredenbeck, J.
12 Following Local Light-Induced Structure Changes and Dynamics of the Photoreceptor
13 PYP with the Thiocyanate IR Label. *Phys. Chem. Chem. Phys.* **2019**, *21*, 6622-6634.
- 14 (343) Schmidt-Engler, J. M.; Blankenburg, L.; Błasiak, B.; Wilderen, L. J. G. W. v.; Cho, M.;
15 Bredenbeck, *J. Anal. Chem.* **2019**, in press.
- 16 (344) Deb, P.; Haldar, T.; Kashid, S. M.; Banerjee, S.; Chakrabarty, S.; Bagchi, S. Correlating
17 Nitrile IR Frequencies to Local Electrostatics Quantifies Noncovalent Interactions of
18 Peptides and Proteins. *J. Phys. Chem. B* **2016**, *120*, 4034-4046.
- 19 (345) Layfield, J. P.; Hammes-Schiffer, S. Calculation of Vibrational Shifts of Nitrile Probes
20 in the Active Site of Ketosteroid Isomerase Upon Ligand Binding. *J. Am. Chem. Soc.*
21 **2013**, *135*, 717-725.
- 22 (346) Okuda, M.; Higashi, M.; Ohta, K.; Saito, S.; Tominaga, K. Vibrational Frequency
23 Fluctuations of Ionic Vibrational Probe in Water: Theoretical Study with Molecular
24 Dynamics Simulation. *Chem. Phys. Lett.* **2017**, *683*, 547-552.
- 25 (347) Park, K.-H.; Jeon, J.; Park, Y.; Lee, S.; Kwon, H.-J.; Joo, C.; Park, S.; Han, H.; Cho,
26 M. Infrared Probes Based on Nitrile-Derivatized Prolines: Thermal Insulation Effect
27 and Enhanced Dynamic Range. *J. Phys. Chem. Lett.* **2013**, *4*, 2105-2110.
- 28 (348) Yamada, S. A.; Thompson, W. H.; Fayer, M. D. Water-Anion Hydrogen Bonding
29 Dynamics: Ultrafast IR Experiments and Simulations. *J. Chem. Phys.* **2017**, *146*,
30 234501.
- 31 (349) Creon, A.; Josts, I.; Niebling, S.; Huse, N.; Tidow, H. Conformation-Specific Detection
32 of Calmodulin Binding Using the Unnatural Amino Acid P-Azido-Phenylalanine (AzF)
33 as an IR-Sensor. *Struct. Dyn.* **2018**, *5*, 064701.
- 34 (350) Thielges, M. C.; Axup, J. Y.; Wong, D.; Lee, H. S.; Chung, J. K.; Schultz, P. G.; Fayer,
35 M. D. Two-Dimensional IR Spectroscopy of Protein Dynamics Using Two Vibrational
36 Labels: A Site-Specific Genetically Encoded Unnatural Amino Acid and an Active Site
37 Ligand. *J. Phys. Chem. B* **2011**, *115*, 11294-11304.
- 38 (351) Zhang, J.; Wang, L.; Zhang, J.; Zhu, J.; Pan, X.; Cui, Z.; Wang, J.; Fang, W.; Li, Y.
39 Identifying and Modulating Accidental Fermi Resonance: 2D IR and DFT Study of 4-
40 Azido-L-Phenylalanine. *J. Phys. Chem. B* **2018**, *122*, 8122-8133.
- 41 (352) Müller-Werkmeister, H. M.; Li, Y.-L.; Lerch, E.-B. W.; Bigourd, D.; Bredenbeck, J.
42 Ultrafast Hopping from Band to Band: Assigning Infrared Spectra Based on Vibrational
43 Energy Transfer. *Angew. Chem. Int. Ed.* **2013**, *52*, 6214-6217.
- 44 (353) Lešetický, L.; Barth, R.; Nêmec, I.; Štícha, M.; Tišlerová, I. Synthesis and Spectra of
45 N-15 Labelled Phenylazides. *Czech. J. Phys.* **2003**, *53*, A777-A782.
- 46 (354) Baumann, T.; Hauf, M.; Schildhauer, F.; Eberl, K. B.; Durkin, P. M.; Deniz, E.; Löffler,
47 J. G.; Acevedo-Rocha, C. G.; Jaric, J.; Martins, B. M. et al. Site-Resolved Observation
48 of Vibrational Energy Transfer Using a Genetically Encoded Ultrafast Heater. *Angew.*
49 *Chem. Int. Ed.* **2019**, *58*, 2899-2903.

- 1 (355) Taskent-Sezgin, H.; Chung, J.; Banerjee, P. S.; Nagarajan, S.; Dyer, R. B.; Carrico, I.;
2 Raleigh, D. P. Azidohomoalanine: A Conformationally Sensitive IR Probe of Protein
3 Folding, Protein Structure, and Electrostatics. *Angew. Chem. Int. Ed.* **2010**, *49*, 7473-
4 7475.
- 5 (356) Park, E. S.; Boxer, S. G. Origins of the Sensitivity of Molecular Vibrations to Electric
6 Fields: Carbonyl and Nitrosyl Stretches in Model Compounds and Proteins. *J. Phys.*
7 *Chem. B* **2002**, *106*, 5800-5806.
- 8 (357) Lim, M.; Jackson, T. A.; Anfinrud, P. A. Ultrafast Rotation and Trapping of Carbon
9 Monoxide Dissociated from Myoglobin. *Nature Structural Biology* **1997**, *4*, 209-214.
- 10 (358) Anselmi, M.; Aschi, M.; Di Nola, A.; Amadei, A. Theoretical Characterization of
11 Carbon Monoxide Vibrational Spectrum in Sperm Whale Myoglobin Distal Pocket.
12 *Biophys. J.* **2007**, *92*, 3442-3447.
- 13 (359) Wang, X. w.; Zhang, J. Z. H.; He, X. Ab Initio Quantum Mechanics/Molecular
14 Mechanics Molecular Dynamics Simulation of CO in the Heme Distal Pocket of
15 Myoglobin. *Chin. J. Chem. Phys.* **2017**, *30*, 705-716.
- 16 (360) Choi, J.-H.; Kwak, K.-W.; Cho, M. Computational Infrared and Two-Dimensional
17 Infrared Photon Echo Spectroscopy of Both Wild-Type and Double Mutant Myoglobin-
18 CO Proteins. *J. Phys. Chem. B* **2013**, *117*, 15462-15478.
- 19 (361) Park, E. S.; Andrews, S. S.; Hu, R. B.; Boxer, S. G. Vibrational Stark Spectroscopy in
20 Proteins: A Probe and Calibration for Electrostatic Fields. *J. Phys. Chem. B* **1999**, *103*,
21 9813-9817.
- 22 (362) Torii, H. Theoretical Analysis and Modeling of the Electrostatic Responses of the
23 Vibrational and NMR Spectroscopic Properties of the Cyanide Anion. *J. Mol. Liq.* **2019**,
24 *284*, 773-779.
- 25 (363) Dluhy, R.; Cameron, D. G.; Mantsch, H. H.; Mendelsohn, R. Fourier Transform
26 Infrared Spectroscopic Studies of the Effect of Calcium Ions on Phosphatidylserine.
27 *Biochemistry* **1983**, *22*, 6318-6325.
- 28 (364) Valentine, M. L.; Cardenas, A. E.; Elber, R.; Baiz, C. R. Physiological Calcium
29 Concentrations Slow Dynamics at the Lipid-Water Interface. *Biophys. J.* **2018**, *115*,
30 1541-1551.
- 31 (365) Guerin, A. C.; Riley, K.; Rupnik, K.; Kuroda, D. G. Determining the Energetics of the
32 Hydrogen Bond through FTIR: A Hands-on Physical Chemistry Lab Experiment. *J.*
33 *Chem. Educ.* **2016**, *93*, 1124-1129.
- 34 (366) Edington, S. C.; Flanagan, J. C.; Baiz, C. R. An Empirical IR Frequency Map for Ester
35 C=O Stretching Vibrations. *J. Phys. Chem. A* **2016**, *120*, 3888-3896.
- 36 (367) Yu, Y.; Shi, L. Vibrational Solvatochromism of the Ester Carbonyl Vibration of PCBM
37 in Organic Solutions. *J. Chem. Phys.* **2019**, *151*, 064501.
- 38 (368) Meng, W.; Jiang, Y.; Wang, L. Structure, Dynamics and Vibrational Spectroscopy of
39 Omega-3 Fatty Acids. *in preparation*.
- 40 (369) Fang, B.; Wang, T.; Chen, X.; Jin, T.; Zhang, R.; Zhuang, W. Modeling Vibrational
41 Spectra of Ester Carbonyl Stretch in Water and DmsO Based on Molecular Dynamics
42 Simulation. *J. Phys. Chem. B* **2015**, *119*, 12390-12396.
- 43 (370) Baryames, C. P.; Teel, M.; Baiz, C. R. Interfacial H-Bond Dynamics in Reverse
44 Micelles: The Role of Surfactant Heterogeneity. *Langmuir* **2019**, *35*, 11463-11470.
- 45 (371) Ghosh, A.; Cohn, B.; Prasad, A. K.; Chuntanov, L. Quantifying Conformations of Ester
46 Vibrational Probes with Hydrogen-Bond-Induced Fermi Resonances. *J. Chem. Phys.*
47 **2018**, *149*, 184501.
- 48 (372) Xu, K. Electrolytes and Interphases in Li-Ion Batteries and Beyond. *Chem. Rev.* **2014**,
49 *114*, 11503-11618.

- 1 (373) Lee, K.-K.; Park, K.; Lee, H.; Noh, Y.; Kossowska, D.; Kwak, K.; Cho, M. Ultrafast
2 Fluxional Exchange Dynamics in Electrolyte Solvation Sheath of Lithium Ion Battery.
3 *Nature Communications* **2017**, *8*, 14658.
- 4 (374) Lim, J.; Lee, K.-K.; Liang, C.; Park, K.-H.; Kim, M.; Kwak, K.; Cho, M. Two-
5 Dimensional Infrared Spectroscopy and Molecular Dynamics Simulation Studies of
6 Nonaqueous Lithium Ion Battery Electrolytes. *J. Phys. Chem. B* **2019**, *123*, 6651-6663.
- 7 (375) Liang, C.; Kwak, K.; Cho, M. Revealing the Solvation Structure and Dynamics of
8 Carbonate Electrolytes in Lithium-Ion Batteries by Two-Dimensional Infrared
9 Spectrum Modeling. *J. Phys. Chem. Lett.* **2017**, *8*, 5779-5784.
- 10 (376) Fulfer, K. D.; Kuroda, D. G. Solvation Structure and Dynamics of the Lithium Ion in
11 Organic Carbonate-Based Electrolytes: A Time-Dependent Infrared Spectroscopy
12 Study. *J. Phys. Chem. C* **2016**, *120*, 24011-24022.
- 13 (377) Fulfer, K. D.; Kuroda, D. G. Ion Speciation of Lithium Hexafluorophosphate in
14 Dimethyl Carbonate Solutions: An Infrared Spectroscopy Study. *Phys. Chem. Chem.*
15 *Phys.* **2018**, *20*, 22710-22718.
- 16 (378) Li, F.; Skinner, J. L. Infrared and Raman Line Shapes for Ice I_h. II. H₂O and D₂O. *J.*
17 *Chem. Phys.* **2010**, *133*, 244504.
- 18 (379) Stenger, J.; Madsen, D.; Hamm, P.; Nibbering, E. T. J.; Elsaesser, T. A Photon Echo
19 Peak Shift Study of Liquid Water. *J. Phys. Chem. A* **2002**, *106*, 2341-2350.
- 20 (380) Stenger, J.; Madsen, D.; Hamm, P.; Nibbering, E. T. J.; Elsaesser, T. Ultrafast
21 Vibrational Dephasing of Liquid Water. *Phys. Rev. Lett.* **2001**, *87*, 027401.
- 22 (381) Schauss, J.; Kundu, A.; Fingerhut, B. P.; Elsaesser, T. Contact Ion Pairs of Phosphate
23 Groups in Water: Two-Dimensional Infrared Spectroscopy of Dimethyl Phosphate and
24 Ab Initio Simulations. *J. Phys. Chem. Lett.* **2019**, *10*, 6281-6286.
- 25 (382) Yeremenko, S.; Pshenichnikov, M. S.; Wiersma, D. A. Hydrogen-Bond Dynamics in
26 Water Explored by Heterodyne-Detected Photon Echo. *Chem. Phys. Lett.* **2003**, *369*,
27 107-113.
- 28 (383) Asbury, J. B.; Steinel, T.; Stromberg, C.; Corcelli, S. A.; Lawrence, C. P.; Skinner, J.
29 L.; Fayer, M. D. Water Dynamics: Vibrational Echo Correlation Spectroscopy and
30 Comparison to Molecular Dynamics Simulations. *J. Phys. Chem. A* **2004**, *108*, 1107-
31 1119.
- 32 (384) Asbury, J. B.; Steinel, T.; Kwak, K.; Corcelli, S. A.; Lawrence, C. P.; Skinner, J. L.;
33 Fayer, M. D. Dynamics of Water Probed with Vibrational Echo Correlation
34 Spectroscopy. *J. Chem. Phys.* **2004**, *121*, 12431-12446.
- 35 (385) Rey, R.; Moller, K. B.; Hynes, J. T. Hydrogen Bond Dynamics in Water and Ultrafast
36 Infrared Spectroscopy. *J. Phys. Chem. A* **2002**, *106*, 11993-11996.
- 37 (386) Lawrence, C. P.; Skinner, J. L. Vibrational Spectroscopy of HOD in Liquid D₂O. III.
38 Spectral Diffusion, and Hydrogen-Bonding and Rotational Dynamics. *J. Chem. Phys.*
39 **2003**, *118*, 264-272.
- 40 (387) Schmidt, J. R.; Roberts, S. T.; Loparo, J. J.; Tokmakoff, A.; Fayer, M. D.; Skinner, J.
41 L. Are Water Simulation Models Consistent with Steady-State and Ultrafast
42 Vibrational Spectroscopy Experiments? *Chem. Phys.* **2007**, *341*, 143-157.
- 43 (388) Corcelli, S. A.; Lawrence, C. P.; Asbury, J. B.; Steinel, T.; Fayer, M. D.; Skinner, J. L.
44 Spectral Diffusion in a Fluctuating Charge Model of Water. *J. Chem. Phys.* **2004**, *121*,
45 8897-8900.
- 46 (389) Colbert, D. T.; Miller, W. H. A Novel Discrete Variable Representation for Quantum-
47 Mechanical Reactive Scattering Via the S-Matrix Kohn Method. *J. Chem. Phys.* **1992**,
48 *96*, 1982-1991.

- 1 (390) Auer, B.; Kumar, R.; Schmidt, J. R.; Skinner, J. L. Hydrogen Bonding and Raman, IR,
2 and 2D-IR Spectroscopy of Dilute HOD in Liquid D₂O. *Proc. Natl. Acad. Sci. U.S.A.*
3 **2007**, *104*, 14215.
- 4 (391) Paarmann, A.; Hayashi, T.; Mukamel, S.; Miller, R. J. D. Nonlinear Response of
5 Vibrational Excitons: Simulating the Two-Dimensional Infrared Spectrum of Liquid
6 Water. *J. Chem. Phys.* **2009**, *130*, 204110.
- 7 (392) Lin, Y. S.; Auer, B. M.; Skinner, J. L. Water Structure, Dynamics, and Vibrational
8 Spectroscopy in Sodium Bromide Solutions. *J. Chem. Phys.* **2009**, *131*, 144511.
- 9 (393) Terranova, Z. L.; Corcelli, S. A. Molecular Dynamics Investigation of the Vibrational
10 Spectroscopy of Isolated Water in an Ionic Liquid. *J. Phys. Chem. B* **2014**, *118*, 8264-
11 8272.
- 12 (394) Stiopkin, I. V.; Weeraman, C.; Pieniazek, P. A.; Shalhout, F. Y.; Skinner, J. L.;
13 Benderskii, A. V. Hydrogen Bonding at the Water Surface Revealed by Isotopic
14 Dilution Spectroscopy. *Nature* **2011**, *474*, 192-195.
- 15 (395) Pieniazek, P. A.; Tainter, C. J.; Skinner, J. L. Interpretation of the Water Surface
16 Vibrational Sum-Frequency Spectrum. *J. Chem. Phys.* **2011**, *135*, 044701.
- 17 (396) Ni, Y.; Skinner, J. L. Communication: Vibrational Sum-Frequency Spectrum of the
18 Air-Water Interface, Revisited. *J. Chem. Phys.* **2016**, *145*, 031103.
- 19 (397) Auer, B. M.; Skinner, J. L. Water: Hydrogen Bonding and Vibrational Spectroscopy,
20 in the Bulk Liquid and at the Liquid/Vapor Interface. *Chem. Phys. Lett.* **2009**, *470*, 13-
21 20.
- 22 (398) Auer, B. M.; Skinner, J. L. Vibrational Sum-Frequency Spectroscopy of the Water
23 Liquid/Vapor Interface. *J. Phys. Chem. B* **2009**, *113*, 4125-4130.
- 24 (399) Auer, B. M.; Skinner, J. L. Vibrational Sum-Frequency Spectroscopy of the
25 Liquid/Vapor Interface for Dilute HOD in D₂O. *J. Chem. Phys.* **2008**, *129*, 214705.
- 26 (400) Ni, Y.; Gruenbaum, S. M.; Skinner, J. L. Slow Hydrogen-Bond Switching Dynamics at
27 the Water Surface Revealed by Theoretical Two-Dimensional Sum-Frequency
28 Spectroscopy. *Proc. Natl. Acad. Sci. U.S.A.* **2013**, *110*, 1992.
- 29 (401) Tainter, C. J.; Ni, Y.; Shi, L.; Skinner, J. L. Hydrogen Bonding and OH-Stretch
30 Spectroscopy in Water: Hexamer (Cage), Liquid Surface, Liquid, and Ice. *J. Phys.*
31 *Chem. Lett* **2013**, *4*, 12-17.
- 32 (402) Tainter, C. J.; Skinner, J. L. The Water Hexamer: Three-Body Interactions, Structures,
33 Energetics, and OH-Stretch Spectroscopy at Finite Temperature. *J. Chem. Phys.* **2012**,
34 *137*, 104304.
- 35 (403) Gruenbaum, S. M.; Pieniazek, P. A.; Skinner, J. L. Vibrational Spectroscopy of Water
36 in Hydrated Lipid Multi-Bilayers. II. Two-Dimensional Infrared and Peak Shift
37 Observables within Different Theoretical Approximations. *J. Chem. Phys.* **2011**, *135*,
38 164506.
- 39 (404) Gruenbaum, S. M.; Skinner, J. L. Vibrational Spectroscopy of Water in Hydrated Lipid
40 Multi-Bilayers. I. Infrared Spectra and Ultrafast Pump-Probe Observables. *J. Chem.*
41 *Phys.* **2011**, *135*, 075101.
- 42 (405) Gruenbaum, S. M.; Skinner, J. L. Vibrational Spectroscopy of Water in Hydrated Lipid
43 Multi-Bilayers. III. Water Clustering and Vibrational Energy Transfer. *J. Chem. Phys.*
44 **2013**, *139*, 175103.
- 45 (406) Roy, S.; Gruenbaum, S. M.; Skinner, J. L. Theoretical Vibrational Sum-Frequency
46 Generation Spectroscopy of Water near Lipid and Surfactant Monolayer Interfaces. II.
47 Two-Dimensional Spectra. *J. Chem. Phys.* **2014**, *141*, 22d505.

- 1 (407) Roy, S.; Gruenbaum, S. M.; Skinner, J. L. Theoretical Vibrational Sum-Frequency
2 Generation Spectroscopy of Water near Lipid and Surfactant Monolayer Interfaces. *J.*
3 *Chem. Phys.* **2014**, *141*, 18c502.
- 4 (408) Bakulin, A. A.; Cringus, D.; Pieniazek, P. A.; Skinner, J. L.; Jansen, T. L. C.;
5 Pshenichnikov, M. S. Dynamics of Water Confined in Reversed Micelles:
6 Multidimensional Vibrational Spectroscopy Study. *J. Phys. Chem. B* **2013**, *117*, 15545-
7 15558.
- 8 (409) Pieniazek, P. A.; Lin, Y.-S.; Chowdhary, J.; Ladanyi, B. M.; Skinner, J. L. Vibrational
9 Spectroscopy and Dynamics of Water Confined inside Reverse Micelles. *J. Phys. Chem.*
10 *B* **2009**, *113*, 15017-15028.
- 11 (410) Li, F.; Skinner, J. L. Infrared and Raman Line Shapes for Ice I_h. I. Dilute HOD in H₂O
12 and D₂O. *J. Chem. Phys.* **2010**, *132*, 204505.
- 13 (411) Shi, L.; Gruenbaum, S. M.; Skinner, J. L. Interpretation of IR and Raman Line Shapes
14 for H₂O and D₂O Ice I_h. *J. Phys. Chem. B* **2012**, *116*, 13821-13830.
- 15 (412) Shi, L.; Skinner, J. L.; Jansen, T. L. C. Two-Dimensional Infrared Spectroscopy of Neat
16 Ice I_h. *Phys. Chem. Chem. Phys.* **2016**, *18*, 3772-3779.
- 17 (413) Gruenbaum, S. M.; Tainter, C. J.; Shi, L.; Ni, Y.; Skinner, J. L. Robustness of
18 Frequency, Transition Dipole, and Coupling Maps for Water Vibrational Spectroscopy.
19 *J. Chem. Theory Comput.* **2013**, *9*, 3109-3117.
- 20 (414) Kananenka, A. A.; Yao, K.; Corcelli, S. A.; Skinner, J. L. Machine Learning for
21 Vibrational Spectroscopic Maps. *J. Chem. Theory Comput.* **2019**, *15*, 6850-6858.
- 22 (415) Corcelli, S. A.; Skinner, J. L. Infrared and Raman Line Shapes of Dilute HOD in Liquid
23 H₂O and D₂O from 10 to 90 °C. *J. Phys. Chem. A* **2005**, *109*, 6154-6165.
- 24 (416) Auer, B. M.; Skinner, J. L. Dynamical Effects in Line Shapes for Coupled
25 Chromophores: Time-Averaging Approximation. *J. Chem. Phys.* **2007**, *127*, 104105.
- 26 (417) Yang, M.; Skinner, J. L. Signatures of Coherent Vibrational Energy Transfer in IR and
27 Raman Line Shapes for Liquid Water. *Phys. Chem. Chem. Phys.* **2010**, *12*, 982-991.
- 28 (418) Yang, M.; Skinner, J. L. Time-Averaging Approximation in the Interaction Picture:
29 Absorption Line Shapes for Coupled Chromophores with Application to Liquid Water.
30 *J. Chem. Phys.* **2011**, *135*, 154114.
- 31 (419) Auer, B. M.; Skinner, J. L. IR and Raman Spectra of Liquid Water: Theory and
32 Interpretation. *J. Chem. Phys.* **2008**, *128*, 224511.
- 33 (420) Torii, H. Time-Domain Calculations of the Polarized Raman Spectra, the Transient
34 Infrared Absorption Anisotropy, and the Extent of Delocalization of the OH Stretching
35 Mode of Liquid Water. *J. Phys. Chem. A* **2006**, *110*, 9469-9477.
- 36 (421) Choi, J.-H.; Cho, M. Computational IR Spectroscopy of Water: OH Stretch Frequencies,
37 Transition Dipoles, and Intermolecular Vibrational Coupling Constants. *J. Chem. Phys.*
38 **2013**, *138*, 174108.
- 39 (422) Li, F.; Skinner, J. L. Erratum: "Infrared and Raman Line Shapes for Ice I_h. II. H₂O and
40 D₂O" [J. Chem. Phys. 133, 244504 (2010)]. *J. Chem. Phys.* **2011**, *134*, 099901.
- 41 (423) Biswas, R.; Carpenter, W.; Voth, G. A.; Tokmakoff, A. Molecular Modeling and
42 Assignment of IR Spectra of the Hydrated Excess Proton in Isotopically Dilute Water.
43 *J. Chem. Phys.* **2016**, *145*, 154504.
- 44 (424) Cowan, M. L.; Bruner, B. D.; Huse, N.; Dwyer, J. R.; Chugh, B.; Nibbering, E. T. J.;
45 Elsaesser, T.; Miller, R. J. D. Ultrafast Memory Loss and Energy Redistribution in the
46 Hydrogen Bond Network of Liquid H₂O. *Nature* **2005**, *434*, 199-202.
- 47 (425) Lindner, J.; Vöhringer, P.; Pshenichnikov, M. S.; Cringus, D.; Wiersma, D. A.;
48 Mostovoy, M. Vibrational Relaxation of Pure Liquid Water. *Chem. Phys. Lett.* **2006**,
49 *421*, 329-333.

- 1 (426) Tan, H.-S.; Piletic, I. R.; Fayer, M. D. Orientational Dynamics of Water Confined on a
2 Nanometer Length Scale in Reverse Micelles. *J. Chem. Phys.* **2005**, *122*, 174501.
- 3 (427) Piletic, I. R.; Moilanen, D. E.; Spry, D. B.; Levinger, N. E.; Fayer, M. D. Testing the
4 Core/Shell Model of Nanoconfined Water in Reverse Micelles Using Linear and
5 Nonlinear IR Spectroscopy. *J. Phys. Chem. A* **2006**, *110*, 4985-4999.
- 6 (428) Bakulin, A. A.; Pshenichnikov, M. S. Reduced Coupling of Water Molecules near the
7 Surface of Reverse Micelles. *Phys. Chem. Chem. Phys.* **2011**, *13*, 19355-19361.
- 8 (429) Cringus, D.; Jansen, T. L. C.; Pshenichnikov, M. S.; Wiersma, D. A. Ultrafast
9 Anisotropy Dynamics of Water Molecules Dissolved in Acetonitrile. *J. Chem. Phys.*
10 **2007**, *127*, 084507.
- 11 (430) Jansen, T. L. C.; Auer, B. M.; Yang, M.; Skinner, J. L. Two-Dimensional Infrared
12 Spectroscopy and Ultrafast Anisotropy Decay of Water. *J. Chem. Phys.* **2010**, *132*,
13 224503.
- 14 (431) Perakis, F.; Hamm, P. Two-Dimensional Infrared Spectroscopy of Neat Ice Ih. *Phys.*
15 *Chem. Chem. Phys.* **2012**, *14*, 6250-6256.
- 16 (432) Adhikari, A.; Re, S.; Nishima, W.; Ahmed, M.; Nihonyanagi, S.; Klauda, J. B.; Sugita,
17 Y.; Tahara, T. Water Orientation at Ceramide/Water Interfaces Studied by Heterodyne-
18 Detected Vibrational Sum Frequency Generation Spectroscopy and Molecular
19 Dynamics Simulation. *J. Phys. Chem. C* **2016**, *120*, 23692-23697.
- 20 (433) Inoue, K.; Nihonyanagi, S.; Singh, P. C.; Yamaguchi, S.; Tahara, T. 2D Heterodyne-
21 Detected Sum Frequency Generation Study on the Ultrafast Vibrational Dynamics of
22 H₂O and HOD Water at Charged Interfaces. *J. Chem. Phys.* **2015**, *142*, 212431.
- 23 (434) Singh, P. C.; Nihonyanagi, S.; Yamaguchi, S.; Tahara, T. Interfacial Water in the
24 Vicinity of a Positively Charged Interface Studied by Steady-State and Time-Resolved
25 Heterodyne-Detected Vibrational Sum Frequency Generation. *J. Chem. Phys.* **2014**,
26 *141*, 18C527.
- 27 (435) Singh, P. C.; Nihonyanagi, S.; Yamaguchi, S.; Tahara, T. Ultrafast Vibrational
28 Dynamics of Water at a Charged Interface Revealed by Two-Dimensional Heterodyne-
29 Detected Vibrational Sum Frequency Generation. *J. Chem. Phys.* **2012**, *137*, 094706.
- 30 (436) Roy, S.; Skoff, D.; Perroni, D. V.; Mondal, J.; Yethiraj, A.; Mahanthappa, M. K.; Zanni,
31 M. T.; Skinner, J. L. Water Dynamics in Gyroid Phases of Self-Assembled Gemini
32 Surfactants. *J. Am. Chem. Soc.* **2016**, *138*, 2472-2475.
- 33 (437) Chin, J. K.; Jimenez, R.; Romesberg, F. E. Direct Observation of Protein Vibrations by
34 Selective Incorporation of Spectroscopically Observable Carbon–Deuterium Bonds in
35 Cytochrome C. *J. Am. Chem. Soc.* **2001**, *123*, 2426-2427.
- 36 (438) Sagle, L. B.; Zimmermann, J.; Dawson, P. E.; Romesberg, F. E. Direct and High
37 Resolution Characterization of Cytochrome C Equilibrium Folding. *J. Am. Chem. Soc.*
38 **2006**, *128*, 14232-14233.
- 39 (439) Thielges, M. C.; Case, D. A.; Romesberg, F. E. Carbon–Deuterium Bonds as Probes of
40 Dihydrofolate Reductase. *J. Am. Chem. Soc.* **2008**, *130*, 6597-6603.
- 41 (440) Groff, D.; Thielges, M. C.; Cellitti, S.; Schultz, P. G.; Romesberg, F. E. Efforts toward
42 the Direct Experimental Characterization of Enzyme Microenvironments: Tyrosine100
43 in Dihydrofolate Reductase. *Angew. Chem. Int. Ed.* **2009**, *48*, 3478-3481.
- 44 (441) Adhikary, R.; Zimmermann, J.; Liu, J.; Forrest, R. P.; Janicki, T. D.; Dawson, P. E.;
45 Corcelli, S. A.; Romesberg, F. E. Evidence of an Unusual N–H···N Hydrogen Bond in
46 Proteins. *J. Am. Chem. Soc.* **2014**, *136*, 13474-13477.
- 47 (442) Le Sueur, A. L.; Schaugaard, R. N.; Baik, M.-H.; Thielges, M. C. Methionine Ligand
48 Interaction in a Blue Copper Protein Characterized by Site-Selective Infrared
49 Spectroscopy. *J. Am. Chem. Soc.* **2016**, *138*, 7187-7193.

- 1 (443) Bukowski, G. S.; Horness, R. E.; Thielges, M. C. Involvement of Local, Rapid
2 Conformational Dynamics in Binding of Flexible Recognition Motifs. *J. Phys. Chem.*
3 *B* **2019**, *123*, 8387-8396.
- 4 (444) Mirkin, N. G.; Krimm, S. A New Vibrational Spectroscopic Tool for the Determination
5 of Peptide Conformation: The Isotope-Edited C^αH^α Stretch Mode. *J. Phys. Chem. A*
6 **2004**, *108*, 10923-10924.
- 7 (445) Mirkin, N. G.; Krimm, S. Conformation Dependence of the C^αD^α Stretch Mode in
8 Peptides. I. Isolated Alanine Peptide Structures. *J. Phys. Chem. A* **2007**, *111*, 5300-
9 5303.
- 10 (446) Bykov, S. V.; Myshakina, N. S.; Asher, S. A. Dependence of Glycine CH₂ Stretching
11 Frequencies on Conformation, Ionization State, and Hydrogen Bonding. *J. Phys. Chem.*
12 *B* **2008**, *112*, 5803-5812.
- 13 (447) Miller, C. S.; Ploetz, E. A.; Cremeens, M. E.; Corcelli, S. A. Carbon-Deuterium
14 Vibrational Probes of Peptide Conformation: Alanine Dipeptide and Glycine Dipeptide.
15 *J. Chem. Phys.* **2009**, *130*, 125103.
- 16 (448) Bukowski, G. S.; Thielges, M. C. Residue-Specific Conformational Heterogeneity of
17 Proline-Rich Sequences Uncovered Via Infrared Spectroscopy. *Anal. Chem.* **2018**, *90*,
18 14355-14362.
- 19 (449) Cremeens, M. E.; Zimmermann, J.; Yu, W.; Dawson, P. E.; Romesberg, F. E. Direct
20 Observation of Structural Heterogeneity in a β-Sheet. *J. Am. Chem. Soc.* **2009**, *131*,
21 5726-5727.
- 22 (450) Horness, R. E.; Basom, E. J.; Mayer, J. P.; Thielges, M. C. Resolution of Site-Specific
23 Conformational Heterogeneity in Proline-Rich Molecular Recognition by Src
24 Homology 3 Domains. *J. Am. Chem. Soc.* **2016**, *138*, 1130-1133.
- 25 (451) Adhikary, R.; Zimmermann, J.; Liu, J.; Dawson, P. E.; Romesberg, F. E. Experimental
26 Characterization of Electrostatic and Conformational Heterogeneity in an SH3 Domain.
27 *J. Phys. Chem. B* **2013**, *117*, 13082-13089.
- 28 (452) Kinnaman, C. S.; Cremeens, M. E.; Romesberg, F. E.; Corcelli, S. A. Infrared Line
29 Shape of an A-Carbon Deuterium-Labeled Amino Acid. *J. Am. Chem. Soc.* **2006**, *128*,
30 13334-13335.
- 31 (453) Sagle, L. B.; Zimmermann, J.; Dawson, P. E.; Romesberg, F. E. A High-Resolution
32 Probe of Protein Folding. *J. Am. Chem. Soc.* **2004**, *126*, 3384-3385.
- 33 (454) Sagle, L. B.; Zimmermann, J.; Matsuda, S.; Dawson, P. E.; Romesberg, F. E. Redox-
34 Coupled Dynamics and Folding in Cytochrome C. *J. Am. Chem. Soc.* **2006**, *128*, 7909-
35 7915.
- 36 (455) Mirkin, N. G.; Krimm, S. Conformation Dependence of the C^αD^α Stretch Mode in
37 Peptides. II. Explicitly Hydrated Alanine Peptide Structures. *Biopolymers* **2009**, *91*,
38 791-800.
- 39 (456) Karow Jr, A. M. Cryoprotectants—a New Class of Drugs. *J. Pharm. Pharmacol.* **1969**,
40 *21*, 209-223.
- 41 (457) Rasmussen, D. H.; Mackenzie, A. P. Phase Diagram for the System Water–
42 Dimethylsulphoxide. *Nature* **1968**, *220*, 1315-1317.
- 43 (458) Oh, K.-I.; Rajesh, K.; Stanton, J. F.; Baiz, C. R. Quantifying Hydrogen-Bond
44 Populations in Dimethyl Sulfoxide/Water Mixtures. *Angew. Chem. Int. Ed.* **2017**, *56*,
45 11375-11379.
- 46 (459) Cutress, N. C.; Grindley, T. B.; Katritzky, A. R.; Shome, M.; Topsom, R. D. Infrared
47 Intensities as a Quantitative Measure of Intramolecular Interactions. Part XXIX. Methyl
48 Phenyl Sulphones and Sulphoxides. *J. Chem. Soc. Perkin Trans. 2* **1974**, 268-273.

- 1 (460) Keating, C. S.; McClure, B. A.; Rack, J. J.; Rubtsov, I. V. Sulfoxide Stretching Mode
2 as a Structural Reporter Via Dual-Frequency Two-Dimensional Infrared Spectroscopy.
3 *J. Chem. Phys.* **2010**, *133*, 144513.
- 4 (461) Baiz, C. R.; Oh, K.-I. Empirical Vibrational Frequency Map for the S=O Stretch. *J.*
5 *Chem. Phys.* **2019**, *151*, 234107.
- 6 (462) Du, X.; Frei, H.; Kim, S.-H. The Mechanism of GTP Hydrolysis by Ras Probed by
7 Fourier Transform Infrared Spectroscopy. *J. Biol. Chem.* **2000**, *275*, 8492-8500.
- 8 (463) Allin, C.; Ahmadian, M. R.; Wittinghofer, A.; Gerwert, K. Monitoring the Gap
9 Catalyzed H-Ras GTPase Reaction at Atomic Resolution in Real Time. *Proc. Natl.*
10 *Acad. Sci. U.S.A.* **2001**, *98*, 7754.
- 11 (464) Liu, M.; Krasteva, M.; Barth, A. Interactions of Phosphate Groups of ATP and Aspartyl
12 Phosphate with the Sarcoplasmic Reticulum Ca²⁺-ATPase: An FTIR Study. *Biophys. J.*
13 **2005**, *89*, 4352-4363.
- 14 (465) Dwyer, J. R.; Szyz, Ł.; Nibbering, E. T. J.; Elsaesser, T. Ultrafast Vibrational Dynamics
15 of Adenine-Thymine Base Pairs in DNA Oligomers. *J. Phys. Chem. B* **2008**, *112*,
16 11194-11197.
- 17 (466) Szyz, Ł.; Yang, M.; Nibbering, E. T. J.; Elsaesser, T. Ultrafast Vibrational Dynamics
18 and Local Interactions of Hydrated DNA. *Angew. Chem. Int. Ed.* **2010**, *49*, 3598-3610.
- 19 (467) Levinson, N. M.; Bolte, E. E.; Miller, C. S.; Corcelli, S. A.; Boxer, S. G. Phosphate
20 Vibrations Probe Local Electric Fields and Hydration in Biomolecules. *J. Am. Chem.*
21 *Soc.* **2011**, *133*, 13236-13239.
- 22 (468) Siebert, T.; Guchhait, B.; Liu, Y.; Costard, R.; Elsaesser, T. Anharmonic Backbone
23 Vibrations in Ultrafast Processes at the DNA–Water Interface. *J. Phys. Chem. B* **2015**,
24 *119*, 9670-9677.
- 25 (469) Floisand, D. J.; Corcelli, S. A. Computational Study of Phosphate Vibrations as
26 Reporters of DNA Hydration. *J. Phys. Chem. Lett.* **2015**, *6*, 4012-4017.
- 27 (470) Falk, M.; Hartman, K. A.; Lord, R. C. Hydration of Deoxyribonucleic Acid. I. A
28 Gravimetric Study. *J. Am. Chem. Soc.* **1962**, *84*, 3843-3846.
- 29 (471) Schauss, J.; Dahms, F.; Fingerhut, B. P.; Elsaesser, T. Phosphate–Magnesium Ion
30 Interactions in Water Probed by Ultrafast Two-Dimensional Infrared Spectroscopy. *J.*
31 *Phys. Chem. Lett.* **2019**, *10*, 238-243.
- 32 (472) Fingerhut, B. P.; Costard, R.; Elsaesser, T. Predominance of Short Range Coulomb
33 Forces in Phosphate-Water Interactions—a Theoretical Analysis. *J. Chem. Phys.* **2016**,
34 *145*, 115101.
- 35 (473) Polyanichko, A. M.; Andrushchenko, V. V.; Chikhirzhina, E. V.; Vorob'ev, V. I.;
36 Wieser, H. The Effect of Manganese(II) on DNA Structure: Electronic and Vibrational
37 Circular Dichroism Studies. *Nucleic Acids Res.* **2004**, *32*, 989-996.
- 38 (474) Krummel, A. T.; Zanni, M. T. DNA Vibrational Coupling Revealed with Two-
39 Dimensional Infrared Spectroscopy: Insight into Why Vibrational Spectroscopy Is
40 Sensitive to DNA Structure. *J. Phys. Chem. B* **2006**, *110*, 13991-14000.
- 41 (475) Choi, J.-H.; Ham, S.; Cho, M. Local Amide I Mode Frequencies and Coupling
42 Constants in Polypeptides. *J. Phys. Chem. B* **2003**, *107*, 9132-9138.
- 43 (476) Lee, C.; Park, K.-H.; Cho, M. Vibrational Dynamics of DNA. I. Vibrational Basis
44 Modes and Couplings. *J. Chem. Phys.* **2006**, *125*, 114508.
- 45 (477) Lee, C.; Cho, M. Vibrational Dynamics of DNA. II. Deuterium Exchange Effects and
46 Simulated IR Absorption Spectra. *J. Chem. Phys.* **2006**, *125*, 114509.
- 47 (478) Lee, C.; Park, K.-H.; Kim, J.-A.; Hahn, S.; Cho, M. Vibrational Dynamics of DNA. III.
48 Molecular Dynamics Simulations of DNA in Water and Theoretical Calculations of the
49 Two-Dimensional Vibrational Spectra. *J. Chem. Phys.* **2006**, *125*, 114510.

- 1 (479) Lee, C.; Cho, M. Vibrational Dynamics of DNA: IV. Vibrational Spectroscopic
2 Characteristics of A-, B-, and Z-Form DNA's. *J. Chem. Phys.* **2007**, *126*, 145102.
- 3 (480) Taillandier, E.; Liquier, J. In *Methods Enzymol.*; Academic Press, 1992; Vol. 211.
- 4 (481) Banyay, M.; Sarkar, M.; Gräslund, A. A Library of IR Bands of Nucleic Acids in
5 Solution. *Biophys. Chem.* **2003**, *104*, 477-488.
- 6 (482) Elsaesser, T. Two-Dimensional Infrared Spectroscopy of Intermolecular Hydrogen
7 Bonds in the Condensed Phase. *Acc. Chem. Res.* **2009**, *42*, 1220-1228.
- 8 (483) Peng, C. S.; Jones, K. C.; Tokmakoff, A. Anharmonic Vibrational Modes of Nucleic
9 Acid Bases Revealed by 2D IR Spectroscopy. *J. Am. Chem. Soc.* **2011**, *133*, 15650-
10 15660.
- 11 (484) Jiang, Y.; Wang, L. Development of Vibrational Frequency Maps for Nucleobases. *J.*
12 *Phys. Chem. B* **2019**, *123*, 5791-5804.
- 13 (485) Tajmir-Riahi, H. A.; Theophanides, T. An FT-IR Study of cis- and trans-
14 Dichlorodiammineplatinum(II) Bound to Inosine-5'-Monophosphate. *Can. J. Chem.*
15 **1984**, *62*, 1429-1440.
- 16 (486) van der Vegte, C. P.; Knop, S.; Vöhringer, P.; Knoester, J.; Jansen, T. L. C. OH-
17 Stretching in Synthetic Hydrogen-Bonded Chains. *J. Phys. Chem. B* **2014**, *118*, 6256-
18 6264.
- 19 (487) Shinokita, K.; Cunha, A. V.; Jansen, T. L. C.; Pshenichnikov, M. S. Hydrogen Bond
20 Dynamics in Bulk Alcohols. *J. Chem. Phys.* **2015**, *142*, 212450.
- 21 (488) Kwac, K.; Geva, E. Mixed Quantum-Classical Molecular Dynamics Study of the
22 Hydroxyl Stretch in Methanol/Carbon-Tetrachloride Mixtures II: Excited State
23 Hydrogen Bonding Structure and Dynamics, Infrared Emission Spectrum, and Excited
24 State Lifetime. *J. Phys. Chem. B* **2012**, *116*, 2856-2866.
- 25 (489) Kwac, K.; Geva, E. A Mixed Quantum-Classical Molecular Dynamics Study of the
26 Hydroxyl Stretch in Methanol/Carbon Tetrachloride Mixtures: Equilibrium Hydrogen-
27 Bond Structure and Dynamics at the Ground State and the Infrared Absorption
28 Spectrum. *J. Phys. Chem. B* **2011**, *115*, 9184-9194.
- 29 (490) Mesele, O. O.; Thompson, W. H. A "Universal" Spectroscopic Map for the OH
30 Stretching Mode in Alcohols. *J. Phys. Chem. A* **2017**, *121*, 5823-5833.
- 31 (491) Ni, Y.; Skinner, J. L. IR and SFG Vibrational Spectroscopy of the Water Bend in the
32 Bulk Liquid and at the Liquid-Vapor Interface, Respectively. *J. Chem. Phys.* **2015**, *143*,
33 014502.
- 34 (492) Falk, M. The Frequency of the H O H Bending Fundamental in Solids and Liquids.
35 *Spectrochimica Acta Part A: Molecular Spectroscopy* **1984**, *40*, 43-48.
- 36 (493) Pavlović, M.; Baranović, G.; Lovreković, D. Raman Study of the Bending Band of
37 Water. *Spectrochimica Acta Part A: Molecular Spectroscopy* **1991**, *47*, 897-906.
- 38 (494) Devlin, J. P.; Sadlej, J.; Buch, V. Infrared Spectra of Large H₂O Clusters: New
39 Understanding of the Elusive Bending Mode of Ice. *J. Phys. Chem. A* **2001**, *105*, 974-
40 983.
- 41 (495) Vinaykin, M.; Benderskii, A. V. Vibrational Sum-Frequency Spectrum of the Water
42 Bend at the Air/Water Interface. *J. Phys. Chem. Lett.* **2012**, *3*, 3348-3352.
- 43 (496) Ashihara, S.; Fujioka, S.; Shibuya, K. Temperature Dependence of Vibrational
44 Relaxation of the OH Bending Excitation in Liquid H₂O. *Chem. Phys. Lett.* **2011**, *502*,
45 57-62.
- 46 (497) Ashihara, S.; Huse, N.; Espagne, A.; Nibbering, E. T. J.; Elsaesser, T. Vibrational
47 Couplings and Ultrafast Relaxation of the O-H Bending Mode in Liquid H₂O. *Chem.*
48 *Phys. Lett.* **2006**, *424*, 66-70.

- 1 (498) Bodis, P.; Larsen, O. F. A.; Woutersen, S. Vibrational Relaxation of the Bending Mode
2 of HDO in Liquid D₂O. *J. Phys. Chem. A* **2005**, *109*, 5303-5306.
- 3 (499) Huse, N.; Ashihara, S.; Nibbering, E. T. J.; Elsaesser, T. Ultrafast Vibrational
4 Relaxation of O–H Bending and Librational Excitations in Liquid H₂O. *Chem. Phys.*
5 *Lett.* **2005**, *404*, 389-393.
- 6 (500) Larsen, O. F. A.; Woutersen, S. Vibrational Relaxation of the H₂O Bending Mode in
7 Liquid Water. *J. Chem. Phys.* **2004**, *121*, 12143-12145.
- 8 (501) Nagata, Y.; Hsieh, C.-S.; Hasegawa, T.; Voll, J.; Backus, E. H. G.; Bonn, M. Water
9 Bending Mode at the Water–Vapor Interface Probed by Sum-Frequency Generation
10 Spectroscopy: A Combined Molecular Dynamics Simulation and Experimental Study.
11 *J. Phys. Chem. Lett.* **2013**, *4*, 1872-1877.
- 12 (502) Jeon, J.; Lim, J. H.; Kim, S.; Kim, H.; Cho, M. Simultaneous Spectral and Temporal
13 Analyses of Kinetic Energies in Nonequilibrium Systems: Theory and Application to
14 Vibrational Relaxation of O–D Stretch Mode of HOD in Water. *J. Phys. Chem. A* **2015**,
15 *119*, 5356-5367.
- 16 (503) Jeon, J.; Hsieh, C.-S.; Nagata, Y.; Bonn, M.; Cho, M. Hydrogen Bonding and
17 Vibrational Energy Relaxation of Interfacial Water: A Full DFT Molecular Dynamics
18 Simulation. *J. Chem. Phys.* **2017**, *147*, 044707.
- 19 (504) Liang, C.; Jeon, J.; Cho, M. Ab Initio Modeling of the Vibrational Sum-Frequency
20 Generation Spectrum of Interfacial Water. *J. Phys. Chem. Lett.* **2019**, *10*, 1153-1158.
- 21 (505) Baiz, C. R.; Kubarych, K. J.; Geva, E.; Sibert, E. L. Local-Mode Approach to Modeling
22 Multidimensional Infrared Spectra of Metal Carbonyls. *J. Phys. Chem. A* **2011**, *115*,
23 5354-5363.
- 24 (506) Nilsen, I. A.; Osborne, D. G.; White, A. M.; Anna, J. M.; Kubarych, K. J. Monitoring
25 Equilibrium Reaction Dynamics of a Nearly Barrierless Molecular Rotor Using
26 Ultrafast Vibrational Echoes. *J. Chem. Phys.* **2014**, *141*, 134313.
- 27 (507) Eckert, P. A.; Kubarych, K. J. Dynamic Flexibility of Hydrogenase Active Site Models
28 Studied with 2D-IR Spectroscopy. *J. Phys. Chem. A* **2017**, *121*, 608-615.
- 29 (508) King, J. T.; Anna, J. M.; Kubarych, K. J. Solvent-Hindered Intramolecular Vibrational
30 Redistribution. *Phys. Chem. Chem. Phys.* **2011**, *13*, 5579-5583.
- 31 (509) Nee, M. J.; Baiz, C. R.; Anna, J. M.; McCanne, R.; Kubarych, K. J. Multilevel
32 Vibrational Coherence Transfer and Wavepacket Dynamics Probed with
33 Multidimensional IR Spectroscopy. *J. Chem. Phys.* **2008**, *129*, 084503.
- 34 (510) Baiz, C. R.; Kubarych, K. J.; Geva, E. Molecular Theory and Simulation of Coherence
35 Transfer in Metal Carbonyls and Its Signature on Multidimensional Infrared Spectra. *J.*
36 *Phys. Chem. B* **2011**, *115*, 5322-5339.
- 37 (511) Eckert, P. A.; Kubarych, K. J. Vibrational Coherence Transfer Illuminates Dark Modes
38 in Models of the Fefe Hydrogenase Active Site. *J. Chem. Phys.* **2019**, *151*, 054307.
- 39 (512) Kirkpatrick, P.; Ellis, C. Chemical Space. *Nature* **2004**, *432*, 823-823.
- 40 (513) Faber, F. A.; Hutchison, L.; Huang, B.; Gilmer, J.; Schoenholz, S. S.; Dahl, G. E.;
41 Vinyals, O.; Kearnes, S.; Riley, P. F.; von Lilienfeld, O. A. Prediction Errors of
42 Molecular Machine Learning Models Lower Than Hybrid DFT Error. *J. Chem. Theory*
43 *Comput.* **2017**, *13*, 5255-5264.
- 44 (514) Zou, H.; Hastie, T. Regularization and Variable Selection Via the Elastic Net. *J. Royal*
45 *Stat. Soc. B* **2005**, *67*, 301-320.
- 46 (515) Muller, K.; Mika, S.; Ratsch, G.; Tsuda, K.; Scholkopf, B. An Introduction to Kernel-
47 Based Learning Algorithms. *IEEE Trans. Neural Netw.* **2001**, *12*, 181-201.

- 1 (516) Kearnes, S.; McCloskey, K.; Berndl, M.; Pande, V.; Riley, P. Molecular Graph
2 Convolutions: Moving Beyond Fingerprints. *J. Comput. Aided Mol. Des.* **2016**, *30*, 595-
3 608.
- 4 (517) Li, Y.; Tarlow, D.; Brockschmidt, M.; Zemel, R.; arXiv:1511.05493, 2015.
- 5 (518) Kwac, K.; Cho, M. Differential Evolution Algorithm Approach for Describing
6 Vibrational Solvatochromism. *J. Chem. Phys.* **2019**, *151*, 134112.
- 7 (519) Storn, R.; Price, K. Differential Evolution – a Simple and Efficient Heuristic for Global
8 Optimization over Continuous Spaces. *J. Global Optim.* **1997**, *11*, 341-359.
- 9 (520) Price, K. V.; Storn, R. M.; Lampinen, J. A. *Differential Evolution: A Practical*
10 *Approach to Global Optimization*; Springer: New York, 2005.
- 11 (521) Rasmussen, C. E.; Williams, C. K. I. *Gaussian Processes for Machine Learning*; The
12 MIT Press: Cambridge, MA, USA, 2006.
- 13 (522) Ramakrishnan, R.; Dral, P. O.; Rupp, M.; von Lilienfeld, O. A. Big Data Meets
14 Quantum Chemistry Approximations: The Δ -Machine Learning Approach. *J. Chem.*
15 *Theory Comput.* **2015**, *11*, 2087-2096.
- 16 (523) Behler, J.; Parrinello, M. Generalized Neural-Network Representation of High-
17 Dimensional Potential-Energy Surfaces. *Phys. Rev. Lett.* **2007**, *98*, 146401.
- 18 (524) Behler, J. Atom-Centered Symmetry Functions for Constructing High-Dimensional
19 Neural Network Potentials. *J. Chem. Phys.* **2011**, *134*, 074106.
- 20 (525) Kwac, K.; Cho, M. Machine Learning Approach for Describing Vibrational
21 Solvatochromism. *J. Chem. Phys.* **2020**, *152*, 174101.
- 22 (526) Krizhevsky, A.; Sutskever, I.; Hinton, G. E. In *Advances in Neural Information*
23 *Processing Systems 25*, 2012.
- 24 (527) Mitchell, T. *Machine Learning*; McGraw Hill, 1997.
- 25 (528) Murphy, K. P. *Machine Learning: A Probabilistic Perspective*; The MIT Press:
26 Cambridge, 2012.
- 27 (529) Gastegger, M.; Behler, J.; Marquetand, P. Machine Learning Molecular Dynamics for
28 the Simulation of Infrared Spectra. *Chem. Sci.* **2017**, *8*, 6924-6935.
- 29